Diss ETH No. 15010

Observations of scattering polarization and the Hanle effect in the Sun's atmosphere

Michele Bianda

Diss ETH No. 15010

Observations of scattering polarization and the Hanle effect in the Sun's atmosphere

Diss ETH No. 15010

Observations of scattering polarization and the Hanle effect in the Sun's atmosphere

A dissertation submitted to the

SWISS FEDERAL INSTITUTE OF TECHNOLOGY
ZURICH

for the degree of
Doktor der Naturwissenschaften

Presented by

Michele Bianda

Dipl. Phys. ETH
born April 24th 1956
from Losone, Ti

accepted on the recommendation of

Prof. Dr. J.O. Stenflo, examiner
Prof. Dr. S.K. Solanki and
Dr. A. Gandorfer, coexaminers

Zurich, 2003

— To my parents —

Preface

It is difficult to summarize the reasons at the origin of a chain of events bringing to a final result. This Thesis reports some scientific results obtained on the basis of observations performed at the Locarno solar observatory Istituto Ricerche Solari Locarno – IRSOL in close collaboration with the Institute of Astronomy of the ETH in Zurich. The aim is to describe how ideas, instruments, observing methods and interpretation evolved to reach the conclusions. But the aspect I will point out in this preface is the role of persons who invested time and energy in this enterprise. In fact the evolution of the institute in Locarno and the achievement of these scientific results are related very closely.

The solar research station constructed in 1960 by the Universitäts-Sternwarte Göttingen in Germany was taken over by a private foundation in 1987, after it was dismantled. The motivation to reconstruct and develop the institute as an independent research center was based on the enthusiasm and on the interest in science of Alessandro Rima and Paul Utermohlen (†1992) at the head of a group of people convinced that the research at IRSOL had to go forward. The decision to sell the institute to this foundation, avoiding more profitable solutions, showed an open mind and real cultural interest of the Deutsche Forschungsgemeinschaft (represented by Axel Zienicke) and the Universitäts-Sternwarte Göttingen – USWG directed by Hans Heinrich Voigt.

The competence of Rima and Utermohlen, based on a large know-how, permitted to define the general direction and objectives of IRSOL. In a second phase the leadership was taken over by Philippe Jetzer, who followed the intentions of his predecessors and could show the direction in which IRSOL should evolve scientifically.

The technical and scientific work was my task. The role played by other people was indispensable help in the reconstruction. I would

like to remember Edi Alge (†2001) who was treasurer and technician of the institute. His optimism, his availability to help and his technical competence were always at disposal for the development of IRSOL. For the instrumental reconstruction, the help received by Karl Heinz Duensing was fundamental. He designed and constructed improved versions of the dismantled mechanical parts, and helped in the refurbishing of the pieces left in Locarno. The alignment of the Gregory Coudé telescope and the spectrograph was done by Eberhard Wiehr, who always stayed in contact with IRSOL for scientific works as well. The help of Axel Wittmann covered many domains: technical questions about the computer system, science (the first scientific work under FIRSOL of the institute in Locarno was with him), bureaucracy. All this contributions were allowed and supported (with the constraint that they should not interfere with the work in Tenerife) by the director of the USWG, H.H. Voigt and his successor Franz Kneer.

The development of electronics devices was possible thanks the collaboration of Gerd Küveler of the Fachochschule in Wiesbaden – FHSW. He did his Ph.D. at USWG in 1982 based on data recorded in Locarno. About 50 students of the FHSW have got their Diploma with a topic related to IRSOL.

The instrument was reconstructed, and some troubles with the government related to the financing of the institute could find a solution. Thus more time could be devoted to the principal objective of the institute: the scientific work. The contacts with Jan Olof Stenflo, director of the ETH Institute of Astronomy in Zurich, were always continued during the reconstruction phase, and it is to mention that his help in critical situations was always decisive. The definition of scientific observating projects with him and Sami Solanki permitted us to explore a solar physics domain which is showing a dramatic increase in interest world-wide. The collaboration of the entire Zurich team was always not only a scientific opportunity, but a way to meet a very amicable group of friends. With all the persons I could mention, I just pick out a few of them: Achim Gandorfer, who worked in Locarno for years to prepare and complete his project *'The atlas of the second solar spectrum'* and contributed in an important way to the life of IRSOL. Daniel Gisler spent long times in Locarno and could give important help. Dominique Fluri, who is completing his Thesis at the same time

as mine, was always ready to give his help in critical moments.

Observing with ZIMPOL (Zurich IMaging POLarimeter), the world-wide best solar polarimeter in the visible and near UV, is a unique experience. The support of Peter Povel, Peter Steiner, Frieder Aebersold was always effective and friendly.

Many scientific projects were started at IRSOL. With Alessandro Cacciani we are working at topics related to his magneto-optical filter. With Meir Semel and Arturo Lopez Ariste polarization observations were performed. Guido Sonnabend and Daniel Wirtz tested the infrared heterodyne sensor THIS.

The help given by Annelise Alge for the keeping of the house and the garden at IRSOL is joined to her kindness.

The experience acquired at IRSOL allowed me to spend more months at the Solar Observatory Sunspot in Sacramento Peak, New Mexico, in the group of Don Neidig. This gave me the opportunity to work in a big observatory together with a large scientific community. There I had the opportunity to know people as friends and not only as scientists.

My occupation after I got my Diploma was at Specola Solare Ticinese in Locarno, where I worked with and learned from Sergio Cortesi.

The Institute of Applied Physics, University of Bern, developed at Specola Solare Ticinese a solar flares observing program in the visible lasting for almost 15 years starting in 1980. I had the opportunity to collaborate with more graduate and PhD students of the Bern Institute. The collaboration with Andreas Magun is still actual.

The persons in the foundation council of FIRSOL are never directly mentioned in the description of the scientific results, but all what is done at the institute would not be possible without their unseen work.

I finally need to point out that the success of the work described in this Thesis is due not only to my work, but to a chain of important contributions from a number of people.

The words I would say to all of them is: thank you!

My hope is that this Thesis will be another small step in the IRSOL development, seen as a contribution to the cultural development of our society.

Abstract

The topic of this Thesis deals with polarization observations in selected regions on the solar disk. While the spatial resolution is modest, the polarimetric sensitivity and spectral resolution are high. The main aim is to investigate coherent scattering polarization and its interaction with magnetic fields. As a spin-off we also explore the impact polarization in solar flares.

The solar atmosphere is in the plasma state under strong influence of magnetic fields. The study of the solar magnetic field was until few years ago related almost exclusively to the Zeeman effect, which requires coherently oriented magnetic field in the observed area.

Another effect related to the magnetic field, the Hanle effect, obeys other symmetries and therefore allows us to study turbulent magnetic fields that do not carry any net flux. This effect manifests itself only by coherent scattering, as it is related to the coherence between the atomic states. The difficulty related to the use of this method has to do with the high polarimetric precision required by the observations.

This Thesis describes the results obtained using two polarimeters. The first one is very simple from a technical point of view: it is the two beams exchange polarimeter. The second one is ZIMPOL2, the world's best polarimeter in the visible and near UV. Scattering polarization observations in the Ca I 4227 Å and Sr II 4078 Å lines allowed us to measure signatures predicted by the theory of the Hanle effect, in terms of depolarization and rotation of the polarization plane. The analysis of these signatures allows us to measure the magnetic fields in a parameter range that is unreachable to the Zeeman effect, and to gain information about their geometry.

Observations with ZIMPOL permitted us to observe in active regions scattering polarization signatures which are in apparent contradiction with available theory. The Hanle effect is expected to operate

in the line center but vanish in the wings. The ZIMPOL observations show Hanle signatures which persist in the wings, an enigmatic behaviour that needs to be explained in the future.

Another solar physics topic where linear polarization is expected to manifest itself is related with solar flares. Impact polarization is an effect measured in laboratories. The literature contains several papers claiming that it has been observed to occur in solar Hα eruptions too. Measurements at IRSOL, in support of the RHESSI project, did not find evidence for Hα impact polarization in any of the 23 Hα flares studied, in spite of the much higher sensitivity of ZIMPOL in comparison with the observations of the published claims.

Riassunto

Il tema trattato in questa tesi è legato a misure di polarizzazione in aree particolari del disco solare con tecniche ad alta risoluzione spettrale e polarimetrica e con risoluzione spaziale media. Lo scopo principale consiste nello studio della polarizzazione presente nella diffusione coerente e la sua interazione con il campo magnetico. È anche stato trattato il tema della polarizzazione da impatto nelle eruzioni solari.

L'atmosfera solare si trova nello stato di plasma ed è intimamente connessa con campi magnetici. Il loro studio fino a pochi anni fa era possibile solamente utilizzando l'effetto Zeeman, che però presuppone la presenza di un campo magnetico orientato nell'area osservata.

Un altro fenomeno fisico, l'effetto Hanle, obbedisce ad altre simmetrie e permette lo studio di campi magnetici turbolenti, anche nel caso di un flusso totale nullo. Si manifesta unicamente nella diffusione coerente essendo legato alla coerenza tra stati atomici. La difficoltà legata all'uso dell'effetto Hanle sta nella precisione polarimetrica richiesta alle osservazioni.

Questa tesi presenta i risultati ottenuti utilizzando due polarimetri. Il primo, tecnicamente semplice, è un sistema a scambio di fascio; il secondo è ZIMPOL2, il miglior polarimetro a livello mondiale nel visibile e nell'ultravioletto vicino. Le misure della polarizzazione da diffusione coerente nelle righe Ca I 4227 Å e Sr II 4078 Å hanno permesso di rilevare comportamenti previsti dalla teoria. In particolare si sono osservati segnali di depolarizzazione Hanle e la rotazione del piano di polarizzazione. Dalla loro analisi è stato possibile determinare l'ordine di grandezza di campi magnetici inaccessibili all'effetto Zeeman e guadagnare informazioni sulla loro geometria.

Misure eseguite con ZIMPOL hanno permesso di osservare in regioni magneticamente attive al bordo solare un comportamento in apparente contrasto con la teoria disponibile al momento. Questa

prevede che l'effetto Hanle si manifesti al centro della riga e che scompaia nelle ali. Le osservazioni con ZIMPOL mostrano invece dei casi in cui l'effetto persiste, dunque una spiegazione teorica deve essere ancora trovata.

Un altro campo di ricerca in cui sono attesi segnali di polarizzazione è legato allo studio delle eruzioni solari. Il fenomeno della polarizzazione da impatto, misurato nei laboratori terrestri, secondo la letteratura si dovrebbe mettere in evidenza pure nel corso di eruzioni solari. Un progetto, pensato come appoggio alle osservazioni RHESSI, non ha però confermato, in 23 casi osservati, i risultati relativi a misure nella riga Hα descritti nella letteratura.

Contents

Chapter 1

Introduction

The information we can acquire from the solar atmosphere needs to be brought by the light emitted or absorbed by it. For observational stellar astrophysics the source of light has almost always to be considered the integrated stellar disk but in solar observations we can spatially discriminate the emitting atmospheric regions. The role of the telescope consists in allowing the selection of regions on the solar disk to be observed. The minimum dimension of the resolved area depends principally on the aperture of the telescope and on the image quality, which is related to the terrestrial atmosphere. The light emitted by such an area and which reaches the telescope can be analysed with spectroscopic and polarimetric techniques. In this way we can receive all information contained in the beam.

1.1 Observatory and instrumentation

The scientific work described in the next chapters were made possible by the facilities of the Istituto Ricerche Solari Locarno – IRSOL. The reconstruction and upgrade of the institute plays a role in achieving the results described later.

1.1.1 IRSOL, short history

Observatory in Locarno-Orselina, was founded and operated as an external station by Universitäts-Sternwarte in Göttingen (USWG) from 1960 to 1984 (Brückner et al. 1967; Wiehr et al. 1980). The USWG left

Locarno and transferred its facilities to Tenerife (Canary Islands). The instruments of Locarno were largely used for the new telescope.

In 1987 the foundation Fondazione Istituto Ricerche Solari Locarno – FIRSOL took over the observatory. I was charged to reconstruct the instrument. After 1984 only the mechanical mounting of the telescope was left in Locarno, without optics and electronics. The first priority was the instrument restoration. Karl Heinz Duensing (USWG) planned and constructed the missing mechanical parts and contributed to restoring the material left in Locarno. The reconstructed slit jaw, monochromator, grating support, were improved versions of the original instruments used in Tenerife. Eberhard Wiehr (USWG) aligned the optics of the telescope and the spectrograph. Electronic instruments were built in collaboration with Gerd Küveler (Fachhochschule Wiesbaden - FHSW): the control system of the spectrograph, the automatic guiding system, the flare detection system were developed as Diploma thesis work at FHSW.

Together with technical works, different bureaucratic problems needed to be resolved in order for IRSOL to be recognized and financed by the government.

In 1991 the first scientific observations were performed. Axel Wittmann (UWSG) started an observing campaign to better define the solar diameter (Wittmann et al. 1991; 1993). Another work in collaboration with Göttingen was related to the study of oscillations in prominences (Sütterlin et al. 1997).

For the development of the scientific work at IRSOL the collaboration with the ETHZ Institute of Astronomy directed by Jan Stenflo played a central role. The first work with Zurich was related to observations of signatures caused by shockwaves in the solar granulation (Solanki et al. 1996).

The observations related to polarimetric measurements described in the next chapters allowed us to explore a topic which is acquiring importance in the solar physics community.

Recordings performed at IRSOL permitted Achim Gandorfer of the Institute of Astronomy in Zurich to publish his first two volumes of the scattering polarization atlas (Gandorfer 2000; 2002).

1.1.2 Telescope and Spectrograph

The main instruments of IRSOL are: the Gregory Coudé telescope and the Czerny Turner spectrograph.

The telescope has an aperture of 45 cm and 25 m effective focal length. It is evacuated, with an entrances and an exit window, in order to avoid turbulences in the tube. The design was proposed by ten Bruggencate & Voigt (1958) and the actual version was constructed by UWSG. The automatic guiding system (Küveler et al. 1998) allows long exposures.

The spectrograph is based on a 300 lines/mm, 180×360 mm grating, has a focal length of 10 m and is controlled by a microcomputer provided by the FHSW. A monochromator based on a prism at the entrance of the spectrograph separates the grating order.

1.1.3 Special properties of IRSOL

The IRSOL instrument was constructed in the early 1960s and even if constantly improved, it cannot be called a new instrument. Nevertheless the concept of the instrument has properties which are still unique. The number of optical surfaces is relatively limited: two windows and four mirrors in front of the focal plane, five mirrors and a prism in the monochromator, 6 mirrors and a grating in the spectrograph. The access to the beam is quite easy, and it is possible to install new and different experiments. For instance with relatively few mechanical changes (new optical benches) it was possible to install the Zurich Imaging POLarimeter ZIMPOL.

The instrumental polarization induced by the telescope, mainly due to the folding mirrors, is low and constant over the day. At the equinoxes it is much reduced, because the effects of each mirror mutually compensate (Sánchez Almeida et al. 1991).

Locarno is easily reachable (in particular from Zurich) and this allows the possibility to develop programs which require time consuming instrumental preparations and long observing times. The experience gained here can then be used in larger telescopes in the USA and in the Canary Islands.

The seeing quality in Locarno is less good than at the best observa-

tories in the USA and in the Canary Islands. A 45 cm instrument may be regarded as a medium size solar instrument. It can nevertheless be used for front-line research for the following reasons. The accuracy of solar observations may be seen as a combination of four parameters: the spatial resolution related to the minimum dimension of a resolved structure, the temporal resolution, i.e. the time required to record the data, the spectral resolution, and the polarimetric precision. The knowledge we have about solar physics may be seen as acquired from observations which are located in particular sectors of this four-dimensional space. All existing instruments allow us in certain areas of the above mentioned space. The aim for an observer is to be able to explore a new area and find there either results predicted by the theory or unexpected results. The combination of the IRSOL instruments with the two beams exchange polarimeter and with ZIMPOL allowed and still allows us to investigate unexplored areas.

Finally political considerations need to be mentioned: the Canton of Ticino is now developing its university, and IRSOL may play a role in this evolution. It will always be more important for a university to offer the students the opportunity to spend time at research institutes during their education.

1.2 Polarized light and polarimetry

The topics treated in the next chapters are related to polarimetry, and some concepts about polarization and how to measure it are summarized in this section.

1.2.1 Stokes formalism

The Stokes formalism can be used to describe the polarization properties of light. A beam is completely defined by a four-dimensional Stokes vector

$$\boldsymbol{S} = \begin{pmatrix} I \\ Q \\ U \\ V \end{pmatrix}, \tag{1.1}$$

describing: its total intensity I, the intensity of linear polarization in a previously defined coordinate basis, Q, the intensity of linear polarization in a second basis rotated by 45º, U, and the intensity of circular polarization, V. I,Q,U and V are known as the Stokes parameters.

Some advantages of this description are its capacity to treat partially polarized beams, i.e. a mixture of polarized and unpolarized light, and to define quantities which are measurable with instruments.

The interaction of a beam with matter may be described by the product a Stokes vector with a Mueller matrix $\hat{M}$:

$$S' = \hat{M}S. \tag{1.2}$$

S' describes the emerging beam, S the incoming beam, and $\hat{M}$ its interaction with the matter. This matrix contains all information about the geometry and the physics of the interaction

A chain of interaction, each described by $\hat{M}_1, \hat{M}_2, \ldots, \hat{M}_n$, can be calculated with the resulting Muller matrix

$$\hat{M} = \hat{M}_n \hat{M}_{n-1} \ldots \hat{M}_2 \hat{M}_1. \tag{1.3}$$

If S' is the polarization vector measured with a telescope and a polarimeter, then the last interactions described by $\hat{M}_n, \hat{M}_{n-1}, \ldots, \hat{M}_{n-k}$ are inside the instrument. Their product is the instrumental Mueller matrix. If it is possible to calculate this matrix, then one can correct the measured signal for instrumental, spurious signatures. Two possible methods to do this are: to insert filters in front of the telescope and thus to remove the instrumental Mueller matrix, or to take into account the symmetries of the measured vector trying to distinguish which are the cross-talk signatures (for example, antisymmetric signals in the linear polarization coordinates are generally caused by cross talk from the circular polarization), deriving the searched matrix. Once the recorded signatures are corrected for known spurious signatures, the physical effects in the solar atmosphere at their origin need to be determinate.

1.2.2 The beam exchange polarimeter

To measure a Stokes parameter we need to take into account that sensors in the visible range (now almost always of CCD type) measure

only the light intensity. They give us values related to the number of photons, but no temporal information about phase and electric vector. Then before we have to analyse the beam with the help of filters, which allow us to reconstruct the polarization state of the original beam. The definition of the Stokes vector helps us, since it refers directs to the difference of intensity quantities which can be measured. For example, to measure V we can use filters which transmit only clockwise circularly polarized light V_+ or only anticlockwise circular polarized light V_-. The difference of the two measured intensities is the waited result $V = V_+ - V_-$.

An example of how to do this is to use retarder plates (a quarter wave plate for circular polarization, a half wave plate for linear polarization) followed by a polarizing beam splitter (Wollaston prism, calcite, Savart plate, etc.). With an adequate orientation of the retarder plate fast axis one can split the incoming beam into two desired components of a Stokes parameter. Travelling along different paths the two beams reach different sensors (in the best case different pixels of the same CCD chip). Nevertheless differences in the optical paths, optical aberrations and different electronic properties of the sensors introduce spurious signatures, which hardly can be removed to reach high accuracy to reconstruct the original two components of the beam.

A way to minimize this inconvenience was suggested by Meir Semel (Donati et al. 1990; Semel et al. 1993) for stellar observations: the beam exchange polarimeter. A similar principle was used even before, e.g. by Brückner (1963). Following Clarke & Ameijenda (2000) the ancestor of this instrument has been proposed in 1873 by Edward Picking and improved by Öhman (1939).

The principle of this polarimeter may be described as follows. The beam is analysed with a retarder plate and a calcite beamsplitter (Savart plate) as described above. Let us, for example, follow a circular polarization recording. A quarter-wave plate, with the fast axis placed in an adequate way, allows to separate the two circular polarization components. They correspond to the V_+ and V_- components of the beam to be analysed. Then the quarter-wave plate is rotated by $90°$ and the two beams now correspond to the V_- and V_+ components. In an analogous way a half-wave plate placed in an adequate way, rotated by $0°$, $45°$, $22.5°$ or $67.5°$, allows us to choose the two beams as

being combinations: Q_+ and Q_-, Q_- and Q_+, U_+ and U_- or U_- and U_+, where $+$ and $-$ refers to the two components.

Two exposures are recorded and the retarder plate is rotated after the first one. Each recording contains two components (which can be either spectrograms or filtergrams). The central point to be taken into account is that the information about the polarization had changed place but not the instrumental spurious signatures, which remain unchanged. A mathematical technique allows us to extract the polarization signature as explained in Section 3.3.

This method permits good quality observations: the noise of the atmospheric turbulence between the two exposures persists, the cross talk introduced by the telescope and the astigmatism problems generated by the calcite plate are not removed, but the results allow us to define this polarimeter as the second best after ZIMPOL. We will see that for selected observations this technique reaches a very high accuracy. Generally this method is good if we are interested in the spatially averaged value.

1.2.3 The ZIMPOL polarimeter

The remaining atmospheric and astigmatic problems which persist in the method described above can be removed by the Zurich IMaging POLarimeter – ZIMPOL developed at the Institute of Astronomy of the ETH and based on a concept of Peter Povel (Keller et al. 1992; Povel 1995). The beam is analysed using fast modulators (i.e. piezo elastic modulator, PEM, at 42 kHz). The same sensor (the same pixel) is used to record the different polarization components. The modulation rate is much higher than the typical atmospheric noise, which is in the range of few hundred Hz. This allows us to freeze the seeing effects in the polarization recordings. No atmospheric spurious signature is therefore generated in the polarization signature.

The ZIMPOL polarimeter has been described in detail before (Povel 1995; Gandorfer 2001), thus here only the main idea will be described.

The polarization signature is modulated by the PEM, and the intensity corresponding to different polarization states (4 phase intervals in ZIMPOL2) are recorded. As it is impossible to read a CCD at kHz

rates some rows of the CCD are masked to create fast hidden buffers. In ZIMPOL2 three out of every four rows are masked. Only the unmasked rows may detect light while the others are used for fast buffer storage. The electric charges of the CCD are shifted in synchrony with the PEM modulation. Long exposure times relative to the PEM cycle can be chosen (typically a few tenths of second to a few seconds). The CCD frame thus contains four images, each corresponding to a different polarization state. Combinations of these four images allow us to derive the desired two-dimensional polarization images.

This instrument brought a revolution in solar polarimetry enabling investigations of domains that were drowned in noise with previous instruments. Indeed before it was only possible to reach similar polarimetric accuracy (with modulators and photo multipliers) for a single point. ZIMPOL allowed polarimetric accuracy in two-dimensional polarimetric images.

1.3   Scattering theory in the presence of magnetic fields

A completely isotropic source does not produce polarization. Only if the physical system contains an asymmetry and thus a preferred direction, polarized light can be originated. A scattering process at a well-defined angle represents such a case. The classic example is electric dipole scattering, for which a 90° scattered electromagnetic wave becomes 100% linearly polarized. If a scattering medium is placed in an isotropic atmosphere, the light intensity reaching it from the underlying hemisphere would be the same from each direction, and for symmetry considerations the integrated scattered light polarization would vanish. The solar atmosphere is anisotropic because it contains a vertical temperature gradient that causes the intensity center to limb variation observed in solar full disk images. Therefore a scattering source is illuminated asymmetrically and this explains why observations near the solar limb can show linear polarization in the continuum and in several Fraunhofer lines.

1.3.1 Coherent scattering

Nonmagnetic line polarization is due to resonant or fluorescent scattering events. The case of a $J = 0 \rightarrow 1 \rightarrow 0$ transition is the equivalent of a classical dipole transition and 90° scattering is expected to be completely polarized. In more general, in a scattering process the coherence between the magnetic substates determine the scattering polarizability of the transition. The coherence is a quantum mechanical property of the scattering atom.

For line transitions we also have to consider the fraction of scattering processes that are undisturbed by depolarizing collisions (which depends on the ratio between the spontaneous emission rate and the collision rate), as well as Hanle depolarization effects due to external magnetic fields.

1.3.2 Continuum scattering

Polarimetric observations of the solar limb show linear polarization of the continuum mainly caused by Rayleigh scattering at neutral hydrogen and by Thomson scattering at free electrons. Both processes behave like classical dipole scattering. The increase of radiative anisotropy if one approaches the limb and the increase with height of the relative importance of continuum scattering govern is at the origin of the center to limb variation of the continuum polarization (see Fluri & Stenflo 1999).

1.3.3 Hanle effect

The effects of magnetic fields on the scattering polarization are covered by the term "Hanle effect".

A classical explanation of the effect can be given by describing the atom as a combination of three electric dipoles along three orthogonal axis (in a coordinate system based on complete spherical vectors). First the non magnetic field case is considered. In a scattering process (imagining unpolarized light travelling along the z direction) the three dipoles can be considered independently. The oscillation along the z axis is not excited, while the x and y oscillations have frequency ω_0 and

damping constant γ (given by the inverse life time of the upper level). Assume an observer in the x direction. The light travelling along this direction is emitted by the dipole along the y axis. The light is therefore completely linearly polarized along the y direction.

Let us now introduce a weak magnetic field aligned along the x axis (in the direction of the observer). In the three dipole model the z and y ones have reduced phase coherence. A coherent combination of the two circular dipoles allow us to describe the scattering. The oscillation frequency is given by $\omega_0 + \omega_L$ and $\omega_0 - \omega_L$, where ω_L is the Larmor frequency. The combination of the two damped circular oscillators results in a rosette motion. Depending on the ω_L/γ ratio the damping can produce a more complete rosette pattern or a strong damped rosette. The ligth emitted in the x direction is then depolarized, and in the case of a strong damped motion, the polarization plane is rotated.

In a quantumechanical description the relaxation of the interference between Zeeman sublevels has to be taken into account. Since this effect is a coherence phenomena, it manifests itself only in scattering processes.

In solar observations two signatures occur: the scattering polarization in a spectral line may decrease in the presence of a magnetic field (depolarization), and the plane of polarization of the scattered light may be rotated. In the latter case a net magnetic flux along the line of sight is required. Depolarization can however occur even if the fields have entirely random orientation.

1.4   Scattering polarization observations

1.4.1   Earlier observations

Attempts to observe scattering polarization on the Sun have been performed with photographic techniques by Redman (1941; 1943) at the Radcliffe Observatory in Pretoria, South Africa, based on the predictions in the work of Zanstra (1941). He searched for polarization signatures in the Ca I 4227 Å line but found that the scattering polarization signals are very faint, well below the sensitivity of his instrument. Jäger (1954; 1957) performed Ca I 4227 Å observations in Göttingen,

but the Hainberg telescope was not a suited instrument for polarization observations. Brückner (1963) could for the first time measure in Locarno the profile of the linear polarization in the Ca I 4227 Å line wings. He used a two beams exchange method rotating a half-wave plate in front of a calcite beam splitter by 22.5° steps and recording the signal at the exit of the spectrograph with two photo-multipliers IP21.

At the Pic du Midi observatory J.L. Leroy performed polarization observations with a low instrumental polarization coronagraph. Using a modulation system he measured the center-to-limb-variation (CLV) of the continuum polarization (Leroy 1972). The sensitivity was very high, but the filters used were quite broad and included more Fraunhofer lines.

Using the Complete Stokes Vector Polarimeter at the Mees Solar Observatory on Mt. Haleakala (Orrall 1971), Mickey & Orrall (1974) could reproduce and slightly improve the Leroy continuum polarization CLV data.

Stenflo (1974) made successful recordings of the polarization profile of the Ca I 4227 Å line at Locarno in 1973.

Eberhard Wiehr observed in Locarno several resonance lines and found scattering polarization in the Sr II 4078 Å, Ba II 4554 Å, Na I D_2 5890 Å Sr I 4607 Å, Ba I 5535 Å lines and some continuum polarization values (Wiehr 1975; 1978).

The High Altitude Observatory Stokes polarimeter (Baur et al. 1980) at Sacramento Peak allowed high polarimetric sensitivity. Observations of Stenflo et al. (1980) revealed the line core peak polarization in the Ca I 4227 Å line, and uncovered the Na I D_1 – D_2 doublet and Ca II K – H doublet scattering polarization shapes which could be explained in terms of quantum-mechanical interference (Stenflo 1980).

The first direct observation of the Hanle effect in terms of depolarization and rotation of the polarization plane was made in the Ca I 4227 Å line at Sacramento Peak by Stenflo (1982).

A survey of the limb scattering polarization in the spectral intervals 3165–4230 Å and 4200–9950 Å was performed by Stenflo et al. (1983a;b) at Kitt Peak. The noise level permitted discovery of only the strongest polarization signatures in the visible part of the spectrum, but the richness of the structures was clearly revealed in the UV part of the spectrum, where the S/N ratio of the observations was higher.

Based on the richness of the UV spectrum shown in Stenflo et al. (1983a), V.V. Ivanov of Leningrad (now Petersburg) coined the term *"Second Solar Spectrum"* to characterize the linearly polarized spectrum that is produced by coherent scattering (Ivanov 1991).

Faurobert-Scholl (1992; 1993) and Faurobert-Scholl et al. (1995) have pioneered the development of the radiative transfer tools to interpret the observations of the "second solar spectrum" and applied these tools to derive turbulent and canopy-like magnetic fields based on the Stenflo observations with the HAO Advanced Stokes Polarimeter at Sac Peak (Stenflo 1982; Stenflo et al. 1980).

1.4.2 Observations in the ZIMPOL era of the "second solar spectrum"

With the implementation of the new ETH-built ZIMPOL system at the world's largest solar telescope (the McMath facility at Kitt Peak) it become possible for the first time to embark on a sytematic exploration of the "Second Solar Spectrum". This spanned a new window for spectroscopy (Stenflo & Keller 1996; 1997).

This new window for solar physics provides us with new tools to study the solar atmosphere and the magnetic field. At the same time new enigmas are introduced. For instance the Na I $D_1 - D_2$ doublet shows structures like the peak polarization in the D_1 line, which should not be polarized according to our present understanding of quantum mechanics.

Molecules, which have very faint signatures in the intensity spectrum, exhibit strong signatures in the second solar spectrum and are unaffected by magnetic fields as explained by Berdyugina et al. (2002).

Observations performed at IRSOL with the two beams exchange polarimeter allowed us to detect signatures of the Hanle effect in the Ca I 4227 Å and Sr II 4078 Å lines as described in this Thesis. They gives a support for the canopy model of Solanki & Steiner (1990).

The earlier survey of scattered polarization (Stenflo et al. 1983a;b) was repeated by Achim Gandorfer, who observed with ZIMPOL2 at IRSOL (Gandorfer 2000; 2002). His two atlas volumes cover the spectral interval 3910–4630 Å and 4625–6995 Å. The richness of structures present in the second solar spectrum is now fully exposed.

Trujillo Bueno (2001) has pointed out that the Hanle effect gives signatures in forward scattering (near the center of the solar disk) in the case of horizontal magnetic fields. First observations of this effect in the He I 10830 Å line were reported by him (Trujillo Bueno et al. 2002). Observations in the Ca I 4227 Å line of this effect have been carried out at IRSOL (Joos 2002; Stenflo 2003).

1.5   Impact polarization in solar flares

Laboratory experiments have demonstrated the existance of impact polarization, i.e. linearly polarized light emitted by a plasma hit by a particle beam (cf. Kleinpoppen 1969, for a review of the experimental and theoretical results). Impact on atoms by energetic particles affects the magnetic substate population, allowing linear polarization to be produced. Observations to investigate if this effect also occurs in solar flares were performed in the S I 1436.9 Å line by Hénoux et al. (1983) using UVST SMM polarimeter data. Hα impact polarization observations are reported by Vogt & Hénoux (1996; 1999).

At IRSOL we decided to improve the quality of published data by using ZIMPOL. A flare detector system that allows us to store intensity images (14 images per second) and to record the GPS time was built for this purpose (FHSW). The ZIMPOL system was not changed, only the optical layout was modified as compared with spectral observations. As shown in the present Thesis our observations showed the absence of impact polarization signatures for all the 23 Hα flares observed.

1.6   Outline of the thesis

Following the suggestion of J.O. Stenflo and S.K. Solanki to use a Semel type polarimeter in Locarno for solar observations a set of tests were performed. The recordings were initially concerned with the scattering polarization of the Sr I 4607 Å line. This for different reasons: the measured signal is quite strong (more than 1%), it is in a wavelength domain accessible by the first versions of ZIMPOL, and at that time it was the most promising candidate to detect the Hanle effect in the solar atmosphere.

Chapter 2 presents the results of these observations. The IRSOL data could be used in a more general work of Stenflo, Keller and Solanki and added to sets of ZIMPOL observations performed at Kitt Peak (Arizona). The aim was to prepare the ground for later investigations of the Hanle effect by exploring the center to limb variation of the scattering polarization and check the consistency of different data sets.

There is good agreement between the data recorded with the two polarimeters: the beam exchange polarimeter at IRSOL and ZIMPOL at Kitt Peak. This gives us confidence in the results obtained with the IRSOL beam splitter system.

As at that time (1995) the ZIMPOL system was not sensitive to the violet (below 4500 Å), we decided to investigate violet lines with the beam splitter, in particular the Ca I 4227 Å and Sr II 4078 Å lines which show strong scattering polarization signatures.

Chapter 3 presents the results of a first set of observations of the Ca I 4227 Å line. In particular the technique of how to reduce the data recorded with the beam exchange technique is presented in an accurate and detailed way. The spatial variations of the scattering polarization, observed in the core of the line but not in the wings, is identified as a Hanle depolarization effect signature due to magnetic fields with different local properties. The theory previously developed (Stenflo 1982; 1994) could be used to cover magnetic field intensities in the 5–15 Gauss range.

In these earlier observations only Q/I, i.e. linear polarization parallel to the limb, was recorded. A mechanical improvement of the beam exchange polarimeter allowed us to record the complete Stokes vector. The first line to be observed with this technique was the Sr II 4078 Å line, as described in Chapter 4.

Besides the line peak depolarization signatures similar to those found in the calcium line, the Sr II recordings showed U/I signatures in the line center. This was identified as a signature of Hanle rotation of the polarization plane. This happens in the case of a net magnetic flux in the observed area. The measured values could be presented in the form of "Hanle histograms".

The improved beam splitter polarimeter was used for new Ca I 4227 Å observations (Chapter 5). U/I signatures were detected (like

in the Sr II observations) and the measured values given in terms of Hanle histograms.

Chapter 6 summarizes the results obtained in the Ca I 4227 Å and Sr II 4078 Å lines. Observations in an active region with good seeing conditions permitted to detect Q/I and U/I changes in regions only a few arcseconds apart. This indicates how spatial structure of magnetic fields can be investigated with the Hanle effect.

The latest ZIMPOL2 version is sensitive to the ultraviolet. Observations, reported in Chapter 7, were performed with this polarimeter to confirm the earlier calcium and strontium observations. An unexpected result was found. The Hanle effect is predicted to occur only in the line centre, but in active regions it appears also in the wings of the Ca I 4227 Å line. This behaviour is not expected by the theory and needs a theoretical explanation.

Eberhard Wiehr (USWG) proposed to measure the CLV of the continuum polarization with the two beams exchange polarimeter and a narrow-band filter in Tenerife, with the Gregory-Coudè instrument there. Using short exposures we could take advantage of the good seeing conditions. Observations were performed by Wiehr and me during different observing runs in 2000–2002. Before we could obtain consistent results it was necessary to find and correct various instrumental problems. The March 2002 results are reliable, as reported in Chapter 8, and agree quite well with the theoretical values of Fluri & Stenflo (1999). The method works but requires good seeing.

The Paul Scherrer Institute in Villigen in collaboration with NASA has constructed the RHESSI satellite for solar flare observations in X- and gamma range. Ground-based observations have been planned to support this project. In collaboration with the Institute of Astronomy in Zurich, the Fachhochschule in Wiesbaden and the Institute of Applied Physics of the University of Bern we decided to participate and contribute with accurate observations of the impact polarization in solar flares. Previous observations reported by Vogt & Hénoux (1996; 1999) show evidence for large signatures, exceeding 5% in the degree of linear polarization. ZIMPOL observations could improve the polarimetric and temporal resolution of previously published data. The results, as seen in Chapter 9, were surprising: never, in the set of Hα flare observations recorded with the ZIMPOL system (for 23 events)

was it possible to detect polarization signatures with amplitudes similar to those reported in the literature. The small signals recorded by us are in the pro mill range, excluding the possibility of stronger sigals in these flares. This costs doubts in previous observations of Hα impact polarization in solar flares.

Bibliography

Baur, T. G., House, L. L., Hull, H. K., 1980, *"A spectrum scanning Stokes polarimeter"*, Sol. Phys. **65**, 111

Berdyugina, S. V., Stenflo, J. O., Gandorfer, A., 2002, *"Molecular line scattering and magnetic field effects: Resolution of an enigma"*, Astron. Astrophys. **388**, 1062

Brückner, G., 1963, *"Photoelektrische Polarisationsmessungen an Resonanzlinien im Sonnenspektrum. Mit 6 Textabbildungen"*, Zeitschrift für Astrophysik **58**, 73

Brückner, G., Schröter, E., Voigt, H. H., 1967, *"The Solar Work at the Göttingen Observatory"*, Sol. Phys. **1**, 487

Clarke, D., Ameijenda, V., 2000, *"Hα polarimetry of the solar limb"*, Astron. Astrophys. **355**, 1138

Donati, J.-F., Semel, M., Rees, D. E., Taylor, K., Robinson, R. D., 1990, *"Detection of a magnetic region on HR 1099"*, Astron. Astrophys. **232**, L1

Faurobert-Scholl, M., 1992, *"Hanle effect with partial frequency redistribution. II. Linear polarization of the solar Ca I 4227 Å line"*, Astron. Astrophys. **258**, 521

Faurobert-Scholl, M., 1993, *"Investigation of microturbulent magnetic fields in the solar photosphere by their Hanle effect in the Sr I 4607 Å line"*, Astron. Astrophys. **268**, 765

Faurobert-Scholl, M., Feautrier, N., Machefert, F., Petrovay, K., Spielfiedel, A., 1995, *"Turbulent magnetic fields in the solar photosphere: diagnostics and interpretation"*, Astron. Astrophys. **298**, 289

Fluri, D. M., Stenflo, J. O., 1999, *"Continuum polarization in the solar spectrum"*, Astron. Astrophys. **341**, 902

Gandorfer, A., 2001, *"High Precision Polarimetry of the Sun"*, Ph.D. thesis, ETH, Zurich, Switzerland

Gandorfer, A. M., 2000, *"The Second Solar Spectrum, Vol.1"*, ISBN no. 3 7281 2764 (Zurich VdF)

Gandorfer, A. M., 2002, *"The Second Solar Spectrum, Vol. 2"*, ISBN no. 3 7281 2844 4 (Zurich VdF)

Hénoux, J. C., Chambe, G., Sahal, S., Semel, M., Woodgate, B., Shine, D., Beckers, J., Machado, M., 1983, *"Impact linear polarization observed in a UV chromospheric line during a solar flare"*, Astrophys. J. **265**, 1066

Ivanov, V. V., 1991, *"Analytical Methods of Line Formation Theory — are they Still Alive"*, in L. Crivellari, I. Hubeny, D. G. Hummer (eds.), *"Stellar Atmospheres: Beyond Classical Models, NATO ASI Series C 341"*, 81, Kluwer, Dordrecht

Jäger, F. W., 1954, *"Polarisationsmessungen an Fraunhoferlinien im Sonnenspektrum. Mit 4 Textabbildungen"*, Zeitschrift für Astrophysik **34**, 237

Jäger, F. W., 1957, *"Zur Theorie und Beobachtung der Polarisation in solaren Fraunhoferlinien. Mit 2 Textabbildungen"*, Zeitschrift für Astrophysik **43**, 98

Joos, F., 2002, *"Vectorpolarimetric observations of anomalous effects in the second solar spectrum"*, Diploma thesis, ETH Zurich, Switzerland

Keller, C. U., Aebersold, F., Egger, U., Povel, H. P., Steiner, P., Stenflo, J. O., 1992, *"Zurich Imaging Stokes Polarimeter Zimpol-I — Design Review"*, Tech. Rep. 53, LEST Foundation

Kleinpoppen, H., 1969, in F. Bopp, H. Kleinpoppen (eds.), *"Advances in Atomic and Molecular Physics"*, 612, North Holland, Amsterdam

Küveler, G., Wiehr, E., Thomas, D., Harzer, M., Bianda, M., Epple, A., Sütterlin, P., Weisshaar, E., 1998, *"Automatic guiding of the primary image of solar Gregory telescopes"*, Sol. Phys. **182**, 247

Leroy, J. L., 1972, *"New Measurements of the Polarization of Photospheric Light near the Solar Limb"*, Astron. Astrophys. **19**, 287

Mickey, D. L., Orrall, F. Q., 1974, *"Broadband Polarization Measurements on the Quiet Sun's Disk near λ 5834"*, Astron. Astrophys. **31**, 179

Öhman, Y., 1939, *"On some observations made with a modified Pickering polarigraph"*, Monthly Notices of the Royal Astronomical Society **99**, 624

Orrall, F. Q., 1971, *"A Complete Stokes Vector Polarimter"*, in R. Howard (ed.), *"Solar Magnetic Fields"*, vol. 43 of *"IAU Symp."*, 30, Reidel, Dordrecht

Povel, H., 1995, *"Imaging Stokes polarimetry with piezoelastic modulators and charge-coupled-device image sensors"*, Optical Engineering **34**, 1870

Redman, R. O., 1941, *"Observational search for polarisation in the calcium line λ 4227 A. near the Sun's limb"*, Monthly Notices of the Royal Astronomical Society **101**, 266

Redman, R. O., 1943, *"Note on a further search for polarization in Fraunhofer lines"*, Monthly Notices of the Royal Astronomical Society **103**, 329

Sánchez Almeida, J., Martinez Pillet, V., Wittmann, A. D., 1991, *"The instrumental polarization of a Gregory-coude telescope"*, Sol. Phys. **134**, 1

Semel, M., Donati, J.-F., Rees, D. E., 1993, *"Zeeman-Doppler imaging of active stars. 3: Instrumental and technical considerations"*, Astron. Astrophys. **278**, 231

Solanki, S. K., Rüedi, I., Bianda, M., Steffen, M., 1996, *"On the detection of shocks in the solar granulation"*, Astron. Astrophys. **308**, 623

Solanki, S. K., Steiner, O., 1990, *"How magnetic is the solar chromosphere?"*, Astron. Astrophys. **234**, 519

Stenflo, J. O., 1974, *"Observations of Resonance Polarization in Ca I 4227 Å"*, Sol. Phys. **37**, 31

Stenflo, J. O., 1980, *"Resonance-line polarization. V. Quantum-mechanical interference between states of different total angular momentum"*, Astron. Astrophys. **84**, 68

Stenflo, J. O., 1982, *"The Hanle effect and the diagnostics of turbulent magnetic fields in the solar atmosphere"*, Sol. Phys. **80**, 209

Stenflo, J. O., 1994, *"Solar magnetic fields: polarized radiation diagnostics"*, Astrophysics and Space Science Library, Kluwer Academic Publishers, Dordrecht

Stenflo, J. O., 2003, *"Scattering Polarization in Magnetic Fields: Anomalies, Surprises, and Enigmas"*, in J. Trujillo Bueno, J. Sánchez Almeida (eds.), *"Solar Polarization, proc. 3rd SPW"*, ASP Conf. Ser., in press

Stenflo, J. O., Baur, T. G., Elmore, D. F., 1980, *"Resonance-line polarization. IV. Observations of non-magnetic line polarization and its center-to-limb variations"*, Astron. Astrophys. **84**, 60

Stenflo, J. O., Keller, C. U., 1996, *"New window for spectroskopy"*, Nature **382**, 588

Stenflo, J. O., Keller, C. U., 1997, *"The second solar spectrum. A new window for diagnostics of the Sun"*, Astron. Astrophys. **321**, 927

Stenflo, J. O., Twerenbold, D., Harvey, J. W., 1983a, *"Coherent scattering in the solar spectrum — Survey of linear polarization in the range 3165–4230 Å"*, Astron. Astrophys. Suppl. Ser. **52**, 161

Stenflo, J. O., Twerenbold, D., Harvey, J. W., Brault, J. W., 1983b, *"Coherent scattering in the solar spectrum — Survey of linear polarization in the range*

4200–9950 Å", Astron. Astrophys. Suppl. Ser. **54**, 505

Sütterlin, P., Wiehr, E., Bianda, M., Küveler, G., 1997, *"Problems in measuring prominence oscillations"*, Astron. Astrophys. **321**, 921

ten Bruggencate, P., Voigt, H. H., 1958, Veröff. Univ. Sternwarte Göttingen **122**

Trujillo Bueno, J., 2001, *"Atomic polarization and the Hanle effect"*, in M. Sigwarth (ed.), *"Advanced Solar Polarimetry — Theory, Observations, and Instrumentation"*, vol. 236 of *"ASP Conf. Ser."*, 161

Trujillo Bueno, J., Landi Degl'Innocenti, E., Collados, M., Merenda, L., Manso Sainz, R., 2002, *"Selective absorption processes as the origin of puzzling spectral line polarization from the Sun"*, Nature **415**, 403

Vogt, E., Hénoux, J., 1999, *"Observations of linear polarization in the H alpha line during two solar flares"*, Astron. Astrophys. **349**, 283

Vogt, E., Hénoux, J.-C., 1996, *"Polarimetric Study of Solar Flares"*, in J. O. Stenflo, K. N. Nagendra (eds.), *"Solar Polarization, proc. 1st SPW"*, 345, Kluwer, Dordrecht, (Sol. Phys. 164, 345)

Wiehr, E., 1975, *"Measurement of solar disc polarization in a number of Fraunhofer lines and their adjacent continuum"*, Astron. Astrophys. **38**, 303

Wiehr, E., 1978, *"Measurement of solar disc polarization in a number of Fraunhofer lines and their adjacent continuum. II. Improved data, new line measurements"*, Astron. Astrophys. **67**, 257

Wiehr, E., Wittmann, A., Wohl, H., 1980, *"Solar Observations at the Gottingen University Observatory"*, Sol. Phys. **68**, 207

Wittmann, A. D., Alge, E., Bianda, M., 1991, *"Recent results on the solar diameter"*, Sol. Phys. **135**, 243

Wittmann, A. D., Alge, E., Bianda, M., 1993, *"Detection of a significant change in the solar diameter"*, Sol. Phys. **145**, 205

Zanstra, H., 1941, *"Theory of a polarisation effect in Fraunhofer lines due to oscillator scattering"*, Monthly Notices of the Royal Astronomical Society **101**, 250

Part I

Scattering polarization and Hanle effect

Chapter 2

Center-to-limb variation of the second solar spectrum [*]

J.O. Stenflo[1], M. Bianda[2], C.U. Keller[3] and S.K. Solanki[1]

Abstract

The linear polarization that is caused by scattering processes in the solar atmosphere has been refered to as the "second solar spectrum", since it is structurally as rich as the ordinary intensity spectrum but quite different in appearance and information contents. One of the most used and theoretically best understood lines in the second solar spectrum is the Sr I 4607 Å line, which has served as a diagnostic tool for determinations of spatially unresolved, turbulent magnetic fields via the Hanle effect. Here we present the detailed center-to-limb variation of the scattering polarization in this line for a number of new data sets obtained both with an electrooptical modulation system (ZIMPOL) and a non-modulating beam splitter system (at IRSOL, Locarno), to provide improved observational constraints for theoretical modelling. The amplitude and width of the polarization profile,

the amount of continuum polarization, as well as the depth and width of the intensity profile have been evaluated and carefully corrected for spectral broadening and stray light. While there is generally good agreement between the five data sets, some systematic differences are shown to be of solar rather than instrumental origin, most likely due to spatially varying Hanle depolarization across the solar disk.

A number of other spectral lines have been observed with the ZIM-POL system at two different limb distances ($\mu = 0.1$ and 0.2) to allow us to compare the steepness of the center-to-limb variation of their polarization amplitudes. The steepest variation is exhibited by the continuum polarization, which declines by approximately a factor of 6 when going the 15 arcsec distance from $\mu = 0.1$ to $\mu = 0.2$. The spectral lines with the steepest center-to-limb variation are molecular lines, the Ca II infrared triplet, and Hα. In contrast the Sr I 4607 and Ba II 4554 Å lines have only moderately steeper center-to-limb variations than that of an ideal, purely dipole-scattering atmosphere, for which the polarization ratio between $\mu = 0.1$ and $\mu = 0.2$ is 1.38. These center-to-limb variations may be used to constrain temperature-density models of the upper photosphere and chromosphere.

2.1　Introduction

Near the Sun's limb the solar spectrum becomes linearly polarized due to scattering processes, which are basically non-magnetic in origin but become modified by magnetic fields via the Hanle effect. The polarized spectrum is as rich in spectral structures as the ordinary intensity spectrum but differs in appearance and information contents (Stenflo & Keller 1996; 1997). It has therefore been found convenient to refer to it as the "second solar spectrum".

Although an increasing number of spectral regions have been surveyed near the limb, generally at a disk position defined by μ (the cosine of the heliocentric angle) = 0.1 (which is about 5 arcsec inside the extreme limb), little observational data on the actual center-to-limb variations (CLV) of the scattering polarization have been available. The prime CLV data set previously published goes back to observations made in 1978 (Stenflo et al. 1980) for a few selected spectral lines.

In this old data set it is the CLV of the Sr I 4607 Å line that has received the most attention, since this line lends itself well to detailed modelling with numerical radiative transfer (Faurobert-Scholl 1993; Faurobert-Scholl et al. 1995). This modelling has been performed mainly for the purpose of diagnosing "hidden" turbulent magnetic fields, a possibility that was first explored by Stenflo (1982). Such fields that are tangled or turbulent on scales that are beyond the attainable spatial resolution are invisible in any magnetogram. In contrast, the Hanle effect offers the best prospect for empirically exploring them.

The previous observations from 1978 suffered from limited spectral resolution, which meant that the narrow polarization peak in the line was reduced in amplitude by about 50 % by spectral smearing. The precise amount of spectral broadening and stray light was not determined but only estimated. Also, the reproducibility of the CLV curve has never been checked.

In the radiative-transfer modelling of Faurobert-Scholl (1993) and Faurobert-Scholl et al. (1995) the spectral smearing was accounted for by applying a macroturbulent broadening that would lead to agreement between the widths of the computed and observed intensity profiles at the various disk positions. Then the comparison between the modelled and observed polarization amplitudes showed that the amplitudes computed for zero magnetic fields were too large. A fit could only be achieved if Hanle depolarization due to a turbulent field with a strength in the range 10–30 G was introduced.

In the present paper we present new data sets on the CLV of the Sr I line, obtained from five different observing runs with different instruments and observing procedures. The extracted parameters (widths and amplitudes of the polarization and intensity profiles) have been carefully corrected for both spectral broadening and stray light. The CLVs of all these calibrated and corrected parameters provide a more complete set of observational constraints for radiative-transfer modelling. The comparison between the data sets illustrates not only the magnitude of the observational uncertainties and the degree of reproducibility, but it also reveals that a substantial part of the spread in the data is due to intrinsically solar causes.

A byproduct of the work on the Sr line is the determination of the polarization of the continuum near the Sr line and its center-to-limb

variation (CLV). We have also measured the slope of the CLV for a number of other spectral lines. An overview of these determinations is presented, which illustrates how the CLV slope differs for different categories of lines and compares with theoretical expressions. As the shapes and slopes of the CLV curves are sensitive functions of the atmospheric structure, they may serve as new constraints on models of the temperature-density stratification of the Sun's atmosphere.

2.2   Observational material

The following new data sets are presented here: (1) Observations with ZIMPOLI (the first generation of the **Z**urich **Im**aging Stokes **Pol**arimeter) made in June 1994, November 1994, and April 1995. (2) Observations at IRSOL, Locarno, on 22 September, 19 October, and 31 October 1995. While the ZIMPOL observations have been carried out at the McMath-Pierce facility of the National Solar Observatory (Kitt Peak, Arizona) with an electrooptical modulation-demodulation system (Povel et al. 1990; Keller et al. 1992; Stenflo 1994; Povel 1995), the IRSOL observations have been made with a stationary beam splitter without modulation but with alternate settings of a half-wave plate to eliminate gain table effects (see below).

2.2.1   ZIMPOL observations

During an observing run with ZIMPOL in June 1994 the Sr I 4607 Å line was recorded with the spectrograph slit oriented perpendicular to the solar limb, which allowed us in a single exposure to obtain the center-to-limb variation (CLV) as a continuous function from the extreme limb ($\mu = 0$) to $\mu \approx 0.3$. For this more exploratory observation no separate recording at disk center was made, which by comparison with FTS spectra could have allowed a direct determination of the spectral broadening and stray light.

The observing run with ZIMPOL in November 1994 was used to make more careful recordings with the spectrograph slit oriented parallel to the solar limb at a number of discrete positions to cover the full μ range from 0.1 to 1.0 that would give us the complete CLV curve. As

the different parts of the 49 arcsec long recorded section of the slit had the same value of μ, we could use spatial averaging along the slit to enhance the signal-to-noise ratio.
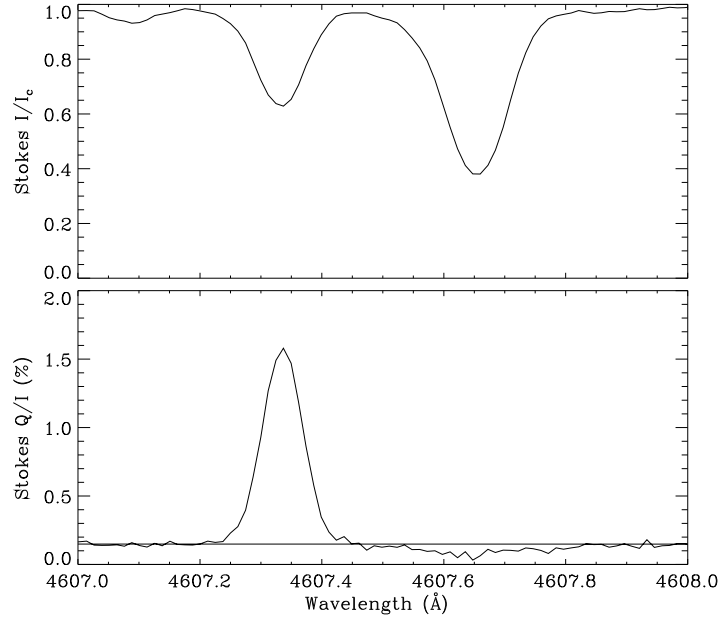
Figure 2.1: Section of a recording at the position $\mu = 0.1$ of the solar disk with the ZIMPOL I Polarimeter system attached to the main spectrograph of the McMath-Pierce facility at NSO/Kitt Peak. While the Sr I 4607.34 Å line to the left shows a symmetric and strong polarization peak, the Fe I 4607.65 Å line to the right depolarizes the continuum.

Figure 2.1 shows an example of a 1 Å wide section of a recording at $\mu = 0.1$ that covered the Sr I line and its surroundings. Since the Sr polarization signal at this limb position is so strong, we used a short integration time resulting in an rms noise of about 7×10^{-5} in the degree of polarization. For most other ZIMPOL recordings in other spectral or spatial regions with weaker signals, we used longer integrations (usually about 10 min), corresponding to rms noise values of typically 2×10^{-5}.

While most other parts of the spectrum that we have explored with ZIMPOL have been recorded at the single limb distance of $\mu = 0.1$, we also observed a number of lines at $\mu = 0.2$. These observations were carried out during the observing runs of both November 1994

and April 1995.

The McMath-Pierce solar telescope suffers from substantial instrumental polarization, which is dealt with as described in Stenflo et al. (1983a); Stenflo & Keller (1996) and will be commented on more in Sects. 2.3.3 and 2.3.4. The dominating term is Stokes $I \rightarrow Q$ cross talk, which is crudely compensated for with a tilting glass plate. The residual part of this cross talk leads to a spectrally flat offset of the zero level of the fractional polarization Q/I. The procedure to recover the lost zero point is described in Sect. 2.3.4.

2.2.2   IRSOL observations

The Gregory-Coudé system at IRSOL (Istituto Ricerche Solari Locarno) in Switzerland, with its 45 cm aperture vacuum telescope and Coudé-Echelle spectrograph, is identical to the corresponding German system (GCT) on Tenerife. It has the advantage of being a nearly polarization-free telescope around the time of the equinox (21 March and 23 September), except for the polarization effects due to stresses in the vacuum windows. The instrumental polarization does not vary during the day but only with the Sun's declination. To optimize the observing conditions the observations were therefore carried out within 6 weeks of the fall equinox, on 22 September, 19 October, and 31 October.

The polarimetric system used consists of a polarizing beam splitter in front of the entrance slit, preceded by a half-wave plate with two different orientations, one neutral with the fast axis parallel to one of the polarizing directions, and one rotated by $45°$ such that the Stokes coordinate system gets rotated by $90°$. To produce a polarization (Q/I) image two exposures with the CCD in the spectral focus are made, corresponding to the two settings of the half wave plate. Each exposure produces a pair of orthogonally polarized images that have identical seeing distortions. While the sign of the polarization signal is reversed between the two exposures, the sign of the spurious instrumental effects remains unchanged. By forming certain ratios between the set of four images, as described in Donati et al. (1990); Semel et al. (1993); Keller (1996), it is possible to form an image of the fractional linear polarization Q/I that is almost free from both gain table and seeing

noise, which are the two main noise sources. This technique turns out to work remarkably well and will be described in detail in next chapter.

Although the major noise sources can be removed in this way, a fixed-pattern Q/I background remains, which we eliminate by making recordings at disk center, where the intrinsic scattering polarization is zero for symmetry reasons, but the fixed, spurious pattern remains the same. We thus alternate recordings at each μ position with recordings at disk center.

Even after removal of this fixed pattern there remains a small but spectrally flat instrumental offset, which makes the zero point of the polarization scale undetermined. This problem is dealt with in the same way as for the ZIMPOL observations (cf. Sect. 2.3.4). The standard deviation in the Q/I amplitudes, as determined from the rms noise in the Q/I continuum, is typically 0.05 % for the IRSOL data, while it is close to 0.01 % for the ZIMPOL data in the case of the Sr I measurements.

2.3 Reduction procedure

The recorded spectra need to be corrected for spectrograph stray light, which significantly affects the polarization amplitudes, spectral broadening, which affects both amplitudes and line widths, and Stokes $I \rightarrow Q$ instrumental cross talk, which displaces the Q/I zero level. The effect of stray light and spectral smearing can be modelled and determined by comparing Stokes I profiles recorded at disk center with corresponding FTS spectra. The true zero point of the polarization scale can be located and determined together with the continuum polarization, as described in Sect. 2.3.4.

2.3.1 Effect of stray light

Spectrograph stray light is produced after the polarization analysis has been optically completed. It therefore adds a contribution to the Stokes I signal but not to Stokes Q. The fractional polarization Q/I is affected because the intrinsic Stokes I is increased to the observed I_{obs}. The

dominant portion of the stray light can be considered to be in the form of a spectrally flat background, which can be expressed as a fraction s of the intensity I_c of the continuous spectrum. Thus

$$I_{\mathrm{obs}} = I + sI_c. \tag{2.1}$$

If we can properly locate the level $I_{\mathrm{obs},c}$ of the observed continuous spectrum we can use Eq. (2.1) to express the true relative intensity I/I_c in terms of its apparent, observed value, and the stray light fraction s.

2.3.2 Determination of stray light and spectral broadening

We have in the past made an FTS atlas of the quiet Sun at disk center (in 1978, in search for a turbulent magnetic field through the possible correlation between line width and Landé factor). FTS spectra can be considered free from any stray light and spectral broadening. We have modeled our observed Stokes I spectra at disk center by adding to the corresponding FTS spectrum stray light according to Eq. (2.1) and applying Gaussian smearing, until a good fit is obtained. Usually this is done with an iterative least squares fitting algorithm.

For our Sr I observations the values obtained for the stray light s and total half width b of the instrumental Gaussian profile through these fits are 10.5 % and 33 mÅ for the ZIMPOL observations of November 1994, 1.5 % and 33 mÅ for the IRSOL 1995 observations. In contrast to the McMath main spectrograph, where the overlapping, unwanted grating orders of the single-pass system are blocked by interference filters, the IRSOL spectrograph uses a predisperser which greatly reduces the stray light.

In the case of the ZIMPOL observations of June 1994 no disk center observations were made that could be used for a model fit, and the set-up had more of an exploratory test character, such that somewhat larger values of s and b are to be expected. Best consistency between the results from June 1994 with the other data sets is obtained if we for this set choose $s = 15$ % and $b = 50$ mÅ (see below).

For comparison we note that the spectral broadening of the previous observations of 1978 was estimated to be about 90 mÅ (Stenflo et al. 1980).

2.3.3 Instrumental polarization

Close to the solar limb at the position angle of geographical north or south (which is not far from the heliographic north or south poles), where all our observations have been made, Stokes V and U are usually intrinsically small, so that $V \to Q$ and $U \to Q$ cross talk is a minor problem. Sometimes significant Stokes V signals due to magnetic fields can infiltrate the Stokes Q spectrum through instrumental polarization, but these spurious signals can always be recognized due to their characteristic anti-symmetric profiles and spatial structuring. Cross talk *from* Q to the other Stokes parameters can in principle reduce the Q amplitudes and thus affect the polarization scale, but model calculations of the McMath-Pierce solar telescope (Bernasconi, private communication) show that this may affect the scale by at most 0.5 % when observing near the solar limb at the geographic north or south directions (which we did), which is a negligible effect in comparison with the scale changes due to uncertainties in the μ position (limb distance). For observations at other position angles, which we have avoided, these effects can be substantially larger.

The main instrumental-polarization effect of concern for the present type of observations is thus cross talk $I \to Q$, which means that a fraction k of the intensity, including the stray light, is added to the intrinsic Q to form the apparent Q_{obs}:

$$Q_{\mathrm{obs}} = Q + k I_{\mathrm{obs}} \,. \tag{2.2}$$

When combining Eq. (2.2) with Eq. (2.1) to derive the true fractional polarization $p = Q/I$ from the apparent p_{obs}, we find that the effect of the $I \to Q$ cross talk is an almost spectrally flat zero-line offset or background, which deviates slightly from flatness due to the stray light, although this is a second-order effect. More details on such second-order effects can be found in Keller (1996).

Since the IRSOL observations were made near an equinox, the above effects are small from the outset. In the case of the ZIMPOL observations at NSO/Kitt Peak we minimized the effects by always setting a tilting glass plate in front of the modulator before each exposure such as to null out the average apparent polarization signal. For these reasons second-order effects can be disregarded.

2.3.4   Determination of the polarization zero level

Since the continuum is polarized by scattering processes, we cannot find any spectral region near the solar limb that with certainty has zero intrinsic polarization. At disk center on the other hand the spatially averaged continuum polarization is zero for symmetry reasons, which may lead us to believe that disk-center observations could be used to calibrate the true zero level. However, the difference in angle of incidence of about $\frac{1}{4}^\circ$ between disk center and limb at the McMath heliostat mirror gives rise to a differential instrumental polarization between disk center and limb on the order of 10^{-4}, and the absolute value of the $I \to Q$ cross talk varies by 10^{-4} in a matter of minutes. Therefore we have not been successful in trying to calibrate directly the absolute zero point of the polarization scale with sufficient accuracy ($< 10^{-4}$) by reference to disk center observations. Instead we have applied another, more indirect technique that we will now describe.

Stenflo et al. (1983a;b) found through statistical analysis of large portions of the second solar spectrum, using scatter plots of p_{obs} vs. I_{obs}, that in spectral regions without many intrinsically polarizing lines (but with at least one depolarizing line) it was possible to identify a linear regression relation between polarization and intensity. Such a regression line can be extrapolated to $I_{\mathrm{obs}} = I = 0$, where Q/I must be intrinsically zero because the ratio between the polarizing continuum opacity and the depolarizing line opacity vanishes. The value reached by the regression line for $I = I_c$ must then represent the true continuum polarization p_c. The apparent linearity of the regression implies that the shape of spectral lines that have no intrinsic polarization but only depolarize the continuum must (statistically) be the same in terms of Q/I as in Stokes I. Such a linear relation may be theoretically expected for weak depolarizing lines, but empirically it seems to work as a statistical average for strong lines as well. This identity in profile shape can be expressed in the form

$$\frac{p_c - p}{p_c} = \frac{I_c - I}{I_c} \, . \tag{2.3}$$

The Fe I line immediately to the red side of the Sr I 4607 Å line (cf. Fig. 2.1) shows no sign of any intrinsic polarization but only depresses the continuum polarization. Assuming this depression to be

of the form given by Eq. (2.3) we can determine both the amount of continuum polarization and the absolute zero point of the polarization scale. The resulting level of the continuum polarization is drawn as the horizontal line in Fig. 2.1.

The value of p_c that we determine this way near the Sr I line is for $\mu = 0.1$ approximately 1.6 times larger than the value that is theoretically predicted by the radiative-transfer code of Auer et al. (1980). If the Fe I line would not only be depolarizing but actually have some intrinsic polarization, then it would be shallower than the corresponding Stokes I profile, and our regression analysis based on Eq. (2.3) would produce too small a value for p_c. In this case our present determination would be an underestimate of p_c, and the discrepancy with the theoretical value would become even larger.

In most other spectral regions that we have explored with ZIMPOL the large majority of spectral lines have some intrinsic line polarization, and it is difficult to identify any purely depolarizing lines with any confidence. For these spectral regions we have used the following procedure to determine the zero point of the polarization scale: We assume that the *shape* of the wavelength variation of the continuum polarization p_c is correctly predicted by the theory of Auer et al. (1980), but we apply a global scaling with a factor of 1.62 to lock the theoretical curve to the empirical value determined by regression analysis for the Sr I region. Equipped with this scaled p_c level we shift the observed polarized spectrum such that the average polarization values for the points with the largest Stokes I values (that are closest to the continuum level) agree with our value for p_c. The shifted spectrum should then have the correct zero point of its polarization scale.

We recognize that this procedure is based on several shaky assumptions and therefore is subject to considerable uncertainty, but it appears to be the best that we can do at present, and it gives results that are consistent with previous measurements of the continuum polarization (see Sect. 2.4.2 below). We will consider these uncertainties more in Sect. 2.4.3.

2.3.5   Correction for spectral broadening

It is not possible to perform a general deconvolution of the observed spectra without knowledge of the precise shape of the instrumental profile, but for the purpose of calculating corrections to the values of the widths and amplitudes of the observed line profiles it is here sufficient to assume that both the line profiles and instrumental profile have Gaussian shapes. When convolving two Gaussians with each other their widths add quadratically to form a new Gaussian profile with unchanged area. If the amplitude (or line depth) and half width of the (Gaussian) line profile are observed to be a_{obs} and h_{obs}, respectively, while the smearing function has half width b, deconvolution gives

$$h = \sqrt{h_{\mathrm{obs}}^2 - b^2} \qquad (2.4)$$

for the corrected half width, while the corrected amplitude is

$$a = a_{\mathrm{obs}}\, b_{\mathrm{obs}}/b\,. \qquad (2.5)$$

For Stokes I the profile that we are correcting is the relative line depth $(I_c - I)/I_c$, while for $p = Q/I$ it is $p - p_c$, the polarization with respect to the continuum level. The half level of the polarization profile is the level halfway between p_c and $p_{\max}$. After the amplitude of $p_{\mathrm{obs}} - p_c$ has been corrected, we have to add p_c again to obtain the corrected polarization amplitude with respect to the zero point of the polarization scale.

No Fourier smoothing has been applied to the ZIMPOL data, but due to the larger polarization noise level of the IRSOL data it was needed to smooth the Q/I spectra before amplitudes and line widths were determined. As Fourier smoothing leads to some non-Gaussian spectral broadening, we have determined by numerical simulation the half width of a Gaussian smearing function that produces the same broadening as the Fourier filter that was applied. This half width depends on the width of the profile to be smeared due to the non-Gaussian nature of the Fourier filter function. For the range of widths occuring in our data the additional smearing due to the Fourier filter corresponds to half widths of 18–28 mÅ for an equivalent Gaussian smearing function. These widths add quadratically to the instrumen-

tal smearing of 33 mÅ, which leads to an effective broadening of the Q/I profiles that is larger but well defined.

2.4 Results

2.4.1 Comparison between the different data sets

Figure 2.2 provides an overview of the center-to-limb variation (CLV) of the Sr I 4607 Å line for all the data sets together. The ZIMPOL data from June 1994 are represented by plusses, those from November 1994 by asterisks, while the IRSOL 1995 data are plotted as diamonds (for 22 September), triangles (for 19 October), and squares (for 31 October). The two upper panels refer to the fractional linear polarization Q/I, the lower panels to Stokes I.

All data sets have been corrected for spectral smearing and stray light as well as instrumental $I \to Q$ cross talk as described in Sect. 2.3. The values given here therefore represent our best estimates of the intrinsic, solar values. Before these corrections were applied the results from the different data sets differed greatly, but Fig. 2.2 shows that after correction there is general agreement and consistency between the data sets. Some systematic differences remain, however, which we will comment on later. The spread of the data points gives us a feeling for the degree of reproducibility of the results. Although much of this spread may be of instrumental origin, there is clear evidence that part of the variation is intrinsically solar.

This evidence is directly seen in the top left panel, where we have plotted both the Q/I amplitude in the line (upper set of points) and the continuum polarization p_c (lower set of points). The Q/I amplitude is measured from the true zero point of the polarization scale, which has been determined together with p_c from the neighboring Fe I line as described in Sect. 2.3.4. As the June 1994 observations were made with the slit perpendicular to the limb, we obtain a smooth CLV curve from a single exposure with the CCD. The CLV of the Q/I amplitude shows a very pronounced kink near $\mu = 0.2$. Closer to the limb the amplitudes from November 1994 are considerably larger than those from June 1994, but the agreement is good for $\mu > 0.2$.
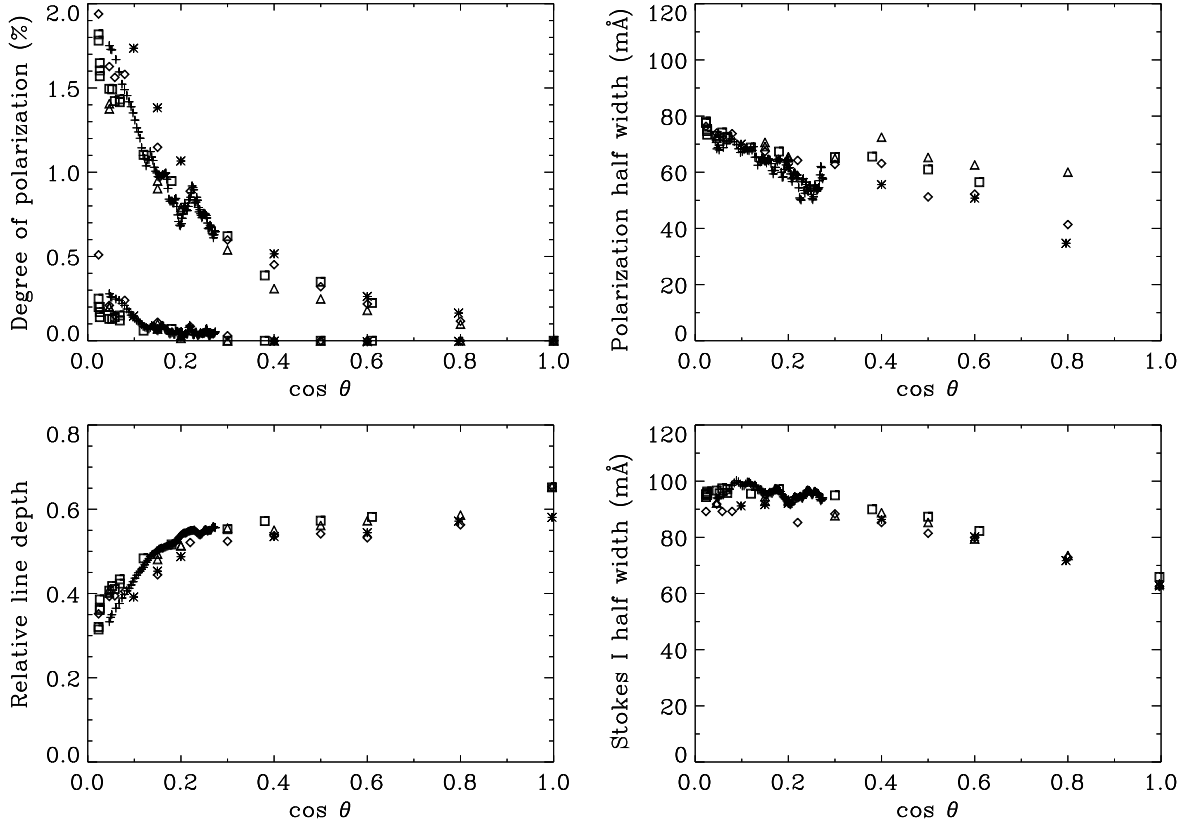
Figure 2.2: Overview of the center-to-limb variation of the Sr I 4607 Å
line parameters. θ is the heliocentric angle ($\mu = \cos\theta$). Top
left panel: Polarization (Q/I) amplitude of the Sr I line (up-
per set of points) and continuum polarization p_c (lower set
of points). Top right panel: Total half width of the polariza-
tion peak ($p - p_c$) of the Sr line. Lower left panel: Relative
line depth of the Sr Stokes I profile. Lower right panel:
Total half width of the Sr Stokes I profile. Pluses and as-
terisks represent ZIMPOL data from June and November
1994, respectively, while diamonds, triangles, and squares
represent IRSOL data from 22 September, 19 October, and
31 October 1995, respectively.

We see no possibility that such a kink in the curve obtained from a single exposure could be produced by instrumental effects, so we conclude that it must be intrinsically solar. $\mu = 0.2$ corresponds to a limb distance of about 20 arcsec. The most natural explanation for the kink is that for the June 1994 observations the slit happened to cut across a region that had more of Hanle-depolarizing magnetic fields inside the 20 arcsec limb zone as compared with the case for the November 1994 observations.

With other (not yet published) ZIMPOL observations in other spectral lines we have found unexpectedly large spatial variations of the Hanle depolarization effect. The best evidence that these variations are really due to the Hanle effect comes from observing the *differential* changes (line ratios) of the polarization amplitudes for combinations of lines with different Hanle sensitivities.

The magnitude of the continuum polarization is less than 10 % of the polarization amplitude in the Sr line. p_c has a much steeper center-to-limb variation as compared with the line polarization, as we will see more clearly later. It becomes approximately zero already at $\mu = 0.3$.

The Stokes I profile becomes shallower by a factor of two when going from disk center, where the line depth is about 0.6, to the limb, where it is about 0.3.

The line width increases from disk center towards the limb, both for Q/I and I. The Q/I width is smaller than the Stokes I width by about 30 %, which is typical when comparing the second solar spectrum with the intensity spectrum. Much of the Stokes I broadening is due to saturation involving optically thick radiative transfer, while the polarization profiles are not subject to this type of saturation. This is well illustrated by the Ba II 4554 Å line (Stenflo & Keller 1996; 1997), for which the polarization profile exhibits spectrally resolved hyperfine structure splitting, while this splitting is invisible in the corresponding Stokes I profile, since it is masked by saturation line broadening.

We do not know why the June 1994 data show such a steep CLV for the width of the polarization peak, in particular in comparison with the IRSOL data.

2.4.2 Shapes of the polarized CLVs

The data set of the ZIMPOL November 1994 observing run has by far the smallest noise and the most detailed calibration. We therefore select it to compare in Fig. 2.3 the shape of the center-to-limb variation of the Sr I amplitude with that of the continuum polarization as well as with the theoretical curve (Chandrasekhar 1950) for an ideal, purely scattering atmosphere.

To facilitate a direct comparison of the shapes of the various curves we have multiplied the continuum polarization by a factor of 12 such that it approximately equals the Sr polarization at $\mu = 0.1$, while the theoretical Chandrasekhar curve has been scaled by the factor 0.2. We see that the CLV of the continuum polarization is by far the steepest, while a purely scattering atmosphere has the smallest slope.

We have found that the following analytical expression provides a good fit to the observed values for the polarization maximum of the line:

$$p_{\max} = \frac{a(1 - \mu^2)}{(\mu + b)} . \tag{2.6}$$

The theoretical considerations leading to the choice of this particular functional form will be discussed at the end of Sect. 2.4. We have chosen the parameter values $a = 0.3\,\%$ and $b = 0.07$ to fit our Sr I data and plotted the resulting function as the dashed curve in Fig. 2.3. For the continuum polarization we have made a parabolic fit with p_c given by

$$p_c(\%) = 0.37 - 2.73\mu + 4.97\mu^2 \tag{2.7}$$

as long as this function is positive, otherwise p_c is set =0. We plot 12 times this function as the dotted curve in Fig. 2.3.

The slightly negative values of the continuum polarization for $\mu \geq 0.4$ are not significant. For these μ values no depolarization of the neighboring Fe I line can be seen, and the almost horizontal regression line in the Q/I vs. I fit may formally have a slope that corresponds to a small negative polarization, but zero polarization is consistent with the error bars.

It is interesting to note that both the magnitude and steepness of the continuum polarization in Fig. 2.3 are fully consistent with previous direct broad-band measurements in coninuum windows of the
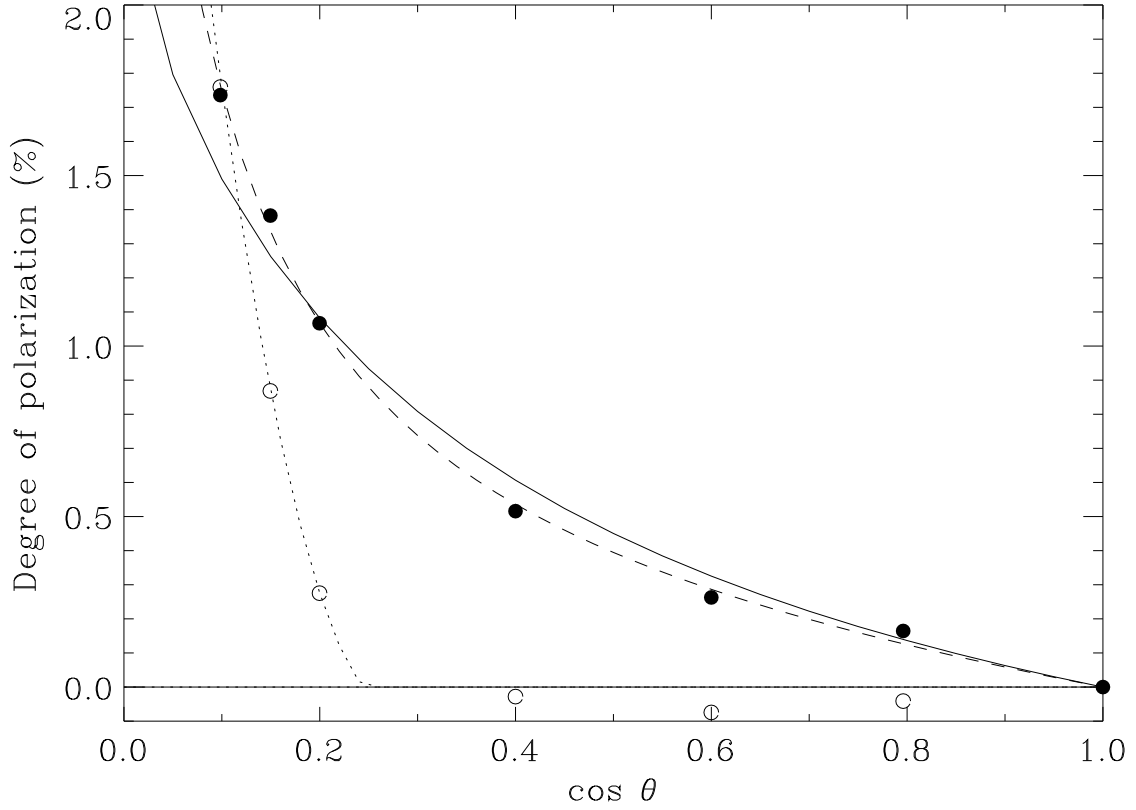
Figure 2.3: Comparison between the shapes of three center-to-limb variation curves. The filled circles represent the values of the polarization maximum in the core of the Sr I 4607 Å line, observed with ZIMPOL in November 1994, and fitted with an analytical function (dashed curve) given by Eq. (2.6) for the parameter values $a = 0.3\%$ and $b = 0.07$. The open circles represent $12p_c$, where p_c is the continuum polarization determined from the same November 1994 data set. The dotted curve is a parabolic fit given by Eq. (2.7). The solid curve represents Chandrasekhar's (1950) solution for an ideal, purely scattering atmosphere, multiplied by a factor of 0.2.

solar spectrum (Mickey & Orrall 1974; Wiehr 1975; Leroy 1977). This supports the validity of our method to determine the zero point of the polarization scale.

In Fig. 2.3 the Sr polarization at $\mu = 0.8$ is anomalously high, considerably higher than the corresponding values of all the other data sets (cf. Fig. 2.2). It should therefore not be considered representative for the typical CLV. At $\mu = 0.8$, which is as much as 6.4 arcmin from the limb, the November 1994 recording showed spatially varying Stokes V-like anti-symmetric polarization profiles along the slit due to instrumental $V \rightarrow Q$ cross talk in combination with longitudinal magnetic fields. The spatial locations of these cross-talk effects were identified by their longitudinal Zeeman-effect signatures in the neighboring Fe I line and excluded from the evaluation of the Q/I profile of the Sr line. As however this μ position was not clean with respect to Zeeman-effect signatures in comparison with the other regions analysed, we have reasons to have less confidence in this data point.

The amount of scattering polarization that we observe at a given disk location depends in the case of a spherically symmetric sun primarily on the degree of limb darkening (anisotropy of the radiation field) seen by the last scattering particle, on the fraction of the opacity that is due to scattering, and on the intrinsic polarizability of each scattering process (i.e., the fraction of scattering processes that behave like classical dipole-type scattering). For line transitions we also have to consider the fraction of scattering processes that are undisturbed by depolarizing collisions (which depends on the ratio between the spontaneous emission rate and the collision rate), as well as Hanle depolarization effects due to external magnetic fields.

The continuum is polarized by Rayleigh scattering by neutral hydrogen and Thomson scattering by free electrons. Both processes behave like classical dipole scattering, which represents the maximum attainable intrinsic polarizability, and this is also the case for scattering in the Sr line. Below the temperature minimum the continuum opacity is dominated by H^-, which is non-polarizing. Around the temperature minimum, where the degree of ionization is the smallest, the relative contribution from Rayleigh scattering by neutral hydrogen reaches a maximum (near 20 %), while higher up Thomson scattering by free electrons dominates the continuum opacity. Since the continuum is

generally formed deep in the atmosphere, while the scattering part of the continuum opacity becomes significant only rather high up, continuum polarization only shows up near the extreme limb, for $\mu < 0.3$, and is expected to increase very steeply, as observed. The quantitative values are sensitive to the temperature-density structure of the atmosphere.

For a spectral line like the Sr I line the line-to-continuum opacity ratio increases with height, and the rate of depolarizing collisions rapidly declines due to the exponential density drop. Therefore the fraction of line scattering processes that are undisturbed by collisions approaches unity with height. For these reasons we expect the CLV of the line polarization to be steeper than that of an ideal, purely scattering atmosphere.

2.4.3 CLV behavior of different spectral lines

We have made recordings with ZIMPOL in November 1994 and April 1995 not only at $\mu = 0.1$ but also at $\mu = 0.2$ for a number of lines. It is of interest to compare the steepness of the center-to-limb variation in the different lines by deriving the ratio between the line polarizations measured at $\mu = 0.2$ and 0.1, and to compare it with the corresponding ratio for the continuum polarization and the Chandrasekhar curve for a purely scattering atmosphere.

In many or even most spectral regions the magnitude of the continuum polarization is comparable to that of the line polarization. Thus, if we would measure the line polarization from the polarization zero level, the results would to variable degrees be affected by the behavior of the continuum rather than of the lines alone. In addition, the amount of continuum polarization cannot be determined well in regions with no well-defined depolarizing lines, and unfortunately most spectral regions are like that.

Although the amount of continuum polarization p_c is difficult to determine, it is much easier to locate the relative level of the continuum by averaging Q/I for the highest I values (which are closest to the continuum level). Thus $p - p_c$ is a well-defined observational quantity that does not depend on the zero-point of the polarization scale and is a first approximation of the polarization that is due to the lines alone.

$p - p_c$ however does not represent the entire line polarization, since in the complete absence of intrinsic line polarization the amount of polarization at line center would not be p_c, but there would be a depression below the continuum level. The contribution p_{line} from the spectral line to the total polarization p (line plus continuum) should rather be measured from this depressed level. This was done in Stenflo et al. (1983a) by defining p_{line} as

$$p_{\text{line}} = p - p_c + p_c d, \qquad (2.8)$$

where d is the Stokes I line depth. We see from Eq. (2.8) that we in the absence of intrinsic line polarization ($p_{\text{line}} = 0$) retrieve Eq. (2.3) for purely depolarizing lines, as expected. p_{line} thus represents the additional polarization that is contributed by the line.

Figure 2.4 provides an overview of the results for the various lines that we have observed. The horizontal lines represent error bars based on an assumed error of 0.003 % in p and p_c (0.006 % is used for Sr I and its neighboring continuum, since shorter exposures were used due to the larger Sr signals). This error is in most cases larger than the actual formal noise and is therefore conservatively chosen. The solid error bars represent for the spectral lines the ratio of the p_{line} values derived from Eq. (2.8) at $\mu = 0.2$ and 0.1, respectively, while the dashed lines represent for comparison purposes the corresponding ratios of the $p - p_c$ values. In the case of the 4607 Å continuum the solid line simply represents the p_c ratio. For reference purposes we have also marked by the solid vertical line the Chandrasekhar (1950) value of 0.726 for a purely scattering atmosphere.

The data of Fig. 2.4 have been corrected for stray light but not for finite spectral resolution. The correction factors for spectral broadening should however be approximately the same for $\mu = 0.1$ and 0.2, so to first order these factors divide out when forming the ratios that represent the CLV slopes.

The error bars of the determined polarization ratio become large when the polarization amplitudes are small, approximately in inverse proportion to the amplitudes, and we divide by small numbers. In several cases, when the continuum polarization is not small in comparison with the line polarization, the positions of the solid and dashed error bars disagree significantly. It is the solid lines representing the p_{line}
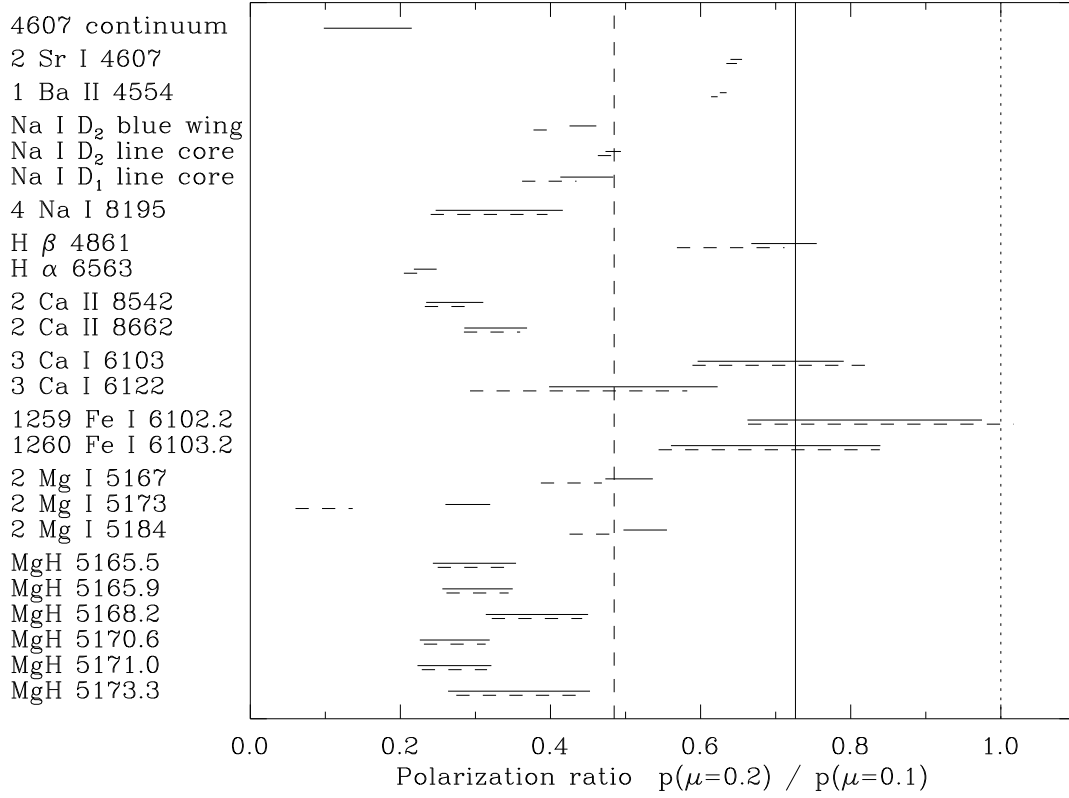
Figure 2.4: Overview of the slopes of the center-to-limb variations for a number of lines observed with ZIMPOL in November 1994 and April 1995. The slopes are represented by the ratio between the Q/I polarizations observed at $\mu = 0.2$ and $\mu = 0.1$. The horizontal lines represent error bars. For the various spectral lines the solid error bars represent the p_{line} ratio, where p_{line} is defined by Eq. (2.8), while the dashed error bars represent the $p - p_c$ ratio. For the 4607 Å continuum it is simply the p_c ratio that is given. The Chandrasekhar (1950) ratio of 0.726 for a purely scattering atmosphere is given by the solid vertical line, while the corresponding ratio of 0.485 for the analytical function $(1-\mu^2)/\mu$ is given by the vertical dashed line. For an optically thin scattering layer the CLV function should be proportional to $(1 - \mu^2)/[\mu I_c(\mu)]$, which at 5000 Å gives a polarization ratio of 0.37.

ratio that are the more relevant ones for the line polarization, and they show a somewhat more consistent behavior than the dashed lines.

Figure 2.4 shows that the CLV of the continuum polarization is steeper than that of any line polarization that we have examined. The steepest p_{line} variations are exhibited by the molecular MgH lines, the Ca II infrared lines (8542 and 8662 Å), Hα, and Na I 8195 Å. For these lines the polarization declines by about a factor of 3 when going from $\mu = 0.1$ to $\mu = 0.2$, as compared with a factor of 6 for the continuum polarization and 1.38 for a purely scattering atmosphere. The CLVs of Sr I and Ba II are only slightly steeper than the CLV of the purely scattering atmosphere, while the Fe I lines that we have looked at agree with the purely scattering case at least within the fairly large error bars.

The molecular lines are expected to be formed in a thin layer in the lower portion of the temperature minimum region, since the optimum conditions for molecule formation requires a combination of low temperature and high density. This layer is well above the layers from where most of the photons at these wavelengths emanate (optical depth unity). For a plane-parallel stratification the optical path length of the optically thin molecular layer scales with μ as $1/\mu$. The source function for Stokes Q on the other hand scales as $1 - \mu^2$ (Stenflo 1994). Therefore it is natural to expect the shape of the resulting CLV to be proportional to the function $(1 - \mu^2)/\mu$, which explains the logic behind the choice of function in Eq. (2.6), where we in addition entered a parameter b in the denominator to control the slope of the analytical function. As the plane-parallel approximation breaks down when approaching the extreme limb, there will be some saturation of the $1/\mu$ part of the CLV curve at the extreme limb.

As pointed out to us by M. Faurobert-Scholl (private communication) we also need to multiply the function $(1 - \mu^2)/\mu$ with $1/I_c(\mu)$ to make it a more complete representation of the CLV for weak lines formed by scattering in an optically thin layer, like our molecular lines. The reason is that while Stokes Q as the nominator in the fractional polarization Q/I scales with $(1 - \mu^2)/\mu$, the intensity I is approximately given by the continuum intensity at that μ position, $I_c(\mu)$. While the $\mu = 0.2/\mu = 0.1$ ratio for the function $(1 - \mu^2)/\mu$ is 0.485, the corresponding ratio for $I_c(\mu)$ is wavelength dependent. Since the ratio for the function $(1 - \mu^2)/[\mu I_c(\mu)]$ would therefore not be a straight line in

Fig. 2.4, we have only plotted the 0.485 value as the vertical dashed line in the figure for reference purposes. At 5000 Å the observed value of $I_c(0.1)/I_c(0.2)$ is 0.76 (Allen 1973). The molecular MgH lines should therefore be compared with the ratio $0.76 \times 0.485 = 0.37$ for an optically thin scattering layer. This value comes close to the observed polarization ratios in Fig. 2.4.

While these considerations provide a good explanation for the steep CLV of optically thin lines like the molecular lines, they are not applicable to our optically thick lines, whose CLV will be governed by more complex radiative-transfer effects. We note in particular that lines like the Sr line has a less steep CLV than the function $(1 - \mu^2)/\mu$, while a number of other optically thicker lines, like Hα and the Ca II infrared triplet, have a steeper variation.

2.5   Concluding remarks

We have assembled the available new observational data on the center-to-limb variation (CLV) of the scattering polarization for various spectral lines and the continuum, and have presented the results in a form that may be directly used to constrain theoretical models. Although some information on the slope of the CLV curve is available for a number of different spectral lines, the only line for which the full CLV curve has been investigated in detail (apart from a few CLV curves from 1978 observations (Stenflo et al. 1980) is the Sr I 4607 Å line. The main reasons for the attention that this line has received are: (1) It has an unusually strong and symmetric polarization peak that is surrounded by a clean continuum and an adjacent depolarizing Fe I line that can be used for reference purposes and for the determination of the continuum level and the zero point of the polarization scale. (2) Its $J = 0 \rightarrow 1 \rightarrow 0$ resonant scattering transition is the quantum mechanical analog to classical dipole scattering, which represents the maximum polarizing case. (3) Its atomic structure and radiative-transfer parameters are well known. (4) It lends itself well to modelling with radiative transfer, in particular since it is sufficient to assume complete frequency redistribution rather than having to do the full partial redistribution problem, because it is not strong enough to have extensive

wings, so all the significant polarization occurs in the Doppler core. (5) Due to these possibilities for detailed quantitative modelling, it has been extensively used to diagnose the strength of the "hidden", spatially unresolved turbulent magnetic field of the Sun (Faurobert-Scholl 1993; Faurobert-Scholl et al. 1995).

The present observations give the detailed CLV of the Sr I line not only for the polarization amplitude, but also for the width of the polarization peak and the width and depth of the corresponding Stokes *I* profile, as well as the CLV of the continuum polarization. These five CLV curves provide powerful joint constraints on any future models for this line and its Hanle depolarization as a measure of the turbulent magnetic field.

The comparison between the different data sets shows that it is possible to obtain consistency after very careful corrections for the effects of spectral broadening and stray light have been made. It also highlights the great sensitivity of the results to these corrections. The spread of the data points illustrates the degree of reproducibility of the results, but we have also shown evidence that at least some of this spread must be intrinsically solar. Thus a conspicuous kink in the CLV curve for the June 1994 data is most likely due to spatially varying Hanle depolarization on the Sun.

Such local fluctuations of the Hanle depolarization across the solar surface may be quantitatively interpreted in an almost model independent way if we observe the polarization in combinations of spectral lines with different sensitivities to the Hanle effect. We have started an observing program with ZIMPOL to calibrate and later exploit such line combinations as diagnostic tools for solar magnetoturbulence. A corresponding complementary program has also been started at IR-SOL in the UV portion of the solar spectrum.

To better understand the scattering physics on the Sun and to exploit it for various diagnostic purposes we need to systematically observe the CLV behavior of many more lines in a similar, rather complete way as we have done for the Sr I line. The CLV of the scattering polarization is a sensitive function of the height variations of temperature and density in the upper photosphere, temperature minimum, and chromosphere, and it thus provides novel constraints for atmospheric modelling.

To gain more control of the Hanle and other magnetic-field effects we need to record the full Stokes vector rather than as here be limited to the Stokes Q and U parameters. Thus spectral signatures in Stokes U may reveal the possible presence of Hanle rotation of the plane of polarization and/or the transverse Zeeman effect, while signatures in Stokes V reveal longitudinal magnetic fields. The regime in which the Hanle and Zeeman effects mix is particularly interesting to explore. For such sensitive vector polarimetry we need improved control and/or compensation of the instrumental polarization. These various problems are different aspects of our long-term program to explore and make diagnostic use of the scattering polarization on the Sun.

Bibliography

Allen, C. W., 1973, *"Astrophysical quantities"*, University of London, Athlone Press, London, 3rd ed.

Auer, L. H., Rees, D. E., Stenflo, J. O., 1980, *"Resonance-Line Polarization. VI. Line Wing Transfer Calculations Including Excited State Interference"*, Astron. Astrophys. **88**, 302

Chandrasekhar, S., 1950, *"Radiative transfer"*, Clarendon Press, Oxford

Donati, J.-F., Semel, M., Rees, D. E., Taylor, K., Robinson, R. D., 1990, *"Detection of a magnetic region on HR 1099"*, Astron. Astrophys. **232**, L1

Faurobert-Scholl, M., 1993, *"Investigation of microturbulent magnetic fields in the solar photosphere by their Hanle effect in the Sr ı 4607 Å line"*, Astron. Astrophys. **268**, 765

Faurobert-Scholl, M., Feautrier, N., Machefert, F., Petrovay, K., Spielfiedel, A., 1995, *"Turbulent magnetic fields in the solar photosphere: diagnostics and interpretation"*, Astron. Astrophys. **298**, 289

Keller, C. U., 1996, *"Recent Progress in Imaging Polarimetry"*, Sol. Phys. **164**, 243

Keller, C. U., Aebersold, F., Egger, U., Povel, H. P., Steiner, P., Stenflo, J. O., 1992, *"Zurich Imaging Stokes Polarimeter Zimpol-I — Design Review"*, Tech. Rep. 53, LEST Foundation

Leroy, J. L., 1977, *"Measurements and Interpreta-tion of Polarization Arising in the Solar Chromosphere and Corona"*, in *In: Stenflo, J.O. (ed.), Rep. Lund Observatory No. 12*, 161

Mickey, D. L., Orrall, F. Q., 1974, *"Broadband Polarization Measurements on the Quiet Sun's Disk near λ 5834"*, Astron. Astrophys. **31**, 179

Povel, H., 1995, *"Imaging Stokes polarimetry with piezoelastic modulators and charge-coupled-device image sensors"*, Optical Engineering **34**, 1870

Povel, H., Aebersold, H., Stenflo, J. O., 1990, *"Charge-coupled device image sensor as a demodulator in a 2-D polarimeter with a piezoelastic modulator"*, Appl. Opt. **29**, 1186

Semel, M., Donati, J.-F., Rees, D. E., 1993, *"Zeeman-Doppler imaging of active stars. 3: Instrumental and technical considerations"*, Astron. Astrophys. **278**, 231

Stenflo, J. O., 1982, *"The Hanle effect and the diagnostics of turbulent magnetic fields in the solar atmosphere"*, Sol. Phys. **80**, 209

Stenflo, J. O., 1994, *"Solar magnetic fields: polarized radiation diagnostics"*, Astrophysics and Space Science Library, Kluwer Academic Publishers, Dordrecht

Stenflo, J. O., Baur, T. G., Elmore, D. F., 1980, *"Resonance-line polarization. IV. Observations of non-magnetic line polarization and its center-to-limb variations"*, Astron. Astrophys. **84**, 60

Stenflo, J. O., Keller, C. U., 1996, *"New window for spectroskopy"*, Nature **382**, 588

Stenflo, J. O., Keller, C. U., 1997, *"The second solar spectrum. A new window for diagnostics of the Sun"*, Astron. Astrophys. **321**, 927

Stenflo, J. O., Twerenbold, D., Harvey, J. W., 1983a, *"Coherent scattering in the solar spectrum — Survey of linear polarization in the range 3165–4230 Å"*, Astron. Astrophys. Suppl. Ser. **52**, 161

Stenflo, J. O., Twerenbold, D., Harvey, J. W., Brault, J. W., 1983b, *"Coherent scattering in the solar spectrum — Survey of linear polarization in the range 4200–9950 Å"*, Astron. Astrophys. Suppl. Ser. **54**, 505

Wiehr, E., 1975, *"Measurement of solar disc polarization in a number of Fraunhofer lines and their adjacent continuum"*, Astron. Astrophys. **38**, 303

Chapter 3

Hanle depolarisation in the solar chromosphere [*]

M. Bianda[1], S.K. Solanki[2] and J.O. Stenflo [2]

Abstract

A new polarimeter and an extension of the polarimetric technique of Donati et al. (1990) to higher polarisation values are presented. With this system, which allows low-noise polarimetric observations in the blue and near-UV part of the solar spectrum, we have recorded more than 200 Q/I profiles of Ca I 4227 Å with an accuracy of 2–3$\times 10^{-4}$.

We find that while the Q/I line shape outside the line core is very stable from one part of the solar surface to the next, the line core exhibits large variations relative to the rest of the profile. These variations are best interpreted in terms of partial depolarisation produced by the Hanle effect in the presence of weak fields. We obtain a quantitative and model-independent estimate of the depolarisation, from which we deduce field strengths of 5–15 G at the level of line-core formation, i.e. in the low to mid chromosphere. We also find evidence that the field strength is distributed around these average values with

a FWHM that is approximately the same as the average value.

3.1   Introduction

Due to its versatility and relative ease of use the Zeeman effect has been the mainstay of observational investigations of solar magnetism, in particular of the intrinsically strong (kG) fields organized into the network, active-region plages and sunspots. The Zeeman effect suffers, however, from a lack of sensitivity to intrinsically weak fields and to fields with mixed polarities or random orientations at small scales (turbulent fields).

A promising alternative is the Hanle effect (Hanle 1924; Moruzzi & Strumia 1991; Stenflo 1994). It makes the polarization in appropriate spectral lines sensitive to very weak fields, and allows their strengths and directions to be determined. In addition, it can detect fields even when they are turbulent and hence practically invisible to the Zeeman effect. The Hanle effect has been employed to deduce the magnetic structure of solar prominences (Leroy et al. 1977; Sahal-Bréchot et al. 1977; Bommier 1980; Landi degl'Innocenti 1982; Querfeld et al. 1985) turbulent fields in the solar photosphere (Stenflo 1982; Faurobert-Scholl 1993; Faurobert-Scholl et al. 1995) and magnetic canopies in the chromosphere (Faurobert-Scholl 1992; 1994). All in all, however, it has been employed relatively rarely. The problem has largely been an observational one, since the proper interpretation of the Hanle effect requires observations that combine high spectral resolution with high polarimetric accuracy. These conditions have recently been met by the Zurich Imaging Stokes Polarimeter (ZIMPOL; Povel 1995) , which has opened new windows for the measurement of polarisation produced by resonant scattering (Stenflo & Keller 1996; 1997; Stenflo 1997 and Chapter 2). One shortcoming of the present version of ZIMPOL is that its detectors are insensitive to wavelengths below about 4500 Å. This is unfortunate, since most of the lines showing strong resonance polarisation, a prerequisite for Hanle depolarisation, are located in the blue or the UV.

In the present paper we briefly describe a simple polarimeter that allows us to obtain Q/I observations with noise levels in the contin-

uum approaching 10^{-4} at wavelengths down to 3800 Å (Q is the net linear polarisation and I is the intensity). It opens up an interesting spectral region to accurate observations of resonance polarisation and possible Hanle depolarisation. We also present and analyse the first observations made with this instrument.

The spectral survey of resonance polarisation carried out by Stenflo et al. (1983a;b) showed that the Ca I 4227 Å resonance line has the strongest Q/I signature in the whole visible and near UV spectrum. This line has also been one of the most often observed, resonantly polarized spectral features (Brückner 1963; Stenflo 1974; Wiehr 1975; Stenflo et al. 1980). Coincidently, Brückner discovered the polarisation of this line with the same telescope with which our observations have been obtained. The line core is formed in the mid chromosphere (Faurobert-Scholl 1992), a height for which hardly any Zeeman-effect based diagnostics exist. Finally, through the Hanle effect it is sensitive to field strengths of about 5–100 G. This range corresponds to the field strengths expected in the mid chromosphere, in particular in the quiet sun. In the present paper we present Q/I observations of this line and analyse them in search for the signature of the Hanle effect.

The centre-to-limb variation (CLV) of the Stokes vector of this line was last recorded by Stenflo et al. (1980) with a noise level of approximately 0.1%. The main disadvantage of these observations is that the solar surface was sampled only at a few locations, so that it is unclear to what extent these data are representative of the quiet Sun. In addition, the spectral resolution was relatively low, although this may not be important for a broad line like Ca I 4227 Å. Based on these observations Faurobert-Scholl (1992; 1994) deduced that there is a magnetic field of 20–100 G at heights between 700 and 1200 km above the continuum-forming level, if she assumes that the field is in the form of a magnetic canopy, i.e., a horizontal magnetic field overlying a field-free atmosphere (cf. Giovanelli 1980).

In the present paper we analyse a large number of Stokes I and Q/I spectra of Ca I 4227 Å obtained in the quiet Sun with both low noise and high spectral resolution. The instrumental setup and observations are described in Sect. 3.2., the reduction technique in Sect. 3.3., the data analysis and results in Sect. 3.4. Finally, conclusions are drawn in Sect. 3.5.

3.2   Instrumentation and observations

3.2.1   Instrumental set-up

Observations were carried out with the now completely refurbished, evacuated Gregory-Coudé telescope and the Czerny-Turner spectrograph of IRSOL (Istituto Ricerche Solari Locarno) located above Locarno in Switzerland. The telescope has an aperture of 45 cm and a total focal length of 25 m, while the spectrograph has a focal length of 10 m and a grating with the dimensions 180×360 mm ruled at 300 l/mm with a blaze-angle of $63°$. To keep different spectral orders from overlapping and minimize stray light a predisperser is used, placed immediately after the spectrograph slit (which has a width of 200 μm, corresponding to 1.65″). The telescope has optics that are almost identical to those of the Gregory-Coudé Telescope operated by Göttingen University on Tenerife. Except for two plane mirrors, all of the optical elements of the telescope are on-axis and should not produce any significant cross-talk between the Stokes parameters (if we disregard the entrance window). Due to the positioning of these two mirrors the instrumental polarisation does not vary during the day, but only with the Sun's declination. Around equinox the two off-axis mirrors, inclined by $45°$ to the beam, compensate each other, since their position angles are $90°$ apart (Martinez-Pillet & Sánchez-Almeida 1991). Thus at this time the telescope may be considered to be nearly polarisation-free (with the exception of the entrance window). All observations discussed in this paper were carried out near an equinox.

The detector used is a blue-enhanced CCD system with 400×600 pixels, each corresponding to $0.18″ \times 2.8$ mÅ at 4227 Å.

We follow the observational technique proposed and applied by Donati et al. (1990), Semel et al. (1993) and Semel (1994; 1995). A total of four spectral images of each observed solar region are obtained (composed of two simultaneous spectral image pairs). By constructing appropriate ratios between these images we can obtain very low noise levels in Q/I (approaching 10^{-4}). We employ a polarizing beamsplitter (a calcite polarizer) together with a manually rotated half-wave plate. The beamsplitter is placed a few cm in front of the spectrograph slit and is aligned (with the aid of pores and the solar limb) in such

a way that it projects the same part of the solar surface twice onto the spectrograph slit (these two images correspond to the two polarisation components, which are aligned to better than 1″). The unvigneted part of each image covers 18″ on the solar surface.

The rotatable half-wave plate precedes the polarizing beamsplitter and can be set in two different orientations. In the first the fast axis is parallel to one of the axes of the polarizer, while in the other the half-wave plate is rotated by 45°, so that the Stokes co-ordinate system is rotated by 90°. In this manner the polarisation of the two images is exchanged.

Two CCD frames are stored at every observed solar location, one per half-wave plate orientation (which is rotated manually while the CCD is being read out and the data are being stored on disc). In order to avoid pixel misalignments care is taken to have the CCD pixels oriented parallel to the spectral dispersion and to have spectral lines exactly aligned with the pixel columns (telluric lines are used for this purpose).

We have verified the efficiency of the polarisation optics with the aid of a Glan Thompson polarizer. At three wavelengths of interest for resonance polarisation measurements, namely those of the Sr I 4607 Å, Ca I 4227 Å and Sr II 4078 Å lines, we find efficiencies of 99.5%, 98.8% and 97%, respectively. The reason for the decreasing efficiency towards the violet is that the achromatic half-wave plate is used outside its specified wavelength range (4600-6800 Å).

3.2.2 Observations

We observed the core and inner wings of the Ca I resonance line at 4227 Å on 12th, 14th, 17th and 20th October 1995, on 23rd, 26th, 28th and 29th March 1996 and on 12th April 1996. The complete wavelength range covered by one CCD setting was 4225.9–4227.4 Å. Since this is not enough to cover the central part of the line and at the same time also obtain a part of the neighbouring continuum we have in some cases made two recordings at the same spatial position, each at a different wavelength location. The recordings were carefully combined using the data points in the wavelength range in which they overlapped. It is necessary to have observations of the line core together with the

continuum in order to determine the stray light and the zero level of the polarisation.

By constructing appropriate ratios between the set of four recorded images it is possible to obtain the fractional linear polarisation Q/I as a function of wavelength and spatial position almost free from gain table, plate transparency and seeing-induced spurious polarisation (see Sect. 3.3.2, Semel et al. 1993) A residual fixed-pattern Q/I background remains, however. It can be removed by making additional recordings at disc centre, where for symmetry reasons the intrinsic scattering polarisation disappears, while the fixed spurious pattern remains unchanged. Thus we alternate recordings at positions near the limb (the actual measurements) with recordings at disc centre (calibrations).[3] Generally we carried out a measurement at disc centre after every third or fourth registration at the limb. To avoid the introduction of unwanted granular Doppler shifts or Zeeman signals from magnetic features the telescope was moved during exposures at disc centre.

A total of 207 solar regions were recorded at $\mu = \cos\theta$ values ranging between 0.8 and 0.05 (here θ is the heliocentric angle). An additional 60 recordings were also made at disc centre. Generally the full centre-to-limb variation (CLV) of Q/I was recorded. Only on 26th March 1996 did we confine ourselves to locations close to the solar limb $(0.05 < \mu < 0.15)$. The aim in that case was to search for variations in Q/I at different positions along the limb.

Exposure times were typically 5 s at disc centre and 20 s at $\mu = 0.05$. Hence the total time needed to record and store a full set of measurements (i.e. an image pair near the limb and at disc centre) ranged between 350 sec and 500 sec (including moving the telescope and confirming the μ value), depending on the observed μ.

During all exposures at $\mu < 1$ the slit was placed parallel to the nearest part of the solar limb. Stokes Q is positive along the slit, i.e. parallel to the limb. In a Gregory-Coudé system the image rotates on

---

[3] This procedure would in principle also permit us to follow the sky transparency evolution for a better determination of the μ-value. We found, however, that although such a procedure works for Sr I 4607 Å and Sr II 4078 Å, it is impracticable with our setup for large numbers of Ca I 4227 Å observations, due to the necessity of determining the continuum co-temporally in every case. We have consequently not made use of it in this paper.

the slit plane, so that at a given time only two parts of the solar limb (180° apart) can be observed due to this requirement. Conversely, a given part of the solar limb can be observed for a few minutes only. An optical image rotation compensator would have to be placed behind the polarimeter (but before the slit) to avoid excessive instrumental polarisation. Since, however, the beam splitter must be located close to a focus, an image rotator would require special transfer optics to reimage the focus placed near the beamsplitter onto the slit, and has consequently not been employed.

For $\mu \leq 0.3$ we determine the position of the slit by measuring its distance from the solar limb, whereas for $\mu > 0.3$ the guiding system is employed. Image motion, seeing and guiding errors limit the exact reproduction of the observed position between the two exposures to 1–3″ (depending mainly on seeing conditions).

3.3 Data reduction

3.3.1 Overview of the reduction procedure

The main steps of the data reduction are as follows: 1. Dark current subtraction; 2. Flat fielding (it is required only for Stokes I, since the technique of Donati et al. (1990) does not require flat fielding to obtain Q/I); 3. Extraction of Q/I from the observed frames (as described in Sect. 3.3.2); 4. Determination of spectral smearing and stray light, as well as removal of the latter from the data (Sect. 3.3.3); 5. Correction of the instrumental zero level and remaining fixed pattern noise using data obtained at disc centre (Sect. 3.3.4); and 6. Fourier smoothing to reduce noise in the data (Sect. 3.3.5).

3.3.2 Extraction of Q/I

Basic technique

Donati et al. (1990) and Semel et al. (1993) proposed that very low noise V/I measurements can be made without having to flat-field or worry about retarder transparency by a simple combination of a polarizing

beamsplitter and a quarter-wave plate, which can be switched to provide $\pm\lambda/4$ retardation. We have applied this technique to determine Q/I using a half-wave plate. The following description is for Q/I measurements, but it is of course possible to apply this technique to Stokes V and U simply by changing the polarisation analysis accordingly. All the equations in this section apply equally to Stokes V and U if Stokes Q is replaced by the desired Stokes parameter.

By carrying out two measurements, one for each retarder setting, and forming

$$F = \frac{1}{2}\left(\frac{f_1^+ f_2^+}{f_1^- f_2^-} - 1\right), \qquad (3.1)$$

one obtains a good approximation for Q/I averaged over both measurements that is free from effects of the detector gain table and half-wave plate transparency at the two settings. In Eq. (3.1) $f_{1,2}^{+,-}$ represent the four images (exposures 1 and 2, for the polarisation states denoted by $+$ and $-$),

$$\begin{aligned}
f_1^+ &= (I_1^l + Q_1^l + \delta_1^l)R_1 G_l, \\
f_2^+ &= (I_2^r + Q_2^r + \delta_2^r)R_2 G_r, \\
f_1^- &= (I_1^r - Q_1^r - \delta_1^r)R_1 G_r, \\
f_2^- &= (I_2^l - Q_2^l - \delta_2^l)R_2 G_l.
\end{aligned} \qquad (3.2)$$

Here $G_{l,r}$ is the detector gain on the left and right parts of the detector array, $R_{1,2}$ the throughput of the polarimeter at the two settings (e.g. due to mechanical misalignments, or if the half-wave plate is not perfect at the observed wavelength), $I_{1,2}$ the Stokes I signal of the two exposures, $Q_{1,2}$ the corresponding Stokes Q signal and

$$\delta_j = \delta_{Ij}I_j + \delta_{Vj}V_j + \delta_{Uj}U_j, \qquad j = 1, 2, \qquad (3.3)$$

a term that takes into account telescopic cross-talk from Stokes I, Stokes V and Stokes U into Stokes Q. Such a term is generally present in solar observations, since most solar telescopes are not axially symmetric, and wavelength dependent V and U signals are produced by the Zeeman effect and – in the case of U – by the Hanle effect. $I^{l,r}$, $Q^{l,r}$ and $\delta^{l,r}$ correspond to the I, Q and δ signals on the left and right sides of the array. They need not be identical due to pixel misalignments. If following Donati et al. (1990) we assume that $Q_j \ll I_j$, neglect pixel

mismatch, i.e. assume that $I_j^r = I_j^l$, $Q_j^r = Q_j^l$ and $\delta_j^r = \delta_j^l$, and perfect modulation, then we obtain

$$F = \frac{Q_1 + \delta_1}{I_1} + \frac{Q_2 + \delta_2}{I_2}, \tag{3.4}$$

which, except for the cross-talk terms neglected by Donati et al. (1990), Semel et al. (1993) and Semel (1994; 1995) is identical to the result of these authors. The important point stressed by Semel and co-workers is that F is independent of R_j and of $G_{l,r}$, making it unnecessary to flat-field and allowing noise levels to be reached in Q/I that lie substantially below those normally achieved with flat-fielding, as Semel et al. (1993) demonstrated for stellar data. In the following we continue to neglect pixel mismatch, imperfect modulation, etc.

Extension to larger polarisation signals

The method of Semel et al. (1993) works well as long as the actual Q/I signal is small. This is due to the fact that they use a linearisation based on the assumption that $Q/I \ll 1$. This assumption introduces significant systematic errors (i.e. errors larger than 10^{-3}) for Q/I signals larger than 1–2%. This means that for scattering polarisation measurements on the Sun this method is restricted to large μ only, or to spectral lines that have intrinsically very low polarisation. This is, given the promise of the method, a very unsatisfactory situation, in particular for the blue and UV, where currently no other instrument is available that can achieve the desired accuracy. In the following we describe some attempts to improve it.

F can be rewritten in terms of

$$\epsilon = \frac{Q_1 + \delta_1}{I_1} + \frac{Q_2 + \delta_2}{I_2} \tag{3.5}$$

and

$$a = 1 + \frac{Q_1 + \delta_1}{I_1} \frac{Q_2 + \delta_2}{I_2}, \tag{3.6}$$

giving

$$F = \frac{1}{2}\left(\frac{a + \epsilon}{a - \epsilon} - 1\right) = \frac{\epsilon}{a - \epsilon}. \tag{3.7}$$

The usual approach is to expand this for $\epsilon < 1$, which gives us

$$F = \frac{\epsilon}{a} + \frac{\epsilon^2}{a^2} + \frac{\epsilon^3}{a^3} + O\left(\frac{\epsilon^4}{a^4}\right), \tag{3.8}$$

where the symbol O signifies "on the order of". Equation (3.8) is a cubic equation in (ϵ/a). However, the desired quantity is ϵ. If we note that $F = O(\epsilon)$ for not too large ϵ, that $a = 1 + O(\epsilon^2)$ and keep only terms to second order in ϵ, then we can solve Eq. (3.8) for ϵ to get

$$\epsilon = \frac{1}{2}(-1 + \sqrt{1 + 4F}). \tag{3.9}$$

Similarly the third order approximation, i.e. taking all terms in Eq. (3.8) up to $O(\epsilon^3)$ into account, is relatively straightforward to write down. However, it is also possible to obtain an exact solution of Eq. (3.7) if we assume that

$$a = 1 + \epsilon^2/4, \tag{3.10}$$

which is exactly fulfilled for the case when

$$\frac{Q_1 + \delta_1}{I_1} = \frac{Q_2 + \delta_2}{I_2}. \tag{3.11}$$

The exact solution then reads:

$$\epsilon = \frac{2}{F}(1 + F - \sqrt{1 + 2F}). \tag{3.12}$$

Of course, if Eq. (3.10) is not fulfilled then Eq. (3.12) is only an approximate solution of Eq. (3.7) whose accuracy needs to be verified. Note that for $F \to 0$ Eq. (3.12) becomes singular. Thus for sufficiently small F (a good choice is $F < 0.001$, as tests have shown) the solution assuming $a = 1$ is more stable and just as accurate:

$$\epsilon = \frac{F}{F + 1}. \tag{3.13}$$

Note also that Eqs. (3.7) and (3.12) are only valid if $\epsilon < 2$, whereas physically $\epsilon = 2$ is allowed. For resonant scattering this last caveat is of academic interest only.

Tests of the various approximations and the exact solution made using artificial data show that the exact solution is always superior to the expansion solutions, although it too loses accuracy as the difference between $(Q_1 + \delta_1)/I_1$ and $(Q_2 + \delta_2)/I_2$ increases. However, for the observed Q/I values of Ca I 4227 Å (which are smaller than 5%) the accuracy is sufficient (i.e. the errors are smaller than 10^{-4}) even in the extreme case when one of the measurements is zero, e.g., $(Q_2 + \delta_2)/I_2 = 0$.

3.3.3 Determination of stray light and spectral smearing

The magnitude of the spectral stray light and the spectral resolution are determined by comparing the completely reduced Stokes I profiles observed at disc centre, I_{obs}, with a Fourier Transform Spectrum (FTS) obtained by Neckel (1994). The FTS profiles, I_{FTS}, are broadened and shifted by various amounts until the two profiles agree.

An intensity profile observed by us can be expressed in terms of an FTS profile by

$$I_{\text{obs}} = I_{\text{FTS}} \otimes P_I + I_s. \tag{3.14}$$

Here $\otimes$ signifies convolution, P_I is the instrumental profile (a Gaussian is used, with the Doppler velocity v_{D} as free parameter) and I_s is the stray-light intensity. After continuum normalization we obtain

$$\frac{I_{\text{obs}}}{I_{c,\text{obs}}} = \left(\frac{(I_{\text{FTS}} \otimes P_I)}{I_{c,\text{FTS}}} + \frac{I_s}{I_{c,\text{FTS}}} \right) \frac{I_{c,\text{FTS}}}{I_{c,\text{obs}}}, \tag{3.15}$$

where $I_{c,\text{obs}}$ and $I_{c,\text{FTS}}$ are the continuum intensities. Making use of $I_{c,\text{obs}} = I_{c,\text{FTS}} + I_s$ we rewrite Eq. (3.15) to

$$\frac{I_{\text{obs}}}{I_{c,\text{obs}}} = \left(\frac{I_{\text{FTS}} \otimes P_I}{I_{c,\text{FTS}}} + \frac{I_s}{I_{c,\text{FTS}}} \right) \left(1 + \frac{I_s}{I_{c,\text{FTS}}} \right)^{-1}. \tag{3.16}$$

The profile corrected for stray light becomes

$$\left(\frac{I}{I_c} \right)_{\text{corr}} \equiv \frac{(I_{\text{FTS}} \otimes P_I)}{I_{c,\text{FTS}}} = \frac{I_{\text{obs}}}{I_{c,\text{obs}}} \left(1 + \frac{I_s}{I_{c,\text{FTS}}} \right) - \frac{I_s}{I_{c,\text{FTS}}}. \tag{3.17}$$

Introducing the relative amount of stray light, $s = I_s/I_{c,\mathrm{FTS}}$, we can then write

$$\left(\frac{I}{I_c}\right)_{\mathrm{corr}} = (1+s)\frac{I_{\mathrm{obs}}}{I_{c,\mathrm{obs}}} - s \; . \tag{3.18}$$

Similarly, using

$$Q_{\mathrm{obs}} = Q_{\mathrm{corr}} + kI_{\mathrm{obs}} \tag{3.19}$$

one can derive

$$\left(\frac{Q}{I}\right)_{\mathrm{corr}} = \left(\frac{Q_{\mathrm{obs}}}{I_{\mathrm{obs}}} - k\right) \frac{I_{\mathrm{obs}}}{I_{\mathrm{obs}} - I_{c,\mathrm{obs}}\, s/(1+s)} \; , \tag{3.20}$$

where k is the fraction of the intensity, including the stray light, which is added to the intrinsic Q. In Q/I it represents a zero-line offset, being to first order spectrally flat. Typical values found for our observations are $v_{\mathrm{D}} = 1.2$ km s^{-1}, which corresponds to 17 mÅ, and $s = 1\%$. s is sufficiently small to make second order effects negligible.

3.3.4 Determination of the polarisation zero level

For symmetry reasons Q/I due to resonance polarization is expected to be zero at solar disc centre. Any Q/I signal seen in such (disc centre) recordings is therefore due to instrumental polarisation or the Zeeman effect. The latter can easily be avoided by measuring in the quiet Sun and moving the telescope. We nevertheless find a sinusoidal fixed-pattern in Q/I with an amplitude of about 0.1%. We believe that the origin of this sinusoidal signal lies in the half-wave plate, since for other projects we measured V/I Stokes signals with a quarter-wave plate and we found no sinusoidal signal at sun centre. Note that exactly the same fixed pattern is also present in the recordings made near the limb, as is best seen when considering a relatively narrow line like Sr I 4607 Å. Therefore, to correct our data for this fixed-pattern background, Q/I recorded at solar disc centre is subtracted from limb recordings. As a consequence the parameter k in Equation (3.20) is eliminated or at least significantly reduced. The zero level of the polarisation is determined from the resulting Q/I polarisation in the cores of the depolarising blends at 4225.96 Å, 4226.43 Å, 4227.34 Å and 4227.43 Å in the wings of Ca I 4227 Å. In the cores of these blends

Q/I is expected to be a fraction (corresponding to the blending line's relative rest intensity) of the continuum polarisation. In the cases in which the continuum polarisation was not co-temporally measured we used the average continuum polarisation at the corresponding μ value. Although the accuracy of the polarisation zero level derived in these cases is somewhat lower, tests have shown the reduction in accuracy to be small. In general, the observed values of the blend line-to-continuum polarisation ratio (after subtraction of disc centre values) showed good agreement with the expected ratios, without having to introduce a non-zero k in Eq. (3.20). Only in 22 cases out of a total of 207 was a non-zero value of k needed. In these cases k varied between 0.05% and 0.5%, with a mean value of $k = 0.2\%$. The reason for these non-zero k values is unclear. Nevertheless, we retained these 22 recordings in our data, since they exhibit no other anomalies. Their results also agree well with those of the other 185 spectra. In Figure 3.1 we show a reduced recording of a CLV. Illustrated is a typical case with no zero-line correction having to be introduced.

We find that the alignment of the predisperser is a critical source of errors in the zero level. Observations with imperfect alignment turned out to require anomalously large k values to correct. These recordings were removed and are not counted among the 207 Q/I spectra used in the further analysis.

3.3.5   Noise reduction: Fourier smoothing

After the reductions described so far each recording consists of approximately 100 I and Q/I spectra at different spatial positions along the slit. In order to reduce the noise we first add all the spectra along the slit together, leading to a single I and Q/I spectrum per recording. This means that we refrain, in the present paper, from detecting any variations in Q/I on scales below 20″. Finally, we smooth the Q/I spectrum by applying a low-pass filter to its Fourier transform. The efficiency of the Fourier filtering technique is illustrated in Figure 3.1b. An unfiltered, but spatially averaged Stokes Q/I profile is plotted in Figure 3.1b. It has been shifted downward for clarity. The corresponding FFT smoothed profile is the solid profile with the smallest amplitude ($\mu = 0.4$) in Figure 3.1b. Fourier smoothing also allows

us to estimate the residual noise in a straightforward manner. We find 2–3×10^{-4} for the residual noise in units of I_c.

3.4   Analysis and results

3.4.1   The Q/I profile

In Figure 3.1 we show an example of the CLV of the fully reduced Stokes Q/I (Figure 3.1b) as well as the corresponding I/I_c profile at two μ values (Figure 3.1a). The dotted I/I_c profile refers to a measurement at $\mu = 0.1$, the solid profile to disc centre. Note the significant weakening of the line from disc centre to the limb. The quantitative agreement of the Stokes I CLV with the observations of Stenflo et al. (1980) is excellent.

The 3 principal blends at 4225.96 Å, 4226.43 Å and 4227.43 Å are due to iron lines.

The Q/I profiles in Figure 3.1b were obtained at $\mu = 0.1$, 0.15, 0.2, 0.3 and 0.4 (from top to bottom). The downward shifted unsmoothed curve for $\mu = 0.4$ has already been discussed in Sect. 3.3.5. The typical features of the Ca I 4227 Å Q/I spectral profile (the narrow peak in the core and the 2 strong peaks in the wings) and the rapid increase of the polarisation towards the limb are clearly seen and are also found in all other CLV series. They agree qualitatively with previous observations. Other, lesser spectral features are found in many, but not all spectra. An example is the slightly negative Q/I seen in Figure 3.1b at 4226.6 Å (i.e., net linear polarisation perpendicular to the limb). It increases with μ until $\mu = 0.4$ and decreases again towards higher μ (not plotted). This effect and others of similar magnitude do not influence our conclusions in any way.

A theoretical understanding of the wing polarisation of Ca I 4227 Å was first provided by Dumont et al. (1973). Later Rees & Saliba (1982) and Saliba (1985) showed how the presence of a narrow polarisation peak in the Doppler core together with the separate peaks in the wings could be understood as an effect of partial frequency redistribution in polarized radiative transfer for strong lines (cf. also Frisch 1996).

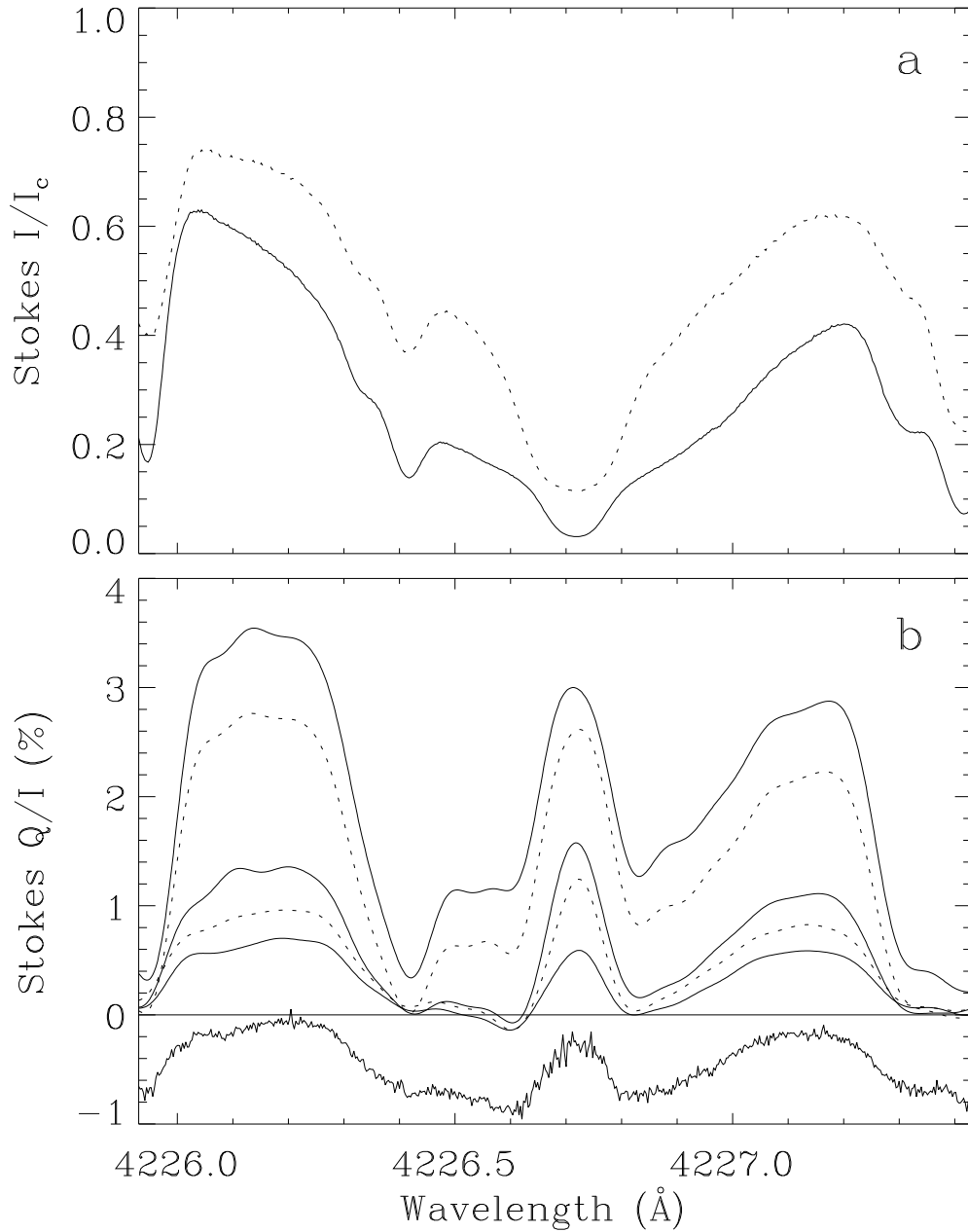Inspection of Figure 3.1b directly reveals that the line core and the

Figure 3.1: a Stokes I/I_c spectra of Ca I 4227 Å, where I_c is the continuum intensity. The solid profile was observed at $\mu = 1$, the dotted profile at $\mu = 0.1$. **b** Stokes Q/I spectra, where Q is net linear polarisation (parallel to the limb minus perpendicular to the limb). The top 5 spectra were obtained at (from top to bottom) $\mu = 0.1, 0.15, 0.2, 0.3$ and 0.4. The noisy spectrum at the bottom of the frame is the same as the spectrum at $\mu = 0.4$, but prior to Fourier smoothing. It has been shifted downwards by 0.75% for clarity.

line wings do not exhibit the same CLV. While the wing polarisation increases in regular steps between $\mu = 0.4$ and 0.2, the line core polarisation makes a large jump between $\mu = 0.4$ and 0.3, but is practically unchanged between $\mu = 0.3$ and 0.2. Also, the maximum line core polarisation is smaller than the maximum blue-wing polarisation in 3 of the 5 plotted spectra. This is in stark contrast to the Q/I FTS spectrum of this line plotted by Stenflo et al. (1983b) and to a certain extent also to the results of Stenflo et al. (1980), who find a considerably higher line-core than blue-wing peak.

3.4.2   Parameters of the Q/I profile

In the following we quantify these differences in behaviour between core and wing. To this end we determine the following three parameters of the Q/I profile: The maximum Q/I value in the blue wing (i.e. at $\lambda < 4226.5$ Å), in the red wing ($\lambda > 4226.9$ Å) and in the line core. In the following we simply refer to these parameters as blue-wing, red-wing and line-centre Q/I, or $(Q/I)_b$, $(Q/I)_r$ and $(Q/I)_c$, respectively.

In Figure 3.2 the CLV of blue-wing and line-centre Q/I of Ca I 4227 Å are plotted. The two most obvious trends are the expected increase of Q/I towards the limb, and the increase of the scatter of *a priori* unknown origin. An analysis of the noise and uncertainties in the line profiles suggests that this increased scatter is not just due to instrumental noise. A major observational uncertainty is the value of μ, which due to the steep CLV of Q/I near the limb leads to a larger scatter there. [4] The rectangles in Figure 3.2a represent the error boxes of the mean Q/I values at each μ. The solid curve in Figure 3.2a is a fit to the boxes with a function of the form

$$\frac{Q}{I} = \frac{a(1 - \mu^2)}{(\mu + b)}, \tag{3.21}$$

where $a = 0.4\%$ and $b = 0.05$ are the best-fit parameters. The choice of this functional form, first introduced by Stenflo et al. (1997), is based on

---

[4] Note that even if μ does not suffer from systematic errors, some scatter is introduced by image motion into Q/I. The μ value may change significantly in an exposure close to the limb lasting several seconds. Since the CLV of Q/I is strongly non-linear near the limb, an average over Q/I obtained at different μ values is not the same as the Q/I measured at the average μ value.

two main considerations. Firstly, in the case of a plane-parallel strat-ification, the path length of an optically thin layer scales as $1/\mu$. Sec-ondly, the source function of Stokes Q scales as $(1 - \mu^2)$. Combining these two dependences we get the form $(1 - \mu^2)/\mu$, which gives a good description for optically thin lines. We can still use it to approximate the CLV of optically thick lines by introducing the free parameters a and b. Parameter b enables us to better account for the breakdown of the plane-parallel approximation when approaching the limb.

The line-centre Q/I, plotted in Figure 3.2b, shows a CLV similar to the blue wing, but with larger scatter. We could find no instrumental reason for this increased scatter and conclude that it is of solar origin. As compared with the CLVs published by Stenflo et al. (1980) our blue-wing Q/I values are about 20% larger, while the line-centre values are smaller, in particular at large μ (the two data sets agree better near the limb, but the error bars and the scatter are also larger there).

The difference in behaviour between line centre and wings is much clearer when one eliminates μ by plotting $(Q/I)_r$ and $(Q/I)_c$ vs. $(Q/I)_b$. In Figure 3.3a we show red-wing Q/I vs. blue-wing Q/I (with each spectrum again being represented by a plus). The relationship between the Q/I of the two wings remains remarkably linear over al-most 2 orders of magnitude and a large range of μ values. It can be described by the linear regression passing through the origin (in units of % polarisation)

$$(Q/I)_r = 0.81(Q/I)_b \, , \tag{3.22}$$

which is also plotted. Even more remarkable is the small scatter exhib-ited by the data points. The standard deviation of the points around this regression is 0.0543 and is a measure of the total uncertainty in the line parameters. This value is less than twice the value expected from the instrumental noise, which suggests that the profile shape in the wings is extremely stable. The tight relationship seen in Figure 3.3a also confirms our suspicion that most of the scatter seen in Figure 3.2a is merely due to uncertainties in μ.

Figure 3.3b, in which the line-centre Q/I is plotted vs. blue-wing Q/I, shows a very different picture. The scatter is very large, much larger than what any observational uncertainties could be expected to introduce. We must therefore search for a solar source of this scat-ter. The most likely source is the Hanle effect, since it acts almost ex-
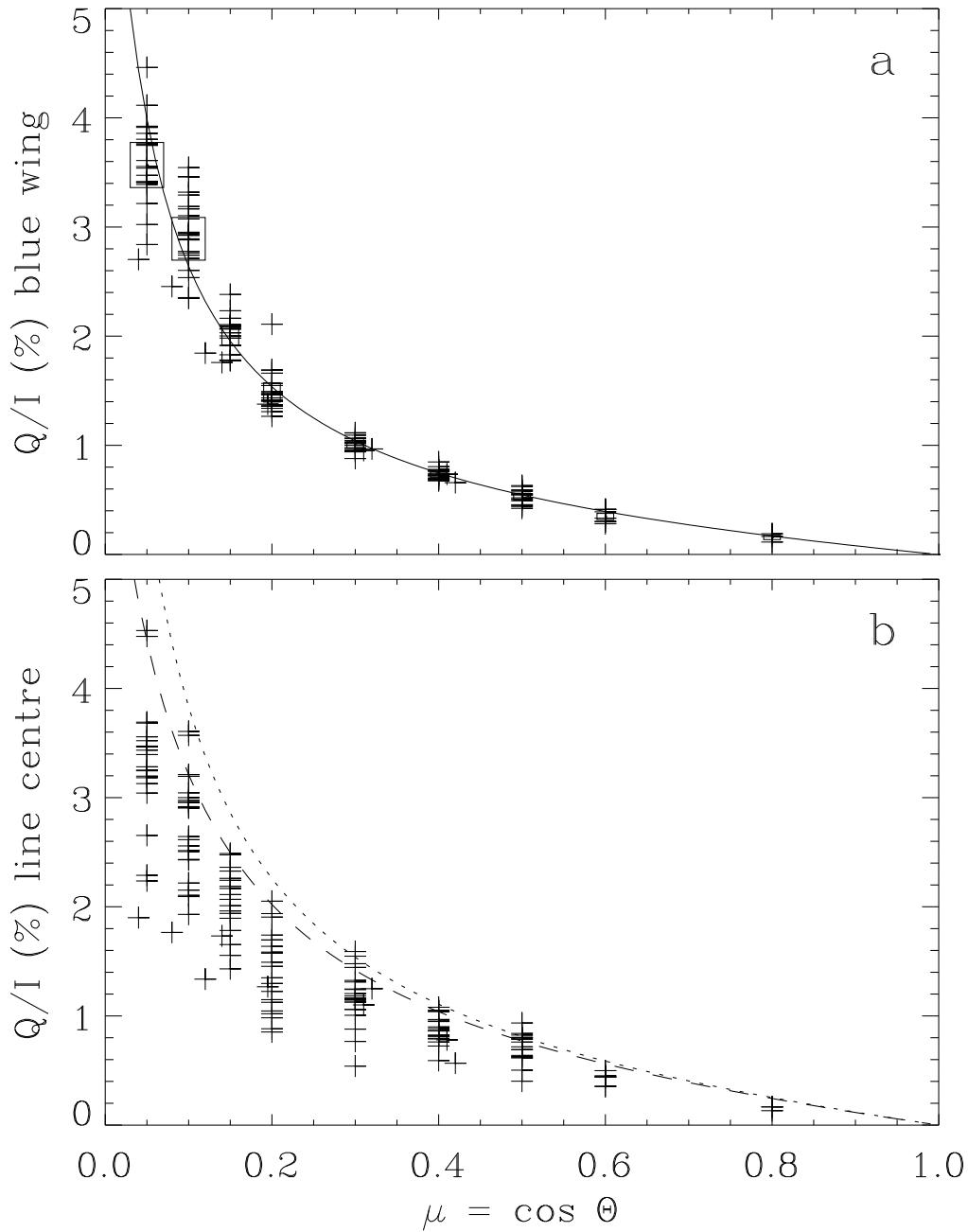
Figure 3.2: Centre-to-limb variation (CLV) of the maximum Q/I in the blue wing (Figure 3.2a) and in the line core (Figure 3.2b). Each plus represents a different spectrum. In Figure 3.2a the rectangles represent the error boxes of the average of Q/I for all the observations at a given μ, while the curve is an analytical fit to these average values. In Figure 3.2b the dotted and dashed curves are upper envelopes to the data points (see text for details)
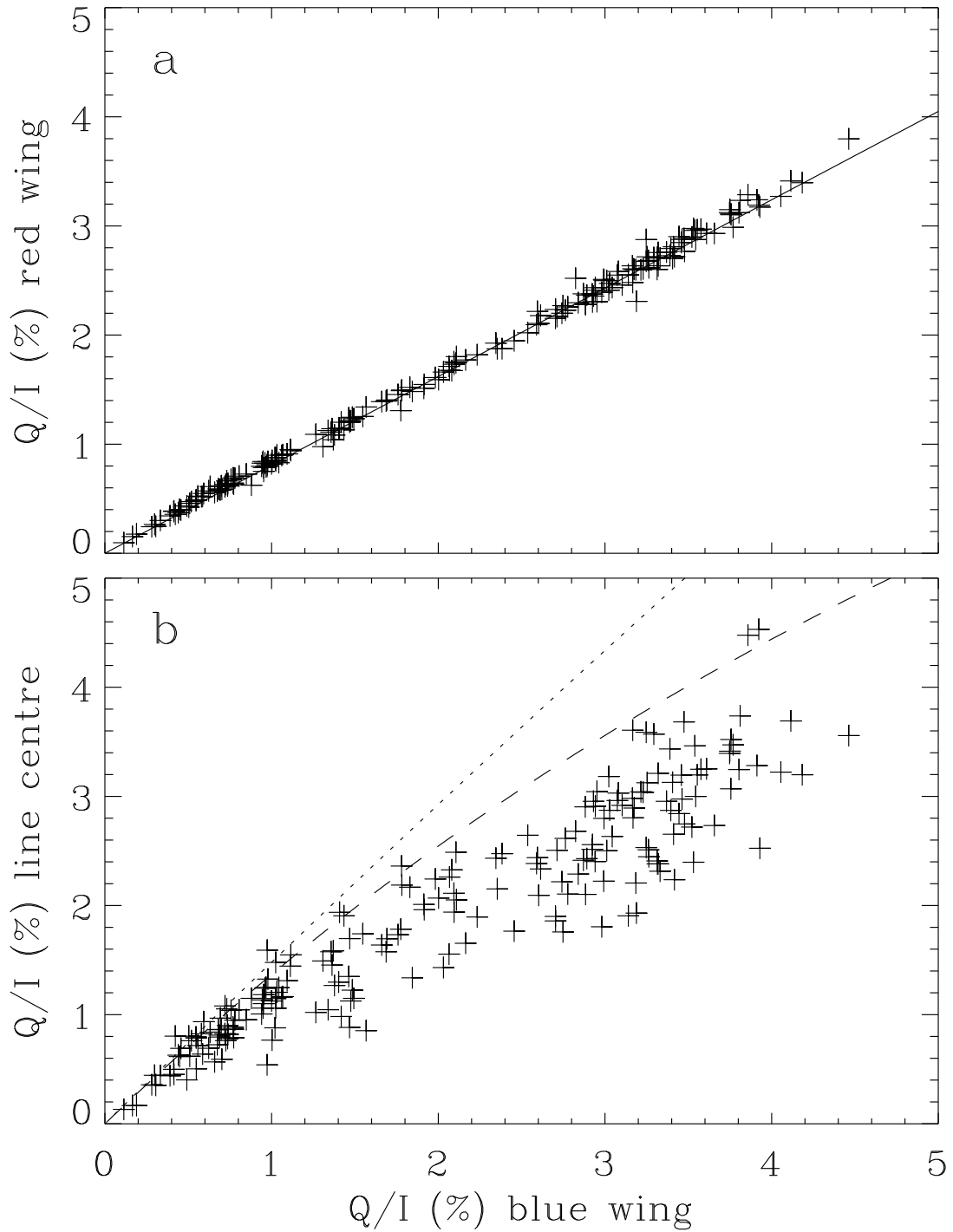
Figure 3.3: Red-wing Q/I (Figure 3.3a) and line-centre Q/I (Figure 3.3b) vs. blue-wing Q/I. The straight line in Figure 3.3a is a linear fit to the data, the dotted and dashed curves in Figure 3.3b are envelopes to the data points corresponding to those plotted in Figure 3.2b

clusively on the line core, while leaving the wings unaffected. In the presence of a magnetic field the Hanle effect depolarizes the line core and rotates the direction of linear polarisation, as was first observed for the Ca I 4227 Å line by Stenflo (1982). The depolarisation depends on the strength and direction of the magnetic field. Therefore a magnetic field that varies spatially in strength or direction can produce a scatter in the core-to-wing Q/I ratio, since we randomly sample solar locations with different field strengths or directions.

Without any further analysis we can immediately conclude that the field whose influence we are observing is relatively weak (since it does not completely destroy the resonance polarisation), and that it is chromospheric (since the core of Ca I 4227 Å is formed in the lower or middle chromosphere).

Interestingly, $(Q/I)_c$ is of approximately the same magnitude as $(Q/I)_b$. This is better seen in Figure 3.4, in which the $(Q/I)_c$ to $(Q/I)_b$ ratio is plotted vs. μ. Although this ratio lies around unity, it does (in its average values, given by the error boxes) show a trend with μ, namely a decrease towards the limb (if we disregard the box at $\mu = 0.8$, since only three observations contribute to it, each with a $Q/I < 0.1\%$).

3.4.3 Depolarisation and field strength

The next step is to quantify the Hanle depolarisation and finally use it to determine the field strength. The main hurdle is estimating the Q/I that one would measure in the complete absence of a weak chromospheric field. Faurobert-Scholl (1992; 1994) estimated this quantity from radiative transfer calculations of the line profile in an atmosphere of the field-free quiet Sun. Here we make use of the large number of observations that we have and attempt a model-independent estimate. We take a conservative approach and assume that there are some locations on the Sun which are practically field-free (in the sense that the Hanle depolarisation is negligible). An upper envelope to the data points in Figure 3.2b can thus be taken to represent the field-free CLV of the line core Q/I. For this envelope we choose the analytical form given by Eq. (3.21), which already successfully described the CLV of $(Q/I)_b$, as well as the Q/I CLV of Sr I 4607 Å (Stenflo et al. 1997). Even after restricting ourselves to this choice the exact shape of the envelope
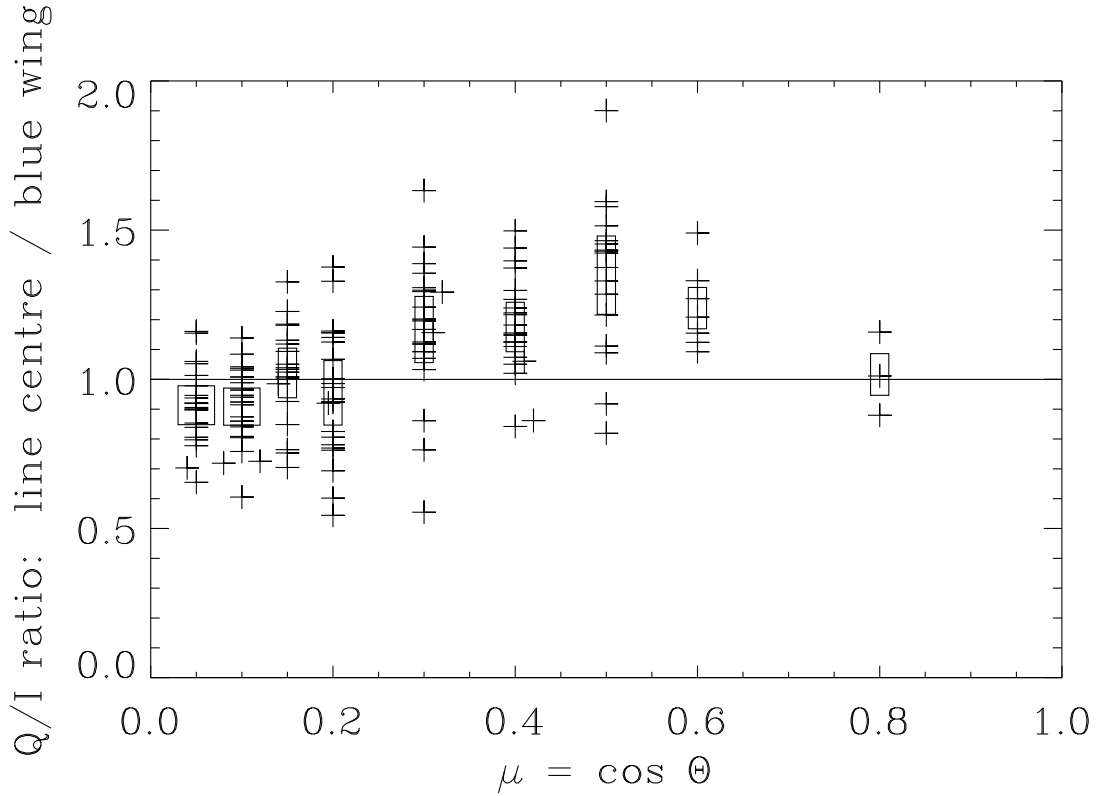
Figure 3.4: CLV of the line-centre to blue-wing Q/I ratio. Rectangles represent the error boxes of the average ratios at each μ

(or equivalently the values of a and b) is not obvious. In Figure 3.2b we have selected two envelopes that appear reasonable. They are represented by the dotted and dashed curves, which have the parameter values $a = 0.6\%$, $b = 0.055$ and $a = 0.6\%$, $b = 0.085$, respectively. We determine the field strength for both these estimates, which allows us to judge the uncertainty in the field strength introduced by the uncertainty inherent in this estimate.

The synthetic line-center Q/I values calculated for a field-free atmosphere by Faurobert-Scholl (1992) lie closer to the dotted envelope – with which they agree very well – so that the results obtained using it are probably more reliable. Unfortunately, the profiles of Faurobert-Scholl (1992) have not been broadened to take into account spectral smearing or macroturbulent velocity broadening, so that we carry out the analysis using both envelopes.

Next, by forming the ratios between the curves in Figure 3.2b and

the solid curve in Figure 3.2a we obtain the 2 envelopes (dotted and dashed curves) in Figure 3.3b. As in Figure 3.2b the dashed curve lies closer to the data points and is a good estimate of a tight envelope (within the uncertainty due to noise). The dotted curve, on the other hand, almost corresponds to a straight line in Figure 3.3b, which also appears reasonable in view of the strictly linear relationship between Q/I of the red and blue wings displayed in Figure 3.3a. According to this choice we assume that the core-to-wing ratio of Q/I produced by resonant scattering (in the absence of a magnetic field) is nearly independent of μ, whereas for the dashed curve the ratio decreases towards the limb.

The main diagnostic of the magnetic field is the fractional depolarisation it causes, i.e. the ratio between line-core Q/I and its envelope. In order to suppress the additional scatter introduced by uncertainties in μ we form this ratio for each given blue-wing Q/I. The ratio is then free from uncertainties in μ. It can nevertheless depend on μ. Consequently, we plot it vs. μ in Figure 3.5. Figure 3.5a shows the depolarisation obtained by employing the dotted envelope, Figure 3.5b that resulting from the dashed envelope.

We can now calculate the strength of the magnetic field responsible for the Hanle depolarisation plotted in Figure 3.5. A detailed description and derivation of the theory underlying such calculations for different field-strength distributions has been given by Stenflo (1982; 1987; 1994, chap. 10) and Landi degl'Innocenti (1985); Landi degl'Innocenti & Landi degl'Innocenti (1988). Since we have no information on Stokes U (which is needed to distinguish between different configurations of a field that is homogeneous within the spatial resolution element) we prefer to simply consider a turbulent field. We must distinguish between an isotropically turbulent magnetic field and what we shall call a canopy field, since they give different field strengths. In the former case it is assumed that the magnetic field distribution is isotropic, i.e. it is randomly oriented at scales smaller than the spatial resolution element. For the canopy case, it is assumed that the field is horizontal and randomly oriented in azimuth. In both cases the magnetic field is assumed to be homogeneous in strength over a spatial resolution element, although it varies in direction. The rationale behind using both distributions is that as long as we do not have
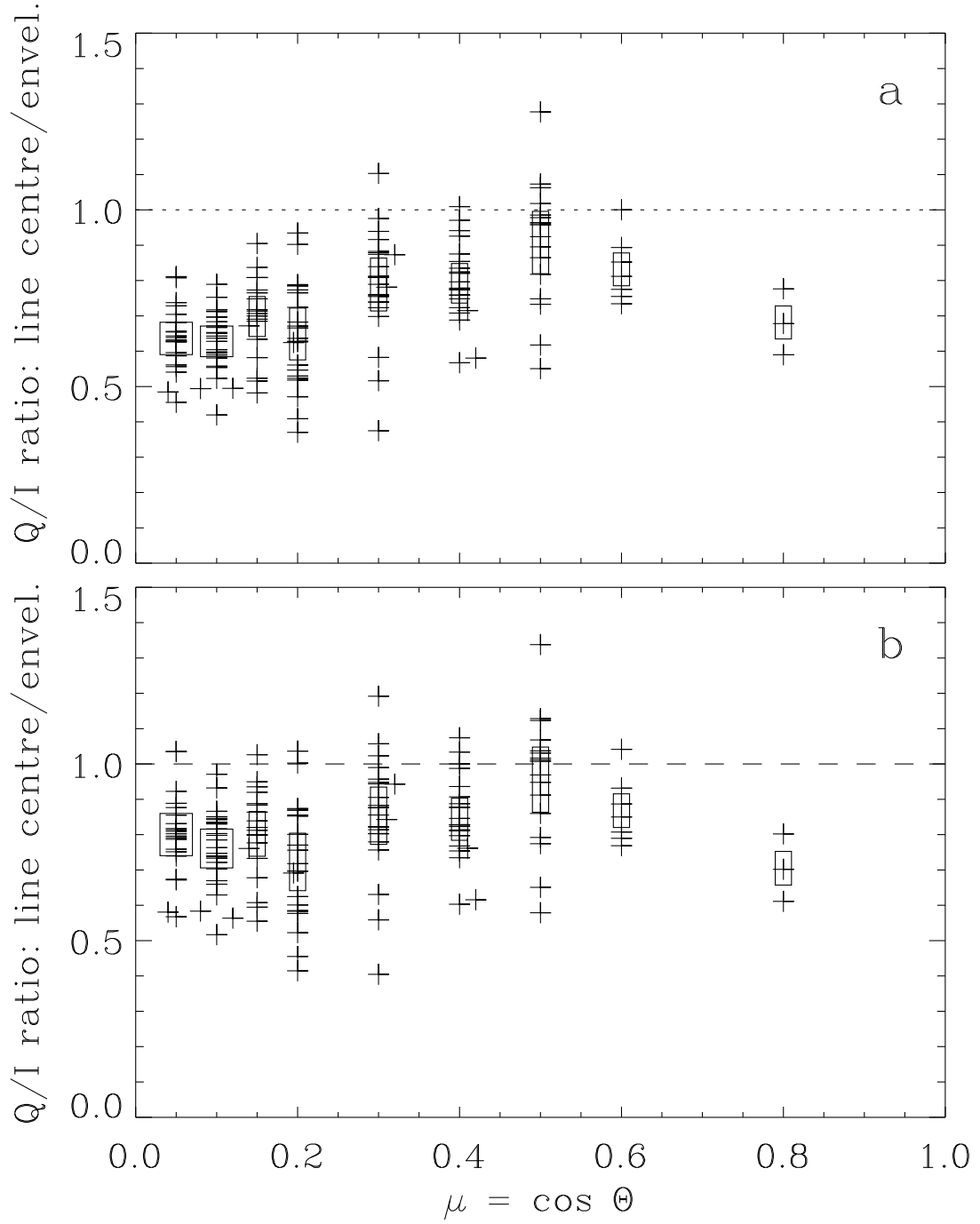
Figure 3.5: The ratio of line-centre Q/I to its envelope vs. μ. The plotted ratio is a measure of the relative depolarisation. **a** The dotted curve in Figure 3.3b is used as envelope, **b** the dashed curve in Figure 3.3b is used. Error boxes for the average values are also plotted

additional information on the magnetic geometry we consider both, in order to judge the uncertainties. We do, however, from both Zeeman effect observations (Giovanelli & Jones 1982) and magnetohydrostatic models (Solanki & Steiner 1990) expect the field in the mid chromosphere to be relatively canopy-like.

Following Stenflo (1982; 1994), the Hanle depolarisation, k_H, i.e. the ratio between Q/I at line centre and its envelope, can be written as

$$k_H^{\text{canopy}} = 1 - 0.75 \sin^2 \alpha_2 \tag{3.23}$$

in the case of a canopy field, and as

$$k_H^{\text{turbulent}} = 1 - 0.4\big(\sin^2 \alpha_1 + \sin^2 \alpha_2\big) \tag{3.24}$$

in the case of a turbulent field. The Hanle mixing angles α_1 and α_2 are given by

$$\tan \alpha_K = \frac{KB}{B_0/k_c^{(K)}}, \tag{3.25}$$

where $K = 1$ or 2, B is the field strength, $k_c^{(K)}$ is the collisional branching ratio for the $2K$-multipole ($k_c^{(1)} \approx k_c^{(2)}$) and B_0 is the "characteristic field strength" for the Hanle effect. From Stenflo (1982) we obtain for Ca I 4227 Å: $B_0/k_c^{(K)} = 24.8$ G. In general Eqs. (3.23) and (3.24) result in different values for B.

We apply Eqs. (3.23)–(3.25) to the depolarisations plotted in Figure 3.5 and obtain four possible values of B for each observed spectrum; two from the combination of Eq. (3.23) with each of the two envelopes and similarly two from Eq. (3.24). The results are plotted in Figure 3.6; filled circles refer to data calculated with the dashed envelope from Figure 3.3b, open circles refer to the dotted envelope.

As expected, the dotted envelope gives larger field strengths by approximately 10–60%. The difference between the results obtained with the two envelopes is largest near the limb since they also differ most strongly from each other there.

There is also a systematic difference between the field strength of a turbulent field and of a canopy field, with the former having to be on average 30% larger in order to produce the same depolarisation.

The uncertainties due to the effects mentioned above are found to be the dominant source of the difference in the field strength values
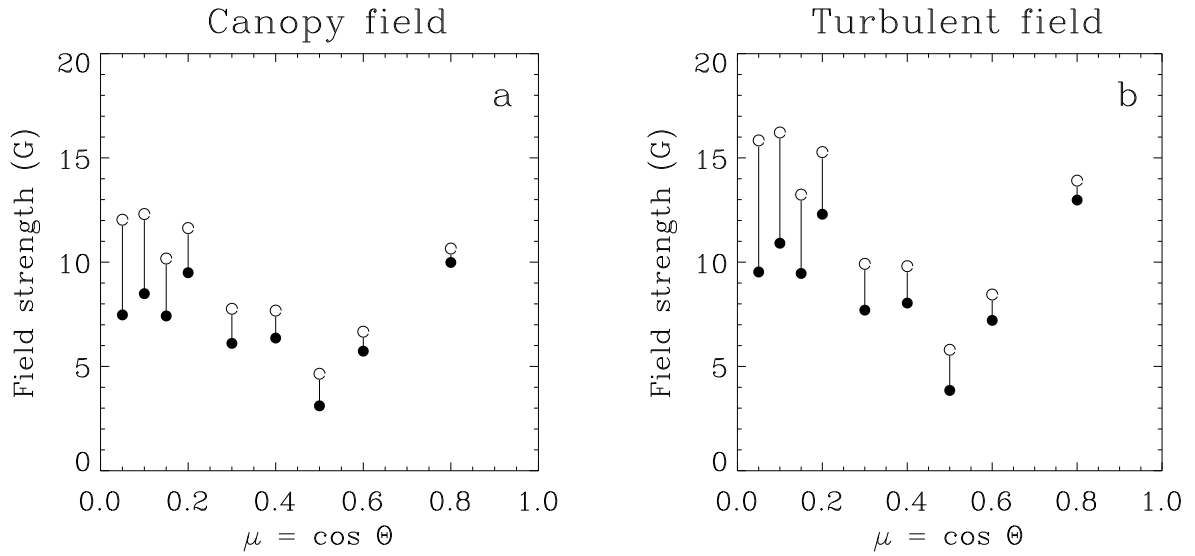
Figure 3.6: CLV of the field strength derived from the average relative depolarisation at different μ values. Filled circles: value resulting when the dashed envelope in Figure 3.3 is chosen. Open circles: value resulting from choosing the dotted envelope. **a** Results of assuming a purely horizontal canopy field, **b** results of an isotropic, "turbulent" field

derived at a given μ. Photon noise only becomes a significant source of error at $\mu > 0.8$.

Keeping all the uncertainties in mind we can nevertheless say that the field strength of the detected canopy fields is on the order of 10 G. More specifically it lies within the range 5–15 G. If we once again neglect the point at $\mu = 0.8$ (due to the low S/N and the poor statistics) then there appears to be a trend towards larger field strengths closer to the limb. Due to the better agreement of the dotted envelope given in Figure 3.2b with the theoretical predictions of Faurobert-Scholl (1992) we expect that the higher field-strength values (open circles in Figure 3.6) are more realistic.

So far we have only considered the average depolarisation at any given μ. The scatter in the depolarisation values of the individual data points is considerably larger than the estimated errors. We therefore expect that most of this scatter is due to a distribution of the magnetic field strength of the canopy; each location on the Sun having a somewhat different field strength (or alternatively a different direction; we

shall not follow this possibility further, however). In the following we therefore determine the field strength from each spectrum individually, obtaining 207 B values. Note that there are some points with negative depolarisation, possibly due to noise, or to small errors in the choice of the envelope. For these anomalous points we have set the field strength to zero. Histograms of the field strength are plotted in Figure 3.7. The two plotted histograms represent the extremes of the four possible histograms arising from the different combinations of turbulent and canopy field, with the dotted and dashed envelopes in Figure 3.3. Note that both histograms are relatively symmetric around their mean and broad, with FWHM roughly the value of the average field strength. In this sense the two histograms differ mainly in the value of the average field strength 7.5 G and 14 G, respectively. These values are to be compared with 7 G and 12.5 G, obtained by averaging the field strengths at the different μ values in Figure 3.6 (filled circles in Figure 3.6a and open circles in Figure 3.6b, respectively). Note, that when carrying out this averaging we have weighted the individual μ values by the number of observations underlying each.

3.5 Discussion and Conclusions

We have presented low-noise (2–$3 \times 10^{-4} I_c$) observations of Q/I at over 200 locations on the quiet Sun. The present data hence not only have lower noise, but also represent a much larger statistical sample of the solar surface than previous data sets. From these observations we derive many CLVs of the scattering polarisation of this line. We find that while the ratio of blue- to red-wing polarisation remains strictly constant, the line core shows a large scatter relative to the wings. This scatter is much larger than expected from the error budget. It is best interpreted in terms of Hanle depolarisation by a weak field. Using an empirical estimate of the field-free line-core Q/I of this line as suggested by our data, we find that a field strength of 5–15 G is required to explain the observations. This field strength refers to the height of formation of the Ca I 4227 Å line core, approximately 800–1000 km above $\tau_{5000} = 1$ (Faurobert-Scholl 1992). The different field-strength values partly refer to different μ values (there is a trend, although not a very
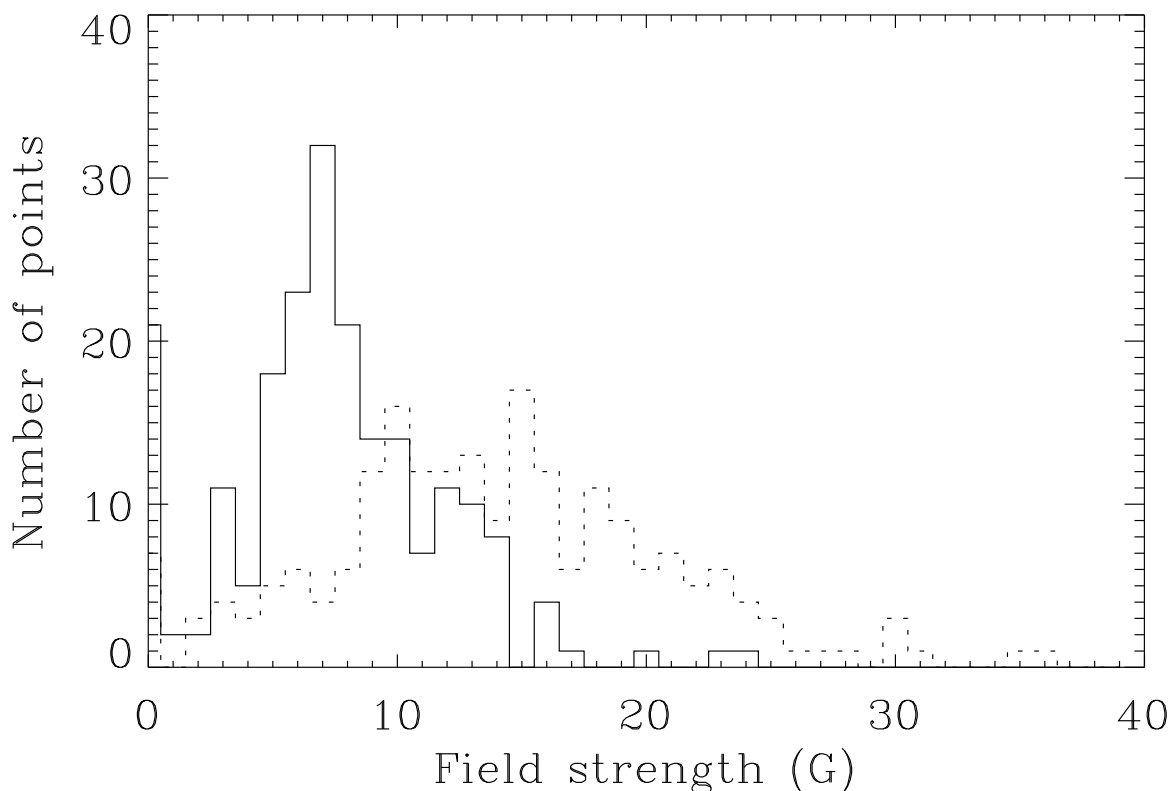
Figure 3.7: Histogram of magnetic field strengths. Solid line: histogram obtained by assuming a canopy field and a depolarisation arising from the use of the dashed envelope in Figure 3.3. Dotted line: turbulent field and dotted envelope.

clear one, for the field strength to increase towards the limb). A large fraction of the uncertainty in the derived field strength stems, however, from the ambiguity in the assumed magnetic geometry and the uncertainty in the estimated CLV of the line core Q/I in the absence of magnetic fields.

Chromospheric field strengths have earlier been derived from the Hanle depolarisation of this line by Faurobert-Scholl (1992) from observations made near the solar limb by Stenflo et al. (1980). She found values between approximately 20 and 100 G, with the spread being due to different assumptions on the field geometry (canopy base height, width of canopy base, inclination of the field). These values are larger than the ones we have derived in the present paper. We identify four possible sources of the discrepancy.

1. Our estimate of the depolarisation is too conservative.

2. The field strengths derived by Faurobert-Scholl are too large, possibly due to errors in the observations they are based on, or due to sampling of non-typical solar regions. While our field strengths are based on averages of many observed CLVs, the previously derived field strengths were based on one single CLV.

3. The difference is due to the different magnetic field structures assumed in the two investigations. While our simple analytical determinations assume a height-independent field strength, Faurobert-Scholl considers a canopy field which changes in strength over the height range of line core formation, and she numerically solves the transfer problem.

4. The quiet sun chromospheric fields have changed between the times at which our observations and those of Stenflo et al. (1980) were obtained.

Some comments to the above points: Possibility 1 is plausible, since our conservative estimate is based on the assumption that there is no depolarisation in at least some of the data, i.e. some parts of the solar surface are free from detectable fields in chromospheric layers. This need not be correct.

Concerning possibility 2, a comparison between our observations and those of Stenflo et al. (1980) shows that relative to the line wing polarisation our line-centre polarisation is lower, in particular at large μ values. Interestingly, it was exactly at these μ that the observations of Stenflo et al. (1980) showed Q/I values significantly larger than those calculated in a standard atmosphere in the absence of a magnetic field (Faurobert-Scholl 1994). Our observations should therefore reduce the discrepancy between observations and theory.

The true source of the discrepancy can only be definitely identified by comparing our observations with model calculations, such as those of Faurobert-Scholl (1992; 1994).

Bibliography

Bommier, V., 1980, *"Quantum theory of the Hanle effect. II. Effect of level-crossings and anti-level-crossings on the polarization of the D3 helium line of solar prominences"*, Astron. Astrophys. **87**, 109

Brückner, G., 1963, *"Photoelektrische Polarisationsmessungen an Resonanzlinien im Sonnenspektrum. Mit 6 Textabbildungen"*, Zeitschrift für Astrophysik **58**, 73

Donati, J.-F., Semel, M., Rees, D. E., Taylor, K., Robinson, R. D., 1990, *"Detection of a magnetic region on HR 1099"*, Astron. Astrophys. **232**, L1

Dumont, S., Omont, A., Pecker, J., 1973, *"Theoretical Study of the Fraunhofer Lines Polarization: The Case of Ca I 4227"*, Sol. Phys. **28**, 271

Faurobert-Scholl, M., 1992, *"Hanle effect with partial frequency redistribution. II. Linear polarization of the solar Ca I 4227 Å line"*, Astron. Astrophys. **258**, 521

Faurobert-Scholl, M., 1993, *"Investigation of microturbulent magnetic fields in the solar photosphere by their Hanle effect in the Sr I 4607 Å line"*, Astron. Astrophys. **268**, 765

Faurobert-Scholl, M., 1994, *"Hanle effect of magnetic canopies in the solar chromosphere"*, Astron. Astrophys. **285**, 655

Faurobert-Scholl, M., Feautrier, N., Machefert, F., Petrovay, K., Spielfiedel, A., 1995, *"Turbulent magnetic fields in the solar photosphere: diagnostics and interpretation"*, Astron. Astrophys. **298**, 289

Frisch, H., 1996, *"Partial Frequency Redistribution of Polarized Radiation"*, in J. O. Stenflo, K. N. Nagendra (eds.), *"Solar Polarization, proc. 1st SPW"*, 49, Kluwer, Dordrecht, (Sol. Phys. 164, 49)

Giovanelli, R. G., 1980, *"An exploratory two-dimensional study of the coarse structure of network magnetic fields"*, Sol. Phys. **68**, 49

Giovanelli, R. G., Jones, H. P., 1982, *"The three-dimensional structure of atmospheric magnetic fields in two active regions"*, Sol. Phys. **79**, 267

Hanle, W., 1924, *"The magnetic influence on the polarization of resonance fluores-*

cence", Zeitschrift für Physik **30**, 93

Landi degl'Innocenti, E., 1982, *"The determination of vector magnetic fields in prominences from the observations of the Stokes profiles in the D_3 line of helium"*, Sol. Phys. **79**, 291

Landi degl'Innocenti, E., 1985, *"Polarization in spectral lines. IV. Resonance polarization in the Hanle effect, collisionless regime"*, Sol. Phys. **102**, 1

Landi degl'Innocenti, M., Landi degl'Innocenti, E., 1988, *"An analytical expression for the Hanle-effect scattering phase matrix"*, Astron. Astrophys. **192**, 374

Leroy, J. L., Ratier, G., Bommier, V., 1977, *"The polarization of the D3 emission line in prominences"*, Astron. Astrophys. **54**, 811

Martinez-Pillet, V., Sánchez-Almeida, J., 1991, *"A proposal for a low instrumental polarization Coudé telescope"*, Astron. Astrophys. **252**, 861

Moruzzi, G., Strumia, F. (eds.), 1991, *"The Hanle Effect and Level-Crossing Spectroscopy"*, Plenum Press, New York

Neckel, H., 1994, *"Solar Absolute Reference Spectrum"*, in *"The Sun as a Variable Star: Solar and Stellar Irradiance Variations"*

Povel, H., 1995, *"Imaging Stokes polarimetry with piezoelastic modulators and charge-coupled-device image sensors"*, Optical Engineering **34**, 1870

Querfeld, C. W., House, L. L., Smartt, R. N., Bommier, V., degl'Innocenti, E. L., 1985, *"Vector magnetic fields in prominences. II. He I D_3 Stokes profiles analysis for two quiescent prominences"*, Sol. Phys. **96**, 277

Rees, D. E., Saliba, G. J., 1982, *"Non-LTE resonance line polarization with partial redistribution effects"*, Astron. Astrophys. **115**, 1

Sahal-Bréchot, S., Bommier, V., Leroy, J. L., 1977, *"The Hanle effect and the determination of magnetic fields in solar prominences"*, Astron. Astrophys. **59**, 223

Saliba, G. J., 1985, *"Non-LTE resonance line polarization with partial redistribution - The solar Ca II K line"*, Sol. Phys. **98**, 1

Semel, M., 1994, *"THEMIS polarimetry*, in R. Rutten, C. Schrijver (eds.), *"Solar Surface Magnetism"*, 509–506, vol. 433 of NATO ASI Series C, Kluwer, Dordrecht

Semel, M., 1995, *Zeeman Doppler Imaging*, in *ASP Conf. Ser. 71: IAU Colloq. 149: Tridimensional Optical Spectroscopic Methods in Astrophysics*, 340

Semel, M., Donati, J.-F., Rees, D. E., 1993, *"Zeeman-Doppler imaging of active stars. 3: Instrumental and technical considerations"*, Astron. Astrophys. **278**,

231

Solanki, S. K., Steiner, O., 1990, *"How magnetic is the solar chromosphere?"*, Astron. Astrophys. **234**, 519

Stenflo, J. O., 1974, *"Observations of Resonance Polarization in Ca I 4227 Å"*, Sol. Phys. **37**, 31

Stenflo, J. O., 1982, *"The Hanle effect and the diagnostics of turbulent magnetic fields in the solar atmosphere"*, Sol. Phys. **80**, 209

Stenflo, J. O., 1987, *"Observational constraints on a 'hidden', turbulent magnetic field of the sun"*, Sol. Phys. **114**, 1

Stenflo, J. O., 1994, *"Solar magnetic fields: polarized radiation diagnostics"*, Astrophysics and Space Science Library, Kluwer Academic Publishers, Dordrecht

Stenflo, J. O., 1997, *"Quantum interferences, hyperfine structure, and Raman scattering on the Sun."*, Astron. Astrophys. **324**, 344

Stenflo, J. O., Baur, T. G., Elmore, D. F., 1980, *"Resonance-line polarization. IV. Observations of non-magnetic line polarization and its center-to-limb variations"*, Astron. Astrophys. **84**, 60

Stenflo, J. O., Bianda, M., Keller, C. U., Solanki, S. K., 1997, *"Center-to-limb variation of the second solar spectrum."*, Astron. Astrophys. **322**, 985

Stenflo, J. O., Keller, C. U., 1996, *"New window for spectroskopy"*, Nature **382**, 588

Stenflo, J. O., Keller, C. U., 1997, *"The second solar spectrum. A new window for diagnostics of the Sun"*, Astron. Astrophys. **321**, 927

Stenflo, J. O., Twerenbold, D., Harvey, J. W., 1983a, *"Coherent scattering in the solar spectrum — Survey of linear polarization in the range 3165–4230 Å"*, Astron. Astrophys. Suppl. Ser. **52**, 161

Stenflo, J. O., Twerenbold, D., Harvey, J. W., Brault, J. W., 1983b, *"Coherent scattering in the solar spectrum — Survey of linear polarization in the range 4200–9950 Å"*, Astron. Astrophys. Suppl. Ser. **54**, 505

Wiehr, E., 1975, *"Measurement of solar disc polarization in a number of Fraunhofer lines and their adjacent continuum"*, Astron. Astrophys. **38**, 303

Chapter 4

Hanle diagnostics of solar magnetic fields: The Sr II 4078 Å line *

M. Bianda[1], J.O. Stenflo [2] and S.K. Solanki[2]

Abstract

The Hanle depolarization and rotation effects in the Sr II 4078 Å line have been explored with the instrumentation at IRSOL (Istituto Ricerche Solari Locarno) by recording the Stokes I, Q, and U line profiles with high spectral resolution and polarimetric accuracy in a large number of regions across the solar disk. From the extracted line parameters we have constructed "Hanle histograms" showing the statistical distributions of the Hanle rotation and depolarization effects. Comparison with theoretical calculations allow these histograms to be understood in terms of magnetic fields with a strength of about 5–10 G, which is similar to the field strengths previously found through analysis of Q/I Hanle depolarization in the Ca I 4227 Å line. While small-scale magnetic fields with spatially unresolved angular distributions contribute to the observed Hanle depolarization effects, the observed Hanle rotation effects in Stokes U are due to spatially resolved fields

with net large-scale orientations (e.g. global or canopy-type fields). We have also for the first time determined empirical "Hanle efficiency profiles", derived independently for the Hanle rotation and depolarization effects. They show how the Hanle efficiency has its maximum in the Doppler core of the line and then rapidly decreases to become zero in the line wings.

4.1　Introduction

The Hanle effect allows magnetic-field diagnostics in a parameter domain that is not well accessible to the usual Zeeman effect. It therefore provides us with a new window for the exploration of solar magnetism, e.g. of weak magnetic fields, turbulent fields, and chromospheric canopy fields (cf. Stenflo 1994). Only through the recent development of highly sensitive imaging polarimeters has it become possible to take full advantage of the Hanle effect, e.g. with ZIMPOL (Zurich Imaging Polarimeter) (Povel 1995; Stenflo et al. 1998) and with the polarimeter at IRSOL (Istituto Ricerche Solari Locarno) (Chapter 3).

The Hanle effect modifies the polarization that is produced by coherent scattering in spectral lines. This modification manifests itself in two ways, as depolarization, and as rotation of the plane of linear polarization. In a recent paper (Chapter 3) we have explored the spatial fluctuations of the Hanle depolarization across the solar disk in the Ca I 4227 Å line with the new polarimeter system at IRSOL. The Ca I 4227 Å line is a normal Zeeman triplet and possesses the largest polarization amplitude in the entire visible solar spectrum (Stenflo et al. 1983a;b). It has a linear polarization profile with three maxima, one in the Doppler core, and one in each of the blue and red line wings. The Hanle effect only operates in the Doppler core and is absent in the wings (cf. Stenflo 1994, pp. 82–83). Because of this property it was possible through observations of only two Stokes parameters (I and Q) to statistically identify the signature of Hanle depolarization and exploit it for field-strength determinations.

Since the diagnostic possibilities with the Hanle effect are based on complex physical processes with subtle observational effects, which have only begun to be explored, it is of great value to extend the ob-

servational domain by using different spectral lines that respond differently to the Hanle effect, and to observe both Stokes Q and U rather than only Q alone, so that both the Hanle depolarization and rotation effects can be recorded. This allows us to better constrain the theoretical interpretations and in particular to check the consistency and uniqueness of the Hanle interpretation, and to explore how the Hanle effect manifests itself in practice.

In the present paper we explore the Hanle effect in the Sr II 4078 Å line. From early surveys of the scattering polarization throughout the solar spectrum (Stenflo et al. 1980; 1983a;b) it has been known that this line belongs to the more strongly polarizing ones, but it has never before been used for Hanle analysis. In contrast to the Ca I 4227 Å line it is not a normal triplet but a $J = \frac{1}{2} \to \frac{3}{2} \to \frac{1}{2}$ scattering transition, similar to the Na I D_2 5889 Å line (if we disregard the hyperfine structure and associated lower-level atomic polarization of that line, cf. Landi degl'Innocenti 1998). Its intrinsic polarizability, represented by the factor W_2, is 0.5 (in contrast to 1.0 for the Ca I 4227 Å line), which means that half of the scattering processes occur as classical dipole scattering, while the other half occurs as isotropic, unpolarized scattering. Like the Ca I 4227 Å line the Sr II 4078 Å polarization profile has three peaks, one core and two wing peaks, but in the case of Sr II the wing peaks lie much closer to the core peak, which means that the Hanle effect may not be entirely absent although greatly suppressed in these wings.

In comparison with Chapter 3 we have in the present paper extended the Hanle diagnostics by observing the three Stokes parameters I, Q, and U (the fourth, Stokes V, was also observed but is not analysed further here), rather than only I and Q, so that we can make simultaneous use of both the Hanle depolarization and rotation effects, explore the relation between them and their statistical distributions, as well as the profile variations of these effects across the core and wing peaks. This significantly extends our insight into the workings of the Hanle effect, and it places the Hanle interpretations on firmer ground. The results on the magnetic field strengths from this more complete Hanle diagnostic in the Sr II line can then be compared with the more limited diagnostic used in our previous Ca I analysis.

4.2   Observational technique

As in Chapter 3 all our observations have been carried out with the Gregory-Coudé telescope, Czerny-Turner spectrograph, and polarizing beam splitter at IRSOL (Istituto Ricerche Solari Locarno) in Switzerland. The polarizer, a polarizing calcite beam splitter system, has been upgraded to allow the recording of all four Stokes parameters. This polarimeter is placed immediately in front of the spectrograph entrance slit, producing two images in orthogonal polarization states, which are then simultaneously recorded by the UV sensitive CCD camera in the spectrograph focal plane. With four settings of a $\lambda/2$ plate in front of the calcite beam splitter, four image pairs are recorded sequentially: $I \pm Q$, $I \mp Q$, $I \pm U$, and $I \mp U$. The $\lambda/2$ plate can be rapidly replaced by a $\lambda/4$ plate, and two settings of this plate gives us the image pairs $I \pm V$ and $I \mp V$.

Two image pairs, i.e., four images, are thus needed to extract each of the Stokes Q, U, and V parameters. This allows us to eliminate the two main noise sources: seeing noise and gain-table noise. The two images in one image pair have identical seeing distortions but different gain tables. For the second image pair the polarization signals have changed sign (which is as if the two images have traded places, and we have exchanged the gain tables), but the seeing has also changed. By forming ratios between the four images in a certain way, as described in great detail in Chapter 3 (cf. also Semel et al. 1993; Semel 1995), we can extract an image of the fractional polarization (Q/I, U/I, or V/I) that is free from both seeing noise and gain-table noise. In this way we have been able to obtain polarized spectra with noise levels approaching 10^{-4} in the fractional polarization. For details we refer to Chapter 3.

The alignment of the beam splitter and the CCD has been done as described in Chapter 3. The position angles for the four settings of the $\lambda/2$ plate and the two settings of the $\lambda/4$ plate have been carefully calibrated with linear and circular polarizers. During the observations the positioning of the wave plate to the fixed, pre-calibrated positions, is done manually between the image pair exposures, while the CCD frame is tranferred to the PC (which takes about 5 s), or while the frames are stored on hard disk (which takes about 15 s).

A new feature of the present observations is the use of a 1-D seeing corrector in the form of a rapidly tilting plate. It eliminates image motions, mechanical drifts, and declination changes of the Sun in a direction perpendicular to the nearest solar limb. In this way the spectrograph slit, which is always aligned parallel to the nearest solar limb, can be kept at a constant and well defined limb distance during the observations. This greatly reduces the observational uncertainty in μ ($= \cos\theta$), which was a significant source of scatter in the Ca I observations of Chapter 3.

This image corrector represents an upgrade of an instrument proposed by E. Wiehr and described by Sütterlin et al. (1997). A $45°$ mirror in front of the calcite beam splitter intercepts a portion of the solar limb just below the beam that enters the spectrograph and is used for the polarimetry. The intercepted portion of the beam is directed through the tilting glass plate to a diode array that senses the position of the solar limb. A servo stepping motor tilts the glass plate to maintain a constant limb position on the diodes. A second glass plate, which is placed between the polarizing beam splitter and the spectrograph slit, is tilted in synchrony with the first glass plate. Since this second plate is located after the polarization optics, it introduces no instrumental polarization. As the two limb portions used for the observations and for the first servo plate are separated from each other by about 30 arcsec along the limb, the seeing is not identical in the two beams, but the largest-amplitude image motions should still be similar in the two beams. This is verified by the practical application of the system, since it brings us a major improvement in the positioning and stability of the portion of the solar limb at which we observe.

If we disregard the instrumental polarization introduced by the vacuum entrance window, the telescope is polarization free during the time of the spring or fall equinox. Our present observations have been carried out on March 18, 19, 20, 21, and 26, near the spring 1997 equinox. We have collected 126 Q/I, 112 U/I, and 91 V/I measurements of the Sr II 4078 Å line. Each image covers about 15 arcsec in the spatial direction and the interval 4077.2 – 4078.8 Å in the spectral direction. This interval includes the line and a portion around 4078.7 Å that is close to the continuum level. This portion aids us in determining the precise limb distance or μ position (see below).

The spectrograph slit was always placed parallel to the nearest solar limb. Stokes Q is defined to be positive along the limb direction. The 1-D image corrector system was used only when observing near the extreme limb, for $\mu < 0.3$. Since no image rotator was used, our choice of limb position was limited in the same way as in Chapter 3. Typical exposure times near the limb were 15–30 s.

As described in Chapter 3, the noise is not only random but contains a fixed-pattern background in the fractional polarization. This background, in the form of an irregular, wavelength-dependent zero-line offset, is determined by making alternating recordings near the limb (for the actual measurements) and at disk center (for the fixed-pattern calibrations), and subtracting the disk-center Q/I, U/I, or V/I data from the corresponding limb data. At disk center the intrinsically solar scattering polarization vanishes for symmetry reasons, while the spurious background that affects the limb observations remains unchanged. Typically one disk-center calibration was carried out for every five limb observations.

4.3   Data reduction

The main steps in the data reduction are the following: (1) Dark current subtraction; (2) Determination of μ (or the precise limb distance); (3) Flat fielding (only required for Stokes I); (4) Extraction of the fractional polarizations Q/I and U/I; (5) Determination and removal of stray light; (6) Correction for the varying zero-line offset of the fractional polarization; (7) Removal of $Q \rightarrow U$ instrumental cross talk; (8) Fourier smoothing for noise suppression. As most of these steps have been explained in detail in Chapter 3, we only comment here on new aspects that have not been discussed before.

To determine the precise μ value we make use of the measurements of the mean intensity (after dark current subtraction) around 4078.7 Å in our spectra, where the intensity is expected to be 0.956 in units of the local continuum intensity. Regular measurements at disk center allow us to follow and interpolate variations in the sky transparency, so that the limb intensities can be expressed in units of the disk center intensity. From these values a μ position can be obtained, using the earlier

determinations of the center-to-limb intensity variations by Pierce & Slaughter (1977).

As in Chapter 3 the Stokes I line profiles at disk center could be used to determine the amount of spectrograph stray light by comparison with corresponding FTS profiles from Kitt Peak obtained by H. Neckel. Values between 1.0 and 1.5 % were found and used to correct the polarization data (assuming that the stray light is unpolarized).

As already mentioned, the fixed-pattern noise or wavelength-dependent zero-line offset was calibrated by the disk-center observations and then subtracted from the data. Special care had to be taken to avoid the influence of magnetic regions in the disk-center recordings. The fixed-pattern background had the same structure in both Q/I and U/I, and it was for the Sr II 4078 Å line similar to that of the Ca I 4227 Å line. All these observations used the same $\lambda/2$ plate. In the case of the circular polarization measurements (V/I), however, for which the $\lambda/2$ plate is replaced by a $\lambda/4$ plate, the fixed pattern is practically zero. This indicates that the source of the fixed pattern is in the $\lambda/2$ plate, but as it is reproducible, it can be removed from the data.

After the fixed pattern has been removed, the near-limb continuum polarization was often far from zero, as expected for Q/I due to intrinsic solar continuum polarization. Although after the fixed-pattern removal the background is spectrally flat, we do not believe that it represents the true zero point of the polarization scale, so we add a constant zero-line shift to the data, determined in the following way: Within each interval of μ we require that all recorded Q/I profiles should have the same polarization amplitude in the farthest portions of the line wings, as close to the continuum as possible, since it is reasonable to assume that the continuum polarization is only a function of limb distance or μ. Next we inspect the Q/I profile shapes of the depolarizing blend lines in the line wings and require their relative shapes and depths to match as closely as possible the corresponding relative shapes and depths of the Stokes I blend profiles. There is an element of subjective judgement in this procedure, which introduces some uncertainty, but no better procedure exists at present (cf. the discussion in Stenflo et al. 1998). All this uncertainty however does not significantly affect our determinations of relative line polarization amplitudes and Hanle depolarizations.

We find substantial $Q \rightarrow U, V$ and $U \rightarrow V$ cross talk in our observations, which most probably originates from stresses in the vacuum entrance window of the telescope, since the polarization of the two mirror reflections should cancel each other at the time of the equinox. Imperfections and misalignment of the $\lambda/2$ plate may also contribute to the cross talk. Since we are not studying Stokes V in the present paper, and infiltration of Stokes V (from the longitudinal Zeeman effect) into Q and U is insignificant in our data (it would be recognized by the spatially structured anti-symmetric line profile signatures), we are here only concerned with cross talk between Q and U.

The dominant $Q \rightarrow U$ cross talk can be easily identified, since the U polarization is exclusively produced by Hanle rotation and only occurs in the Doppler core, while Q/I has strong non-magnetic polarization in the line wings. $Q \rightarrow U$ cross talk can then be eliminated by subtracting from the observed U/I a certain fraction of the observed Q/I, determined by the requirement that the corrected U/I profile should be zero in the distant line wings. Application of this method leads to both positive and negative Stokes U/I profiles, as expected, since the Hanle rotation can have both signs. A sign change can happen in recordings taken only few minutes apart in different solar regions. In this case subtraction of the same amount of cross talk gives very consistent results, which supports the validity of the method.

$U \rightarrow Q$ cross talk cannot be identified so readily in the data, since Q/I has large and variable polarization in the Doppler core, where a spurious U/I contribution may be present. However, since the intrinsic U/I amplitude (which is exclusively due to the Hanle effect) is much smaller than the Q/I amplitude in the majority of the cases (cf. Fig. 4.7 below), the $U \rightarrow Q$ cross talk will not be a very serious problem, although it will introduce some additional noise (of both signs) in the Q/I core polarization. Note that this additional noise only occurs if Hanle rotation is present.

4.4 Analysis and results

4.4.1 The Stokes I, Q/I, and U/I profiles

Figure 4.1a shows a typical disk center profile of Stokes I (normalized to the intensity I_c of the local continuum). It can be compared with the near-limb profiles in Fig. 4.1b, at $\mu = 0.1$ (dotted line), $\mu = 0.25$ (dashed line), and the average of the recorded profiles in the interval $0.1 \leq \mu \leq 0.25$ (solid line). All the profiles have been normalized to 0.95 at 4078.7 Å (since no clear continuum is reached). Note the disappearance of the lanthanium blend line at 4077.36 Å as we approach the limb.

In Fig. 4.1c we have plotted averages of the Q/I (solid and dashed lines) and U/I (dotted line) profiles recorded in the interval $0.1 \leq \mu \leq 0.25$. Since many individual U/I spectra did not show significant signals above the noise level, we have when forming the U/I average in Fig. 4.1c only selected the profiles with a U/I amplitude greater than 0.08 %, a total of 16 profiles. Before averaging, the U/I profiles have been multiplied by either $+1$ or -1 to ensure that all the averaged profiles have a positive polarization amplitude in the line core. The corresponding mean Q/I profile for this sample of 16 recordings is represented by the solid line. In the considered $0.1 \leq \mu \leq 0.25$ interval 46 recordings had a U/I amplitude below 0.08 %. The mean Q/I profile for these 46 recordings is given by the dashed line. The average μ value for this sample of 46 recordings is slightly smaller (0.16) than for the sample of 16 recordings (0.19). This may contribute somewhat to the systematically larger polarizations of the dashed curve.

We notice that the Q/I profiles of the Sr II line have a triplet structure (disregarding the influence of the blend lines): A polarization peak in the Doppler core as well as peaks in the blue and red line wings. This is qualitatively similar to the behavior of the Ca I 4227 Å line, except that the wing peaks are much closer to the core in the case of Sr II (about 0.15 Å as compared with about 0.5 Å for Ca I). The Q/I profile is also locally depolarized by blend lines at 4077.36, 4077.97, 4078.36, and 4078.47 Å.

The mean U/I profile in Fig. 4.1c only exhibits a single peak in the Doppler core of the line and is zero outside. This is expected as U/I is
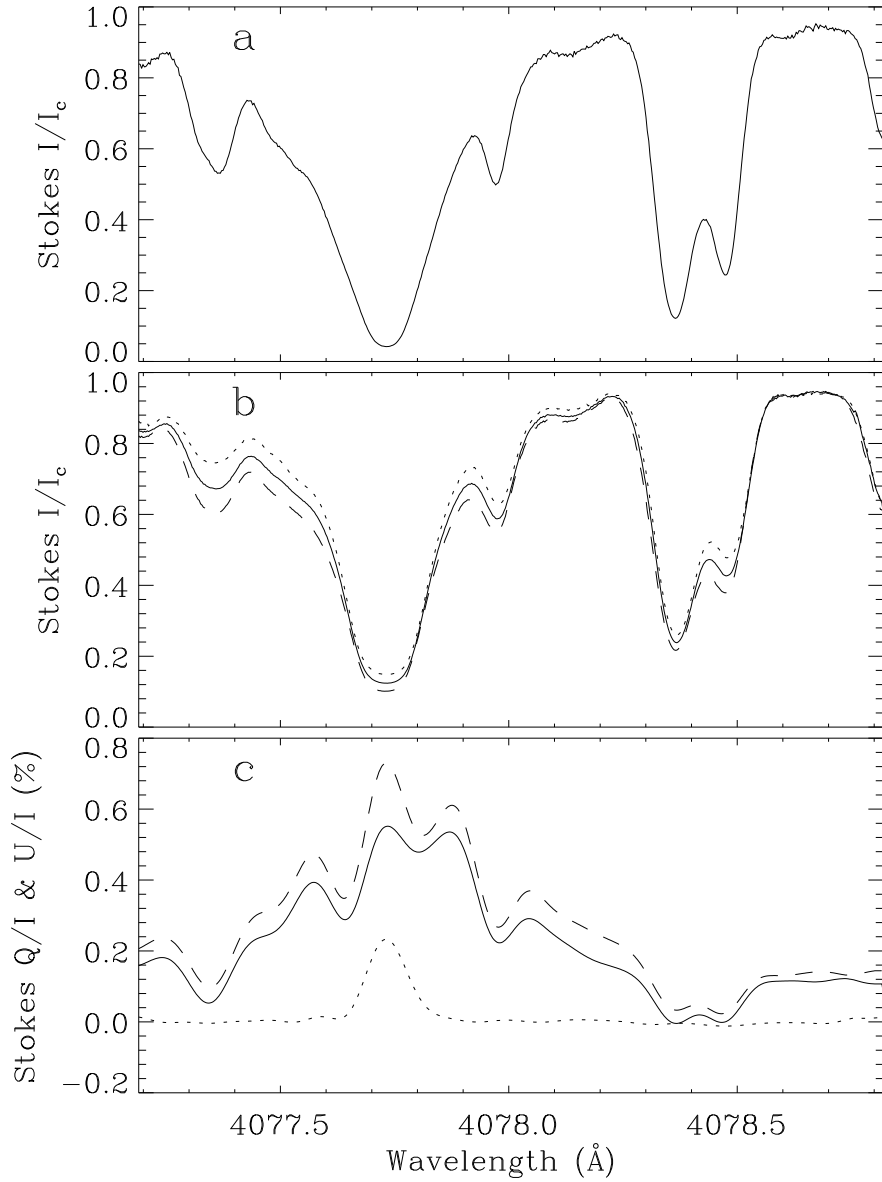
Figure 4.1: Stokes I, Q, and U line profiles of the Sr II 4078 Å line. (a) Stokes I at disk center, normalized to the intensity I_c of the local continuum. (b) Stokes I/I_c near the solar limb. Dotted line: $\mu = 0.1$. Dashed line: $\mu = 0.25$. Solid line: Average of all the profiles recorded within $0.1 \leq \mu \leq 0.25$. (c) Dotted line: Average of all the Stokes U/I profiles with an amplitude exceeding 0.08 %. Solid line: Average of the Stokes Q/I profiles for the same sample of solar regions as used for the mean U/I. Dashed Line: Average of all the Stokes Q/I profiles, for which the corresponding U/I profile had an amplitude less than 0.08 %.
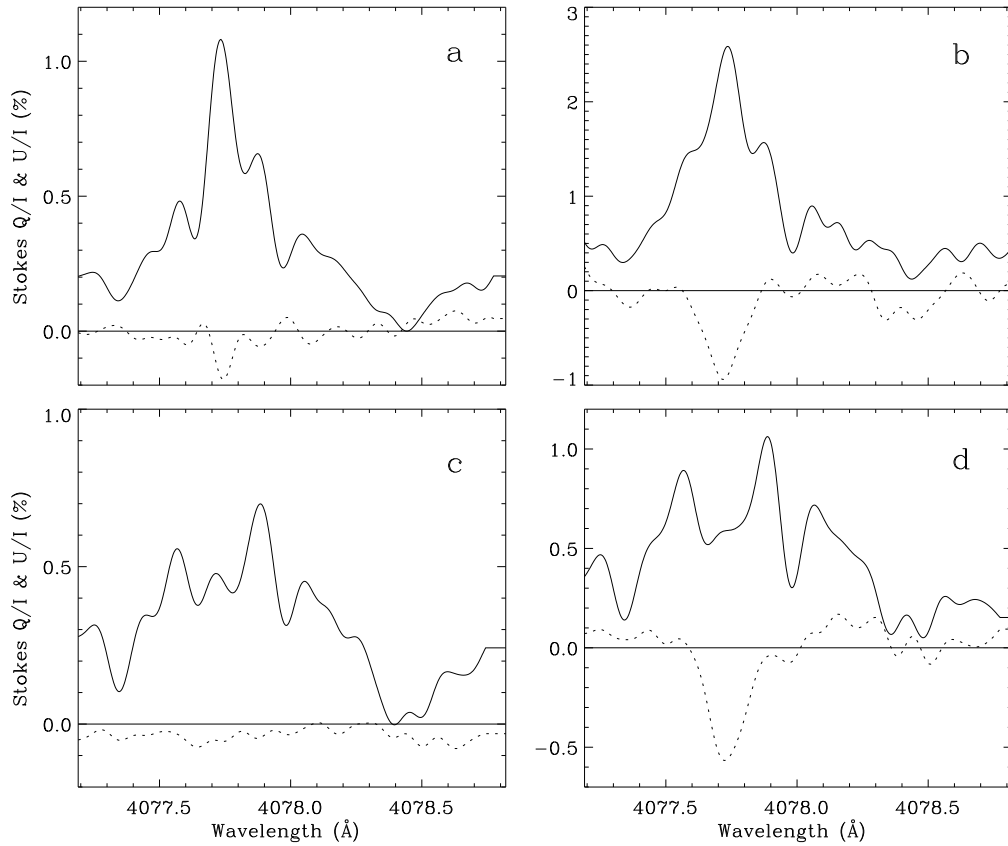
Figure 4.2: Examples of variations in the Stokes Q/I (solid curves) and U/I (dotted curves) line profiles due to variable Hanle depolarization and rotation. Note that these variations occur almost exclusively in the line core. In (b) and (a) we see strong Q/I core peaks both with and without a strong U/I signature, while in (d) and (c) we see that the near absence of a Q/I core peak can be accompanied by a U/I spectrum that both does or does not have a strong U/I signal.

exclusively due to the Hanle rotation effect, which only operates in the Doppler core and is absent in the wings (cf. Stenflo 1994, pp.82–83).

Figure 4.2 illustrates how the individual polarization profiles may vary from place to place on the Sun (each place representing a spatial average of 15 arcsec along the slit). Thus Fig. 4.2a shows a strong Q/I core peak while U/I remains small, Fig. 4.2b shows a combination of strong Q/I and U/I core peaks, Fig. 4.2c a greatly suppressed Q/I core peak together with the absence of a U/I signal, Fig. 4.2d a suppressed Q/I peak in combination with a strong U/I peak. This

demonstrates how the Hanle depolarization, which only occurs in the Q/I Doppler core, can vary greatly across the solar surface, with or without an accompanying Hanle rotation (represented by U/I). There is thus no simple correlation between Hanle depolarization and rotation. The relation between them will be elucidated later in connection with histograms showing the distribution of these effects.

4.4.2 Behavior of the Q/I wing and core maxima

Like in Chapter 3 for Ca I we explore the relative behavior of the Q/I maxima in the blue wing, line core, and red wing. In comparison with the Ca I case, the blue and red wing maxima lie much closer to the core for Sr II: 160 and 150 mÅ as compared with 500 and 400 mÅ for Ca I. Some Q/I profiles (about 10 % of them) have no well-defined maxima, e.g. Fig. 4.2b in the blue wing, and Fig. 4.2d in the line core. In these cases we have simply extracted the Q/I value at the wavelength where the maximum is otherwise supposed to be.

Figure 4.3 illustrates the behavior of the CLV (center-to-limb variation) of the three Q/I maxima. When we compare Fig. 4.3a with the corresponding Fig. 2a in Chapter 3 for Ca I, we notice that the spread of the points at small μ values, in particular for $0.05 \leq \mu \leq 0.2$, is smaller for Sr II. This is largely the result of our present use of a 1-D image stabilizer and better determination of the μ position, as described in Secs. 4.2 and 4.3. The solid curve in Fig. 4.3a represents a fit with a function of the form

$$Q/I = \frac{a(1 - \mu^2)}{\mu + b} \,, \tag{4.1}$$

first introduced by Stenflo et al. (1997). The fit in Fig. 4.3a has been obtained with $a = 0.16\,\%$ and $b = 0.095$.

The solid curve in Fig. 4.3b for the red wing has been derived by combining the curve for the blue wing in Fig. 4.3a and the second-order polynomial fit of the relation between the red and blue wings in Fig. 4.4a (see below).

In contrast to the well-defined CLV relations for the line wings, the line-center data in Fig. 4.3c exhibit a large scatter which, like in the Ca I case, can be naturally understood in terms of spatially varying Hanle
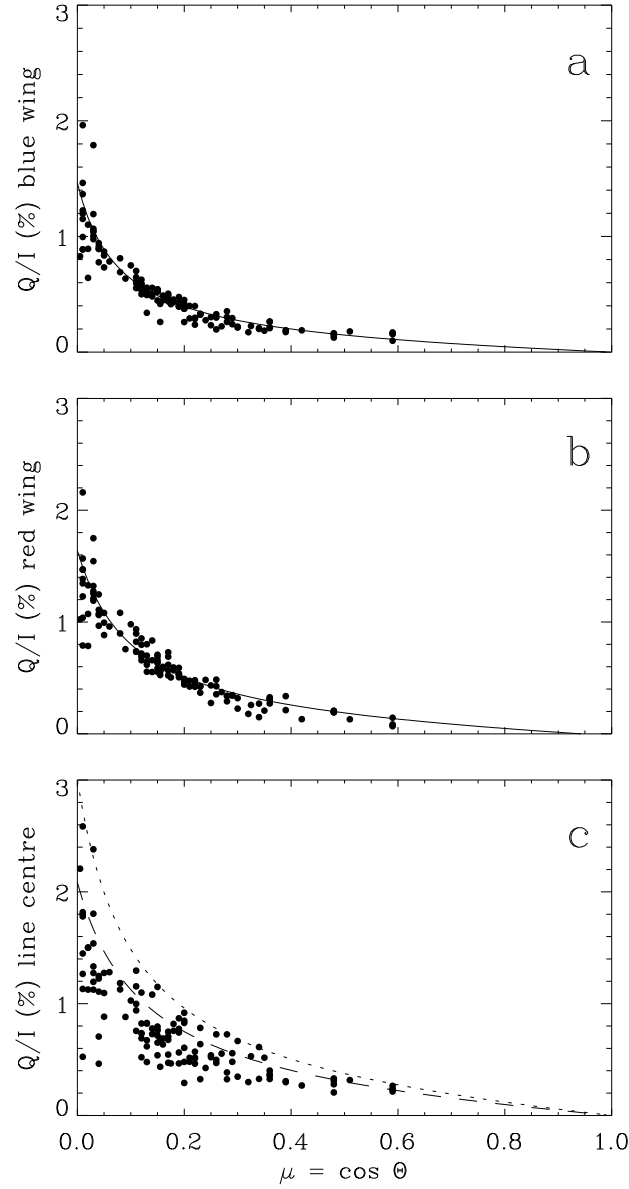
Figure 4.3: Center-to-limb variations of the Q/I maxima in the (a) blue line wing, (b) red wing, and (c) line center. The solid line in (a) represents a fit with the analytical function of Eq. (4.1), using the values $a = 0.16\%$ and $b = 0.095$ for the free parameters. The solid line in (b) is obtained from a combination of the fit function used for (a) and the second-order polynomial fit in Fig. 4.4a. The dotted and dashed curves in (c) represent estimated envelopes (later refered to as env. 1 and env. 2, respectively) to the data points, using the analytical function of Eq. (4.1) with different values for the two free parameters.

depolarization, since such magnetic-field effects only affect the core but not the wings. In the absence of magnetic fields we would expect the spread in the core to be the same as that in the wings. Using the functional form (4.1) with different values for the a and b parameters, we have plotted in Fig. 4.3c two different "envelope curves", which are supposed to represent our estimate of what the line-center CLV curve would be in the absence of magnetic fields, for vanishing Hanle depolarization. If there were no observational errors, we would for small values of μ (see Fig. 4.11 below for a discussion of the larger μ values) expect practically all observed points to fall below the envelope curve. This is approximately the case for the dotted curve. Since however we do have observational scatter, we need to allow for the possibility that some points may fall on the "wrong" side of the envelope. The dashed curve in Fig. 4.3c represents the lowest possible choice for a non-magnetic envelope that would still be consistent with the Hanle interpretation and the observational scatter. Although there is thus a lowest envelope choice, there is in principle no direct upper bound on the choice. A higher choice of envelope however implies larger Hanle depolarizations and thus larger field strengths.

The relations between the red and blue wing polarizations Q_r/I and Q_b/I are given in Figs. 4.4a and 4.5, while Fig. 4.4b gives the relation between the line center and the blue wing. Figures 4.4a and 4.5 show that the relation between the polarizations in the two line wings is not linear, in contrast to our results for Ca I (cf. Fig. 3a in Chapter 3). This can be understood in terms of a difference in the CLV of the blend lines in the blue and red line wings. As the blend in the blue wing is stronger than in the red wing and weakens towards the limb (cf. Fig. 4.1), the Q_r/Q_b ratio will decrease towards the limb, which can account for the curvature in Fig. 4.4a and the slope of the dotted line in Fig. 4.5.

The standard deviation of the points around the solid curve in Fig. 4.4a, which represents a second-order polynomial fit to the data, is found to be 0.075 %. This may be compared with the value 0.034 % for the corresponding scatter of the Ca I data within the interval $0 < Q/I < 2$ % in Fig. 3a of Chapter 3. Approximately the same value of 0.075 % is obtained as the instrumental noise directly from the invdividual Q/I and U/I profiles when the Fourier smoothed profiles are
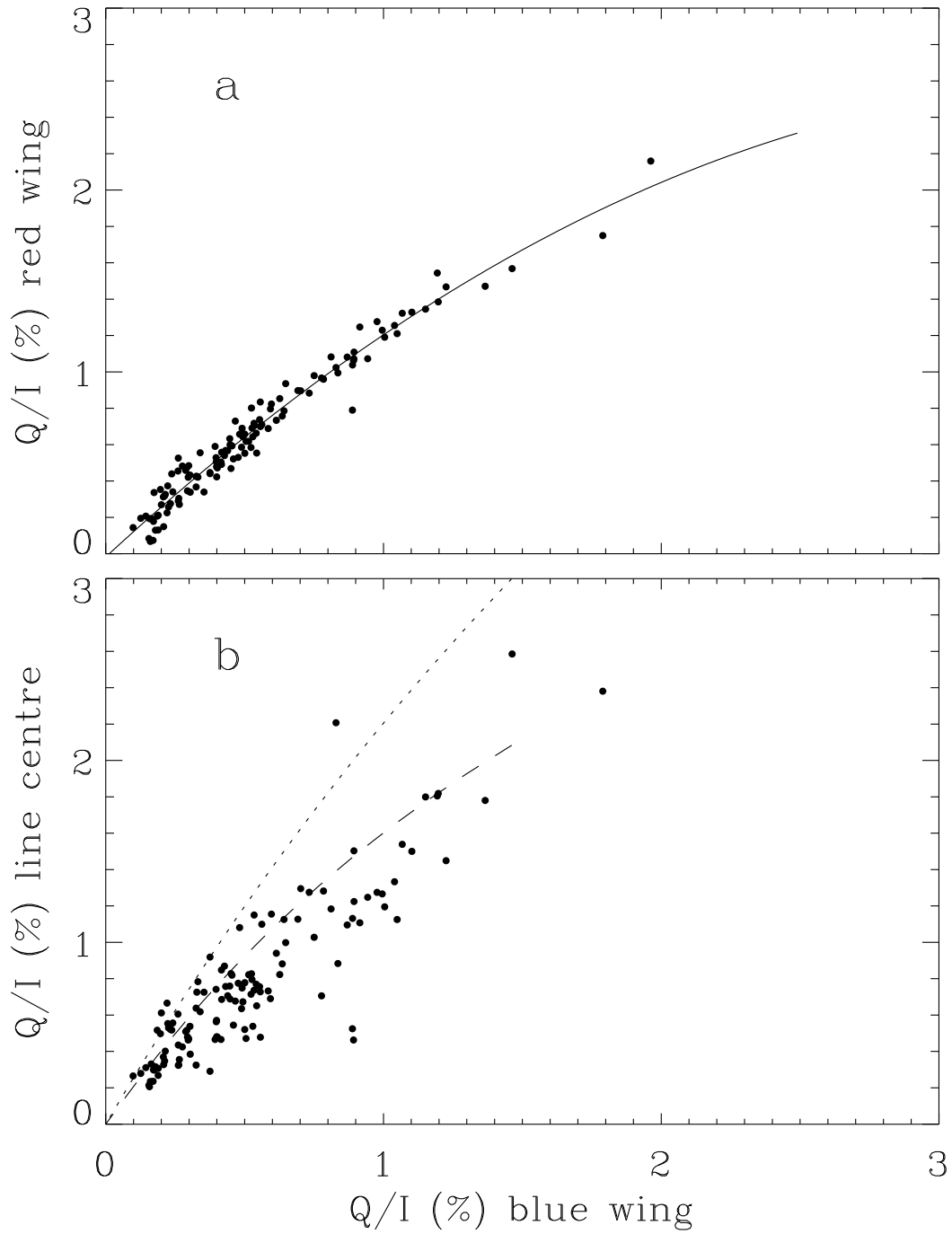
Figure 4.4: Relations between the polarization amplitudes in (a) the red and blue line wings, and (b) the line center and blue wing. The solid curve in (a) is a second-order polynomial fit to the data. The dotted and dashed curves in (b) have been derived from the corresponding dotted and dashed envelope curves in Fig. 4.3c when combined with the fit curve for the blue wing in Fig. 4.3a.
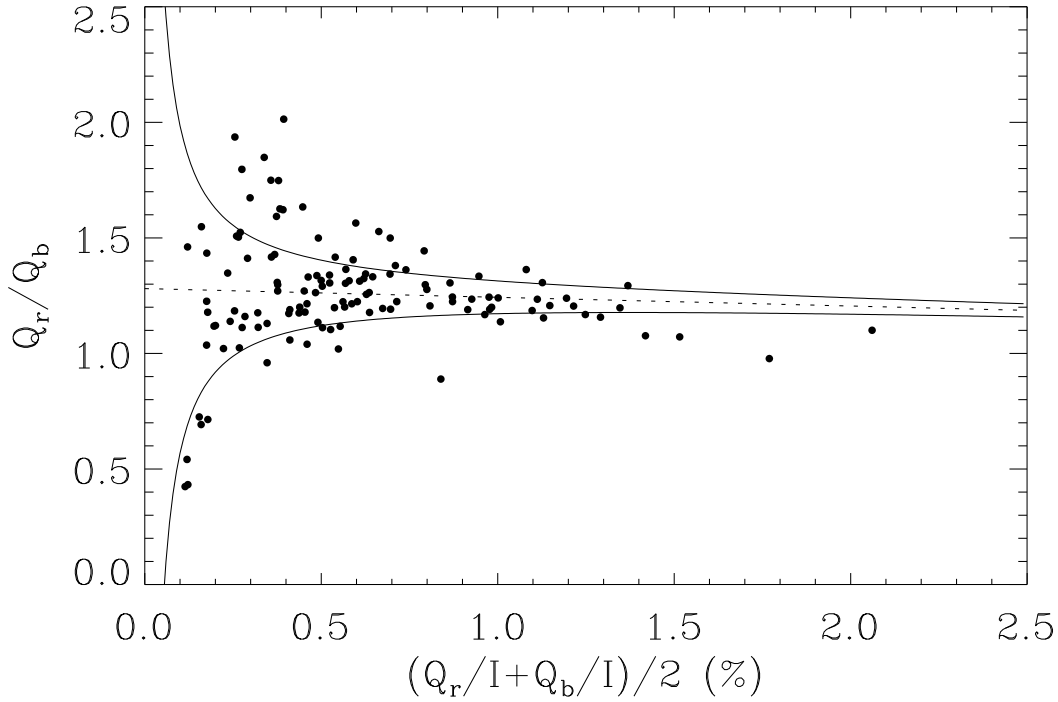
Figure 4.5: Ratio between the polarization amplitudes in the red and blue line wings as a function of their mean value. The dashed line is a slightly slanted linear fit to the data. The solid curves are obtained if we add or subtract the standard deviation in the Q_r/Q_b ratio, derived from the scatter of 0.075 % of the points in Fig. 4.4a around the polynomial fit.

subtracted from the raw profiles and the standard deviation is calculated. From this value for the instrumental noise in Q/I we can then derive the standard deviation in the Q_r/Q_b ratio of Fig. 4.5, σ_{Q_r/Q_b}. In Fig. 4.5 the dotted line represents a linear fit to the data, while the solid curves are obtained when we add and subtract σ_{Q_r/Q_b} to this fit.

The much larger scatter of the points in Fig. 4.4b is interpreted as in Chapter 3 in terms of Hanle depolarization. The dotted and dashed curves have been obtained from the corresponding envelope curves in Fig. 4.3c in combination with the blue-wing fit curve of Fig. 4.3a. They are supposed to represent two estimates of the relation between the line center and the blue wing in the absence of magnetic fields. We notice that the dotted curve is more nearly linear than the dashed curve.

We use Fig. 4.4b to calculate the amount of Hanle depolarization rather than Fig. 4.3c, since the ratios between the points and the envelopes are affected by the μ uncertainties in Fig. 4.3c, while this is not the case in Fig. 4.4b. Figure 4.6 shows the results obtained when forming these line center / envelope ratios from the data in Fig. 4.4b. Figure 4.6a is based on the dotted envelope curve (env. 1), Fig. 4.6b on the dashed curve (env. 2). Note that points with a depolarization factor larger than unity are more abundant in Fig. 4.6b, since the envelope used represents the lowest possible one in Fig. 4.3c that is barely compatible with the instrumental noise. For $90°$ scattering (approximating observations at the extreme limb, i.e., at $\mu = 0$) ratios larger than unity are unphysical and must be due to noise, but for larger μ values ratios somewhat larger than unity are allowed (cf. the histograms in Fig. 4.11 below).

4.4.3 Hanle rotation and its relation to the depolarization

In the absence of magnetic fields Stokes U is zero for symmetry reasons. It becomes non-zero when there is Hanle rotation of the plane of linear polarization. Figure 4.7a shows the absolute value of the U/I amplitude at line center as a function of μ. For comparison the Q/I line-center envelopes from Fig. 4.3c are plotted as the dotted (env. 1) and dashed (env. 2) curves. In Fig. 4.7b we have plotted $|U|/Q$ (which equals $|\tan 2\beta|$, where β is the rotation angle) vs. μ. We notice that there is no systematic CLV trend for $|U|/I$ or $|U|/Q$. The occurrence of Hanle rotation depends on the local magnetic field present, not directly on μ.

To explore the relation between Hanle rotation and depolarization we have in Fig. 4.8 plotted $|U|/I$ (which is a measure of the Hanle rotation) normalized to the Q/I disk-center envelope (i.e., the ratio between the points and the curves in Fig. 4.7a) vs. the amount of Hanle depolarization, represented by $1 - (Q/I)/\text{env.}$ (i.e., one minus the values in Fig. 4.6), with one diagram for each envelope choice. The error bars are based on an error of $0.075\,\%$ in U/I (cf. Sec. 4.4.2). To get a better feeling for the expected appearance of such a diagram we can be guided by the following theoretical considerations:
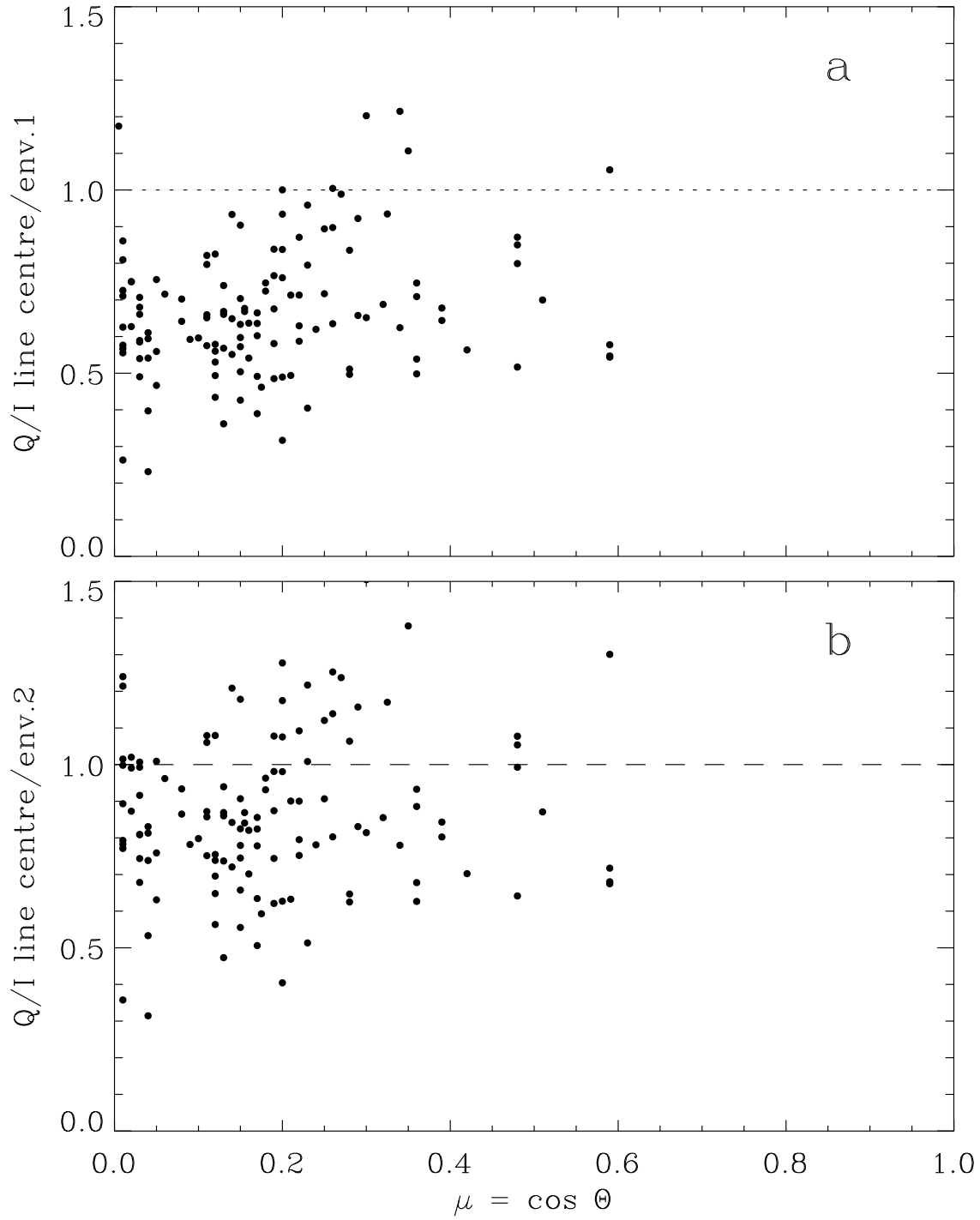
Figure 4.6: Ratio between the observed Q/I polarization amplitudes at line center and the corresponding Q/I envelope values, obtained as the ratio between the points in Fig. 4.4b and the dotted (env. 1) and dashed (env. 2) curves. The envelopes represent the values of the line center Q/I that we would have in the absence of magnetic fields.
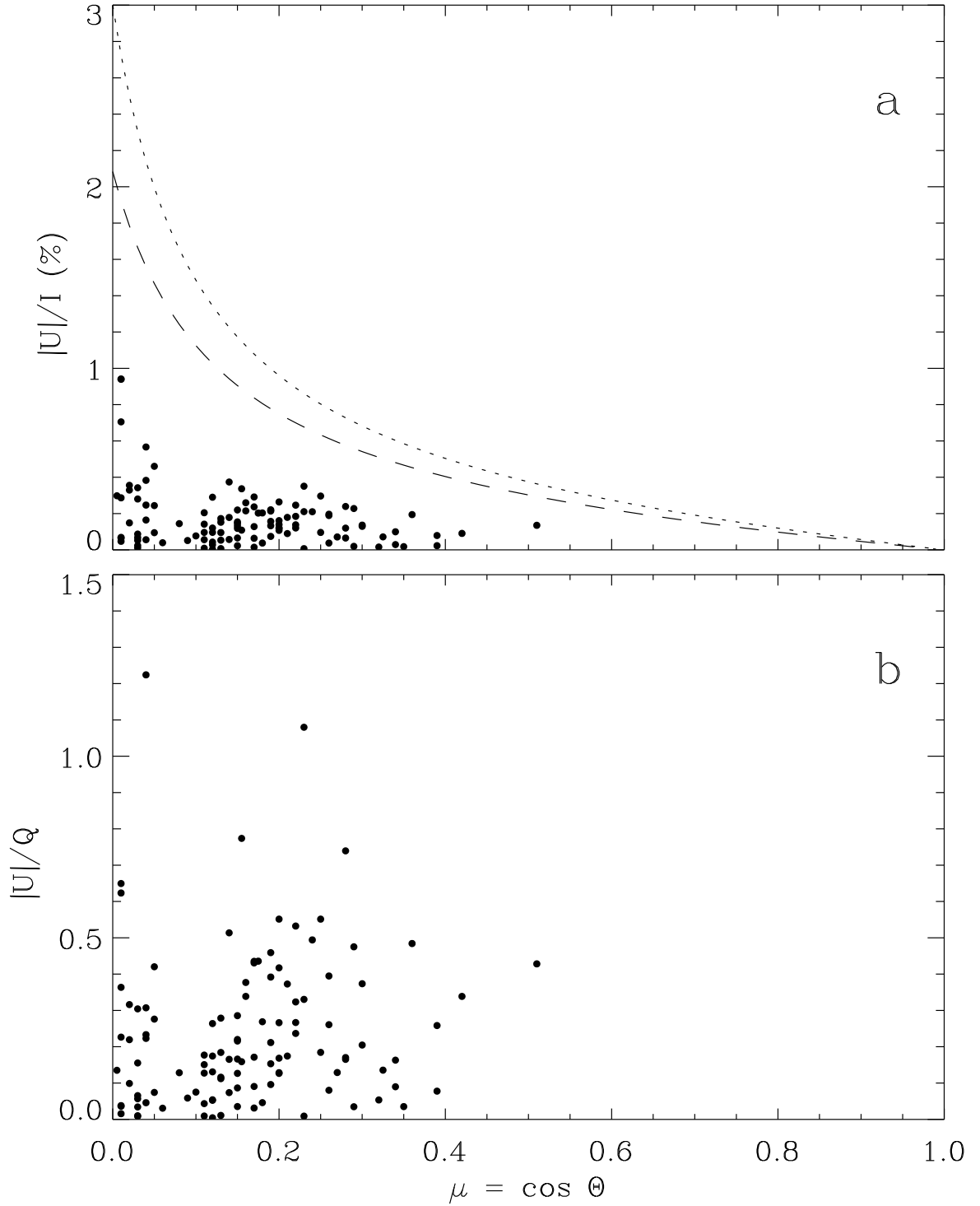
Figure 4.7: Center-to-limb behavior of the Stokes U amplitude in the line core. (a) The degree of polarization $|U|/I$. The dotted and dashed curves are the same Q/I line center envelope curves that were plotted in Fig. 4.3c. (b) The $|U|/Q$ ratio, which equals $|\tan 2\beta|$, where β is the Hanle rotation angle.

For mathematical simplicity we consider the case of single 90° scattering, as if the Sun had extreme limb darkening (such that all illumination of the scattering particles comes from the disk center), and we would be observing at the extreme limb. Due to moderate limb darkening and observations inside the limb the actual polarization amplitudes will of course be much smaller, but since we normalize all our U/I and Q/I values in Fig. 4.8 in terms of the Q/I line center envelopes, the amplitude scaling factors (due to the actual limb darkening or μ position) divide out to first order. The 90° single scattering case therefore still provides useful insight into the behavior of the normalized data. Note, however, that smaller scattering angles (corresponding to observations at larger μ values) give different distributions of the Q and U values, something that will be discussed more in connection with the histograms in Fig. 4.11 below.

Maximum Hanle rotation occurs when the magnetic field is directed along the line of sight, which is horizontal to the solar surface at the extreme limb. Since the for us relevant canopy magnetic fields are nearly horizontal, we will restrict our considerations here to the case of horizontal fields at the extreme limb. Then the field direction is characterized by the single parameter χ_B, the azimuth angle counted counter-clockwise from the direction towards the observer. The magnetic field strength is contained in the Hanle rotation angle α_2, where

$$\tan \alpha_K = \frac{K g_u \omega_L}{\gamma_N + \gamma_c/2},$$
(4.2)

where K can be 1 or 2 (cf. Stenflo 1994, p. 212). g_u is the Landé factor of the upper level, ω_L the Larmor precession frequency (which is proportional to the magnetic field strength), γ_N the natural, radiative damping width, and γ_c the damping width due to elastic collisions.

The polarizability of a scattering transition is as usual represented by the factor W_2, the fraction of scattering processes that occur as classical dipole scattering (while the remaining fraction occurs like isotropic, unpolarized scattering). For the Sr II 4078 Å line $W_2 = 0.5$, for Ca I 4227 Å it is unity. Then, according to Stenflo (1994, p. 92), the scattering of incident unpolarized radiation gives

$$
\begin{aligned}
Q &= \tfrac{3}{8} W_2 \big[\sin^2 \chi_B + (1 + \cos^2 \chi_B) \cos^2 \alpha_2 \big], \\
U &= \tfrac{3}{8} W_2 \cos \chi_B \sin 2\alpha_2,
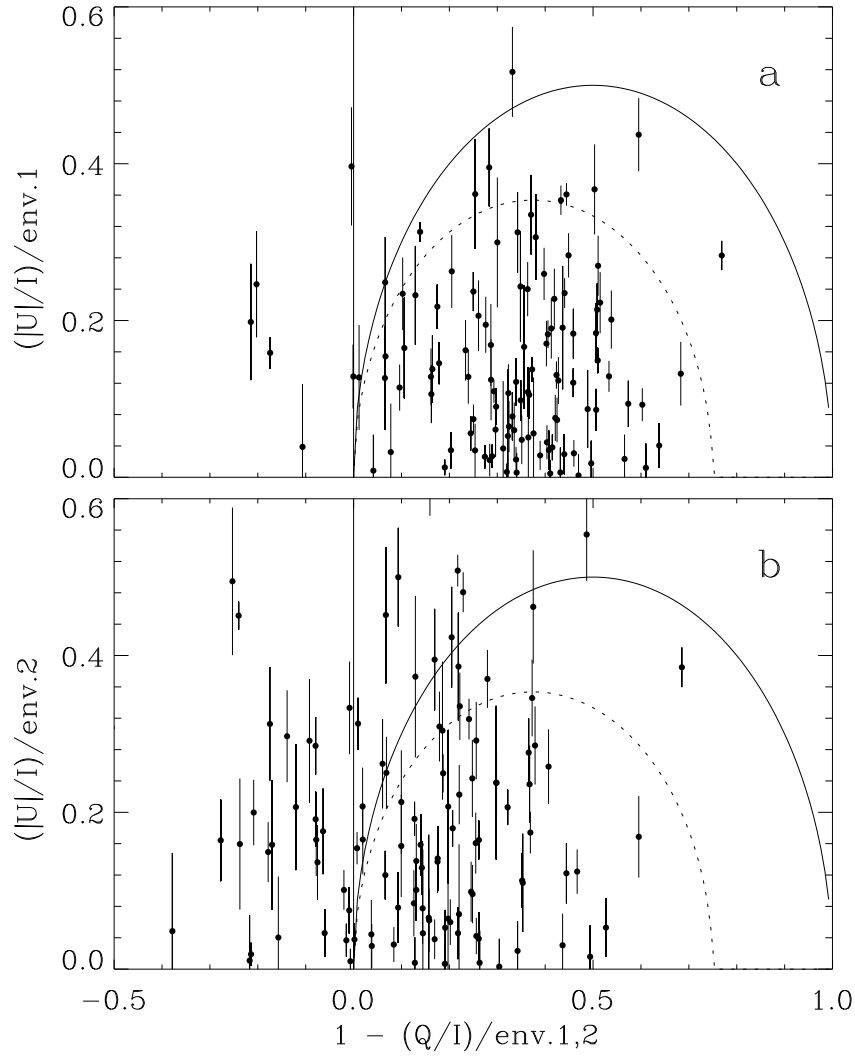\end{aligned}
$$
(4.3)

Figure 4.8: Relation between the Hanle rotation and depolarization effects. On the horizontal axis is $x = 1 - (Q/I)/\text{env.}$, where $(Q/I)/\text{env.}$ is obtained from the upper (env. 1) and lower (env. 2) diagrams of Fig. 4.6. On the vertical axis is plotted $y = (|U|/I)/\text{env.}$, obtained from Fig. 4.7a as the ratio between the points and the two envelope curves. x is proportional to the amount of Hanle depolarization. The solid and dotted lines represent analytical curves obtained from idealized single scattering theory using the weak-field Hanle phase matrix. They are given by Eqs. (4.8) and (4.9), respectively. We expect all points to fall below the solid line, but because of noise and inadequate choice of the Q/I envelope, the data spread outside this region, in particular in the lower diagram (based on env. 2).

where we have rotated the Stokes coordinate system by $90°$ with respect to that used in Stenflo (1994, p. 92), so that Stokes Q is defined to be positive in the direction parallel to the solar limb. In contrast to Q and U, Stokes I is largely formed by non-scattering processes which do not need to be specified here.

We get maximum Q polarization in the absence of magnetic fields, i.e., for $\alpha_2 = 0$. Thus

$$Q_{\max} = \tfrac{3}{4}W_2 \,. \tag{4.4}$$

On the other hand, what we in our figures have called env. (the Q/I envelope) is the same as Q/I in the absence of magnetic fields:

$$Q_{\max}/I = \text{env.} \tag{4.5}$$

The x and y axis in Fig. 4.8 represent

$$\begin{aligned} x &= 1 - (Q/I)/\text{env.} \\ y &= (|U|/I)/\text{env.} \end{aligned} \tag{4.6}$$

According to Eqs. (4.3)–(4.6)

$$\begin{aligned} x &= \tfrac{1}{2}(1 + \cos^2 \chi_B)\sin^2 \alpha_2 \\ y &= \tfrac{1}{2}\left| \cos \chi_B \sin 2\alpha_2 \right| \,. \end{aligned} \tag{4.7}$$

The maximum value of y (Hanle rotation) possible is obtained when $\chi_B = 0$. In this case we find from Eq. (4.7) the following relation between x and y:

$$y = \sqrt{x(1 - x)} \,. \tag{4.8}$$

This relation is plotted as the solid curves in Fig. 4.8. For reference, as an intermediate case, we plot the corresponding relation obtained for $\chi_B = 45°$,

$$y = \sqrt{\tfrac{2}{3}x(1 - \tfrac{4}{3}x)} \,, \tag{4.9}$$

as the dotted curves in Fig. 4.8. When $\chi_B = 90°$ (magnetic field perpendicular to the line of sight), $y = 0$, i.e., the Hanle rotation vanishes.

We have plotted all the data points in Fig. 4.8, also those with negative x values. Ideally, without instrumental scatter, all points should fall inside the area bounded by the solid curve in the case of $90°$ scattering (observations at $\mu = 0$), but they spread into the outside region,
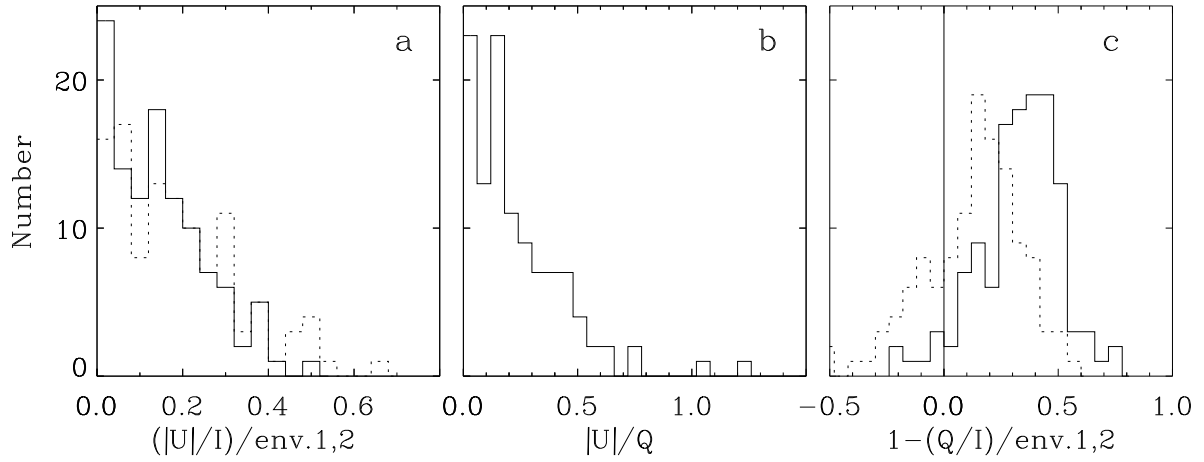
Figure 4.9: Histograms showing the distributions of the observational data. The solid lines in (a) and (c) are based on the use of env. 1, the dotted lines on env. 2. Panel (a) represents the distribution of the y values in Fig. 4.8, panel (c) the distribution of the x values in Fig. 4.8, while panel (b) gives the distribution of the points in Fig. 4.7b.

either because of noise or from contributions from larger μ values (for which negative x values are allowed), or because the non-magnetic Q/I envelope in Fig. 4.3c was chosen too low. The large spread in Fig. 4.8b suggests that env. 2 (dashed curve in Fig. 4.3c) was chosen too low, and that env. 1 (dotted curve in Fig. 4.3c) is to be prefered.

4.4.4   Histograms of the Hanle effect

The statistical distributions of the data can be expressed in the form of different "Hanle histograms", which may be compared with theoretical histograms based on various models. Such a comparison would then allow us to gain information on the actual distribution of the magnetic field. Our empirical histograms are given in Fig. 4.9, in which the solid lines are based on env. 1, the dotted lines on env. 2. Figure 4.9a gives the distribution of the $|U|/I$ polarization expressed in units of the Q/I non-magnetic envelope, which is the parameter that was used as the y axis in Fig. 4.8. Figure 4.9b gives the distribution of the ratio $|U|/Q$, which equals $|\tan 2\beta|$, where β is the Hanle rotation angle (cf. Stenflo 1994, p. 92). The maximum at $|U|/Q = 0.15$ thus corresponds

to a rotation angle $\beta \approx 4°$. Note that the values of β do not depend on the choice of Q/I envelope.

Figure 4.9c gives the relative amount of Hanle depolarization, $1 - (Q/I)/\mathrm{env.}$, which was used as the x axis in Fig. 4.8. We notice that the "spill-over" of the distribution into the negative domain is large for env. 2, as we saw in Fig. 4.8b, which again suggests that env. 1 is to be prefered (see however Fig. 4.11 below).

The observed Hanle histograms can be understood as complex mappings of the distribution of magnetic field vectors with respect to both direction and magnitude. It is in principle conceivable to invert this problem and use the observed histograms to derive the properties of the magnetic-field distributions. As such an undertaking would be far beyond the scope of the present paper, we here limit ourselves to compute theoretical histograms for a few selected special cases, which provides insight into the problem and indicates what kind of field distributions and parameter ranges that would be required to be compatible with the observed histograms.

To compute such theoretical histograms we make use of the general, weak-field Hanle phase matrix that Landi degl'Innocenti & Landi degl'Innocenti (1988) has given in analytical form for arbitrary scattering geometries and magnetic field vectors. As before we consider a single scattering process and assume that the incident radiation is unpolarized and along the vertical direction. Since the resulting histograms depend on the scattering angle we will compute a set of histograms for two different values of the scattering angle, $90°$ (corresponding to $\mu = 0.0$) and $60°$ (corresponding to $\mu = 0.5$). Almost all our observations fall between these two extreme values. As we do not use a limb-darkening function, the polarization scale will be wrong, but this scale factor divides out when we normalize the polarization data with the Q/I envelope. In contrast to our discussion of Fig. 4.8 we now consider all possible azimuth angles χ_B and colatitudes θ_B (angle with respect to the vertical direction) of the magnetic field vector.

The magnetic field can thus be characterized by the three parameters θ_B, χ_B, and the Hanle angle α_2, which is a measure of the field strength. It is however more convenient to parametrize the field strength in terms of γ_B, which is related to α_2 by

$$\tan \alpha_K = K \gamma_B \qquad (4.10)$$

($K = 1, 2$). γ_B is proportional to the field strength B:

$$B = (B_0/k_c^{(2)})\, \gamma_B \,. \tag{4.11}$$

B_0 is the field strength for which the Larmor precession rate equals the spontaneous radiative decay rate of the excited state. It is thus an atomic-physics constant determined by this decay rate. For our Sr II transition it is $11.8\,\mathrm{G}$. The collisional factor is

$$k_c^{(2)} = \frac{\gamma_N}{\gamma_N + \gamma_c/2}\,, \tag{4.12}$$

where γ_N and γ_c are the radiative and collisional damping constants as in Eq. (4.2). In the higher layers of the solar atmosphere, where Sr II is formed near the solar limb, the collision rate is low, so that $k_c^{(2)}$ is not far from unity. According to the (rather crude) estimates in Stenflo (1982) it is about 0.75 at the height of formation for Sr II. In this case

$$B \approx 15.8\gamma_B \;(\mathrm{G})\,. \tag{4.13}$$

The rather large uncertainty in the depolarizing collision rate introduces a corresponding uncertainty in the field-strength scale. A too small collision rate leads to too small values for the derived field strengths.

We may now compute, for any combination of θ_B, χ_B, and γ_B, the values of Q and U that result from a single scattering process. These values are called Q_B and U_B. The value of Q_B in the absence of magnetic fields is denoted Q_0. Then $|U_B|/Q_0$ represents our observed quantity $(|U|/I)/\mathrm{env.}$, while $1 - Q_B/Q_0$ represents our observed $1 - (Q/I)/\mathrm{env.}$

For the computation of theoretical histograms we divide the unit sphere into equal-area boxes, with one grid-point at the center of each box. The boxes have equal width in colatitude θ_B, namely π/n, where $n = 160$. For each value of θ_B we divide the parallel circle for azimuth χ_B in $2m \sin\theta_B$ intervals, rounded to the nearest integer. m is chosen to be 153 rather than 160 so that $2m \sin\theta_B$ is almost exactly an integer when $\sin\theta_B$ is small. With this division the sphere contains 31,167 equal-area boxes. A set of new grid points is generated by a small rotation of the described grid around the polar axis. Histograms for these various grids are superposed to improve the statistics.

For each grid point and each value of the field-strength parameter γ_B we compute the values of $x_1 = |U_B|/Q_0$, $x_2 = |U_B|/Q_B$, and $x_3 = 1 - Q_B/Q_0$. The angular distribution function determines how the grid points will be weighted. We make use of two different angular distributions, previously introduced for Hanle diagnostics by Stenflo (1982): (a) An isotropic distribution, and (b) a distribution that is confined to the horizontal plane and has random azimuth angles χ_B. In the case of the horizontal distribution the whole sphere does not need to be subdivided, only the equator. We then use 32,000 intervals in χ_B. For each of the two distributions, and for each given value of γ_B, we count the number of x_i values ($i = 1, 2, 3$) that fall in different x_i intervals. This gives us the theoretical histograms for x_i. Since we are here only interested in the shapes of the histograms and not in their absolute values (which depend on the choice of x_i interval widths), we have normalized all histogram curves to their maximum value.

Let us at this point note that the computation described so far implicitly assumes that the magnetic field is spatially resolved for each recording. For most fields this is not the case, but some fields must be at least partially resolved by the observations. If this were not the case and the field distribution were random *within* each spatial resolution element, then there could be no net Hanle rotation, since the positive and negative contributions would cancel each other, so all values of U would be zero. The distribution over a range of U values (or over x_1 and x_2) is only possible for partially resolved or non-random magnetic fields. For the Hanle depolarization, however, there is no such cancellation, since it occurs with only one sign. Therefore a random field distribution inside the spatial resolution element will produce a net Hanle depolarization, the amount of which is determined by the field strength. A distribution of observed amounts of Q/I polarization may then be due to a large-scale variation of the rms field strength of a random small-scale field, rather than to a large-scale variation of a resolved field. We will come back to this issue when comparing the theoretical histograms with the observed ones.

The results of our computations (based on the assumption of spatially resolved fields) are displayed in Figs. 4.10 and 4.11. The upper halves of the figures show the results for the isotropic distribution, the lower halves for the horizontal distribution of field vectors. The solid,

dashed, and dotted curves correspond to the values 1, 0.5, and 0.25, respectively, for the field-strength parameter γ_B. Note that in the lower left diagram of Fig. 4.10 the solid and dotted curves coincide.

For each value of γ_B only a certain range of x_i values are possible. A curve can end at its maximum value unity at one edge of its x_i range, or it can end at an intermediate value. Beyond these end points no points can exist. Due to our normalization all curves reach unity somewhere. In the lower $|U|/Q$ panel of Fig. 4.10 the solid curve turns up and reaches unity only for higher x_i values outside the displayed range.

Let us now compare the theoretical histograms of Figs. 4.10 and 4.11 with the observed ones in Fig. 4.9 to see if the observations can be understood within the framework of our idealized theoretical model. The shapes of the theoretical curves look quite different from those of the observed histograms, but we have to remember that the theoretical curves have been obtained for fixed, single-valued field strengths. With a more realistic field-strength distribution we would have to make weighted averages of different shifted curves, like the solid, dashed, and dotted ones in Figs. 4.10 and 4.11, which would result in rounded distributions similar to the observed ones in Fig. 4.9. A refined treatment should also account for the μ distribution of the observations.

The range covered by the observational histogram for the Hanle depolarization $1 - (Q/I)/\mathrm{env.}$ (Fig. 4.9c) is best represented by the theoretical dashed curves in Figs. 4.10 and 4.11, for $\gamma_B = 0.5$. According to Eq. (4.13) this correspondence requires the field strengths to be about 5–10 G.

Note that the distributions of the depolarization x_3 spill over more and more into the negative regime as the value of μ increases, as shown by the panels to the right in Fig. 4.11. Therefore the data points that fall into this regime need not all be due to noise, since some spill-over is actually expected. This μ dependence of the histograms needs to be accounted for in future more detailed quantitative interpretations. We also have to deal with another quite fundamental interpretational problem, namely the finite spatial resolution of the observations.

The observational histograms for the Hanle rotation (Figs. 4.9a and b) spread over a considerably smaller range of $(|U|/I)/\mathrm{env.}$ and $|U|/Q$
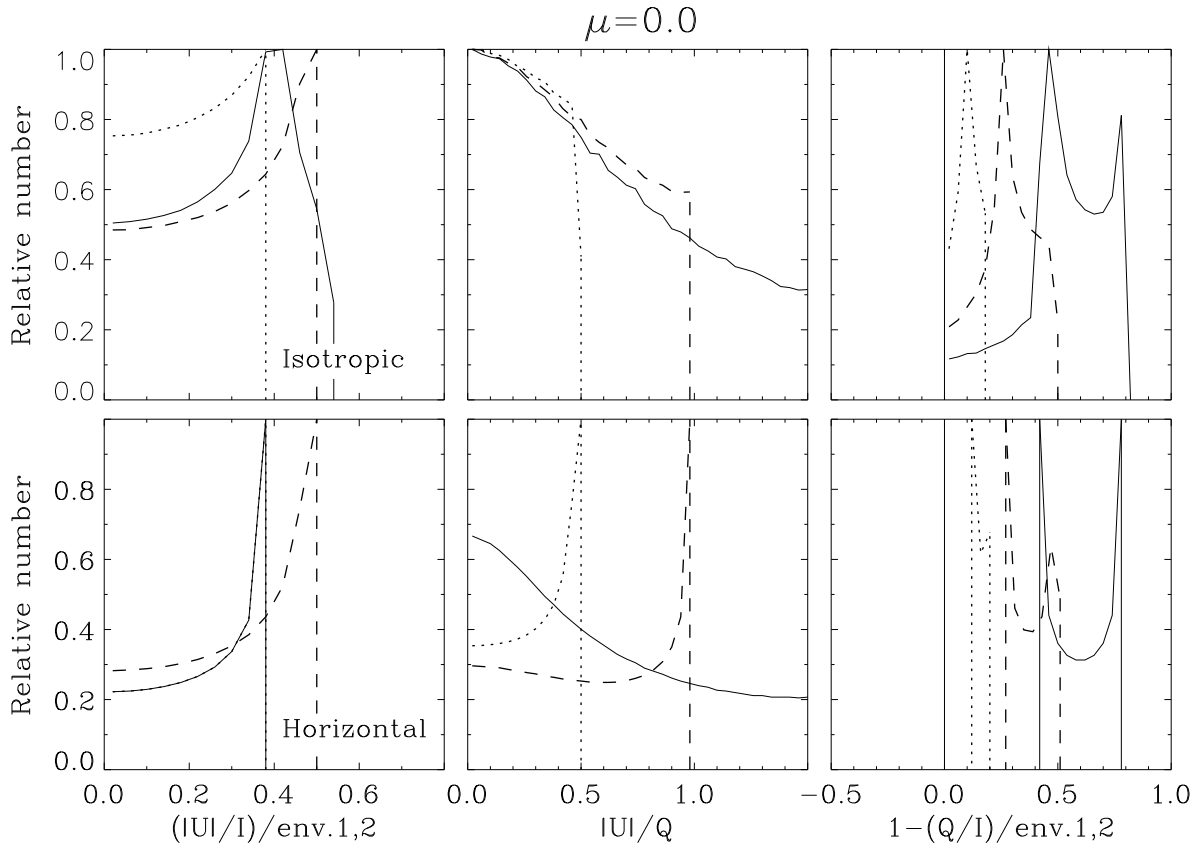
Figure 4.10: Theoretical histograms for the same parameters as deter-
mined observationally in Fig. 4.9. The curves are based on
an idealized single-scattering model assuming spatially
resolved magnetic fields and two different angular distri-
butions of field vectors, an isotropic (upper panels) and a
random horizontal (lower panels) distribution. 90° scat-
tering is assumed, corresponding to observations at the
extreme limb ($\mu = 0$). The solid, dashed and dotted curves
correspond to the values 1.0, 0.5, and 0.25 for the field-
strength parameter γ_B that is related to the field strength
B via Eq. (4.13). For details, see the text.

(x_1 and x_2) values than would be expected from a 5–10 G field accord-
ing to the corresponding diagrams in Figs. 4.10 and 4.11. This incon-
sistency between Hanle depolarization and rotation indicates that the
underlying assumption for the theoretical histograms, namely that the
magnetic fields are spatially resolved (homogeneous within each solar
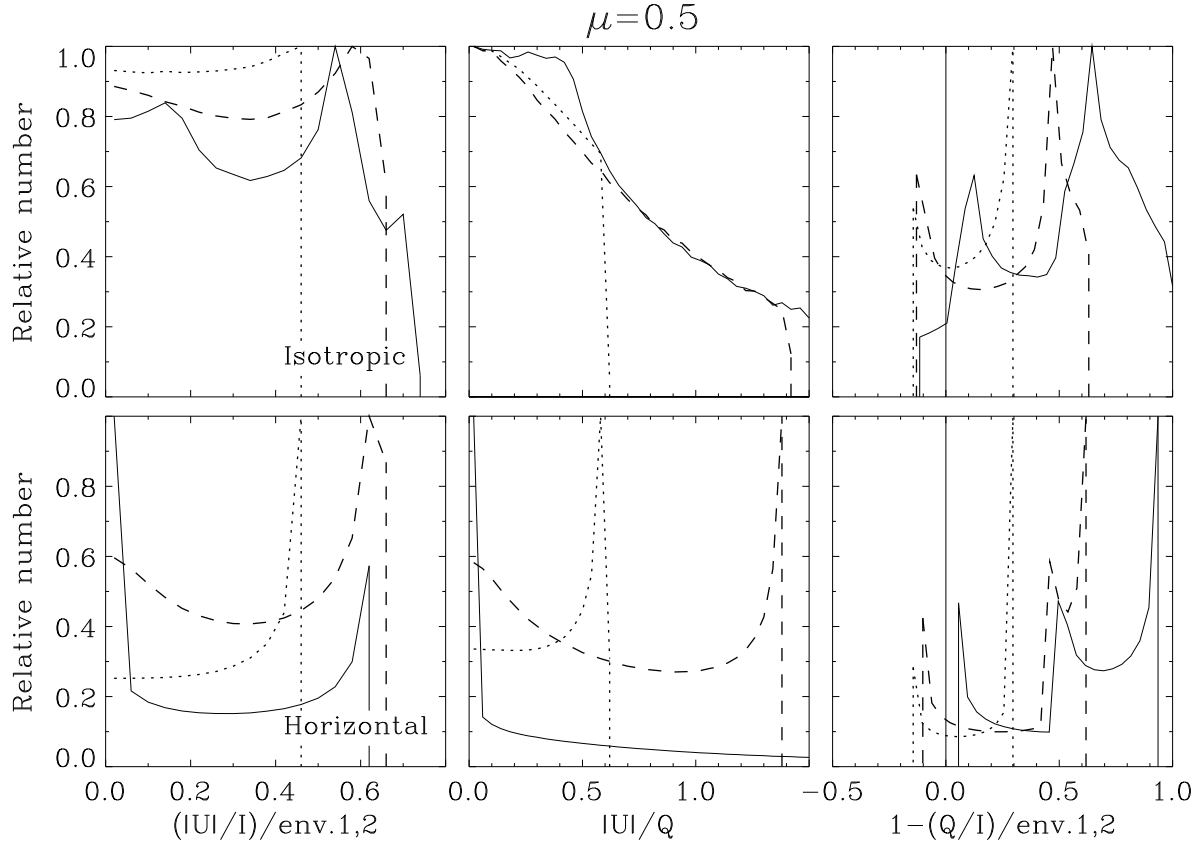region to which an observed spectrum corresponds), is not correct.

Figure 4.11: Same as Fig. 4.10, except that the scattering angle is assumed to be 60°, corresponding to observations at $\mu = 0.5$.

From our previous knowledge about the structure of solar magnetic fields we know that most of the magnetic flux is indeed spatially unresolved. On the other hand, if all the unresolved flux had no net orientation when averaged over the spatial resolution element, then no non-zero values for the Hanle rotation could occur, all U values would be zero, and the histograms in Figs. 4.9a and b would just have a peak at $x_{1,2} = 0$, with some spread due to observational noise. The circumstance that the spread is much larger than the noise indicates that large-scale orientations of the field which do not average out over small scales are indeed present. Such a large-scale field with a strength on the order of 5–10 G can have contributions either from a global component of the Sun's general magnetic field, or from canopy fields, which have their sources in the supergranular network and spread nearly horizontally in the lower chromosphere over the supergranular cells (cf. Giovanelli 1980; Solanki & Steiner 1990). The canopy fields

can be expected to statistically obey a nearly horizontal, random distribution of field vectors with a spatial coherence over scales comparable to the supergranulation (30 Mm), while the global field component can be coherent over larger scales.

On a much smaller, even subtelescopic or optically thin scale, we can expect the presence of an isotropically distributed turbulent field, which reveals itself through Hanle depolarization but not through Hanle rotation (Stenflo 1982; 1994; Faurobert-Scholl 1993; Faurobert-Scholl et al. 1995). If such a field had a single-valued field strength, it would in the Hanle depolarization diagram (Fig. 4.9c) for each given μ value contribute to a peak located at a non-zero value of the depolarization x_3. A field-strength and μ distribution would widen the peak, to make it look more like the observed distribution in Fig. 4.9c. Again, for the depolarization peak to be located at the observed place the field strengths would need to be around 5–10 G, as we will derive more directly in the next subsection. However, regardless of field strength, the turbulent field would try to make the Hanle rotation histograms in Figs. 4.9a and b peak around zero x_1 and x_2. If we now to this small-scale turbulent field add a large-scale field (like a canopy field or a global field) with net large-scale field orientations, then we see that with a proper combination of these two kinds of fields (small and large scale), we may build Hanle rotation histograms that look like those of Figs. 4.9a and b. The apparent inconsistency between the histograms for the Hanle rotation and depolarization can indeed be resolved if we have a mixture of contributions from resolved and unresolved fields.

This rather involved discussion shows that with the present data no unique interpretation is possible, but that the observed histograms can be understood in terms of plausible magnetic-field scenarios. These scenarios would be differently constrained by other lines with different sensitivities to the Hanle effect. It should therefore be possible to greatly reduce the ambiguity in the interpretations by making use of the differential Hanle effect for combinations of spectral lines, and of course also by combining Hanle diagnostics with high spatial resolution.

4.4.5 Field strengths from the observed Hanle depolarization

We will now adopt the assumption (contrary to the assumption on which the theoretical histograms in Figs. 4.10 and 4.11 were based) that the fundamental magnetic structures are spatially unresolved, and that we average over a complete angular distribution of field vectors within each spatial resolution element. The Hanle depolarization factor k_H that results from this averaging is then identified with our observed depolarization factors $(Q/I)/\mathrm{env}$. The factor k_H can be obtained in analytical form for various angular distributions, as has been shown by Stenflo (1982) for a horizontal (canopy-type) random distribution, and for an isotropic (turbulent-type) distribution. The resulting expressions obtained by averaging the weak-field Hanle phase matrix over these two types of angular distributions are

$$
\begin{aligned}
k_H^{\mathrm{turbulent}} &= 1 - 0.4\left(\sin^2 \alpha_1 + \sin^2 \alpha_2\right), \\
k_H^{\mathrm{canopy}} &= 1 - 0.75 \sin^2 \alpha_2 .
\end{aligned}
\tag{4.14}
$$

The Hanle mixing angles α_1 and α_2 have been given by Eqs. (4.2) and (4.10)–(4.13), which allow us to translate the quantity $(Q/I)/\mathrm{env.}$ into field strength.

We have thus taken all the values in Fig. 4.6 (after the values > 1 have been set $= 1$, since to be compatible with Eq. (4.14) such values are unphysical and must be due to noise) and converted them with the above equations, to obtain the four diagrams in Fig. 4.12. In these diagrams we have also determined the mean value and standard deviation of the points within μ intervals of width 0.05 and plotted them as diamonds with error bars. Note that the converted "unphysical" values enter into the diagrams with $B = 0$ and also contribute to the derived means and error bars.

We notice in Fig. 4.12 that the diagrams based on env. 1 (the prefered envelope) gives field strengths that are systematically somewhat larger than those based on env. 2, which produces many more "unphysical" points. The field strengths obtained with env. 2 can be regarded as a lower limit to the field strengths that would be obtained if a "true" non-magnetic Q/I envelope could be used. The assumption of an isotropic, turbulent field distribution results in somewhat
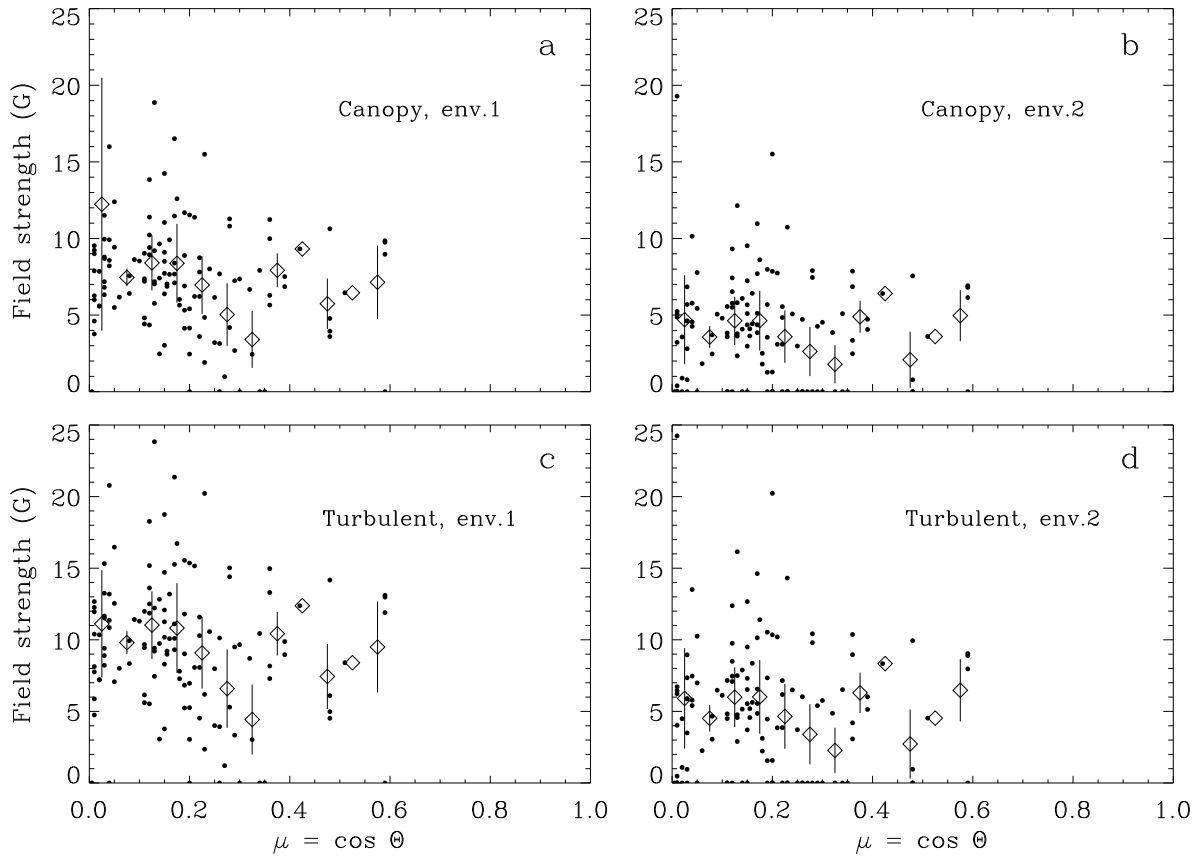
Figure 4.12: Magnetic field strengths derived from the observed Hanle depolarization in Q/I with the assumption that the fields are spatially unresolved, and that we average over a complete angular distribution of field vectors within each spatial resolution element. The figure has been obtained by converting the data in Fig. 4.6, which are supposed to represent the Hanle depolarization factor k_H, into field strengths via Eq. (4.14) for isotropic (lower panels) and random horizontal (upper panels) field distributions. The diamonds with error bars represent averages and standard deviations of the data points within μ intervals of width 0.05.

larger field strengths than when a horizontal, canopy-type angular distribution is used, but these differences are smaller than the scatter of the points. The typical mean field strengths are 5–10 G, the same as we estimated from the Hanle histograms in Sect. 4.4.4. These results are consistent with and similar to those of Chapter 3 for the Ca I 4227 Å

line. The Sr II line gives on average 30 % lower values, but due to the uncertainties in the rate of depolarizing collisions, this difference cannot be regarded as very significant.

4.4.6   Profile shape of the Hanle effect

One fundamental and non-trivial property of the Hanle effect is that it is present in the Doppler core but absent in the line wings. There must therefore be a wavelength variation of the Hanle efficiency with a transition from core to wings, i.e., the Hanle efficiency has a certain profile shape. With our extensive statistical material of polarized line profiles with various amounts of Hanle rotation and depolarization, we are now for the first time in a position to determine empirically the profile shape of the Hanle effect.

One very direct way to do this is to simply form the ratio between the mean U/I and Q/I profiles (the dotted and solid curves in Fig. 4.1c). As U/Q equals $\tan 2\beta$, where β is the Hanle rotation angle, the resulting ratio profile, which is plotted in Fig. 4.13a, represents the profile of the Hanle rotation effect. Its width and shape are in full accord with theoretical expectations, although a detailed quantitative comparison with theory is outside the scope of the present paper.

The general profile behavior (the requirement that U should be zero in the far wings) has however been assumed by us in the procedure for the elimination of the instrumental $Q \rightarrow U$ cross talk. It would therefore be good to have a confirmation of this profile shape independent of this assumption.

Such an independent determination can be made by using the statistical Hanle depolarization information in the Q/I profiles alone, without reference to U. The procedure is the following: Using the value of Q/I at a fixed wavelength λ_{ref} in the far line wings as a reference, we form the ratio

$$r(\lambda) = \frac{Q(\lambda)/I(\lambda)}{Q(\lambda_{\text{ref}})/I(\lambda_{\text{ref}})} \tag{4.15}$$

as a function of wavelength λ. The choice of λ_{ref} is not critical (although it should be chosen in an unblended portion of the line wing),
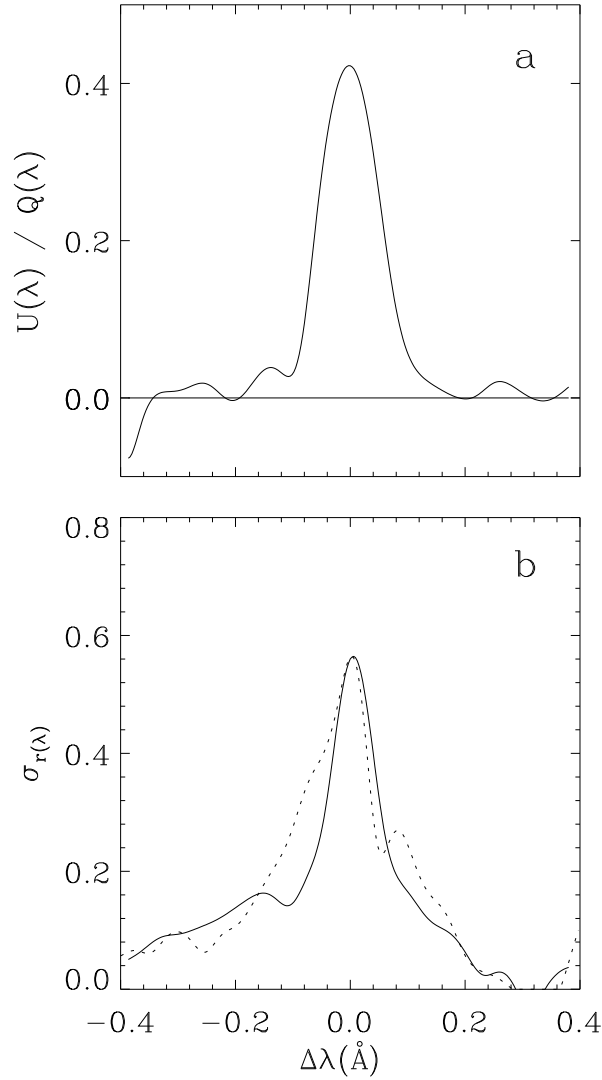
Figure 4.13: Empirical profiles for the Hanle efficiency, showing how the Hanle effect is active in the line core but vanishes in the line wings. (a) Profile of the Hanle rotation efficiency, obtained as the ratio between the dotted (U/I) and solid (Q/I) curves in Fig. 4.1c. (b) Profile of the Hanle depolarization efficiency, represented by the standard deviation or scatter $\sigma_{r(\lambda)}$ of the observed values of $r(\lambda)$, where r is defined by Eq. (4.15). The solid curve has been derived from the present Sr II data, the dotted curve from the Ca I data of Chapter 3. To facilitate the comparison between the different profiles, the Ca I curve has been rescaled, and the zero points for the two curves have been slightly shifted, as described in the text.

it mainly determines the unit or scale for r, but this scale factor is immaterial anyway, since we are only interested in the profile shape.

For each given value of λ the different recordings will give different values of r. We interpret this variation in the r value as being due to the varying Hanle depolarization in Q/I. The variation will be larger when the Hanle depolarization efficiency is larger. We therefore determine, for each given λ, the standard deviation $\sigma_{r(\lambda)}$ in the values of $r(\lambda)$ for all our Q/I recordings. $\sigma_{r(\lambda)}$ should be proportional to the amount of Hanle depolarization.

This kind of analysis is also possible for our previous Ca I 4227 Å Q/I line profiles that were used in Chapter 3. In Fig. 4.13b we plot the results for $\sigma_{r(\lambda)}$ for both lines: The solid curve for Sr II, the dotted for Ca I. Since the normalization of $r(\lambda)$ (through the choice of λ_{ref}) is different for Sr II and Ca I, we have multiplied the $\sigma_{r(\lambda)}$ values for Ca I by the constant factor 2.3 to make the profile scales comparable for the two spectral lines.

Since $\sigma_{r(\lambda)}$ is a standard deviation, it can never be negative, and it reaches zero by definintion at the chosen reference wavelength λ_{ref} (in the right portion of Fig. 4.13b). Noise contributes to σ with only one sign (positive) and causes the far wings to be elevated above the zero level (except at λ_{ref}). To bring this elevated noise level down we have subtracted a constant from the $\sigma_{r(\lambda)}$ values. We have chosen this constant to be 0.065 for Sr II and somewhat less, 0.046, for the scaled Ca I values, since the noise level was smaller for the Ca I data.

A comparison between the profile shapes and widths of the different curves shows that there is general agreement, both between Sr II and Ca I, and between $\sigma_{r(\lambda)}$ and $U(\lambda)/Q(\lambda)$. This agreement further confirms the Hanle interpretation of our data, and we now have the first empirical Hanle efficiency profiles, which later may be compared with corresponding theoretical profiles. We note in particular the good agreement between the independently determined Hanle rotation and depolarization profiles.

4.5 Conclusions

In the present paper we have for the Sr II 4078 Å line applied the same observational and analysis techniques that we used in Chapter 3 for the Ca I 4227 Å line, but we have also significantly extended and refined the Hanle diagnostics. From the observational point of view the main new features are the recording of not only Stokes I and Q, but also of Stokes U, which allows us to detect the Hanle rotation of the plane of polarization, and the use of a rapidly tilting servo glass plate to stabilize the solar limb with respect to image motions. From the analysis point of view the main new highlights are the introduction of Hanle histograms for the diagnostics of magnetic field distributions, and the first empirical determination of the profile shape of the Hanle efficiency, showing the way in which the Hanle rotation and depolarization effects vary when we go from the line core to the wings.

In the areas where our analysis methods have been the same as those of Chapter 3, we find that the scattering polarization in the Sr II and Ca I lines behave very much the same with respect to the Hanle effect, although these lines have different atomic structures (and intrinsic polarizabilities) and polarized line shapes. Assuming spatially unresolved angular field distributions we derive from the Sr II analysis typical field strengths of 5–10 G, similar to those derived from the Ca I data. These field strengths are confirmed by the shapes and widths of our Hanle histograms, which in addition provide information on the strengths and angular distributions of spatially resolved fields. Such fields reveal themselves by producing a non-zero Stokes U signature, which can only occur if there are resolved, net large-scale orientations of the field, e.g. from a global component of the Sun's magnetic field, or from magnetic canopies across the supergranulation cells. The consistency between the various analysis methods and results, and the derived Hanle efficiency profile shapes, confirm the Hanle interpretations of the data and put the astrophysical use of the Hanle effect on firmer ground.

Hanle histograms offer us a new potentially powerful tool to derive detailed information on the distributions of magnetic field strengths and orientations. We have to be aware, however, that both spatially resolved and unresolved fields (with field distributions within the res-

olution element) contribute to these observed histograms. With our present data set it is not possible to unambiguously separate all the different kinds of contributions from each other. Such ambiguities can be greatly reduced and hopefully eliminated by using differential Hanle diagnostics, i.e., by comparing the scattering polarization in certain combinations of spectral lines with different sensitivities to the Hanle effect, a new technique that has been explored by Stenflo et al. (1998). This will allow additional observational constraints to be added, such that a unique inversion of the Hanle problem may become possible. Observationally we need to develop better methods to eliminate the instrumental polarization cross talk, which in our case has its probably main source in the entrance window of the telescope. We also need to include Stokes V for full vector polarimetry to combine the diagnostic powers of the Zeeman and Hanle effect and access a broader parameter domain of solar magnetism.

Bibliography

Faurobert-Scholl, M., 1993, *"Investigation of microturbulent magnetic fields in the solar photosphere by their Hanle effect in the Sr I 4607 Å line"*, Astron. Astrophys. **268**, 765

Faurobert-Scholl, M., Feautrier, N., Machefert, F., Petrovay, K., Spielfiedel, A., 1995, *"Turbulent magnetic fields in the solar photosphere: diagnostics and interpretation"*, Astron. Astrophys. **298**, 289

Giovanelli, R. G., 1980, *"An exploratory two-dimensional study of the coarse structure of network magnetic fields"*, Sol. Phys. **68**, 49

Landi degl'Innocenti, E., 1998, *"Evidence against turbulent and canopy-like magnetic fields in the solar chromosphere"*, Nature **392**, 256

Landi degl'Innocenti, M., Landi degl'Innocenti, E., 1988, *"An analytical expression for the Hanle-effect scattering phase matrix"*, Astron. Astrophys. **192**, 374

Pierce, A. K., Slaughter, C. D., 1977, *"Solar limb darkening. I. At wavelengths of 3033-7297"*, Sol. Phys. **51**, 25

Povel, H., 1995, *"Imaging Stokes polarimetry with piezoelastic modulators and charge-coupled-device image sensors"*, Optical Engineering **34**, 1870

Semel, M., 1995, *Zeeman Doppler Imaging*, in *ASP Conf. Ser. 71: IAU Colloq. 149: Tridimensional Optical Spectroscopic Methods in Astrophysics*, 340

Semel, M., Donati, J.-F., Rees, D. E., 1993, *"Zeeman-Doppler imaging of active stars. 3: Instrumental and technical considerations"*, Astron. Astrophys. **278**, 231

Solanki, S. K., Steiner, O., 1990, *"How magnetic is the solar chromosphere?"*, Astron. Astrophys. **234**, 519

Stenflo, J. O., 1982, *"The Hanle effect and the diagnostics of turbulent magnetic fields in the solar atmosphere"*, Sol. Phys. **80**, 209

Stenflo, J. O., 1994, *"Solar magnetic fields: polarized radiation diagnostics"*, Astrophysics and Space Science Library, Kluwer Academic Publishers, Dor-

drecht

Stenflo, J. O., Baur, T. G., Elmore, D. F., 1980, *"Resonance-line polarization. IV. Observations of non-magnetic line polarization and its center-to-limb variations"*, Astron. Astrophys. **84**, 60

Stenflo, J. O., Bianda, M., Keller, C. U., Solanki, S. K., 1997, *"Center-to-limb variation of the second solar spectrum."*, Astron. Astrophys. **322**, 985

Stenflo, J. O., Keller, C. U., Gandorfer, A., 1998, *"Differential Hanle effect and the spatial variation of turbulent magnetic fields on the Sun"*, Astron. Astrophys. **329**, 319

Stenflo, J. O., Twerenbold, D., Harvey, J. W., 1983a, *"Coherent scattering in the solar spectrum — Survey of linear polarization in the range 3165–4230 Å"*, Astron. Astrophys. Suppl. Ser. **52**, 161

Stenflo, J. O., Twerenbold, D., Harvey, J. W., Brault, J. W., 1983b, *"Coherent scattering in the solar spectrum — Survey of linear polarization in the range 4200–9950 Å"*, Astron. Astrophys. Suppl. Ser. **54**, 505

Sütterlin, P., Wiehr, E., Bianda, M., Küveler, G., 1997, *"Problems in measuring prominence oscillations"*, Astron. Astrophys. **321**, 921

Chapter 5

Hanle effect observations with the Ca I 4227 Å line[*]

M. Bianda[1], J.O. Stenflo[2] and S.K. Solanki[2]

Abstract

The Hanle effect in the Ca I 4227 Å line has been explored through the analysis of a large number of Stokes profile recordings obtained on the quiet Sun with the beam-splitter polarimeter system at IRSOL (Istituto Ricerche Solari Locarno). In contrast to previous Hanle observations with this line, which were limited to the Stokes I and Q parameters, we are now in a position to study the combined effects of Hanle depolarization (via Stokes Q) and rotation of the plane of linear polarization (via Stokes U) with the same methods that we recently applied to the Sr II 4078 Å line. The Hanle histograms for the distributions of the depolarization and rotation parameters are very similar for the two lines and show that there must be mixed contributions to the Hanle signals from spatially unresolved magnetic fields with random orientations (which do not contribute to Stokes U) and partially resolved magnetic fields with a net orientation of the field vectors. Field strengths in the

---

[1] Istituto Ricerche Solari Locarno (IRSOL), Switzerland
[2] Institut für Astronomie, ETH Zürich, Switzerland

range 5–10 G are preferred. We also determine the "Hanle efficiency profile", which shows how the Hanle effect is confined to the Doppler core but vanishes in the line wings. It is wider than the corresponding profile for the Sr line, as expected from the difference in atomic weight and wavelength between the two lines. The Q/I profiles of the Ca I 4227 Å line have minima around the Doppler core which turn negative (polarization perpendicular to the limb) for limb distances $\mu = \cos\theta \gtrsim 0.2$, a likely signature of partial redistribution effects.

5.1 Introduction

With the availability of high-precision imaging Stokes polarimeters it has become possible to make use of the Hanle effect as a new tool for magnetic-field diagnostics across the solar disk. The Hanle effect is sensitive to magnetic fields in a different parameter regime as compared with the Zeeman effect, in particular to weak fields, turbulent fields, and chromospheric fields. While the most sensitive polarimeter system ZIMPOL (Zurich Imaging Polarimeter, cf. Povel 1995) has been used to explore differential depolarization effects in various spectral lines due to the Hanle effect (Stenflo et al. 1998) , the most promising spectral region for Hanle diagnostics is in the blue and ultraviolet below the sensitivity limit of about 4500 Å for ZIMPOL.

As the only sufficiently sensitive imaging Stokes polarimeter for this spectral region is the beam-splitter system at IRSOL (Istituto Ricerche Solari Locarno), we have embarked on a program to use the versatile IRSOL facility for systematic explorations of scattering polarization physics, the Hanle effect, and associated magnetic-field diagnostics. The general observing and reduction technique was described in detail in Chapter 3 in which we also studied the behavior of the Stokes I and Q profiles for the Ca I 4227 Å line and developed a method to determine the Hanle depolarization and corresponding field-strength values. In a subsequent work (Chapter 4) we did a similar study for the Sr II 4078 Å line, but extended the observations and analysis to also include Stokes U, to allow us to determine the combined effects of Hanle depolarization and rotation of the plane of linear polarization. Histograms of different Hanle parameters were in-

troduced as a new diagnostic tool for magnetic-field distributions in a regime inaccessible to the Zeeman effect. While Chapter 3 and 4 exclusively dealt with the quiet Sun, observations of the full Stokes vector in active regions will be presented in Chapter 6 which will illustrate how the Hanle and Zeeman effects mix in the intermediate field regime, and how these polarization effects exhibit large spatial fluctuations on scales of a few arcsec or less.

In the present Chapter we return to the exploration of the Hanle effect in quiet regions in the Ca I 4227 Å line that was initiated in Chapter 3, but our new data set is richer and includes recordings of the Stokes U parameter, which allows us to explore for the Ca I line the combined effects of Hanle depolarization and rotation as was done for Sr II in Chapter 4. We also here introduce a method to determine the absolute zero point of the polarization scale and substantially improve the technique of accurately determining the μ (cosine of the heliocentric angle) value used as the parameter for the center-to-limb distance. We can then construct histograms for the Hanle depolarization and rotation as well as for the field strength and also determine the efficiency profile that describes how the Hanle effect varies from line core to the wings.

The results presented here agree closely with the corresponding results for the Sr II line in Chapter 4. This consistency between results obtained in different spectral lines places the Hanle-type interpretation of the observed polarization effects on firmer ground and also helps constrain the intrinsic field distributions on the Sun. Although we have converted the observed Hanle depolarizations to field-strength distributions (with maxima typically around 5–10 G), more detailed quantitative interpretations require numerical radiative-transfer modelling like that of Faurobert-Scholl (1992, 1994), but this is outside the scope of the present Chapter.

Because of our improved control of the true zero point of the polarization scale we are able to show how negative values of the Q/I polarization appear at the wavelengths, where we have a transition from the Doppler core to the dispersion wings, and the center-to-limb variation of these negative values, including their sign reversal near $\mu \approx 0.2$, are determined. Since these line frequencies are sensitive to the details of partial frequency redistribution of scattering polariza-

tion, these center-to-limb curves offer an interesting testing ground for radiative-transfer physics and may contain information of significant diagnostic value.

5.2 Observational and data reduction techniques

As in Chapters 3, 4 and 6 all our observations were carried out with the Semel-type polarimeter (cf. Semel et al. 1993; Semel 1995) and the Gregory-Coudé telescope at IRSOL (Istituto Ricerche Solari Locarno). For details concerning the observing procedure and reduction methods we refer to these papers and limit our presentation here to the features that are new or special to the present investigation.

5.2.1 Data set

The present Chapter deals with observations of the Stokes profiles of the Ca I 4227 Å line. While the circular polarization (V/I) was recorded in addition to the linear polarization (Q/I and U/I), we will only discuss the linear polarization results here, since the weak-field Hanle effect only affects the linear polarization. The Stokes V recordings were made for completeness, to monitor instrumental effects (like polarization cross talk), and to verify that the observations were made in quiet solar regions.

To take advantage of the minimum telescope polarization that occurs near the equinoxes, our observations were carried out during 5 days around the 1997 fall equinox, during 7 days around the 1998 spring equinox, and during one day near the 1998 fall equinox. The collected data set, after removal of the most noisy spectra (about 20 % of the total), consists of 353 Q/I, 353 U/I, and 131 V/I spectra. All recordings, except for 27 of them, were recorded in quiet regions. Examples of the 27 test recordings in active regions were presented and discussed in Chapter 6 and will not be used here. Like Chapters 3 and 4 the present Chapter deals exclusively with quiet regions.

The 4227 Å line has been observed in the 11th, 12th, or 13th grating orders, corresponding to different spectral fields of view (1.5 Å in the

13th order, 2.4 Å in the 11th order) covered by the CCD sensor. We have checked whether the appearance of the polarized spectra depend on grating order and have not found such a dependence.

The typical exposure times were 10–20 s, and slit widths of 150 or 200 μm (corresponding to 1.2 or 1.6 arcsec on the Sun) were used.

Two CCD exposures are needed for each of Stokes Q, U, or V. During the readout of a given frame the retarder is being rotated for the setting of the next frame. Each frame contains two orthogonally polarized spectra, and it is through the special combination of four such spectra (from two frames) that the fractional polarization (Q/I, U/I, or V/I) can be determined. To enhance the polarimetric accuracy we spatially average along the slit, which is oriented parallel to the limb, over a length of 15–18 arcsec.

5.2.2 Scattered light and polarization cross talk

All our data have been corrected for stray light in the spectrograph. This stray light has been determined by making recordings at disk center and comparing with corresponding FTS spectra recorded at Kitt Peak. The procedure for determining and correcting for the stray light is discussed in detail in Sect. 3.3.3 of Chapter 3. In the 1997 data we find stray light levels of 1.2–2 % (as a fraction of the continuum intensity), while for the 1998 data the stray light is down at 0.5–0.7 % . This decrease is the result of improvements, like cleaning of mirrors and better blocking of undesired light sources.

As in Chapters 3 and 4 we find that the observations contain substantial cross talk from $Q \to U$ and $Q \to V$. Cross talk in the opposite direction is unimportant here, because Q generally dominates over U and V in our data (since for the spatially smeared 4227 Å line in quiet regions it is the non-magnetic scattering polarization that dominates). The source of this cross talk (which was much larger than theoretically expected) has been discovered and eliminated. Due to a too thin aluminum coating of the third, flat telescope mirror, this mirror acted as a partial retarder. The mirrors have since been recoated, so that the telescope now behaves as it nominally should, but the data of the present Chapter were collected before this recoating. Nevertheless we could remove this cross talk problem in the data reduction process, as de-

scribed in some detail in Chapter 4. The removal consists of subtracting some fraction of the Q/I spectrum from the U/I and V/I spectra, with the constraint that the intrinsic U/I and V/I polarization should approach a constant level in the distant line wings (where Q/I remains highly structured). As a second step the zero point of the polarization scale is shifted to make the constant level in the line wings zero (cf. Sect. 5.2.3 below). This procedure leads to good and consistent results.

Since the iron lines in the wings of the Ca I 4227 Å line are narrow and Zeeman sensitive, their polarization signatures allow us to make good cross talk corrections between the linear and circular polarizations. Let us however again point out that in the present Chapter we only analyse the linear polarization and do not deal with the circular polarization, which was always very small in the quiet regions studied here. The circular polarization in the Ca I 4227 Å line in active regions was discussed and compared with the linear scattering polarization in Chapter 6.

Figure 5.1 gives examples of profiles of the intensity and linear polarization. The intensity profile in the top panel was recorded at disk center. The Q/I profiles in the middle panel illustrate the center-to-limb variation of the scattering polarization. They represent averages of individual Q/I profiles, after zero-level correction (see next subsection), within the μ windows 0.0–0.1, 0.1–0.15, 0.15–0.25, 0.25–0.35, 0.35–0.45, and 0.45–0.55, respectively. As μ represents the cosine of the heliocentric angle, the profiles for the smalles μ (closest to the limb) have the largest amplitudes. The arrows mark wavelength positions that we will refer to later.

The bottom panel of Fig. 5.1 shows the U/I profiles that represent averages of individual profiles within the first four of the above-mentioned μ intervals. For these averages only those U/I profiles that had an absolute core amplitude in excess of 0.05 % were used. Since both positive and negative U profiles occur (determined by the sign of the Hanle rotation angle), profiles with a negative core amplitude were first multiplied by -1 before being used for the average.
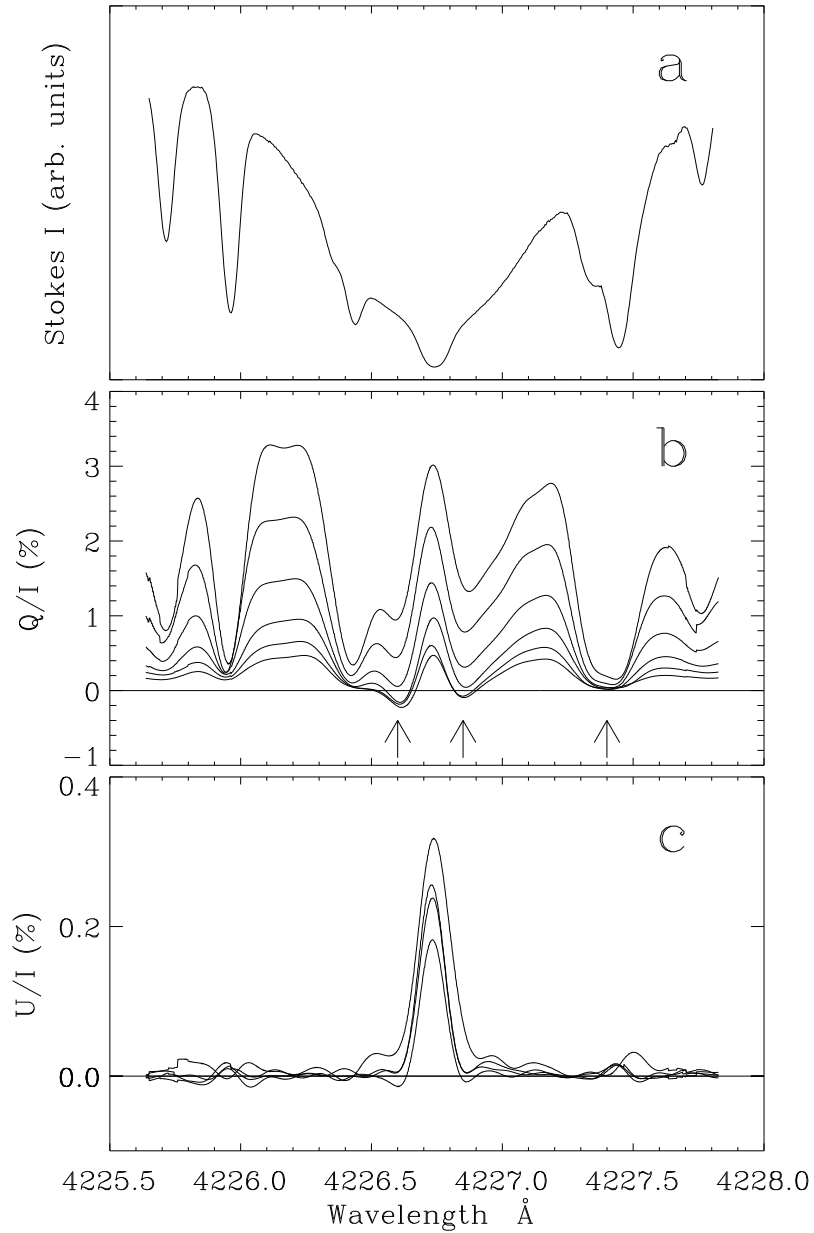
Figure 5.1: Examples of Stokes I, Q/I, and U/I profiles of the Ca I 4227 Å line. **a** Stokes I profile at disk center. **b** Q/I profiles averaged over a sequence of μ windows, to illustrate the center-to-limb variation. The arrows mark wavelengths referred to later in the text. **c** U/I profiles averaged over four of the μ windows that were used in the Q/I panel. Only profiles with core amplitudes in excess of 0.05 % have been included in these averages.

5.2.3 Polarization zero level

The observational zero level is nominally represented by the Stokes Q/I and U/I recordings at disk center, which should be intrinsically zero for symmetry reasons. The observational procedure is therefore always to alternate between limb and disk center recordings, such that the disk center spectra of the fractional polarization can be subtracted from the corresponding spectra elsewhere on the disk.

Although this procedure generally works well, there is a remaining scatter or uncertainty in the zero-level position, since the limb and disk spectra are not observed simultaneously. It is however possible to improve on this "preliminary" zero level to locate it more precisely. We do this by first examining the observed behavior of the values of the Q/I minimum at the wavelength near 4227.4 Å marked by the right arrow in Fig. 5.1b. They are plotted in Fig. 5.2 vs. the Q/I maximum in the blue wing (near 4226.2 Å), which is a well-defined function of limb distance or μ. We assume that the scatter of the points is due to random errors in the zero level and have therefore made a least squares fit with a second-order polynomial to represent the true behavior of the minimum Q/I polarization near 4227.4 Å (dashed curve in Fig. 5.2). We notice that the points and the dashed curve approach zero for small values of the wing peak polarization, i.e., as we approach disk center.

It is now possible to find the true zero level, by subtracting from every Q/I profile the difference between the corresponding point in Fig. 5.2 and the second-order dashed curve. The profiles displayed in Fig. 5.1b have been corrected this way.

In the case of the U/I and V/I profiles the zero-level problem is much easier. We only have to assume that the mean value of the polarization far from the line center is zero and shift the observed profiles accordingly.

5.2.4 Determination of the limb distance

The slit is always oriented parallel to the nearest solar limb, and the limb distance defines the value of μ. To compensate for image motions perpendicular to the solar limb a servo-controlled tilt-plate system is used for μ values smaller than 0.3. The value of μ is then determined
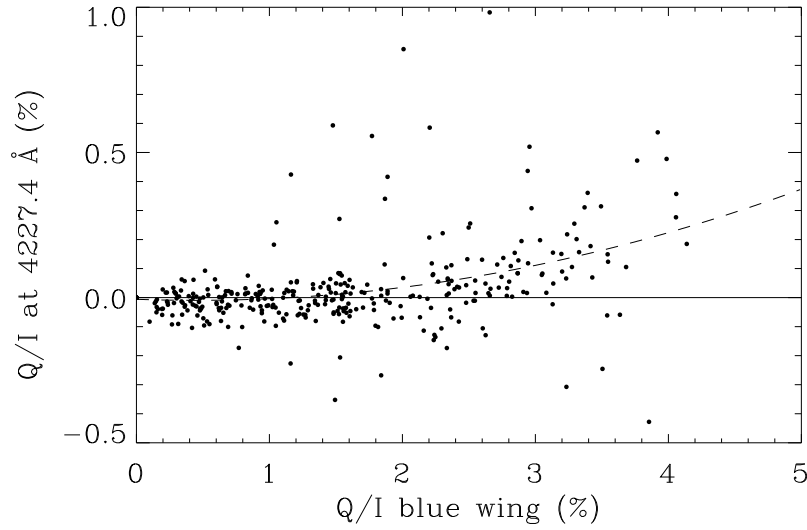
Figure 5.2: Relation between the observed Q/I minimum at 4227 Å (marked by the right arrow in Fig. 5.1) and the Q/I maximum in the blue wing. The dashed curve is a second-order polynomial fit.

from the reading of the tilt-plate sensor (read on the scale of the micrometer used to adjust the sensor). For $\mu \geq 0.3$ (when the tilt plate is switched off) the limb distance is determined from the setting of the guider telescope.

Another method to obtain information on the μ position would be to compare the alternating Stokes I profiles recorded near the limb and at disk center, while accounting for possible changes in the sky transparency. To convert such intensity ratios to μ values we need to apply a center-to-limb curve, but such curves are well known only for the continuum, not for wavelengths inside the Ca I line. Since our spectral window is not wide enough to include a portion of the continuum, we are not able to use this method here to improve on our μ values, only for more qualitative checks.

In our previous exploratory work on the Q/I polarization in the Ca I 4227 Å line in Chapter 3, an analytical expression from Chapter 2

$$\frac{Q}{I} = \frac{a(1 - \mu^2)}{\mu + b},\tag{5.1}$$

was used with $a = 0.4\,\%$ and $b = 0.05$ to represent the observed Q/I amplitude in the blue line wing. To reexamine this relation with our

present data set we select the three days that had the best sky transparency and therefore the smallest scatter in the determined μ values (March 19 and 20, and September 21 in 1998). The blue wing maxima for these days are plotted in Fig. 5.3a with three different symbols for the three days. We find that the earlier fit function is improved if we replace the old parameter values with $a = 0.33\,\%$ and $b = 0.02$. The new fit is represented by the solid curve in Fig. 5.3a, the old fit (of Chapter 3) by the dashed curve.

Very close to the limb, for $\mu < 0.075$, we see considerable scatter in Fig. 5.3a, but we are presently unable to determine whether this scatter is of solar or instrumental origin, although it is most likely instrumental. Our polarimeter system is currently being equipped with an image rotator that will compensate for the image rotation of the Gregory telescope on the spectrograph slit. This will allow better control of the slit position near the extreme limb.

Magnetic fields do not contribute (via the Hanle effect) to the scatter of the points around the solid curve in Fig. 5.3a, since the Hanle effect has zero efficiency at the wavelength of the blue wing maximum. Assuming therefore that the solid curve represents the true center-to-limb variation of the Q/I blue-wing maximum and that the scatter of the points are due to errors in μ, we can shift the points horizontally until they all fall on the solid curve. This method corresponds to inverting Eq. (5.1), using it to determine μ from the observed Q/I. Since this method is almost independent of varying sky transparency, in contrast to the other methods, and since the noise in Q/I has a much smaller influence on the center-to-limb curves than uncertainties in μ, we consider it to be the most accurate one, and have therefore adopted it to correct all our μ values. The scatter around the linear relation in Fig. 5.4a below illustrates how small the noise in Q/I indeed is.

5.3   Analysis and results

5.3.1   Hanle depolarization

Though the Hanle effect is always depolarizing for resonance scattering at 90°, it may lead to an increase of the linear polarization for cer-
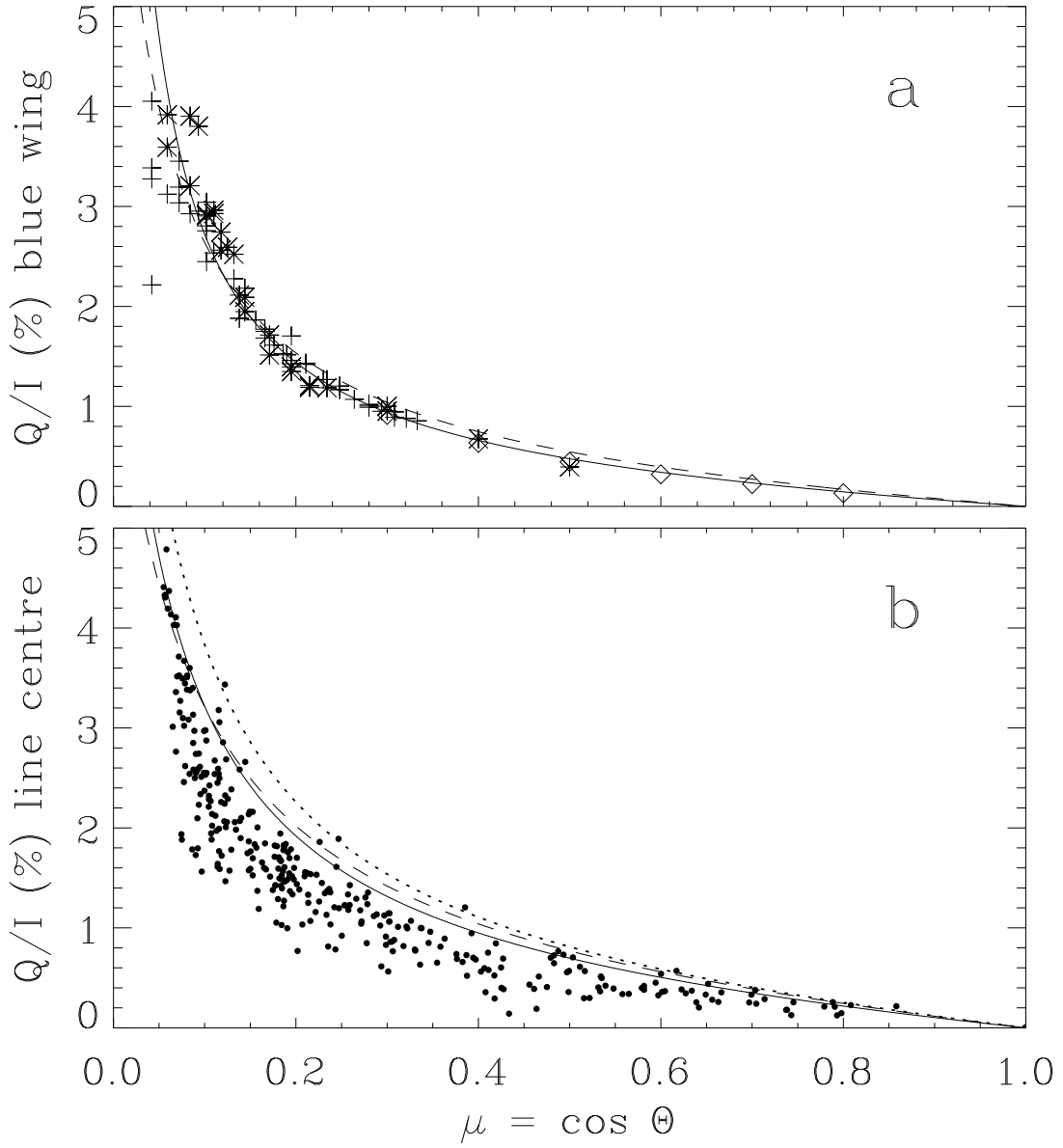
Figure 5.3: a Q/I amplitude in the blue line wing, observed on three different days in 1998 (represented by the three symbols). The solid curve represents a fit with the function of Eq. (5.1), with the parameter values $a = 0.33\%$ and $b = 0.02$. The dashed curve is the corresponding center-to-limb variation given in Chapter 3. **b** Center-to-limb variation of the Q/I amplitude at line center. The three curves represent envelopes based on the functional form of Eq. (5.1). The solid and dotted curves are the envelopes used in the later analysis.

tain field strengths and directions, when the scattering angle is different, as in the present observations. This effect, which was mentioned and briefly discussed in Chapter 4, increases when the scattering angle decreases. However, when the magnetic field has an unresolved structure like magnetic canopies or turbulent fields, the Hanle effect leads to depolarization for all scattering angles, due to the angular averaging over the highly non-linear Hanle effect. As our preliminary interpretation is only concerned with such unresolved fields, it will be self-consistent to assume a depolarizing behavior for the Hanle effect in the following data analysis.

Figure 5.3b shows the Q/I amplitude at line center as a function of the center-to-limb distance parameter μ. Here all the μ values have been corrected with the blue-wing Q/I data as described above. They thus correspond to the case when the scatter of the points around the solid curve in Fig. 5.3a has been removed by adjustment of the μ values. The scatter of the points in the diagram for the line-center (Fig. 5.3b) can be understood as due to Hanle depolarization (for the justification of this, see also Fig. 5.4 below). Since the Hanle depolarization works in the direction of reducing the polarization, the non-magnetic center-to-limb curve must lie above the points (if we disregard the instrumental noise). The amount of depolarization, which is a function of the field strength, is given by the ratio between the observed polarization and the level of the non-magnetic curve for the same μ.

The non-magnetic curve must be an envelope to the points in Fig. 5.3b, which we may represent in terms of the functional form of Eq. (5.1). The dotted and dashed curves represent the envelope choices made in Chapter 3, and correspond to the Eq. (5.1) parameter choices $a = 0.6\,\%$, $b = 0.055$, and $a = 0.6\,\%$, $b = 0.085$, respectively. Since the dashed curve intercepts the points for small values of μ, we find it better to replace it with the solid curve, which has $a = 0.52\,\%$, $b = 0.06$, and better represents a lowest possible envelope (accounting for the instrumental scatter). In the following we will use the solid and dotted curves as two possible envelope choices (to represent the non-magnetic center-to-limb variation).

Figure 5.4 shows in the upper panel a scatter plot of the Q/I red-wing maximum vs. the corresponding blue-wing maximum, while the
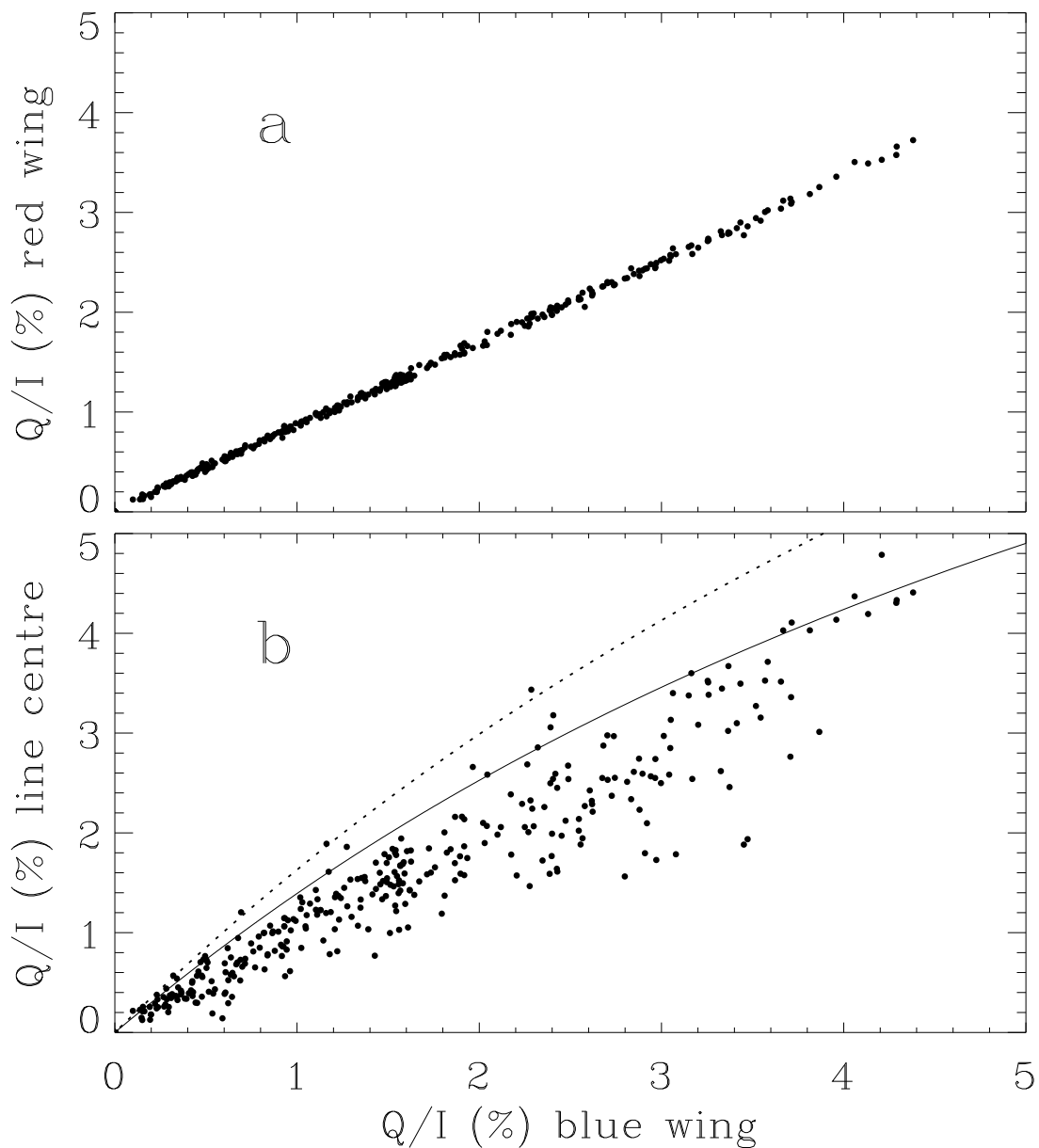
Figure 5.4: Red-wing (**a**) and line center (**b**) Q/I polarization amplitude vs. the Q/I amplitude in the blue line wing. The solid and dotted curves are obtained from the corresponding curves in Fig. 5.3b, using the solid curve in Fig. 5.3a for the relation between μ and the blue-wing amplitude.

lower panel gives the line-center amplitude vs. the blue-wing maximum. As found for the corresponding plot in Chapter 3 there is an excellent one-to-one correlation between the red and blue wings, while the linear polarization in the line core exhibits much scatter, as expected from the Hanle effect due to spatially varying magnetic fields. From the analytical expressions for the curves in Fig. 5.3, the solid and dotted envelope curves in Fig. 5.3b can be translated into the solid and dotted curves in the representation of Fig. 5.4b. The fractional distance (in the vertical direction) of the points from the envelope curves represents the magnetic-field induced Hanle depolarization.

5.3.2 Polarization oriented perpendicular to the limb

Since in the present work we have been able to accurately determine the zero point of the polarization scale, as described in Sect. 5.2.3 above, we are in a position to explore the detailed center-to-limb variation of the polarization minima around the core peak, at the wavelength positions marked by the left and middle arrows in Fig. 5.1b (the blue-wing minimum near 4226.6 Å, and the red-wing minimum near 4226.85 Å). They show the remarkable behavior of turning negative as we move away from the limb. For the blue-wing minimum this sign change occurs at $\mu \approx 0.2$, for the red-wing minimum at $\mu \approx 0.3$ (cf. Fig. 5.5). Negative Q/I means that the plane of linear polarization is oriented perpendicular to the limb. From our analysis and control of the zero-line problem we conclude that this behavior cannot be instrumental but is of solar origin.

Since the wavelengths of the two polarization minima are located near the profile region where we have a transition between frequencies in the Doppler core and in the dispersion wings, it appears likely that partial frequency redistribution (PRD) plays a central role in generating the sign change, and that modelling of the center-to-limb curves in Fig. 5.5 requires that full account of angle-dependent PRD of polarized radiation is taken. This expectation is supported by the PRD calculations by Rees & Saliba (1982) and Saliba (1985), who have shown how the PRD physics indeed leads to a polarization maximum in the Doppler core, which is often surrounded by negative minima. The shapes of the polarized profiles depend on the details of both the chro-
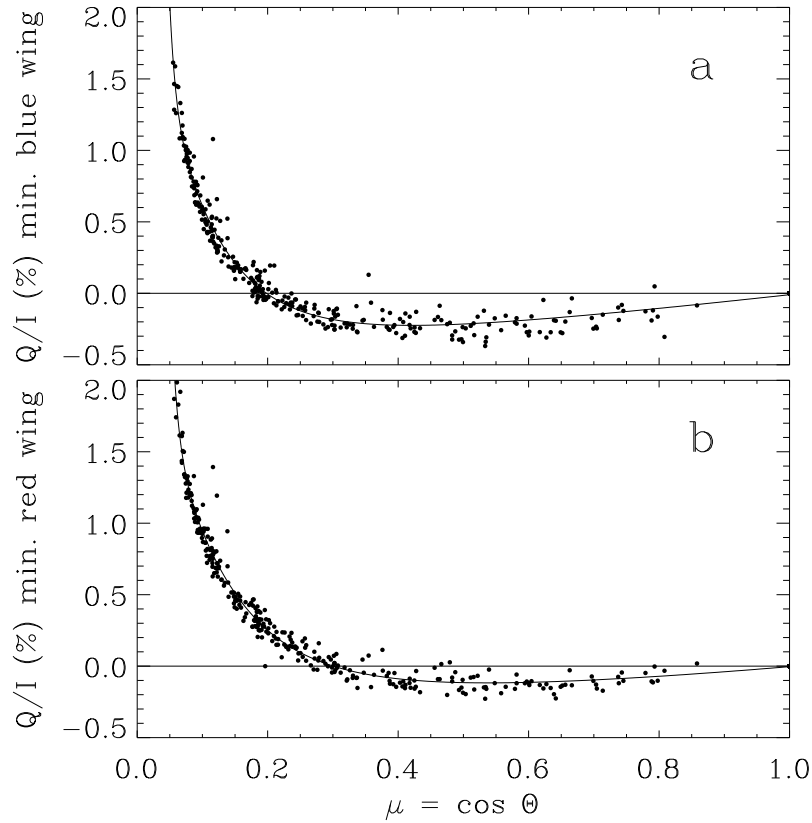
Figure 5.5: Center-to-limb variations of the Q/I minima on the blue (**a**) and red (**b**) side of the core peak. The solid curves represent 4th order fits as described in the text. Negative Q/I represents linear polarization oriented perpendicular to the solar limb.

mospheric models and the PRD approximations used. We therefore expect the observed center-to-limb curves in Fig. 5.5 to be of considerable diagnostic use to constrain both the atmospheric models and to explore the details of PRD physics.

The solid curves in Fig. 5.5 have been obtained by making 4th order polynomial fits to the Q/I minima vs. the Q/I blue-wing maximum, and then translating the blue-wing amplitude to μ, using the previously found analytical relation (represented by the solid curve in Fig. 5.3a).
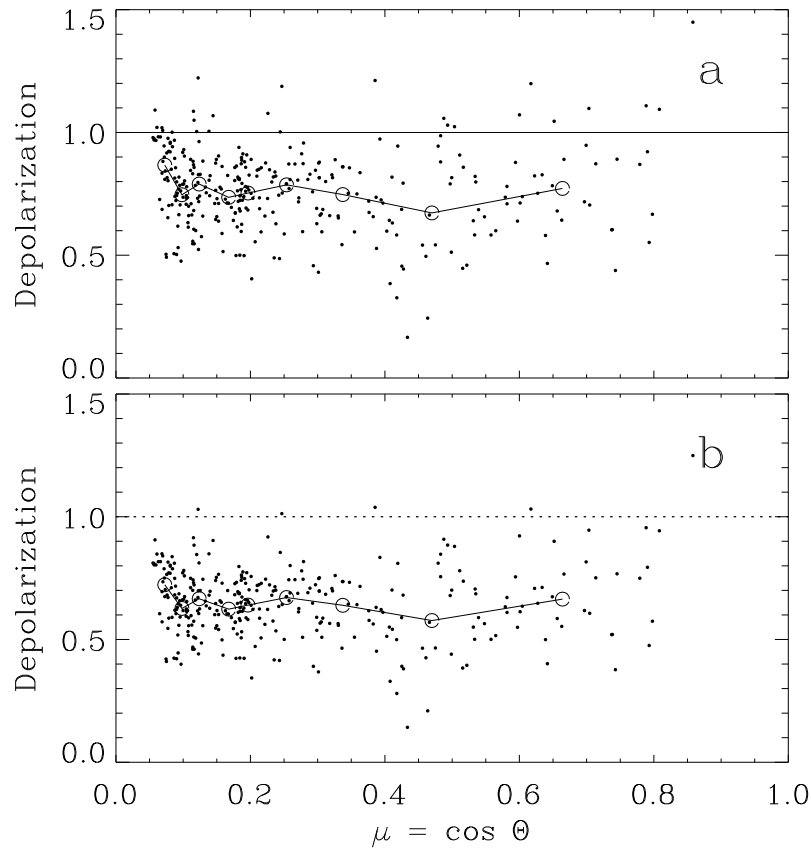
Figure 5.6: Values of the Hanle depolarization, determined as the ratio between the points in Fig. 5.4b and the two envelope curves. The top panel is based on the solid, the bottom panel on the dotted envelope curve.

5.3.3   Field strength determinations

Figure 5.6 shows the extracted values for the Hanle depolarization, determined from the line core data as the ratio between the points in Fig. 5.4b and the two envelope curves. Figure 5.6a refers to the solid envelope curve, Fig. 5.6b to the dotted envelope curve (therefore the horizontal lines at depolarization unity have been drawn solid and dotted in the two panels). As depolarization values by definition should not exceed unity, the points that lie above this level may be considered as falling there either because of instrumental noise, or because the respective envelope curve in Fig. 5.4b has been chosen too low. However, some "spill-over" may be physically allowed (cf. Sects. 5.3.4 and 5.3.5).
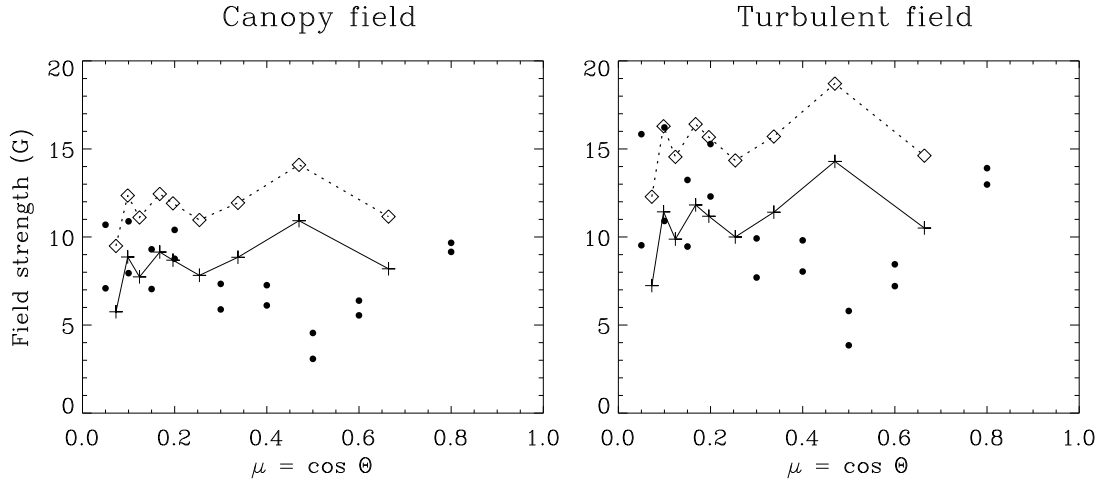
Figure 5.7: Field strengths derived from the average depolarization values (open circles in Fig. 5.6). The pluses are based on Fig. 5.6a, the diamonds on Fig. 5.6b, while the filled circles represent the results in Fig. 3.6 of Chapter 3. The left panel is based on a canopy field model, the right panel on a turbulent field model.

To examine if there is any dependence on limb distance we have formed average values within μ windows chosen so that each window contains 36 points. These average values are represented by the open circles, which are connected by straight lines. The standard deviation of the points around the mean values is between 0.1 and 0.2. Neither the mean values nor the standard deviations vary significantly with μ.

We may now use the depolarization values in Fig. 5.6 to derive field strengths, in the manner that was described in detail in Sect. 3.4.3 of Chapter 3. As before, we use two models to describe the distribution of spatially unresolved magnetic field vectors: (a) The field vectors have a random distribution that is confined to the horizontal plane (canopy field). (b) The field vectors have an isotropic distribution (turbulent field). Figure 5.7 is obtained for these two models if we use the average depolarization values represented by the open circles in Fig. 5.6. The plus signs, which are connected by solid lines, are based on the solid envelope (the data in Fig. 5.6a), while the diamonds, which are connected by dotted lines, are based on the dotted envelope (data in Fig. 5.6b).

For comparison we have also plotted as the filled circles the field
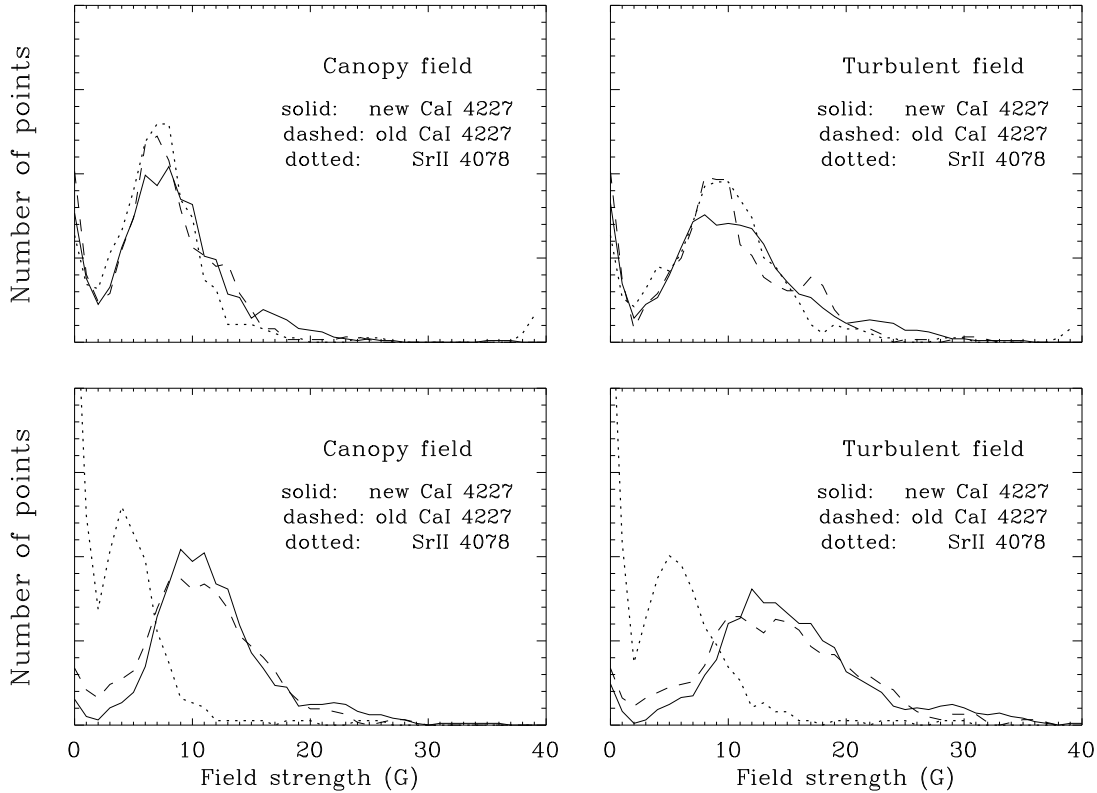
Figure 5.8: Smoothed histogram distributions for the magnetic field strengths derived from the observed values of the Hanle depolarization. The solid curves are based on the data of the present Chapter (the points in Fig. 5.6), the dashed and dotted curves on the data of Chapters 3 and 4, respectively. The left (right) panels are based on the canopy (turbulent) field model. The top and bottom panels are based on different choices of envelope, as described in the text.

strengths derived for the Ca I line in Chapter 3. The agreement with the present data is good for small μ, but the difference becomes fairly large for intermediate μ, in particular around $\mu \approx 0.5$, where the old data have a minimum, while the new data have a maximum. We notice for instance in Fig. 5.6 that around $\mu = 0.45$ some points have unusually small depolarization values, which corresponds to large values for the field strength. This can be partly due to the varying distribution of magnetic regions on the Sun (the observations of Chapter 3 were made during a less active phase of the solar cycle).

Since there is no clear center-to-limb variation of the field strengths

in Fig. 5.7, we may improve the statistics by using all the μ values together and construct histograms for the distribution of the field strengths derived from each individual depolarization value in Fig. 5.6. For points that have "unphysical" depolarization in excess of unity (due to instrumental noise and/or incorrect choice of envelope), the field strength is set to zero (the value that one would obtain for a depolarization of unity). This artificially produces a maximum in the histogram for zero field strength, which becomes more pronounced when the lower envelope is used. This secondary zero-field maximum is thus most likely an artefact of the reduction procedure and not of solar significance.

Such histograms were previously calculated for the Ca I 4227 Å data of Chapter 3 and the Sr II 4078 Å data of Chapter 4 and presented together in Fig. 6.2 of Chapter 6 to compare the distributions obtained with the two spectral lines. In Fig. 5.8 we now compare the newly obtained distributions (solid curves) with the previous ones from the Chapter 3 data (dashed curves) and the Chapter 4 data (dotted curves). To facilitate the comparison between the distributions from the three data sets we plot the histograms in smoothed form, normalized to equal area. The panels to the left are based on the canopy field model, those to the right on the turbulent field model. In the two top panels we have used the lower envelopes for the Ca I data, the higher envelope for the Sr II data, while in the two lower panels the other envelopes have been used to derive the values of the field strengths.

Figure 5.8 shows that there is excellent agreement between the distributions based on the Ca I line of the present data and those of Chapter 3. There is also an excellent agreement with the results for the Sr II line (Chapter 4) if for Ca I the lower envelopes are chosen and for Sr II the higher envelope, as shown by the two top panels of Fig. 5.8. However, all other combinations of envelopes result in smaller field strengths for Sr II as compared with Ca I. The particular choice of envelopes used in the upper panels of Fig. 5.8 would imply that the noise levels are substantially larger for Ca I than for Sr II, which is not the case.

An alternative interpretation could be that the Sr II 4078 Å line is formed somewhat deeper in the atmosphere, where the magnetic fields are different. The smaller field strengths in Sr II would then seem
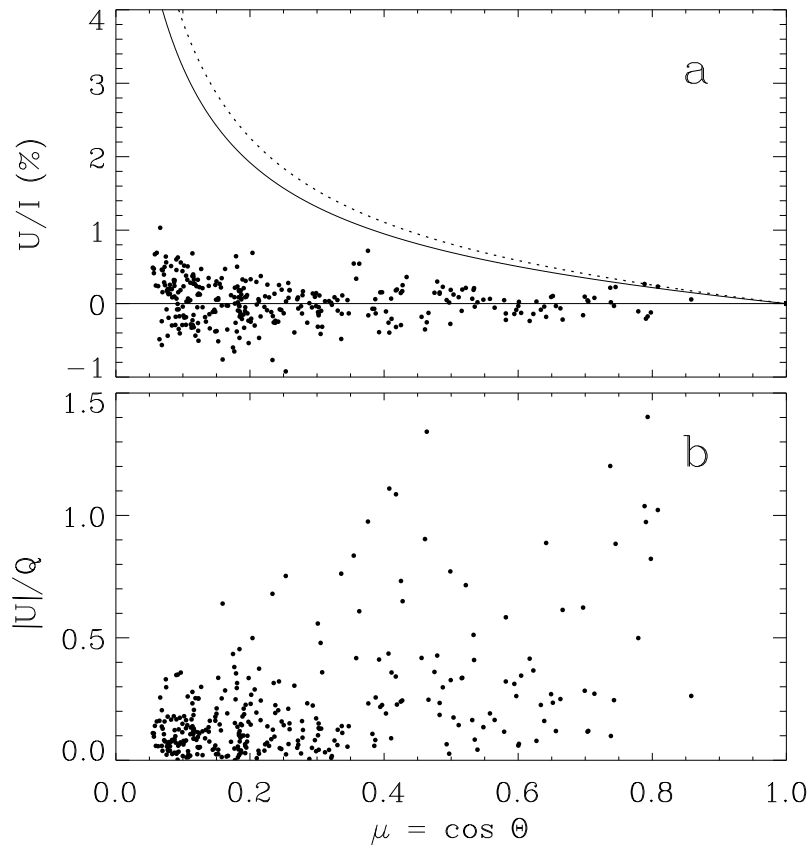
Figure 5.9: Scatter plot of U/I (top panel) and $|U|/Q$ (bottom panel) vs. center-to-limb distance parameter μ. The solid and dotted curves in the upper panel are the same as the solid and dotted Q/I envelope curves in Fig. 5.3b.

to imply that the field strength decreases with depth, which may appear counter-intuitive. There are however two effects that can lead to a decrease of the Hanle depolarization with depth: (1) The fields become increasingly more vertical with depth. The Hanle effect decreases and vanishes when the field inclination goes to zero. (2) The magnetic filling factor decreases with depth, if we only consider the flux tubes and disregard the contribution from turbulent magnetic fields. Only the fraction of the volume occupied by fields with a significant horizontal component can contribute to the Hanle effect.
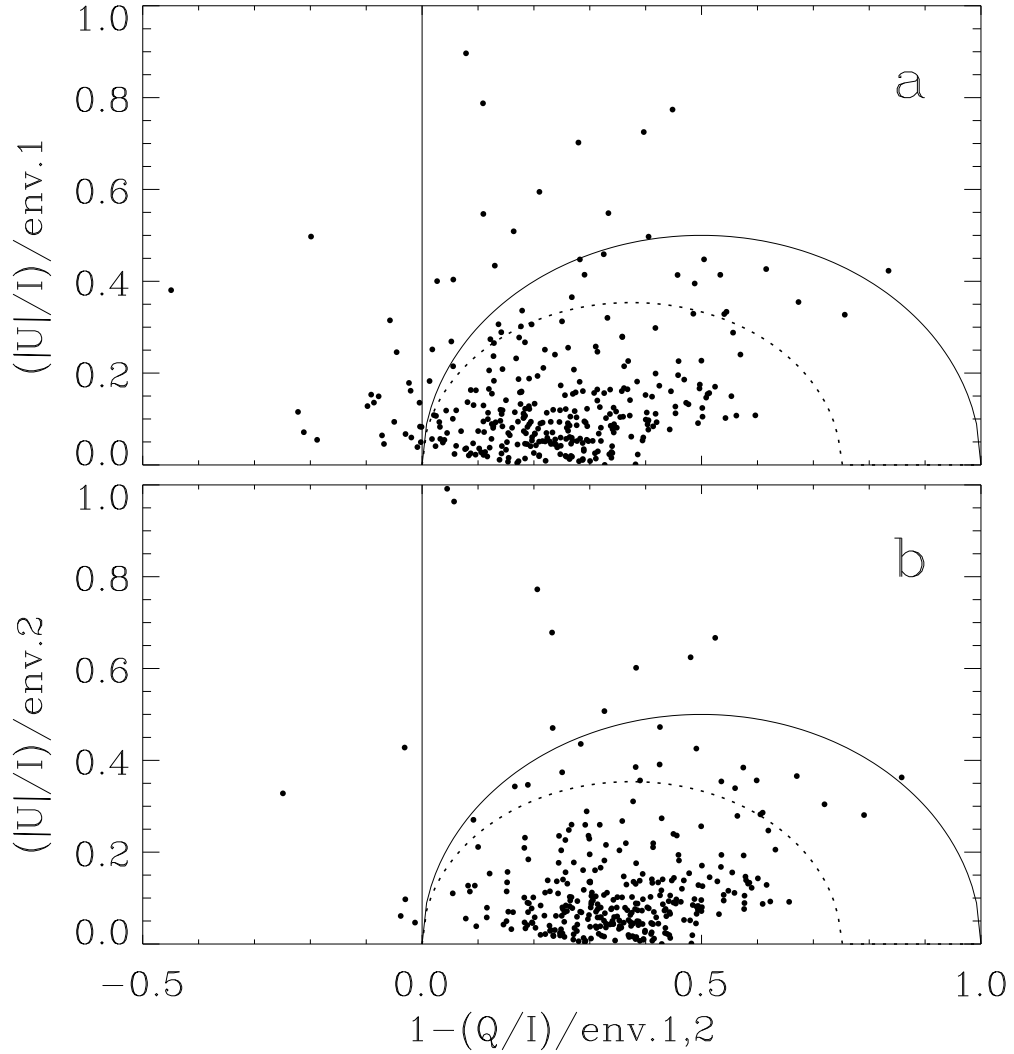
Figure 5.10: Scatter plot of Hanle rotation (here represented by $|U|/I$) vs. amount of Hanle depolarization (represented by $1 - (Q/I)/$env.). While the upper panel is based on the lower Q/I envelope (env. 1, solid curve in Fig. 5.3b), the lower panel is based on the higher envelope curve (env. 2, dotted curve in Fig. 5.3b). The solid and dotted curves are given by Eqs. (5.2) and (5.3), respectively, which are explained in the text.

5.3.4   Hanle rotation

If the directional distribution of the field vectors is not random within the spatial resolution element the Hanle effect may generate a Stokes U signal in the line core but not in the line wings, where the Hanle effect is absent. In Fig. 5.1c we saw examples of such observational signatures for the rotation of the plane of linear polarization due to the Hanle effect. If the angle of rotation is β, then $|\tan 2\beta| = |U|/Q$. Figure 5.9a shows a scatter plot of all the measured U/I amplitudes in the line core. For comparison the solid and dotted Q/I envelope curves from Fig. 5.3b are also plotted. In Fig. 5.9b we show the scatter plot of the $|U|/Q$ ratio. The trend is that the relative number of points with large rotation angles tends to increase as we move away from the limb. Geometric foreshortening may produce such a trend, because the effective spatial resolution is lower towards the limb, so that we have less resolved fields and therefore smaller net rotation angles there.

Figure 5.9 can be compared with the corresponding Fig. 4.7 of Chapter 4 for the Sr II observations, which however did not extend beyond a μ value of about 0.5, while our present data set for the Ca I line extends to $\mu \approx 0.85$ and represents a larger statistical sample.

As in Chapter 4 we next make scatter plots of the Hanle rotation vs. Hanle depolarization in Fig. 5.10 (which corresponds to Fig. 4.8 of Chapter 4). The Hanle rotation is represented by $|U|/I$, normalized to one of the Q/I envelopes of Fig. 5.3b. The amount of Hanle depolarization on the horizontal axis is represented by $1 - (Q/I)/\mathrm{env.}$ (i.e., one minus the values in Fig. 5.6). Env. 1, used for the top panel, refers to the solid envelope curve of Figs. 5.3b and 5.9a, while env. 2, used for the bottom panel, refers to the dotted envelope curve in those figures.

To get a better feeling for these diagrams, we have in Fig. 5.10, as we did in Chapter 4, plotted the functions

$$y = \sqrt{x(1 - x)} \tag{5.2}$$

as the solid curves, and

$$y = \sqrt{\tfrac{2}{3}x\left(1 - \tfrac{4}{3}x\right)}, \tag{5.3}$$

as the dotted curves. These curves represent the loci where the points would fall in the case of scattering at the extreme limb (approximat-
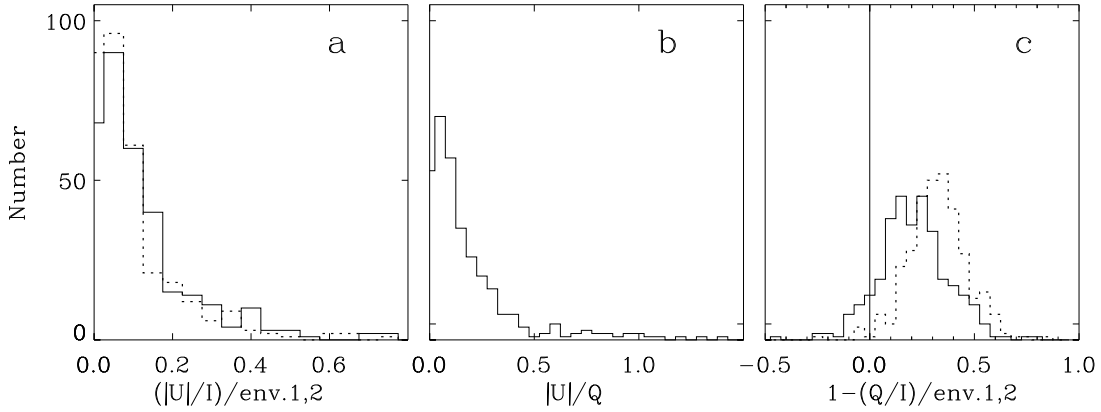
Figure 5.11: Hanle histograms, showing the distribution of the ob-
served parameters representing Hanle rotation (panels **a**
and **b**) and Hanle depolarization (panel **c**). Panel **a** repre-
sents the distribution of y values in Fig. 5.10, panel **b** the
y values in Fig. 5.9b, panel **c** the x values in Fig. 5.10. The
solid histograms are based on the lower (solid) Q/I en-
velope in Fig. 5.3b (env. 1), the dotted histograms on the
upper (dotted) Q/I envelope in Fig. 5.3b (env. 2).

ing the 90° scattering case) when the magnetic field lies in the hori-
zontal plane (canopy-type field). The solid curves correspond to the
case when the magnetic field vector is directed towards the observer,
while for the dotted curves the magnetic field is at an angle of 45° to
the line of sight (assuming that the magnetic field orientation remains
unchanged over the resolution element). The field strength increases
from zero as we move along the curves from left to right.

Maximum Stokes U polarization (due to Hanle rotation) should oc-
cur when the magnetic field is along the line of sight. Therefore we
would expect all points to fall below the solid curves in Fig. 5.10 in
the case of this model, which refers to $\mu = 0$. The great majority of
the points do indeed satisfy this expectation. The circumstance that
some points in the diagrams scatter outside the region bounded by
the solid curve may have different causes. One is the choice of the
non-magnetic Q/I envelope, as we see by comparing the top and bot-
tom panels of Fig. 5.10. Since the top panel is based on the lower of
the two envelope choices, we find more points that scatter outside the
bounded region as compared with Fig. 5.10b, which may suggest that

the higher envelope choice is to be prefered. Another cause is of course instrumental noise, so we need to allow for some noise spill-over into the "forbidden regime". However, the "allowed regime" expands into the previously "forbidden regime", in particular towards negative values of x, as we go to larger μ values, as was shown in Chapter 4 (e.g. in Fig. 4.11 of Chapter 4). Therefore we should not interpret the solid curve as a definite, sharp boundary (since it is based on a simplistic model with $\mu = 0$), but rather as an approximate tool to guide us in our overview of the data.

When there are unresolved magnetic fields with different orientations of the field vector within the spatial resolution element, there will be suppression of the U/I signal due to cancellation effects. This has the result that the distribution of U values tends to cluster towards a maximum near zero U, as evidenced by Fig. 5.10, where we find the majority of the points well below the dotted boundary, clustering towards the zero line for the Hanle rotation.

5.3.5   Hanle histograms

Since there is no clear correlation between the x and y values in Fig. 5.10, we may as in Chapter 4 make separate histograms for the distribution of x and y values. Thus Fig. 5.11a shows the distribution of y values (representing Hanle rotation), while Fig. 5.11c shows the distribution of x values (representing Hanle depolarization). Similarly, ignoring the possible, slight center-to-limb variation of the points in Fig. 5.9b, we have derived the distribution of the y values of that diagram ($|U|/Q$) and plotted it in Fig. 5.11b.

The derived Hanle histograms in Fig. 5.11 are practically identical to those previously derived for the Sr II line in Chapter 4. Thus the parameters representing Hanle rotation (panels a and b in Fig. 5.11) show a distribution that monotonically increases towards smaller rotation values. The amount of Hanle depolarization, however, has a distribution with a maximum centered around a non-zero value. The location of this maximum varies between a depolarization (x) value of 0.2 and 0.4, depending on the choice of non-magnetic Q/I envelope. The lower envelope choice (solid line) gives a distribution with more "spill-over" towards negative depolarization values. However,

this does not necessarily imply that this envelope choice should be rejected, since somewhat negative depolarization values are physically allowed for non-zero μ values (away from the extreme limb), and instrumental noise also contributes to such spill-over. In addition, radiative-transfer modelling by Faurobert-Scholl (1994) has shown that under certain circumstances, depending on the height of the magnetic canopy layer, the Hanle effect can enhance rather than diminish the polarization, which may also contribute to the "spill-over" in our diagram.

It is possible to calculate theoretical Hanle histograms from models of magnetic-field distributions, and then constrain these models by comparing the theoretical and observed histograms. Such a comparison was made in Chapter 4. As the present observational histograms are very similar to those of Chapter 4, we refer to this it for details and limit ourselves here to summarizing the conclusions that can be made.

For the interpretation of the histograms we need to conceptually distinguish between two classes of magnetic fields: those that are spatially resolved, and those that are unresolved. Most observations correspond to the intermediate regime of partially resolved fields, but to elucidate the main features of the physical situation it is useful to assume that we can decompose the field into two distinctly separate components. Resolved fields then refer to the component for which the field vector can be considered to have constant strength and direction within the spatial resolution element. The spatially unresolved component will for the present idealized discussion be represented by fields that have random orientations such that there is no net orientation when averaging over the resolution element.

With these definitions, if all the fields were spatially unresolved with no net orientation of the field, then there would still be Hanle depolarization, and Fig. 5.11c could be explained with the field-strength distributions that we actually derived in Fig. 5.8. However, this component would not contribute to any non-zero U values (Hanle rotation). The existence of an extended distribution of substantial Hanle rotation values (panels a and b in Fig. 5.11) can only be understood if there are contributions from (partially) resolved magnetic fields with a net orientation of the field vectors after averaging the contributions over the spatial resolution element. Contributions to this large-scale

field component may come from the general, background magnetic field on the Sun, or from a canopy-type field that remains coherent over scales comparable to the supergranulation.

It is outside the scope of the present work to try to derive more quantitative field-distribution models from the present Hanle histograms. Future observations with higher spatial resolution and with different spectral lines will help constrain the problem to enhance the diagnostic possibilities that the Hanle histograms offer.

5.3.6 Efficiency profile of the Hanle effect

According to theory the Hanle rotation and depolarization effects only occur in the Doppler core of spectral lines but not in their wings. In Chapter 4 we could for the first time (for the Sr II line) empirically verify this property and determine the shape of the Hanle efficiency profile. Now we do this again for the Hanle rotation effect in the Ca I 4227 Å line. The procedure is the following: We collect all the observations within the μ interval 0.10–0.25 for which we have recordings of both the Q and U line profiles, and for which the core peak value of $|U|/I$ exceeds 0.12 % . For these observations we then average the Q/I and $|U|/I$ spectra and form the ratio between the averaged $|U|/I$ and the averaged Q/I profiles. The result is plotted as the dashed curve in Fig. 5.12.

To compare the Ca I results with those of Sr II we have in Fig. 5.12 plotted as the dotted curve the Sr II efficiency profile from Fig. 4.13a of Chapter 4. Since we are here only interested in the relative profile shape, we rescale the dashed Ca I curve to get the solid curve that has the same amplitude as the dotted Sr II curve. The difference in amplitude between the dashed and dotted curves is not of interest here, since it is only partly due to a real difference in the distribution of rotation angles. It is also to a significant degree due to the particular way that we selected the U and Q recordings to construct the corresponding U/Q profile in Chapter 4.

Our results for Ca I are consistent with the theoretical expectation that the Hanle effect operates in the Doppler core but vanishes in the wings. We also notice that the Ca I profile is broader than that of Sr II. This width difference is expected and of the correct magnitude. It has
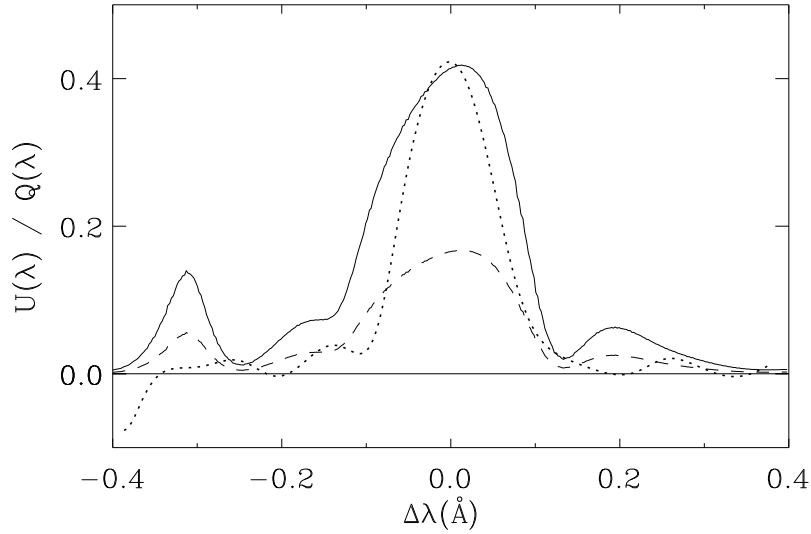
Figure 5.12: Efficiency profiles illustrating how the Hanle effect is con-
fined to the Doppler core of the line but vanishes in the
wings. The dashed and dotted curves represent the av-
erage U/Q ratios in the μ interval 0.10–0.25 for the Ca I
4227 Å line (from the present data) and for the Sr II 4078 Å
line (from Chapter 4), respectively. The solid curve repre-
sents the dashed curve scaled to have the same amplitude
as the dotted curve, to allow better comparison between
the line widths. The side lobes of the solid and dashed
curves are likely to be artefacts, because at these wave-
lengths Q/I is almost zero, which leads to great amplifi-
cation of the instrumental noise in U/Q.

two main causes: (1) The larger thermal broadening for atoms with
smaller atomic weight. This contribution to the width ratio scales with
the square root of the ratio between the atomic weights 87.6 of stron-
tium and 40.1 of calcium. (2) The wavelength difference. This con-
tribution to the width ratio scales linearly with the wavelength ratio
4227/4078 for the two lines.

The side lobes seen in the wings of the Ca I profile in Fig. 5.12 are
most likely due to instrumental noise, since they occur around the
wavelengths, where Stokes Q is very small or even has a zero crossing,
as seen from Figs. 5.1b and 5.5. Instrumental noise in Q will greatly
magnify the errors in the U/Q ratio at places where Q is small. These

places, and thus the spurious side lobes, should therefore be ignored in Fig. 5.12.

5.4   Concluding remarks

In the present Chapter we have extended the exploration of the Hanle effect in quiet solar regions in the Ca I 4227 Å line that we began in Chapter 3 by recording a large number of both Stokes Q and U profiles, which allows us to study the effect of Hanle rotation, to construct Hanle histograms for rotation and depolarization, and to determine the Hanle efficiency profile. A similar extension has been done in Chapter 4 for the Sr II 4078 Å line. A more complete comparison between the behavior of the Hanle effect in these two lines is therefore now possible.

We have in addition developed a special technique to determine the usually so elusive true zero point of the polarization scale, and have used this information to show how intrinsically negative Q/I polarizations (with the plane of linear polarization perpendicular to the limb) occur at certain places within the Ca I line profile, and how this intriguing polarization varies with center-to-limb distance (all the way to $\mu \approx 0.85$). The explanation of these center-to-limb curves will be a future challenge for partial redistribution physics in polarized radiative transfer.

The comparison between the results in the Ca I and Sr II lines shows very good qualitative agreement, but there are also some indications of systematic, quantitative differences. As in our previous investigations with the Hanle effect we find that the field strength distributions peak approximately in the range 5–10 G, but the apparent field strengths found with the Sr II line tend to be somewhat smaller than those found with the Ca I line. As explained at the end of Sect. 5.3.3, a possible interpretation of this difference could be in terms of the height variations of the field inclination and filling factor, combined with the difference in height of formation of the two lines. There is also a tendency for the rotation angles to be smaller for the Ca I line as compared with the Sr II line.

The histograms of Hanle rotation and depolarization can only

be consistently explained if there is a mixture of contributions from both partially resolved and unresolved fields with mixed orientations within the spatial resolution element. Since our present spatial resolution is quite low (on the order of 20 arcsec in the slit direction) because of the observational trade-off with polarimetric accuracy, it is not surprising that there is a major component of spatially unresolved magnetic fields of mixed orientations in our data, but it is also interesting that we with the present Hanle technique can diagnose the weak, large-scale component of the field as well. With increasing spatial resolution a larger proportion of the field structures can be resolved, and this can be expected to change the character of the observed Hanle histograms. We believe that this dependence on spatial resolution may have considerable diagnostic potential.

Ideally, it is therefore desirable to carry out the Hanle observations with the highest possible spatial resolution, for similar reasons as we need high spatial resolution in Zeeman-effect observations. Because of the weak signals involved, there will always have to be trade-offs between the polarimetric accuracy and the spatial, spectral, and time resolutions, even with the largest, future solar telescopes (cf. Stenflo 1999), but with increasing telescope aperture these scientific compromises will become less restrictive.

Bibliography

Faurobert-Scholl, M., 1992, *"Hanle effect with partial frequency redistribution. II. Linear polarization of the solar Ca I 4227 Å line"*, Astron. Astrophys. **258**, 521

Faurobert-Scholl, M., 1994, *"Hanle effect of magnetic canopies in the solar chromosphere"*, Astron. Astrophys. **285**, 655

Povel, H., 1995, *"Imaging Stokes polarimetry with piezoelastic modulators and charge-coupled-device image sensors"*, Optical Engineering **34**, 1870

Rees, D. E., Saliba, G. J., 1982, *"Non-LTE resonance line polarization with partial redistribution effects"*, Astron. Astrophys. **115**, 1

Saliba, G. J., 1985, *"Non-LTE resonance line polarization with partial redistribution - The solar Ca II K line"*, Sol. Phys. **98**, 1

Semel, M., 1995, *Zeeman Doppler Imaging*, in *ASP Conf. Ser. 71: IAU Colloq. 149: Tridimensional Optical Spectroscopic Methods in Astrophysics*, 340

Semel, M., Donati, J.-F., Rees, D. E., 1993, *"Zeeman-Doppler imaging of active stars. 3: Instrumental and technical considerations"*, Astron. Astrophys. **278**, 231

Stenflo, J. O., 1999, *"Solar magnetism and the second solar spectrum: Future directions"*, in K. N. Nagendra, J. O. Stenflo (eds.), *"Solar Polarization, proc. 2nd SPW"*, vol. 243 of *"ASSL"*, 1, Kluwer, Dordrecht

Stenflo, J. O., Keller, C. U., Gandorfer, A., 1998, *"Differential Hanle effect and the spatial variation of turbulent magnetic fields on the Sun"*, Astron. Astrophys. **329**, 319

Chapter 6

Observations of the Hanle effect in the Ca I 4227 and Sr II 4078 Å lines [*]

M. Bianda[1], J.O. Stenflo[2] and S.K. Solanki[2]

Abstract

The Hanle effect in the second solar spectrum has been explored with a beam splitter based polarimeter at IRSOL in Locarno. It is the only existing imaging solar polarimeter system that is sensitive to the ultraviolet part of the spectrum, where the scattering-polarization effects are the largest. We discuss results of full vector polarimetry (all four Stokes parameters) in the Ca I 4227 and Sr II 4078 Å lines in quiet and active solar regions, and show how the signatures of Hanle depolarization in Stokes Q, Hanle rotation in Stokes U, and the longitudinal Zeeman effect in Stokes V can exhibit strong spatial variations over a few arcsec. We further illustrate how the Hanle observations can be used to derive information on both the spatially unresolved and partially resolved weak magnetic fields outside the supergranulation network.

6.1   Introduction

In Chapters 3 and 4 we have embarked on a program to explore the Hanle effect in the second solar spectrum with the polarimeter system at IRSOL in Locarno. In Chapter 3 we described the observational technique in detail and reported on observations of Hanle depolarization effects in the Stokes Q/I profiles of the Ca I 4227 Å line. In Chapter 4 we turned to the Sr II 4078 Å line and extended the previous work by exploring also the Hanle rotation of the plane of polarization in Stokes U/I. Histograms of the distributions of the observed Hanle depolarizations and rotations were presented, and it was indicated how these histograms could be interpreted and understood in terms of the combined contributions from both spatially unresolved and partially resolved magnetic fields.

In the present work we compare the results from the Ca I and Sr II lines and go one step further by presenting new Ca I observations in all four Stokes parameters, both in quiet and active regions, illustrating how the Hanle and Zeeman effects combine, and how they can exhibit strong spatial variations over a few arcsec.

6.2   Observational technique

All our observations have been carried out with the Gregory-Coudé telescope at IRSOL in Locarno and a beam-splitter polarimeter system based on the design concept proposed by Donati et al. (1990) and Semel et al. (1993) for stellar polarimetry. A wave plate (either a $\lambda/2$ or a $\lambda/4$ plate) followed by a polarizing calcite beam splitter immediately in front of the spectrograph slit produces two images in orthogonal polarizations. With four settings of the $\lambda/2$ plate we obtain $I \pm Q$, $I \mp Q$, $I \pm U$, and $I \mp U$. Two settings of the $\lambda/4$ plate give $I \pm V$ and $I \mp V$.

We need two image pairs, i.e., four images, for each of the Q, U, and V parameters to be able to extract images of the fractional polarization Q/I, U/I, and V/I that are free to first order from *both* seeing and gain table effects. As these two effects are the main sources of spurious polarization features, we obtain a system that is basically limited by photon statistics down to noise levels as low as 10^{-4}. It is here

very essential how the four images of the image pair are combined. To eliminate the gain-table noise, the crucial trick is to form *ratios* rather than differences between the four images in a very special way, as described in great detail in Chapter 3. With the present IRSOL system we reach an accuracy of about 3×10^{-4} in the degree of polarization in vector polarimetry combined with high spectral resolution, if we average spatially along the 18 arcsec portion used along the slit to improve the photon statistics.

Figure 6.1 shows an example of the fractional polarization profiles Q/I, U/I, and V/I recorded in a quiet region near the solar limb in the Ca I 4227 Å line. The Q/I profile (solid line) has the characteristic shape known from early observations (e.g. Stenflo et al. 1980; Stenflo (1982)), with polarization peaks in the line core and the wings. While the wing peaks are unaffected by the Hanle effect, the relative amplitude of the core peak fluctuates as a result of Hanle depolarization due to varying magnetic fields (cf. Chapter 3). The small core polarization peak in U/I (dotted curve) is a typical signature of Hanle rotation of the plane of linear polarization due to partially resolved magnetic fields, here most probably canopy-type fields in the lower chromosphere (cf. Faurobert-Scholl 1992; 1994). There is no significant signal in V/I.

A major disadvantage of the beam splitter system as compared with ZIMPOL II (Stenflo et al. 1992; Gandorfer & Povel 1997) is that six separate exposures are needed to recover the full Stokes vector, while ZIMPOL II does it in a single exposure. With ZIMPOL II all the Stokes images have identical seeing distortions and use the identical pixels, so the four Stokes images can be perfectly superposed and combined without the need for any destretching whatsoever. In contrast, although the three polarization images Q/I, U/I, and V/I derived from the beam splitter observations do not contain seeing-induced spurious polarization features, the seeing distortions and blurring of the polarization structures will be different in the three fractional polarization images, which causes problems when one wants to combine them to a single Stokes vector image. However, this becomes a major problem only when the polarimetry is combined with high spatial resolution. As we in the present paper do spatial averaging over several arcsec or more, it is not a concern for us right now.
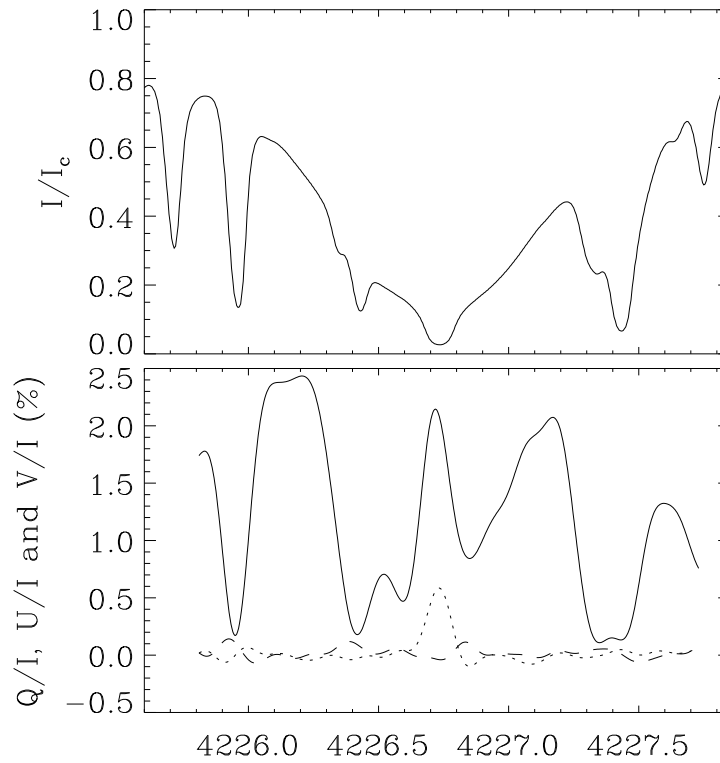
Figure 6.1: Examples of Stokes line profiles in the Ca I 4227 Å line. The upper panel shows the intensity profile at disk center, while the bottom panel shows the fractional polarization profiles Q/I (solid), U/I (dotted), and V/I (dashed) recorded in a quiet solar region near the limb, at $\mu = \cos\theta = 0.1$ (θ is the heliocentric angle). The U/I core peak is caused by Hanle rotation of the plane of polarization, most likely due to chromospheric canopy fields.

The main advantage of the beam splitter system with respect to ZIMPOL is that the current versions of ZIMPOL are not sensitive to wavelengths below about 4500 Å, while the IRSOL polarimeter does not have such a limitation but can be used down to the atmospheric cut-off in the ultraviolet. As the amplitudes of the scattering polarization features in the second solar spectrum increase substantially as we go towards shorter wavelengths, the region below 4500 Å is the most fertile domain of scattering physics, and the IRSOL system is currently the only existing imaging solar polarimeter that gives us access to this rich and largely unexplored world of solar physics.

6.3   Results for the quiet Sun

We have made a large number of recordings of the scattering polarization in the Ca I 4227 and Sr II 4078 Å lines in different solar regions, at various latitudes, center-to-limb distances, and times. Usually the observations have been made around the spring or fall equinox, when the instrumental polarization of the Gregory-Coudé telescope is minimal. In Chapter 3 the Q/I profiles (with Q defined as the linear polarization oriented parallel to the nearest solar limb) of the Ca I line were analyzed, in Chapter 4 the behavior of the Q/I and U/I profiles of the Sr II line were explored.

Both the Ca I and Sr II lines have polarization peaks in the line core as well as in the blue and red line wings. While the ratio between the Q/I peak amplitudes in the red and blue wings do not exhibit spatial variations, the ratio between the core peak and the wing peaks fluctuates greatly. The only known explanation for this behavior is that we have varying amounts of Hanle depolarization in the line core due to spatially varying magnetic fields, while the wing peaks are unaffected by the Hanle effect (because of the influence of the anomalous-dispersion part of the complex Voigt function, as explained in Stenflo 1998). This interpretation is supported by the observed U/I profiles, which exhibit both positive and negative core peaks but no polarization outside the core, as expected from the Hanle rotation effect.

In a regression analysis of Q/I core vs. wing peak amplitude we thus ascribe the scatter as due to varying Hanle depolarization. The magnitude of the depolarization is the ratio between the observed core amplitude and the value that this amplitude would have in the absence of magnetic fields. This non-magnetic reference value is estimated from the observations as the upper envelope to the points in the scatter-plot diagram of core vs. wing polarization, as described in detail in Chapters 3 and 4. The definition of the exact position of this envelope introduces a certain element of subjectivity, which we take into account by considering extreme choices of such envelopes.

With a given envelope we have well-defined observed values of the Hanle depolarization, which next should be converted into field strengths. For this conversion we need to introduce a model for the spatially unresolved magnetic fields that may reproduce the observed

depolarization. The present observations only allow such models to be characterized by one free parameter (since we only have one observable, the amount of depolarization).

The kG magnetic fields in the photospheric network do not significantly affect or contribute to the Hanle signal, for three reasons: (i) The Hanle effect is insensitive to vertical magnetic fields, and the network fields are predominantly vertical in the photospheric layers. (ii) The photospheric network fields have a small filling factor (typically 1 %), in contrast to the much weaker fields in the remaining 99 % of the volume, which also contribute to the Hanle depolarization (since the depolarization only comes with one sign, in contrast to the Zeeman effect, for which the contributions from opposite polarities cancel each other). (iii) The kG field strengths fall in the saturated, strong-field Hanle regime. In contrast, the results from the Hanle observations show that much weaker fields that fall in the optimum sensitivity range for the Hanle effect are main contributors.

The conclusion from these considerations is that the contributions to the Hanle observations come either from the chromosphere, where the field is weaker and inclined (canopy like), or from the non-network portion of the photosphere, or from a combination of the two, depending on the height of line formation. The chromospheric contributions become larger close to the solar limb, while the photospheric contributions increase in importance as we move away from the limb.

We have chosen two types of models for the spatially unresolved magnetic fields to interpret the Hanle depolarization data: (1) A canopy-type model, representative of the chromospheric contributions, for which it is assumed that the field vectors are confined to the horizontal plane but have random orientations. (2) A "turbulent" field model, representative of the photospheric contributions, with the assumption that the orientations of the field vectors have an isotropic distribution. In both cases it is assumed that the field strength is single-valued (the only free parameter of the model), and that the filling factor is unity (for interpretative models where the filling factor is allowed to be a second free parameter, see Stenflo 1999).

Figure 6.2 gives the histograms of the field strengths that have been extracted from the Hanle depolarizations observed in the Ca I (solid) and Sr II (dotted) lines. In the left panels the canopy field model has
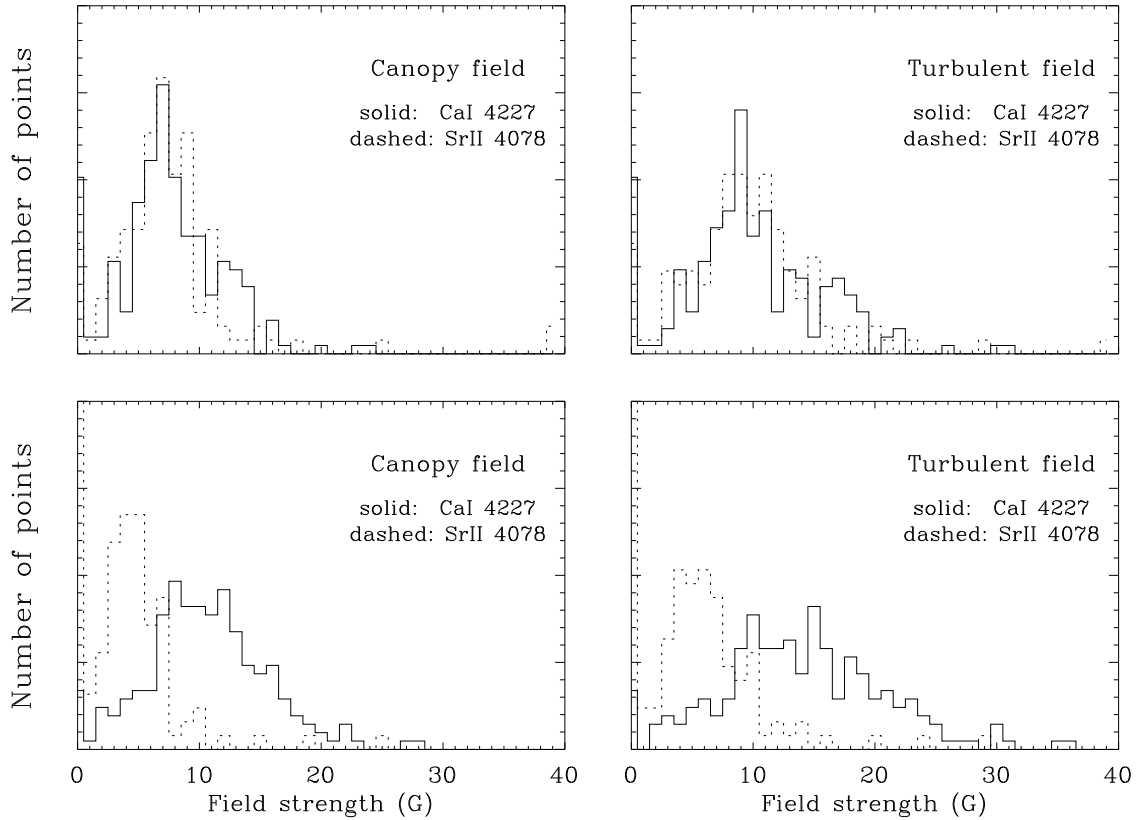
Figure 6.2: Histograms of field strengths, derived from our observations of the Hanle depolarization, using a canopy-field model (left panels) and a turbulent field model (right panels) and two different choices for the envelopes that represent the non-magnetic core polarization (upper and lower panels). The Ca I histograms are based on 207 recordings, the Sr II histograms on 126 recordings. For details, see text.

been used for the interpretation, in the right panels the turbulent field model. The upper and lower panels represent two extreme choices of envelopes used to characterize the non-magnetic core polarization amplitude as described above. The two upper panels represent the "best" choice in our judgement, while the lower panels represent extreme choices that are less likely but still barely admissible in view of the observational uncertainties. The difference between the upper and lower panels gives an impression of the degree of uncertainty in the derivation of the field strengths, within the framework of the magnetic field models used.

The results obtained with the two spectral lines are consistent with each other within the observational and interpretative uncertainties. An additional uncertainty that enters into the derivation of the field strengths is the collisional depolarization factor (for which we have used crude estimates in the absence of radiative-transfer calculations). Real differences between the histograms may also be caused by the difference in height of formation of the two lines, which then sample regions in the solar atmosphere in which the field strength may be systematically different.

Our canopy and turbulent models with random distributions of the field vectors within each spatial resolution element would for symmetry reasons predict that U/I, representing polarization at 45° with respect to the nearest solar limb, would always be zero. Our observations presented in Chapter 4 of U/I in the Sr II line however show many cases with a clear core polarization signal in U/I, as expected if there is Hanle rotation of the plane of polarization. An example of such a U/I core peak was shown in Figure 6.1 for the Ca I line. Such a signal can only occur if there is a *net* orientation of the field vectors when integrated over the spatial resolution element, i.e., if the magnetic field is at least partially resolved.

In Chapter 4 we presented histograms of the observed U/I polarizations and the Q/I depolarizations in the Sr II line, and discussed how such Hanle histograms need to be interpreted in terms of combined contributions from both spatially unresolved and partially resolved magnetic fields, and how they may be used to model and constrain the field strength and geometry. Since then we have obtained a considerable number of new observations of U/I (and Q/I) in the Ca II line as well (an example of which was shown in Figure 6.1), which will enhance the observational constraints that we can use for such modelling.

6.4 Results for active regions

When we go to active regions it becomes essential to also measure the circular polarization V/I and keep full control of the instrumental polarization. We have done some test observations of the full Stokes vec-

tor in active regions, which illustrate the combined Hanle and Zeeman effects and their large spatial variations over small scales. For more systematic observations of active regions, including spatial mapping, we need to introduce an image rotator to compensate for the rotation of the solar image, and to re-aluminize the two $45°$ mirrors to try to make the telescope as polarization free as it should be according to theory.

Figure 6.3 gives examples of the different types of Ca I Stokes profiles that one encounters in active regions. The top panel shows the disk center intensity, while the three lower panels give the Q/I (solid), U/I (dotted), and V/I (dashed) profiles in three different active regions, chosen to illustrate different cases of behavior. The second panel shows a region with very strong longitudinal Zeeman effect (V/I), combined with a strong U/I Hanle rotation signal and Q/I scattering polarization, all of comparable magnitude. The third panel shows a region with extreme Hanle depolarization (Q/I core peak absent), combined with almost no U/I and V/I signals. Finally the bottom panel shows a region with both large Hanle depolarization and moderately large longitudinal Zeeman effect, but with no Hanle rotation. Note that the scales of the polarization diagrams are different, since the regions were located at different center-to-limb distances.

The very different Hanle and Zeeman signatures in the Q/I, U/I, and V/I parameters allow us to identify and remove the instrumental cross talk between the Stokes parameters. All the polarized profiles presented here have been corrected for such instrumental cross talk. These examples show that it is possible to remove the instrumental polarization in the data analysis, although the observations have been carried out with a telescope that is not polarization free.

In the previous figures we have ignored spatial variations along the spectrograph slit and integrated over the 18 arcsec field covered by the slit to improve the S/N ratio. In active regions, however, large spatial fluctuations of the Stokes vector line profiles can occur on small scales, down to the spatial resolution limit. When exploring such effects one has to make a trade-off between spatial resolution and polarimetric accuracy, since increased spatial resolution means smaller S/N ratio. The results presented in Figure 6.4 have been derived from one recording in an active region, for which we have divided the 18 arcsec long slit
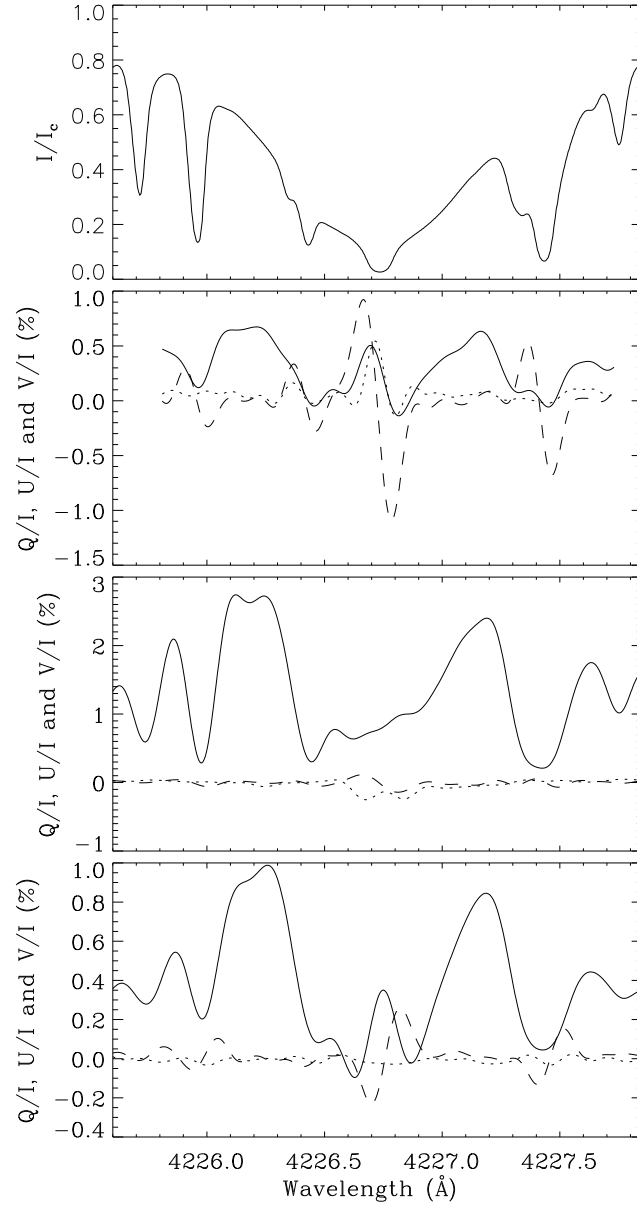
Figure 6.3: Examples of the various types of Stokes Ca I line profiles that we encounter in active regions. While the top panel shows the intensity profile at disk center, the three bottom panels show the Q/I (solid), U/I (dotted), and V/I (dashed) profiles for three different active regions.
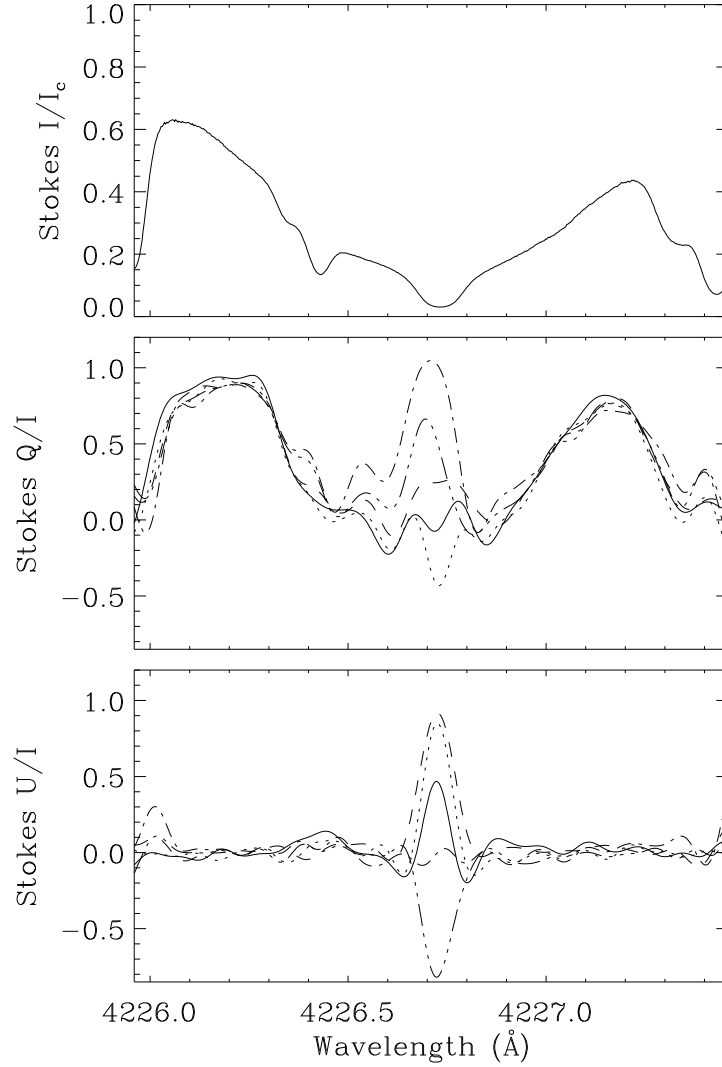
Figure 6.4: Illustration of spatial variations of the Hanle effect in the Ca I 4227 Å line along the spectrograph slit in an active region. The slit has been divided into five 3.6 arcsec sections. The five curves in each of the two bottom panels show the Q/I and U/I line profiles of these sections, demonstrating how the Hanle depolarization (in Q/I) and rotation (in U/I) effects exhibit large fluctuations over scales of a few arcsec. The top panel shows the intensity profile at disk center for reference.

portion in five sections of 3.6 arcsec each, and derived averaged Stokes line profiles for each of these five sections. The three Stokes parameters I, Q, and U were recorded. The five slit sections are represented by the sequence of solid, dotted, dashed, dash-dot, and dash-dot-dot-dot curves. We see that while the wing polarization remains invariant, the core polarization changes dramatically, with sign reversal in U/I, over a few arcsec. This example demonstrates the pronounced spatial structuring of the Hanle effect due to changing magnetic-field geometry and strength over small scales.

6.5   Outlook

The results that we have presented show that a simple non-modulating, beam-splitter based polarimeter system at a solar telescope of intermediate size can deliver a spectro-polarimetric accuracy that is sufficient for many scientific programs for vector polarimetry of the second solar spectrum to make combined diagnostic use of the Hanle and Zeeman effects. Although such a system has the disadvantage that all the three polarized Stokes parameters Q/I, U/I, and V/I are not recorded simultaneously on the same detector area, in contrast to the ZIMPOL II system, the performance is sufficient for systematic Hanle-Zeeman diagnostic work in strongly polarizing scattering lines like the Ca I 4227 and Sr II 4078 Å lines that we have used here. The great majority of these strongly polarizing lines are found in the blue or ultraviolet portion of the spectrum, which is not accessible by existing versions of the ZIMPOL system. The IRSOL polarimeter is the only existing observing system that allows high-precision imaging polarimetry in this most important part of the second solar spectrum.

Our observations of both the Hanle rotation and depolarization effects in a large number of solar regions have allowed us to construct various "Hanle histograms", which contain information on the distributions of both spatially unresolved and partially resolved magnetic fields not accessible by the usual Zeeman effect. In particular we are able to diagnose the canopy and turbulent magnetic fields outside the network.

Vector polarimetry of scattering lines in active regions illustrate

how the Hanle and Zeeman signatures combine, and how they exhibit large fluctuations over spatial scales of a few arcsec or less. This shows that we in the future need to produce high-resolution spatial maps of the Hanle and Zeeman effects, which can then be used as powerful observational constraints on the magnetic field structure. Such observing programs force us to make difficult trade-offs between spatial resolution and polarimetric accuracy. Such trade-offs would of course be less severe with larger telescopes, but they will always be necessary. The accurate removal of instrumental polarization cross talk will remain a challenge, which however can be overcome. The theoretical interpretation of the data is far from straightforward, but the theoretical tools are being developed.

In conclusion, the use of the second solar spectrum for combined Hanle-Zeeman diagnostics of solar magnetic fields is a new and promising area that has just opened up. Pioneering work in this area is possible with simple and cheap polarimeter systems.

Bibliography

Donati, J.-F., Semel, M., Rees, D. E., Taylor, K., Robinson, R. D., 1990, *"Detection of a magnetic region on HR 1099"*, Astron. Astrophys. **232**, L1

Faurobert-Scholl, M., 1992, *"Hanle effect with partial frequency redistribution. II. Linear polarization of the solar Ca I 4227 Å line"*, Astron. Astrophys. **258**, 521

Faurobert-Scholl, M., 1994, *"Hanle effect of magnetic canopies in the solar chromosphere"*, Astron. Astrophys. **285**, 655

Gandorfer, A. M., Povel, H. P., 1997, *"First observations with a new imaging polarimeter"*, Astron. Astrophys. **328**, 381

Semel, M., Donati, J.-F., Rees, D. E., 1993, *"Zeeman-Doppler imaging of active stars. 3: Instrumental and technical considerations"*, Astron. Astrophys. **278**, 231

Stenflo, J. O., 1982, *"The Hanle effect and the diagnostics of turbulent magnetic fields in the solar atmosphere"*, Sol. Phys. **80**, 209

Stenflo, J. O., 1998, *"Hanle-Zeeman scattering matrix"*, Astron. Astrophys. **338**, 301

Stenflo, J. O., 1999, *"Solar magnetism and the second solar spectrum: Future directions"*, in K. N. Nagendra, J. O. Stenflo (eds.), *"Solar Polarization, proc. 2nd SPW"*, vol. 243 of *"ASSL"*, 1, Kluwer, Dordrecht

Stenflo, J. O., Baur, T. G., Elmore, D. F., 1980, *"Resonance-line polarization. IV. Observations of non-magnetic line polarization and its center-to-limb variations"*, Astron. Astrophys. **84**, 60

Stenflo, J. O., Keller, C. U., Povel, H. P., 1992, in *"LEST Foundation Techn. Report No. 54"*, Inst. Theoret. Astrophys., Univ. of Oslo

Chapter 7

Enigmatic magnetic field effects in the scattering polarization of the Ca I 4227 Å line [*]

M. Bianda[1], J.O. Stenflo[23], A. Gandorfer[2] and D. Gisler[2]

Abstract

The scattering polarization of the Ca I 4227 Å line shows unexpected behavior in the presence of magnetic fields. Standard theory predicts the Hanle effect to be present in the line core, while it should disappear in the wings, where pure, non-magnetic scattering polarization is expected. Observations show however that even in the wings, far from the core, depolarization and rotation of the plane of linear polarization are sometimes present, in apparent contradiction with Hanle-effect theory.

7.1　Introduction

The observations were carried out with the 45 cm Gregory-Coudé telescope of IRSOL in Locarno (Switzerland) using the new UV-sensitive version of the ZIMPOL II polarimeter developed at the Institute of Astronomy of ETH Zurich The very fast polarization modulation of the beam (42 kHz for the circular polarization, 84 kHz for Stokes Q) effectively freezes the seeing to allow high precision polarization measurements (down to 10^{-5} in the degree of polarization). The initial aim of the observations was to confirm previous results obtained with a Semel-type double beam polarimeter, which showed Hanle effect signatures close to the limb. We here report unexpected results in active regions near the limb.

7.2　Observations

The observations were carried out in November and December 2001 with a set-up similar to the one used by Gandorfer (2000) for his atlas. The main difference was our use of a new UV-sensitive camera and new telecentric reduction optics with better transmission in the near UV. The modulator package consists of a piezoelastic modulator made from fused silica, and a Glan linear polarizer. The calibration optics for the violet part of the spectrum were not available at the time of these observations. Despite of this, the data could still be calibrated, as will be described below.

To avoid image drifts during the observations, the Primary Image Guider (PIG) was used (Küveler et al. 1998) in combination with a secondary image stabilizer (Sütterlin et al. 1997) The slit width of 200 μm corresponds to 1.6 arcsec. The spatial dispersion is 2.31 arcsec per pixel.

The exposure time was 5 s per frame. 16 such frames were added to obtain a stored image. A two phase observing mode was used to correct for charge pocket effects in the CCD (cf. Gandorfer and Povel 1997 for details). One PEM modulator modulates one component of the linear and circular polarization simultaneously, but not Q/I and U/I simultaneously. An observation therefore consists of the following

steps: After a recording of Q/I and V/I, the modulator package is rotated by $45°$ to record Stokes U/I and V/I. This is repeated 4 to 6 times, to increase the statistics. 100 dark frames, recorded with the same exposure time as used for the limb observations, are averaged to obtain the dark current image.

Two kinds of observation were done: (1) with the solar limb parallel to the spectrograph slit, to keep $\mu = \cos\theta$ constant along the slit, and (2) with the solar limb perpendicular to the slit, to directly obtain the center-to-limb variation of the different parameters.

7.3 Data reduction

The reduction of the ZIMPOL data is described in Gandorfer et al. (2002). To correct for cross talk the symmetry properties of the Zeeman signatures, combined with qualitative knowledge about the Hanle signatures, was used, as described in Stenflo et al. (2001). In some cases, as will be discussed later, Q/I signatures persist in U/I even after cross talk correction and cannot be explained in terms of instrumental effects.

Figure 7.1 gives an example of an observation, after cross-talk correction and wavelet smoothing of the four bidimensional Stokes images.

As mentioned in the previous section, the appropriate calibration UV optics were not available at the time of observation. To determine the polarization scale the center-to-limb variation (CLV) of the blue Q/I wing was scaled to fit the curve obtained with Eq. (5.1) in Chapter 5, i.e., $Q/I = a(1 - \mu^2)/(\mu + b)$ with $a = 0.33\%$ and $b = 0.002$. In Figure 7.2 the analytical (dot-dashed) and the observed and scaled Q/I blue wing (solid line) CLV profiles are shown.

7.4 Results

Figure 7.1 shows a recording in an active region, obtained on December 19, 2001. The slit was perpendicular to the limb. The Stokes I panel shows the Ca I line with the blends. As the zero point of the
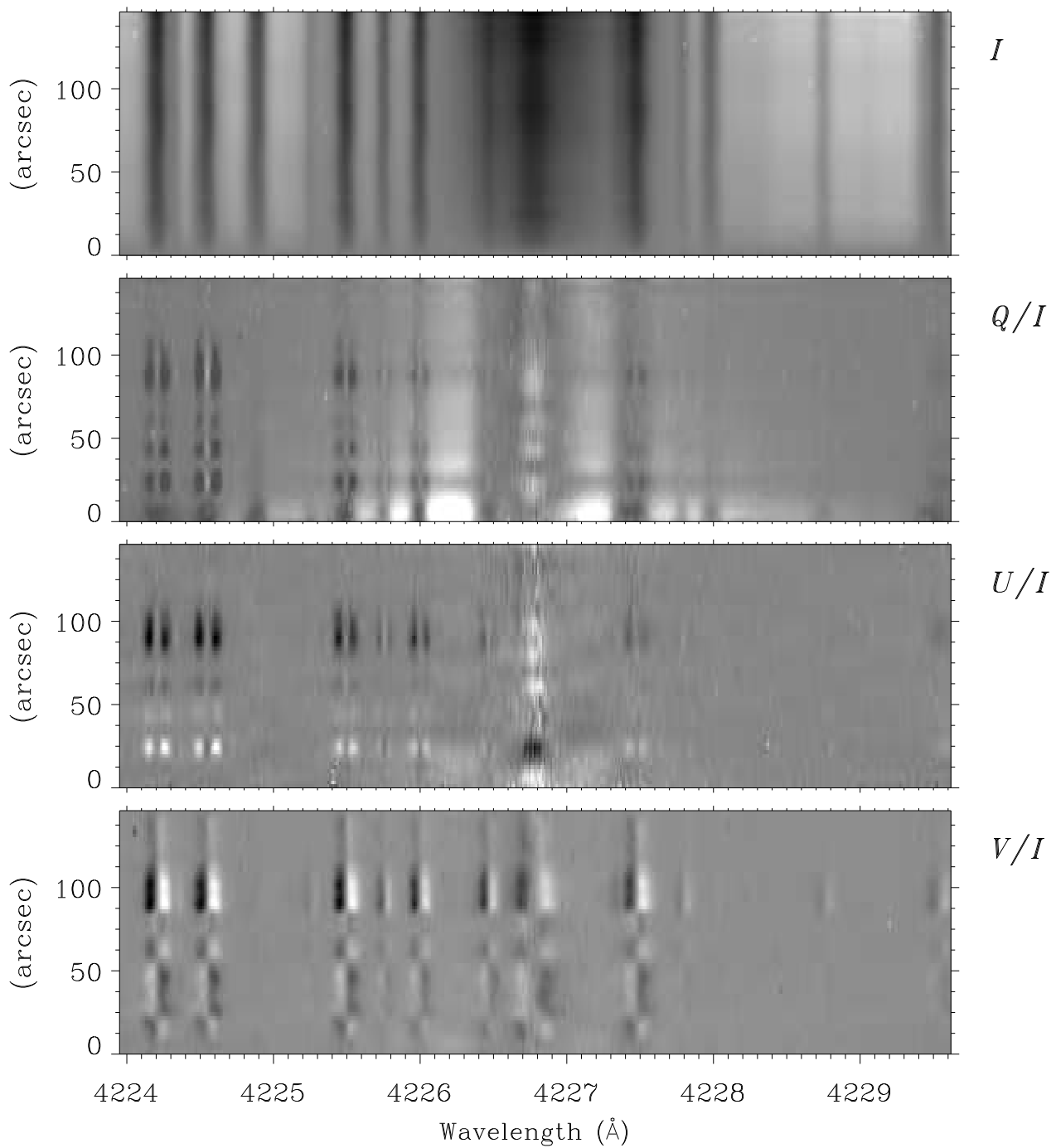
Figure 7.1: Images of the four Stokes parameters recorded with the spectrograph slit perpendicular to the limb. The zero point of the spatial scale corresponds to the solar limb. The field of view thus extends 150 arcsec inside the limb.

spatial scale is at the limb, we can follow the CLV of the Stokes parameters 150 arcsec towards disk center. The Q/I linear polarization panel (white means polarization parallel to the solar limb) shows the expected strong increase towards the limb of the non-magnetic polarization in the Ca I wings and the transverse Zeeman effect patterns in the blend lines (except for the CH 4224.86 Å line, which only depolarizes near the limb). The core polarization is changing irregularly along the spatial direction, as expected from Hanle depolarization, due to local fluctuations of the magnetic field. The unexpected feature is the horizontal depolarizing strip 25 arcsec inside the limb, as will be discussed later. The U/I panel (linear polarization oriented $45°$ to the limb) shows transverse Zeeman patterns in the blend lines, as well as polarization in the Ca I line center caused by Hanle rotation of the plane of polarization. Note the qualitative difference between these Zeeman and Hanle signatures. Again we see enigmatic strips in the wings, which need to be explained. The V/I panel shows longitudinal Zeeman patterns but with absence of any signature in the CH line. Some minor artifacts introduced by the wavelet smoothing are present as minor striations in the core peak of the U/I panel.

Figure 7.2 shows the CLV of Q/I for the blue wing maximum (solid line) and the core peak (dotted line), while the dot-dashed line represents the analytical function mentioned in Sect. 7.3. We notice a large blue wing depolarization around $\mu \approx 0.22$, and possibly a small depolarization around $\mu \approx 0.42$. The wavelength variation of this Q/I depolarization is shown in Figure 7.3. The depolarization feature seen in Figure 7.2 is not an isolated case, but is confirmed by observations made in other active regions.

Spatial variations of the polarization peak at line center in active regions have been seen in previous observations with the double beam polarimeter (Chapter 6). In quiet regions the ratio between the Q/I line center peak and the blue wing maximum was found to always be less than one (Chapter 3) the line center value at $\mu = 0.4$ is larger than expected: here we have an enhancement that is cospatial with the magnetic region in Figure 7.1 at 80 arcsec from the limb (which corresponds to $\mu = 0.4$). A general and systematic correspondence between depolarization in the wings and the line center peak amplitude was not found, although there seemed to be a relation in most of our
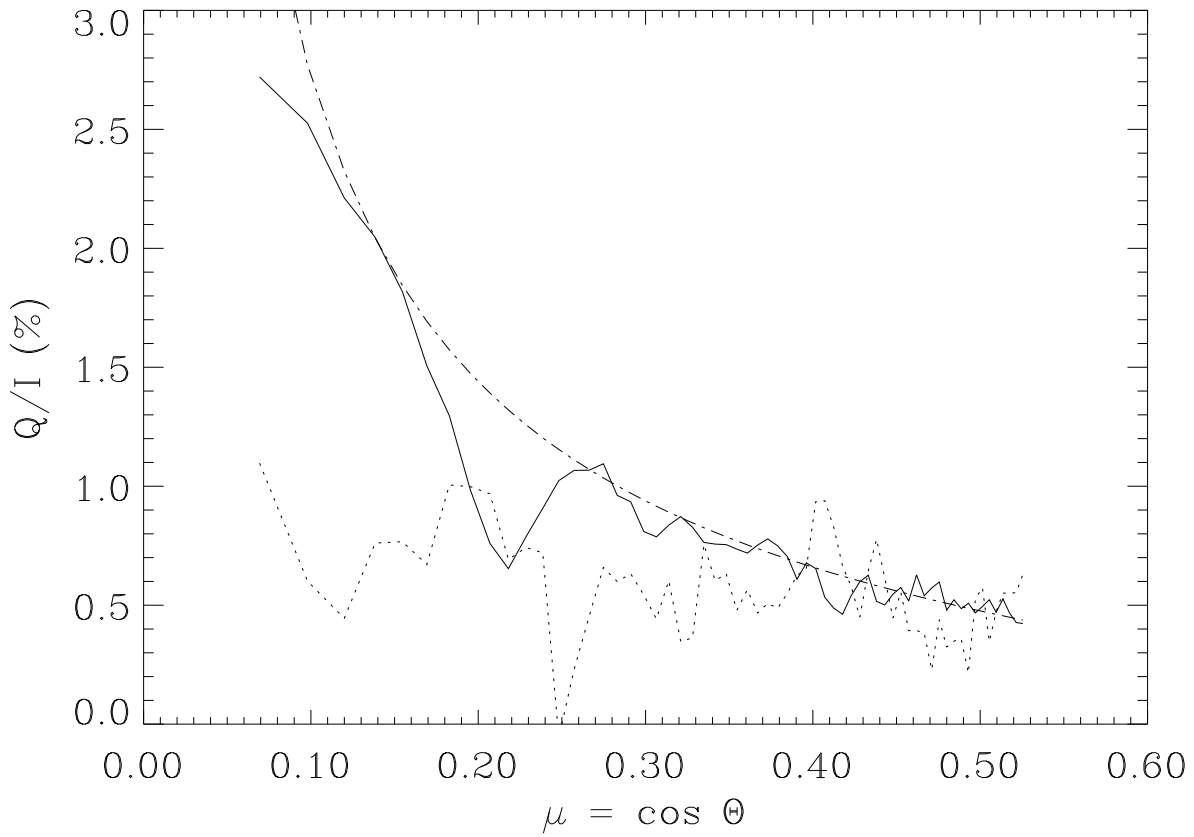
Figure 7.2: Center-to-limb variation of Q/I, derived from the observations in Figure 7.1. Solid line: Blue-wing (4226.2 Å) maximum. Dotted line: Core peak maximum. Dot-dashed line: Analytical function representing the blue-wing maximum (see Sect. 7.3).

observations. In the case shown here the location of the line center maximum is shifted towards the limb relative to the maximum of the wing depolarization, but we have other observations that do not show such a shift.

When examining all our observations we however find a general relation: Depolarization in the far wings of the Ca I line is always accompanied by transverse Zeeman-effect signatures in the surrounding blend lines.

Figure 7.3 shows profiles of three Stokes parameters at certain spatial locations in the recording that was presented in Figure 7.1. The I profile refers to a position 15 arcsec inside the limb ($\mu = 0.17$), while the two Q/I profiles refer to 25 arcsec ($\mu = 0.23$, solid line) and 35 arcsec
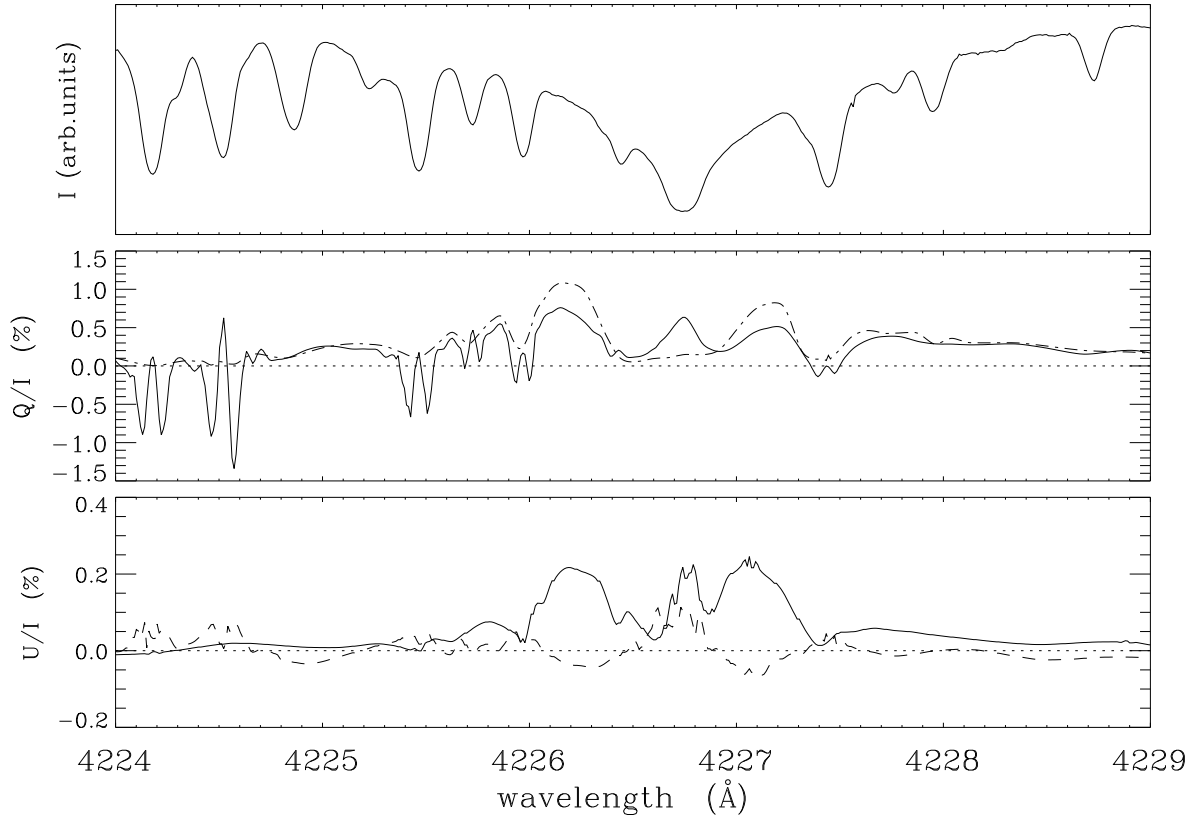
Figure 7.3: I, Q/I, and U/I profiles extracted from Figure 7.1 at different μ values. The I profile refers to $\mu = 0.17$. The Q/I profiles refer to $\mu = 0.23$ (solid line) and $\mu = 0.26$ (dot-dashed line). The U/I profiles refer to $\mu = 0.15$ (solid line) and $\mu = 0.31$ (dashed line).

($\mu = 0.26$, dot-dashed line), i.e., to a depolarized and to a more normal quiet region. These profiles are very different in their Zeeman signatures and also differ in their line center polarizations (the dot-dashed curve shows strong core depolarization). Otherwise the two profiles have very similar shapes and asymptotically agree in the far wings. This supports a depolarization interpretation, in which the wing depolarization decreases as we move away from the line center. Two U/I profiles, observed 11 arcsec inside the limb, i.e., at $\mu = 0.15$ (solid line), and at 48 arcsec, i.e., at $\mu = 0.31$ (dashed line), exhibit a Q/I-type profile shape in the wings. Due to their complementary behavior (opposite signs) it is not possible to explain them in terms of instrumental cross talk (from Q to U), but their origin appears to be solar. This be-

havior is confirmed by many other examples. The interpretation in terms of Hanle rotation of the polarization plane is supported by the sign variations of this effect, since they correspond to both clockwise and anti-clockwise rotation.

7.5   Discussion

Standard theory predicts that magnetic fields affect the scattering polarization only in the Doppler core of the line (in the form of Q/I depolarization and rotation of the plane of polarization, which creates a U/I signal), while the wings should remain unaffected (Omont et al. 1973; Stenflo 1994 (p. 83)). In contrast we observe Q/I depolarization and rotation of the polarization plane in the Ca I wings. This apparent contradiction suggests that the theory for the Hanle effect in the solar atmosphere is not sufficiently understood and may be in need of revision.

A possible explanation could be that the Ca I Zeeman effect extends far into the wings, but observations in active regions far from the limb do not show any such behavior at all.

As an alternative to the Hanle effect, the Q/I wing depolarization might have an explanation in terms of either "geometrical" depolarization, meaning that the plane-parallel stratification of the atmosphere breaks down in magnetic regions, or enhanced collisional depolarization, which could occur if the density and thereby the collision rate becomes enhanced in certain magnetic regions (A. van Ballegoijen suggested such a possibility in the discussion after the conference presentation). Both these mechanisms are however unlikely to account for the observed U/I signatures. In principle the anisotropy in the illumination of the scattering Ca atoms could deviate locally from the anisotropy given by the limb-darkening function, such that the radial symmetry gets broken and the resulting plane of polarization for the scattered radiation is no longer perpendicular to the radius vector (i.e., parallel to the nearest solar limb). However, since the spatial resolution was modest (several arcsec) in our observations, the fluctuations in the local anisotropy have to be of fairly large scale and of relatively large amplitude to be able to produce observable effects. We see no

fluctuations in the Stokes I images that could indicate such variations in the radiation field. Although we cannot presently rule out this possibility, we consider it to be an unlikely explanation.

Another possibility has to do with subtleties in partial frequency distribution (PRD) of radiative transfer. PRD contains combined contributions from frequency coherence (the R_{II} function) and complete frequency redistribution (the R_{III} function), which mix in a complex way in the presence of magnetic fields. In the case of a balanced mixture of R_{II} and R_{III} it is possible for the Hanle effect to appear in the wings, and this effect is larger when the angular dependence of the frequency redistribution is taken into account (Nagendra et al. 2002). Conceptually, the mechanism might be understood as follows: We first have radiative excitation at a frequency in the line core, followed by Hanle precession of the excited oscillator until a collision shifts the frequency (without destroying the atomic polarization) so that the emission occurs in the wings. The details of this possibility however needs to be explored for a realistic model system.

The reasons why we believe that instrumental effects cannot explain our observations are: The Q/I and U/I signatures are spatially localized and occur at different limb distances, where signatures of the transverse Zeeman effect are found. There is no clear relation with intensity. In active regions we have depolarization both outside and inside sunspots. The signatures described may be confined within a few arcsec, and, in the case of Q/I-like signatures in U/I, it is possible to find examples where the sign is changing over a few arcsec. Such localized instrumental effects have never been seen in other observations at other wavelengths. Another argument is that spatial scans (done by changing the slit position in steps of 5 arcsec) give consistent results, showing that the spatial location of the effect is tied to the Sun and not to the position on the detector or within the field of view. Therefore we believe that the described effects are of solar origin.

Bibliography

Gandorfer, A. M., 2000, *"The Second Solar Spectrum, Vol.1"*, ISBN no. 3 7281 2764 (Zurich VdF)

Gandorfer, A. M., Povel, H. P., 1997, *"First observations with a new imaging polarimeter"*, Astron. Astrophys. **328**, 381

Küveler, G., Wiehr, E., Thomas, D., Harzer, M., Bianda, M., Epple, A., Sütterlin, P., Weisshaar, E., 1998, *"Automatic guiding of the primary image of solar Gregory telescopes"*, Sol. Phys. **182**, 247

Nagendra, K. N., Frisch, H., Faurobert, M., 2002, *"Hanle effect with angle-dependent partial redistribution"*, Astron. Astrophys. **395**, 305

Omont, A., Smith, E. W., Cooper, J., 1973, *"Redistribution of Resonance Radiation. II. The Effect of Magnetic Fields"*, Astrophys. J. **182**, 283

Stenflo, J. O., 1994, *"Solar magnetic fields: polarized radiation diagnostics"*, Astrophysics and Space Science Library, Kluwer Academic Publishers, Dordrecht

Stenflo, J. O., Gandorfer, A., Wenzler, T., Keller, C. U., 2001, *"Influence of magnetic fields on the coherence effects in the Na I D1 and D2 lines"*, Astron. Astrophys. **367**, 1033

Sütterlin, P., Wiehr, E., Bianda, M., Küveler, G., 1997, *"Problems in measuring prominence oscillations"*, Astron. Astrophys. **321**, 921

Part II

Continuum scattering polarization

Chapter 8

High spatial resolution solar polarimetry with interference filters[*]

E. Wiehr[1]**, M. Bianda**[2]

Abstract

A new type of two-dimensional polarimeter is used to measure the center-to-limb variation of the scattering induced polarization in a narrow continuum window up to the extreme limb. The polarimeter is set on the Tenerife Gregory Coudé telescope's hour axis, where the two folding flat mirrors cancel their polarizing effects for zero solar declination at the equinox. The short CCD exposure of only 5 ms allows high spatial resolution images in polarized light. A beam switching technique together with an integration parallel to the solar limb over $20''$, yields a high polarimetric accuracy with an rms noise of $2 \cdot 10^{-4}$. Our results for a continuum window at 4506–4508 Å agree with model calculations down to limb distances of $0.32''$ (i.e. $\cos \vartheta < 0.025$).

8.1 Introduction

Scattering processes in the solar atmosphere produce deviations from a Planckian source function. Since the incident radiation shows limb darkening, the scattered part of the light exhibits a preferential direction, affecting a linear polarization which increases strongly toward the solar limb. If the lifetime of the respective transition is not short enough, the scattering process is disturbed by collisions. Hence, only favorable absorption lines show a limb polarization (e.g. Stenflo 1973). The continuum radiation also exhibits a limb polarization mostly arising from Rayleigh scattering of neutral hydrogen (cf., Unsöld 1955).

The limb polarization in the continuum has been observed by Leroy (1972), Mickey & Orall (1974), and Wiehr (1975, 1978). The results agree for limb distances down to a few arcsec. In particular for wavelengths near 5850 Å, these authors consistently find Q/I values of 0.9×10^{-4} and 6×10^{-4} at 25″ and 5″ limb distance, respectively. Closer to the limb, only Mickey & Orall (1974) give values which, however, hardly yield a smooth curve (cf., their Fig. 3). Model calculations by Fluri & Stenflo (1999) nicely fit these observations. However, a much stronger test would be the comparison of data with theory at the very limb where the rise of the polarization is very steep particularly at blue wavelengths. Such observations are rather difficult since the continuum limb polarization (i) is of very small amount, (ii) is superposed with the strong intensity gradient at the very limb, and (iii) interferes with the usually much larger instrumental polarization.

The use of a spectrograph for high spectral resolution, involves multiple telescopic reflections which introduce polarization. For a 'German type' Coudé mounting with two nearly orthogonal folding flat mirrors (as, e.g., the telescopes at Locarno and at Tenerife), the instrumental polarization varies only with the solar declination thus being largely constant over a day (cf., Wiehr 1971) and very small near the equinoxia, (where the two deflections are precisely orthogonal). The high suitability of such a Coudé type telescope allowed the detection of limb polarization in spectrally well resolved line profiles as Ca I 4227 Å (Brückner 1963), Sr II 4078 Å, Ba II 4554 Å, Na I 5890 Å (Wiehr 1975), Sr I 4607 Å, Ba I 5535 Å (Wiehr 1978). Recent polarimetry with the 'Zürich polarimeter' (ZIMPOL; Povel 1995) extended these
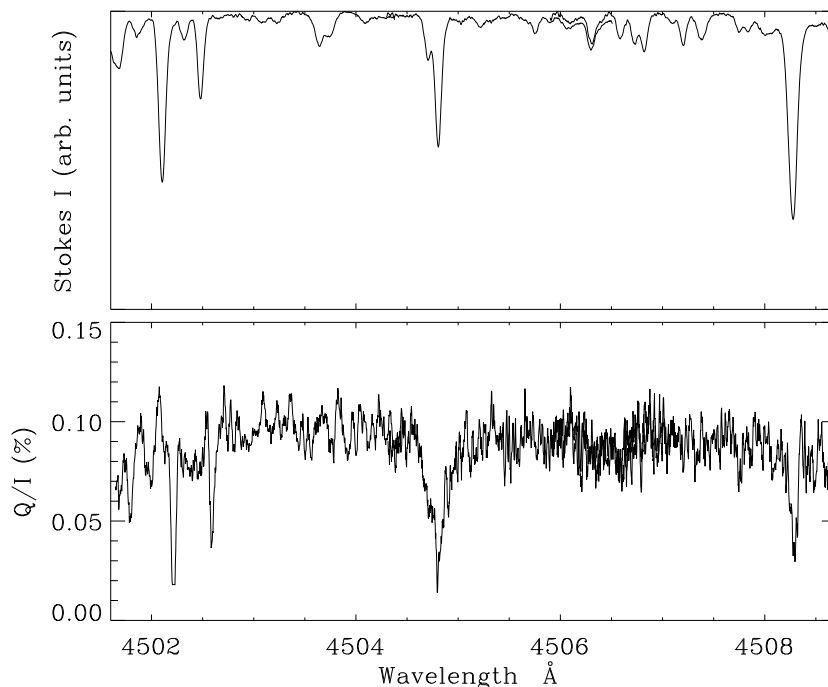
measurements.

Figure 8.1: Linear polarization at 5″ limb distance through the blue region, selected for measurements of the continuum polarization; two sub-spectra joined at at 4506.5 Å display the full wavelength window were taken with the spectrograph instead of the 2-D optics (cf., text); ordinate scale = polarization in %; intensity in arbitrary units.

The Gregory Coudé Telescope at Locarno also enabled first measurements of the continuum polarization in spectrally well defined narrow windows free from absorption lines: at 5″ limb distance ($\cos\vartheta = 0.23$) the continuum polarization decreases from 10^{-3} at 4234.8 Å to $5 \cdot 10^{-5}$ at 6578.0 Å (Wiehr 1975). Such observations have also been made by Leroy (1972) who, however, used broader filters covering more lines, and did not reach the very limb. For the present continuum observations, the wavelength selection is done via filters instead of a spectrograph, a method which has already been used by Clarke & Ameijenda (2000) for the determination of the center-to-limb variation of the Hα resonance polarization. It yields very short exposure times of a few milliseconds which largely 'freeze' seeing. The
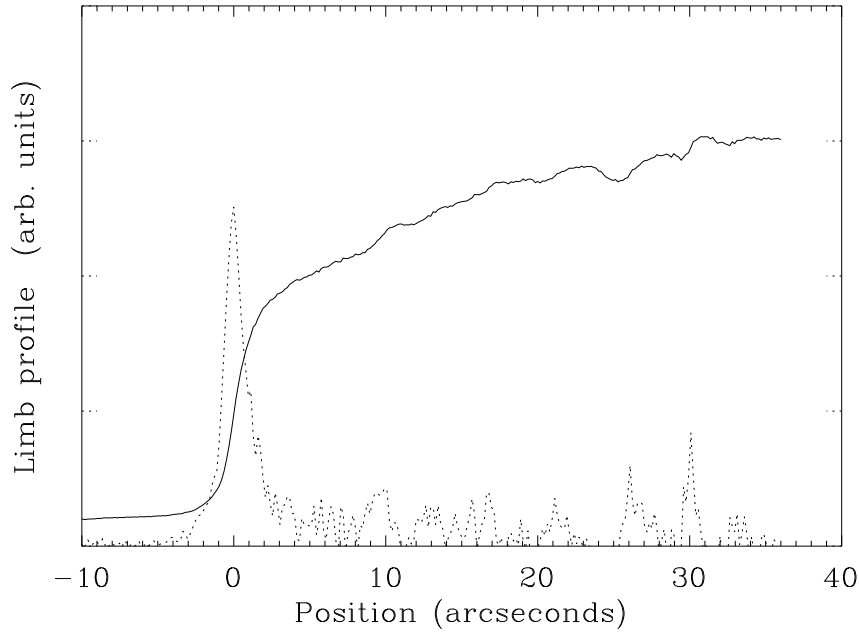
Figure 8.2: Intensity profile of the solar limb (full line) and first derivative (dash points) of $2''$ half-width showing the high spatial resolution achieved with the polarimeter described.

much longer exposures with 'ZIMPOL' do not allow a determination of the strong increase of the linear polarization at the very limb, presented in this paper.

8.2 Observing method

We observed close to the spring equinox 2002, where the two folding flat mirrors of the Gregory Coudé Telescope (GCT) are orthogonally oriented, thus yielding very small instrumental linear polarization. The measurement of the polarized light was done with a beam switching technique where a $\lambda/2$ plate in front of a calcite (Savart plate) is operated alternately in two orthogonal orientations (Semel et al., 1993). We placed these optical components directly on the telescope's hour axis thus avoiding any further reflections. The finite field-of-view required for the Savart plate, is defined by a $32'' \times 125''$ aperture in front of the polarization optics and is imaged by telecentric optics on a CCD.
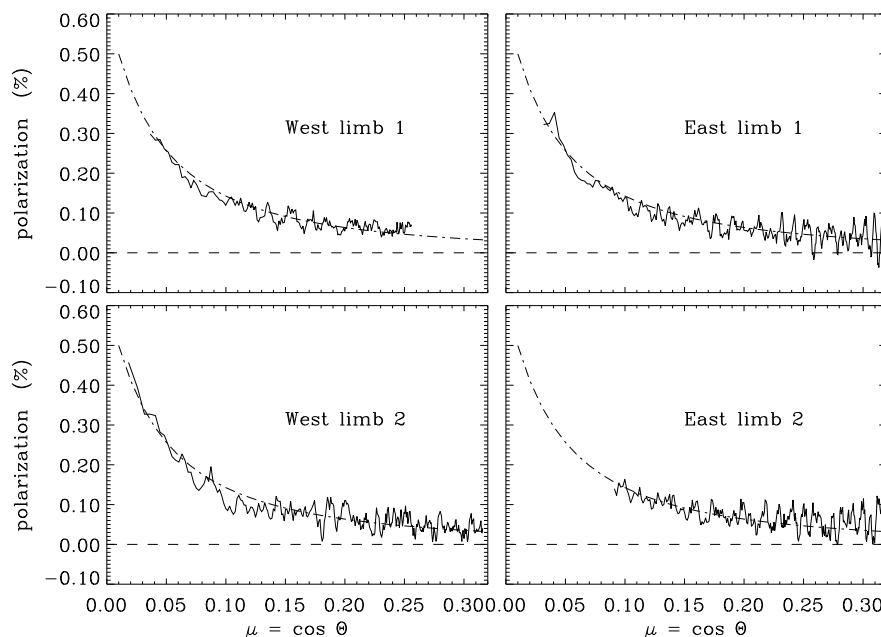
Figure 8.3: Linear polarization in the 4506 Å window as function of the heliocentric angle cosΘ in comparison with calculations by Fluri and Stenflo (1999; dash points); the four curves represent data from different limb positions obtained when following the Coudé rotation: 9 pairs for 'west-limb-1', 2 pairs for 'west-limb-2', 6 pairs for 'east-limb-1', and 3 pairs for 'east-limb-2'.

Between the two lenses, an image of the telescope's entrance pupil occurs, which is precisely baffled in order to reduce scattered light from the optics. The total set-up can easily be removed, allowing a quick check of the filter transmission with the spectrograph.

The possibility of an alternate use of the spectrograph keeping the polarization analyzer unchanged, also allowed us to check the adjustment and the accuracy of the polarimeter.

We selected a spectral window near 4505 Å with the filter used by Sütterlin & Wiehr (1998) for two-dimensional continuum photometry. Its transmission maximum of 3 Å half-intensity width was electrically heated to fit the 4505 – 4508 Å region which is free of polarization from lines. Since our blue region is not covered by the polarization atlas (Gandorfer 2000), this was proven switching to the spectrograph and

orienting the slit at $5''$ distance parallel to the solar limb. The linear polarization was measured successively in two wavelength intervals, overlapping each other near 4506 Å (cf., Figure 8.1). Averaging ten Q/I profiles in the two wavelength intervals yields a high inner accuracy, as seen from the good agreement of the two Q/I profiles in the overlapping interval in Figure 8.1. Since no significant line polarization occurs at 4505 Å $< \lambda < 4508$ Å, that wavelength range can be considered as a sufficiently clean 'continuum window' for limb polarization.

Alternate control by means of the spectrograph also ensured the high wavelength stability of the filter heating. The transmission of the 3 Å filter allows exposures as short as 5 ms with more than 10000 CCD counts, - as compared to about 600 CCD counts for our 500 ms spectrographic measurements. We selected images with 'frozen seeing', i.e. without marked influences from the earth's atmosphere. The spatial resolution is then given by the two-pixel limit of $0.32''$.

For a correction of instrumental polarization, we took data at disk center where a polarization of solar origin is assumed to be zero for symmetry reasons. The measured disk center signal yields an instrumental linear polarization of 0.0017 (0.17%) showing that near the equinox the GCT is, indeed, largely free from linear polarization. We subtract this value from the limb observations, assuming that the instrumental polarization does not differ between disc center and limb (the maximum declination difference over the solar disk being only $0.25°$). The amount of linear polarization was checked by a tilted glass plate.

8.3   Continuum polarization near the limb

We measured the continuum polarization at locations where the solar limb is oriented perpendicularly to the CCD rows. The corresponding limb position slightly varies with the Coudé rotation, which was not compensated in order to avoid additional polarization from a derotator. The linear polarization was measured with the method introduced by Semel, Donati, and Rees (1993): two exposures taken with perpendicular orientations of the half wave plate give a total of four images. Since these are not subtracted but crosswise divided, varia-
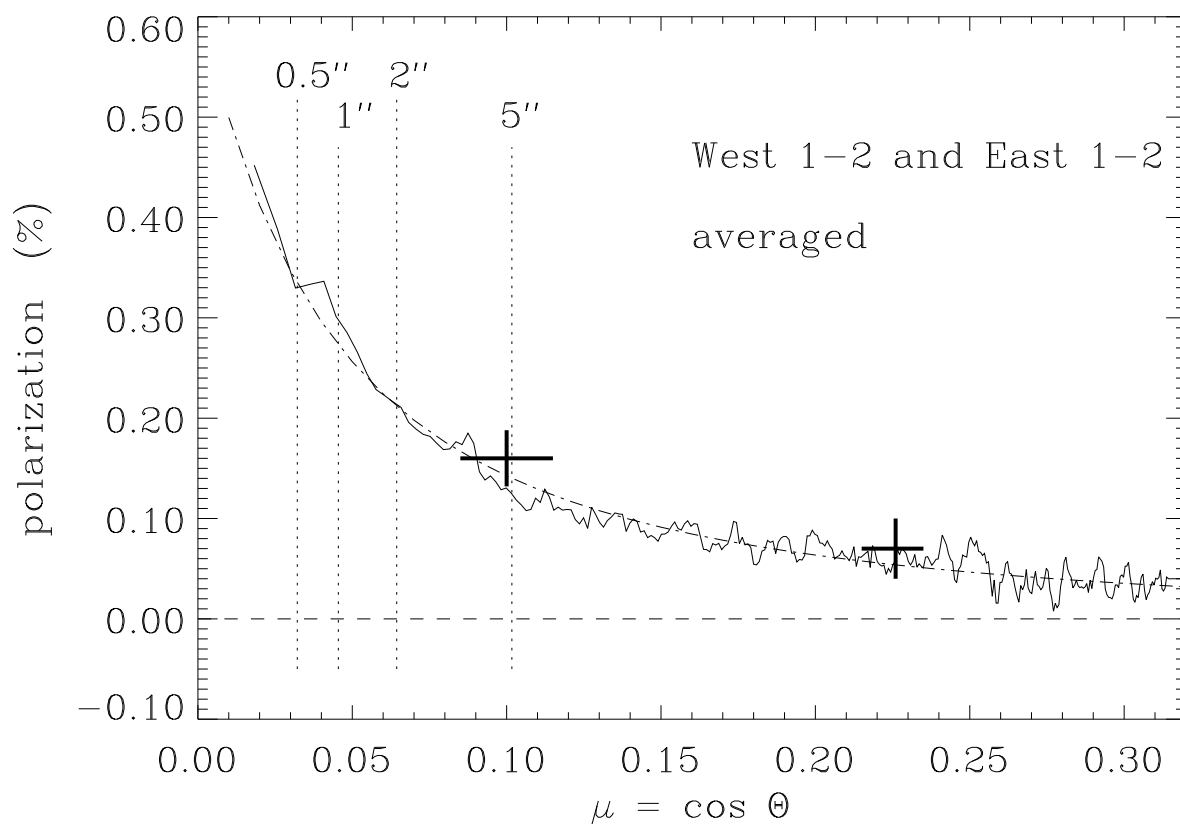
Figure 8.4: Average of the four profiles in Fig.8.3 together with calculations by Fluri and Stenflo for model FALC-5 from Fontenla et al.; vertical bars indicate the limb distance in arcsec; crosses give the data by Wiehr (1978).

tions of pixel response over the CCD chip and differences in the transmittances of the orthogonal beams are canceled out without the need of any flat-fielding exercise. For the final determination of the degree of polarization, we use the algorithm described in Chapter 3.

The method of two successive exposures, taken with orthogonal orientations of the half-wave plate, requires constancy of both, the location and the steepness of the solar limb on the CCD. The first is assured by the primary image guider of the GCT (Küveler et al. 1998) which compensates drifts in the telescope pointing. The constant limb sharpness requires highly constant seeing and is assured by the short CCD exposures and by frame selection among several exposures at each limb position. The most suitable pairs of sub-images were se-

lected via amount and location of the first derivative of the limb intensity profiles (Fig. 8.2). Only those pairs of sub-images were used which have largely equal sharpness and locations of the solar limb.

The noise was significantly reduced by averaging the two-dimensional polarization images in the direction parallel to the solar limb. For this 32″ tangent, the curvature of the limb yields a 0.13″ deviation which is below the 0.32″ spatial resolution achieved. This integration also smears spatial structures of the sun. The high inner accuracy of our method is demonstrated in Fig. 8.3 which gives the results from different limb positions following the Coudé rotation. Fig. 8.4 shows the average of the profiles in Fig. 8.3 together with the data by Wiehr (1978; Fig. 1) at 5″ and at 25″ limb distance, interpolated for 4506 Å. The calculations by Fluri & Stenflo (1999) yield a good coincidence for their model FALC-5 (from Fontenla et al.) up to a limb distance of 0.32″ ($\cos\vartheta = 0.025$). Although we regard values closer than 1″ from the limb with caution, the agreement with the calculations is amazing. Since the model assumes a homogeneous atmosphere, our results would indicate no significant influence of inhomogeneities.

8.4 Conclusion

The present study shows that polarimetry from two-dimensional images can be applied to research areas which require only limited spectral resolution such as for continua (or e.g. prominence emission lines). The short exposure time required for such 2-D observations with filters yields very high spatial resolution. The limitation of the polarimetric accuracy by the CCD's gain table is largely avoided using a differential method from pairs of images which, however, requires the consideration of different image degradation by seeing. The scattering induced linear polarization of the continuum agrees with model calculations up to to 0.32″ limb distance (i.e. $\cos\vartheta = 0.0228$).

The evacuated Gregory Coudé telescope on Tenerife is operated by the Universitäts-Sternwarte, Göttingen (USG), at the Spanish 'Observatorio del Teide' of the Instituto de Astrofísica de Canarias.

Bibliography

Brückner, G., 1963, *"Photoelektrische Polarisationsmessungen an Resonanzlinien im Sonnenspektrum. Mit 6 Textabbildungen"*, Zeitschrift für Astrophysik **58**, 73

Clarke, D., Ameijenda, V., 2000, *"Hα polarimetry of the solar limb"*, Astron. Astrophys. **355**, 1138

Fluri, D. M., Stenflo, J. O., 1999, *"Continuum polarization in the solar spectrum"*, Astron. Astrophys. **341**, 902

Gandorfer, A. M., 2000, *"The Second Solar Spectrum, Vol.1"*, ISBN no. 3 7281 2764 (Zurich VdF)

Küveler, G., Wiehr, E., Thomas, D., Harzer, M., Bianda, M., Epple, A., Sütterlin, P., Weisshaar, E., 1998, *"Automatic guiding of the primary image of solar Gregory telescopes"*, Sol. Phys. **182**, 247

Leroy, J. L., 1972, *"New Measurements of the Polarization of Photospheric Light near the Solar Limb"*, Astron. Astrophys. **19**, 287

Mickey, D. L., Orrall, F. Q., 1974, *"Broadband Polarization Measurements on the Quiet Sun's Disk near λ 5834"*, Astron. Astrophys. **31**, 179

Povel, H., 1995, *"Imaging Stokes polarimetry with piezoelastic modulators and charge-coupled-device image sensors"*, Optical Engineering **34**, 1870

Semel, M., Donati, J.-F., Rees, D. E., 1993, *"Zeeman-Doppler imaging of active stars. 3: Instrumental and technical considerations"*, Astron. Astrophys. **278**, 231

Stenflo, J. O., 1973, *"Magnetic-Field Structure of the Photospheric Network"*, Sol. Phys. **32**, 41

Sütterlin, P., Wiehr, E., 1998, *"Temperature mapping of sunspots and pores from speckle reconstructed three colour photometry"*, Astron. Astrophys. **336**, 367

Unsöld, A., 1955, *"Physik der Sternatmospharen, mit besonderer Berücksichtigung der Sonne"*, Springer, Berlin, 2nd ed.

Wiehr, E., 1971, *"On Polarimetry in Solar Active Regions. IV. Influence of Tele-*

scopic Phase Retardation", Sol. Phys. **18**, 226

Wiehr, E., 1975, *"Measurement of solar disc polarization in a number of Fraunhofer lines and their adjacent continuum"*, Astron. Astrophys. **38**, 303

Wiehr, E., 1978, *"Measurement of solar disc polarization in a number of Fraunhofer lines and their adjacent continuum. II. Improved data, new line measurements"*, Astron. Astrophys. **67**, 257

Part III

Solar flares impact polarization

Chapter 9

Search for impact polarization in Hα flares[*]

M. Bianda[1], J.O. Stenflo[23], G. Küveler[4], A. Gandorfer[3], and D. Gisler[3]

Abstract

Polarimetric filter observations of solar flares in Hα have been carried out with ZIMPOL at IRSOL. The aim was to search for impact polarization with high polarimetric accuracy and a time resolution of a few seconds. Against expectations we could not detect polarization signatures above 0.15 % for any of the 23 flares that were observed except one with 0.4 %. However, even this 0.4 % signal is unlikely to be of solar origin. This indicates that the large majority of flares do not exhibit any impact polarization.

9.1   Introduction

In 1999 we decided that IRSOL (Istituto Ricerche Solari Locarno) would contribute to the RHESSI project by performing ground based observations of impact polarization in solar flares with ZIMPOL. The reasons for this choice are the unique capabilities of the ZIMPOL system when combined with the IRSOL telescope. ZIMPOL is a fast single-beam system that is free from seeing-induced polarization noise or gain-table effects and therefore allows higher polarimetric precision than alternative systems. The Gregory Coudé Telescope of IRSOL has low instrumental polarization that is independent of hour angle. Abundant observing time could be allocated to optimize the project.

Observations of Hα impact polarization at the Meudon Observatory have been reported by Hénoux & Chambe (1990) and Hénoux et al. (1990). These observations however needed minutes of integration time to detect signals in the range of percents. Our set-up constitutes a significant improvement on this.

Solar flares are characterized by fast intensity variations that give rise to spatial and temporal intensity gradients, which can easily be the source of spurious polarization produced by image motion, too slow modulation, differential optical aberrations, and/or gain-table effects. With the ZIMPOL system these problems are eliminated, since the modulation frequency (42 kHz for circular, 84 kHz for linear polarization) is well above the characteristic seeing frequencies, and the different polarization states are recorded by the same pixels (Povel 1995).

In July and August 2002 we recorded 23 events for which the Hα images showed significant intensity enhancements. Table 9.1 gives the date, time of maximum X-ray emission, and the maximum linear polarization signals seen.

9.2   Instrumentation and observational procedure

We used the following optical set-up, which is directly mounted on an optical bench along the hour axis at the exit of the telescope. First comes the polarization modulation package, which contains a piezoe-

Table 9.1: List of recorded events

Date	Time of max (UT)	max pol. (%)	Date	Time of max (UT)	max pol. (%)
July 4	10:47	0	July 4	13:28	0.05
July 4	14:57	0.03	July 5	13:32	0.1
July 7	13:03	0.05	July 11	07:12	0
July 11	ca 09:40	0.05	July 11	11:21	0.08
July 11	ca 12:00	0.06	July 11	12:08	0.05
July 11	ca 13:07	0.08	July 11	ca 15:25	0.03
July 11	14:19	0.08	July 11	14:48	0.4
July 12	10:35	0.1	July 18	07:44	0.05
July 18	11:57	0.15	July 20	10:46	0.1
July 22	ca 10:10	0.1	July 29	07:51	0.06
August 2	10:51	0.08	August 4	07:20	0
August 4	09:55	0			

lastic modulator (PEM) and a Glan polarizer. Second comes the 0.6 Å
Hα filter. Third, an image derotator compensates for the image ro-
tation of the Gregory Coudé telescope. Fourth, a beamplitter allows
the ZIMPOL CCD camera and the flare detector system, built by Fach-
hochschule (FHS) Wiesbaden, to be fed simultaneously.

The present ZIMPOL configuration (with one PEM) allows the
simultaneous recording of one linear (Stokes Q) and the circular
(Stokes V) polarization components. The field of view of the telescope
is 200 arcsec. The image is magnified by a telecentric system to match
the image scale with the CCD pixels to 1 arcsec per pixel.

The flare detection system developed at FHS Wiesbaden (Küveler
et al. 2002) stores 14 8-bit intensity images per second, records the GPS
time, and detects intensity enhancements.

The ZIMPOL and FHS systems use separate buffers to store data
recorded in an active region in advance of the occurence of any flare
with a frame rate of one set of Stokes images I, Q/I, and V/I per sec-
ond. After a specified time interval the data are overwritten. Should
an Hα enhancement be detected, the buffered data are transfered to

permanent storage, together with the subsequent data recorded during the flare event itself. Dark and calibration images were obtained before or after the flare recordings.

The use of ZIMPOL together with an Hα filter is similar to previous ZIMPOL observations with the Universal Birefringent Filter at NSO/Sac Peak (Stenflo et al. 2002) and the night-time observations of Jupiter and Saturn with interference filters at NSO/Kitt Peak (Gisler & Schmid 2003). The flare observations were preferentially done in active regions close to the limb, where the largest impact polarization signals would be expected for geometrical reasons. The particle beams are believed to be directed in the direction normal to the solar surface on the average, and impact polarization should be maximum for transverse beams. The analyser was oriented such that the Stokes Q direction was aligned with the limb in order to have a well defined polarization basis, and because the impact polarization for symmetry reasons should be larger in Stokes Q than in Stokes U. Care was taken to set the integration time such that the CCD would not saturate during a flare. An optimum orientation of the active region on the CCD was obtained with the help of the image derotator. The automatic guiding system (Küveler et al. 1998) keeps the observed region on the sensor with a positional stability of a few arcsec. The flare detection system was set to recognize intensity enhancements above a specified threshold. If this would happen, then a signal is transmitted to the ZIMPOL system, and both systems store the data as described above.

Just before the end of several of the flare sequences a linear polarizer was briefly inserted in front of the analyser and aligned parallel and perpendicular to the limb. A tilted glass plate was also inserted on a few occasions to introduce a known small amount of linear polarization. These operations were done to verify that the instrument was working correctly and recording polarization as it should. Another test we did consisted in recording the Zeeman-effect circular polarization in active regions by tuning the filter to the line wings. The change of polarity of the V/I image and the linear polarization signals with the tilt plate confirmed the proper functioning of the system.

9.3 Results

As shown in Table 9.1 the observations were carried out in the period July – August 2002, during which 23 events were detected, although none of the flares was very large. For each event data were stored for periods of 10–30 minutes. Figure 9.1 illustrates one case of the 18 July 2002 flare, which had its maximum X-ray emission (1–8 Å, $0.056\,\mathrm{W/m^2}$) at 7:44 UT and was located at N19 W30. The top row shows the time sequence of the usual intensity images. The linear polarization (Q/I) images are given in the second row, while the third row gives the V/I images. The three bottom rows represent a continuation of the time sequence of the top rows. The displayed area has the size $120 \times 120\,\mathrm{arcsec^2}$.

This flare recording started in the last part of the impulsive phase. The system was set to produce one image each 4 s. Each image in 9.1 is an average of 10 such images. The time increment between successive images is therefore 40 s. For this flare the initial enhancement in Hα was quite intense, so that several pixels were saturated during the first few minutes in spite of the conservative choice of exposure time. In the right top corner of the Q/I images two small squares are over-plotted. The bright square corresponds to 0.1 % polarization perpendicular to the limb, and the dark square to 0.1 % polarization parallel to the limb. Mere visual inspection allows us to exclude the existence of strong polarizations signals for this event. In the V/I images we have similarly in the top right corner overplotted two squares, corresponding to +0.5 and -0.5 %. The signals seen in V/I are due to the longitudinal Zeeman effect. The filter pass band was slightly shifted from the Hα line center. The same features are noticed in the Q/I images (with opposite sign), and are due to telescope cross talk.

Spatial profiles are shown in the left panels of 9.2. The top panel gives Q/I along a row located 5 arcsec down from the top of a single Q/I image. The middle panel gives the values in the same row but after the averaging of 10 images. The third panel gives V/I in the same row for a 10 image average.

To determine the upper limit of a possible signal, we inspect the movies of the time sequences to identify the location where the largest Q/I variations seem to occur. There we place a small rectangle and de-
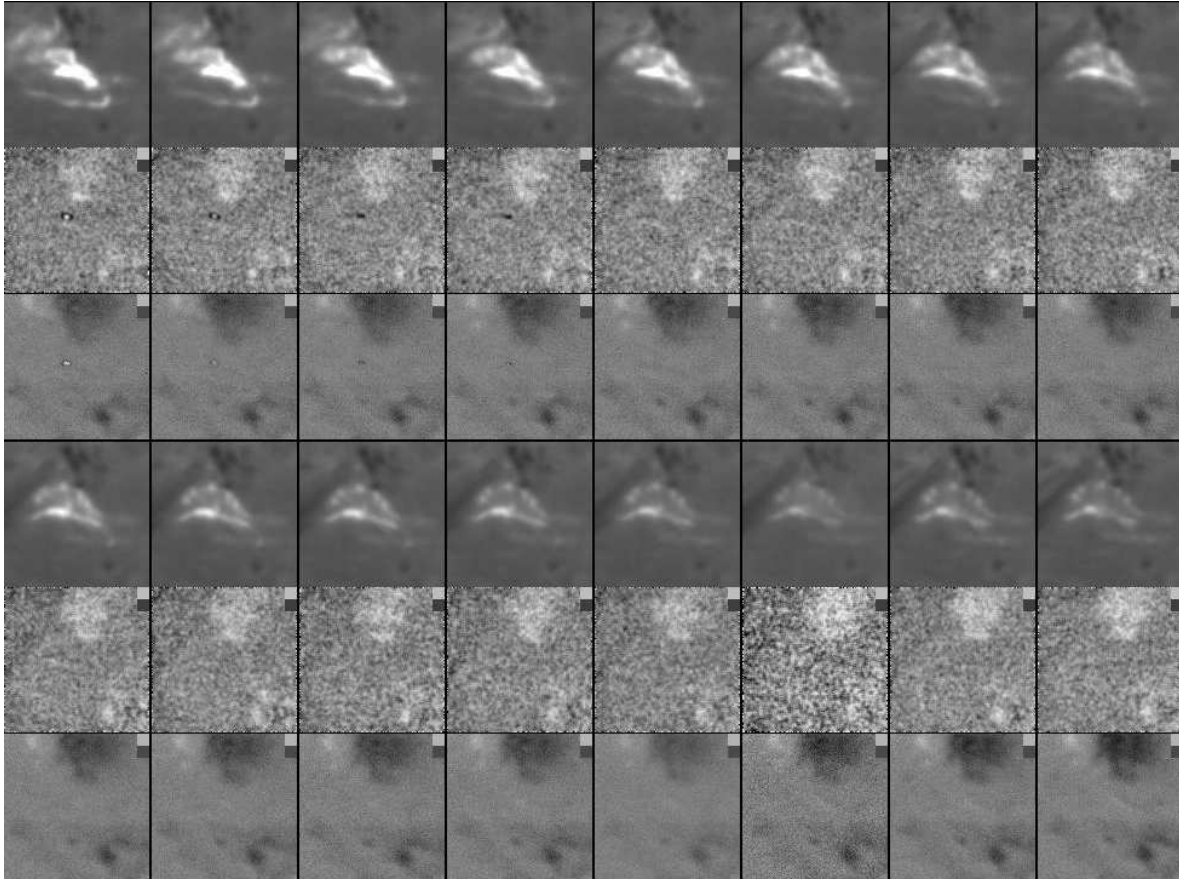
Figure 9.1: Flare of 18 July 2002, time sequence with 40 s between the set of intensity, Q/I, and V/I images, each having a field of view of $120 \times 120 \, \text{arcsec}^2$. See text for details.

termine the averaged value in the rectangular area for each image. The right panels of 9.2 show the resulting sequence obtained with such a rectangular area of $11 \times 11 \, \text{arcsec}^2$ to the right of the brightest point, chosen to avoid the saturated pixel area. The top panel gives the evolution of the brightness in time steps of 4 s with respect to a quiet area (data gaps are caused by calibration and by the transit of a small cloud). The evolution of the averaged Q/I and V/I values are given in the middle and bottom panels, respectively.

All the other events have been reduced in this way, and the maximum polarization values found are given in Table 9.1. In one event a polarization signal as large as 0.4 % is found, but its spatial morphology is highly correlated with that of the intensity gradients, and the orientation of the plane of polarization is parallel to the limb instead
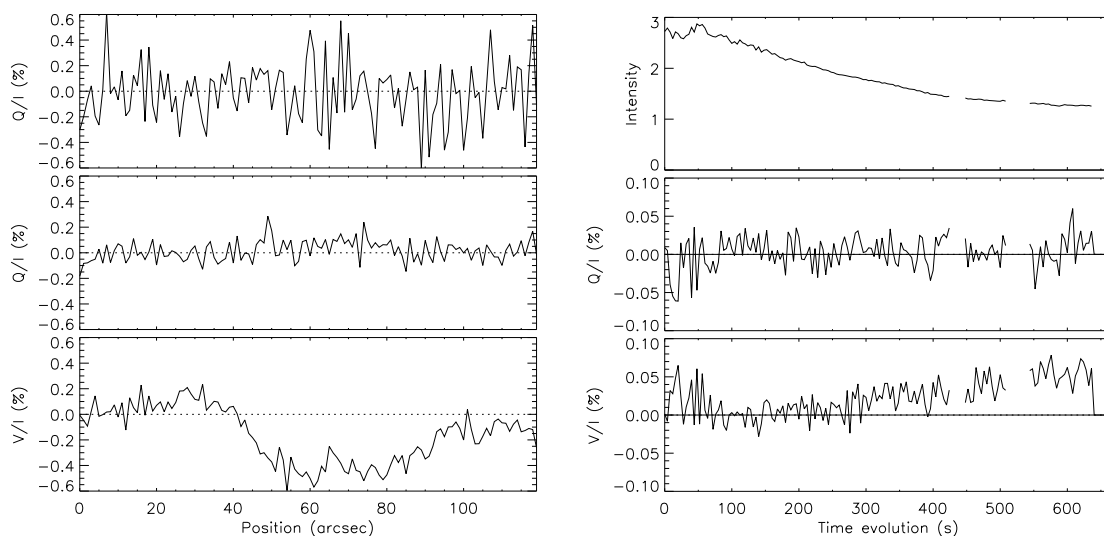
Figure 9.2: Left panels: Spatial profiles from single (top) and averaged frames. Right panels: Time evolution of the values averaged over a small area to the right of the brightest point. See text for details.

of radial as one would expect. Problems related to the recording of the dark current are a possible explanation of the observed signal. It is therefore doubtful whether the detected signal is of solar origin.

9.4 Conclusion

We do not find any significant impact polarization in any of the 23 flares that we have observed, although our observing system has considerably higher sensitivity than previous instruments used to study this effect. This null result can hardly be explained in terms of observational errors, since weak polarization introduced artificially with a tilting glass plate shows that the system is capable of detecting weak signals without problems. We are therefore led to the conclusion that no impact polarization above a few promille was present in any of the flares. It should however be noted that our observations did not include any major flare event.

According to the observations of Kashapova (2003), only some but not all flares show impact polarization. On the contrary our results suggest that impact polarization must be a quite rare phenomenon.

Based on our limited sample of 23 flares we however cannot conclude that impact polarization does not occur at all. To clarify this point it would be important to perform coordinated observations of the same flares with different instruments and compare the results.

Discussion

SEMEL: Let us remember that polarization is not a scalar. In the Henoux observations the orientation of the polarization mainly directed to the limb is a crucial information.

KELLER: I suggest to put a quarter wave plate with its fast axis at $0°$ in front of the modulator to convert Stokes U to V so that you get Q and U simultaneously and therefore also the linear polarization direction.

ZHARKOVA: What makes you think that this is impact polarization? Is it not linear polarization that is more likely caused by the external radiation?

BIANDA: We do not think that anything that we see is impact polarization. On the contrary ours is a null result: the absence of impact polarization for our sample of flares.

HENOUX: The Hα emission you observed on August 4 was coming from the top of a loop. The plasma there may be just thermal plasma coming from chromospheric evaporation and cooling down. In that case you don't expect Hα to be polarized by impact.

GANDORFER: In polarimetry of flares one encounters very difficult challenges, which are due to the very steep intensity contrasts, in both the spatial and temporal regimes. We can clearly state that a fast single beam polarimeter like ZIMPOL is free from spurious effects down to the noise levels in the presented observations. However, slow polarization modulation will definitely be affected by (apart from seeing) infiltration of the increasing intensity during flare evolution. Therefore the detected polarization signal will be proportional to the temporal derivative of the flare intensity! On the other hand, a dual beam polarimeter will be limited by the *spatial* derivative of the intensity structures, due to differential aberrations in the two beams. The only way to get out of this dilemma is to use the beam-exchange technique.

HENOUX: Beam exchange makes the measurements of Stokes param-

eters dependent on image motion and flare intensity time evolution. It introduces cross talk in intensity.

Bibliography

Gisler, D., Schmid, H. M., 2003, *"Non-solar applications with the ZIMPOL polarimeter"*, in J. Trujillo Bueno, J. Sánchez Almeida (eds.), *"Solar Polarization, proc. 3rd SPW"*, ASP Conf. Ser., in press

Hénoux, J. C., Chambe, G., 1990, *"Hα impact polarization observed in solar flares as a diagnostic of energy transport mechanisms"*, Journal of Quantitative Spectroscopy and Radiative Transfer **44**, 193

Hénoux, J. C., Chambe, G., Smith, D., Tamres, D., Feautrier, N., Rovira, M., Sahal-Bréchot, S., 1990, *"Impact line linear polarization as a diagnostic of 100 keV proton acceleration in solar flares"*, Astrophys. J., Suppl. Ser. **73**, 303

Kashapova, L., 2003, *"Spectropolarimetric Investigation of Hα Line Profiles in Moustaches"*, in J. Trujillo Bueno, J. Sánchez Almeida (eds.), *"Solar Polarization, proc. 3rd SPW"*, ASP Conf. Ser., in press

Küveler, G., Klein, G., Thomas, D., Bianda, M., 2002, *"Automatische Erkennung und Registrierung von solaren Eruptionen (Flares)"*, in *Virtuelle Instrumente in der Praxis, VIP2002*, 79–83

Küveler, G., Wiehr, E., Thomas, D., Harzer, M., Bianda, M., Epple, A., Sütterlin, P., Weisshaar, E., 1998, *"Automatic guiding of the primary image of solar Gregory telescopes"*, Sol. Phys. **182**, 247

Povel, H., 1995, *"Imaging Stokes polarimetry with piezoelastic modulators and charge-coupled-device image sensors"*, Optical Engineering **34**, 1870

Stenflo, J. O., Gandorfer, A., Holzreuter, R., Gisler, D., Keller, C. U., Bianda, M., 2002, *"Spatial mapping of the Hanle and Zeeman effects on the Sun"*, Astron. Astrophys. **389**, 314

Chapter 10

Outlook: Future developments

10.1 Some outstanding programs for the immediate future

The last Chapters have highlighted some puzzling questions that are still unanswered. One such enigma has to do with the appearance of the Hanle effect in the line wings. Observations are needed to define under which conditions the effect can occur. Till now only few observations are available, but more recordings in different solar regions with more statistics are needed. This effect could be observed in the Ca I 4227 Å line, but observations are needed in the Sr II 4078 Å line too. The observations will then help to guide the theoretical efforts.

The null result of the flare impact polarization observations is puzzling. Coordinated observations are planned with other observers, in particular with Jean Claude Henoux of Paris.

The continuum polarization still represents a great observational challenge that needs renewed efforts, since still no reliable determinations of its wavelength dependence are available. Both ZIMPOL observations, two beams exchange observations, should be tried again and the role of the seeing should be explored.

10.2 Development of IRSOL

In the preface it was pointed out that the present work has depended on the development of IRSOL, and I would like to conclude with some considerations about this.

The Institute of Astronomy in Zurich is developing a fully tuneable narrow-band filter based on lithium niobate Fabry Perot etalons. This system together with ZIMPOL would us allow to explore two-dimensional structures in narrow spectral bands (few tens of mÅ). Such instrument used at IRSOL could help us to explore previously unknown domains of solar physics.

Curriculum Vitae

of Michele Guglielmo Bianda, born April 24th 1956 in Locarno, Switzerland

1962–1967	elementary school in Ascona
1967–1976	secondary school and high school in Ascona
June 1976	Maturità federale
1976–1981	studies in Physics at the ETH Zurich
1981	Diploma thesis at the Institute of Astronomy in Zurich
1982	Diploma in Physics of ETH Zurich
1982–1987	researcher at the Specola Solare Ticinese in Locarno
1983–1985	part time Mathematics and Physics high school teacher
since 1987	scientific responsibility of the IRSOL
1999	3 months sommer student at Sacramento Peak, New Mexico
2001	3 months research scholar at Sacramento Peak